

Selbstorganisationsmechanismen niedrigdimensionaler Halbleiterstrukturen

Kumulative Habilitationsschrift

zur Erlangung des akademischen Grades

Dr. rer. nat. habil.

vorgelegt der Mathematisch-Naturwissenschaftlichen Fakultät II

der Martin-Luther-Universität Halle-Wittenberg

von

Herrn Dr. rer. nat. Michael Hanke

geb. am 04.09.1972 in Dessau

Gutachter:

1. Prof. Dr. Hans-Reiner Höche, Martin-Luther-Universität Halle-Wittenberg
2. Prof. Dr. Christian Teichert, Montanuniversität Leoben, Österreich
3. Prof. Dr. Günther Bauer, Universität Linz, Österreich

Halle/Saale, verteidigt am 12.Juni 2008, Probevorlesung am 07.Juli 2008

urn:nbn:de:gbv:3-000014007

[<http://nbn-resolving.de/urn/resolver.pl?urn=nbn%3Ade%3Agbv%3A3-000014007>]

Danksagung

Mein Dank geht an alle, die zum Gelingen dieser Arbeit beigetragen haben. An erster Stelle gilt er Prof. Dr. Hans-Reiner Höche und Dr. Christian Eisenschmidt für die vielfältige Unterstützung und die inspirierende Arbeitsatmosphäre in der Fachgruppe Festkörperanalytik. Seit meiner Zeit in Halle verbindet mich eine sehr enge und freundschaftliche Zusammenarbeit mit Dr. Frank Heyroth und Frank Syrowatka vom Interdisziplinären Zentrum für Materialwissenschaften der Martin-Luther-Universität Halle-Wittenberg, für die ich mich aufrichtig bedanke.

Die hier präsentierten Röntgenmessungen an niedrigdimensionalen Halbleiterstrukturen sind ausnahmslos entweder an der Hamburger Strahlungsquelle HASYLAB oder der European Synchrotron Radiation Facility (ESRF) in Grenoble durchgeführt worden. Es freut mich sehr, dass meine ehemaligen Berliner Kollegen, Dr. Peter Schäfer, Dr. Daniil Grigoriev und Dr. Martin Schmidbauer ihr *Know-how* in diverse gemeinsame Strahlzeiten einbrachten. Darüber hinaus möchte ich aber auch den *beamline scientists* an der ESRF Dr. Hartmut Metzger, Dr. Oleg Konovalov, Dr. Bernd Struth sowie am HASYLAB Dr. Wolfgang Drube, Dr. Horst Schulte-Schrepping, Dr. Oliver Seeck für die exzellenten Arbeitsbedingungen vor Ort danken.

Die untersuchten Proben wurden zum großen Teil speziell für die verschiedenen Untersuchungen hergestellt. Hier gilt mein Dank insbesondere Dr. Markus Pristovsek, Dr. Roman Sellin, Dr. Udo Pohl und Prof. Dr. Dieter Bimberg (Technische Universität Berlin), Dr. Yuriy Mazur, Dr. Zhiming Wang und Prof. Gregory Salamo (University of Arkansas, Fayetteville, USA), Dr. Euclides Marega Jr. (Instituto de Fisica de Sao Carlos, Sao Carlos, Brasilien) sowie den Herren Dr. Peter Werner und Dr. Nikolai Zakharov (Max-Planck-Institut für Mikrostrukturphysik, Halle). Eine in gewisser Weise herausragende Stellung kommt jedoch der Zusammenarbeit mit dem Institut für Kristallzüchtung (IKZ) in Berlin zu. Eine ganze Reihe von Arbeiten entstanden zusammen mit Dr. Torsten Boeck, Dr. Anne-Katrin Gerlitzke, Gerd Schadow und Herbert Wawra im Rahmen dreier gemeinsamer, zum Teil noch laufender Drittmittelprojekte.

Mein herzlichster Dank geht an Herrn Prof. Dr. Rolf Köhler für die beständige Förderung meiner Arbeit.

Inhaltsverzeichnis

Publikationen	1
1 Einleitung	5
1.1 Zielsetzung	5
1.2 Gliederung der Arbeit	5
2 SiGe/Si Stranski-Krastanow Inseln	7
2.1 Gleichgewichtsform	7
2.2 Laterale Positions korrelation	11
2.2.1 Entstehung lateraler Inselkorrelation auf Si(001)	11
2.2.2 Unidirektionale Ordnung auf höherindizierten Siliziumsubstraten .	15
2.2.3 Straininduziertes Wachstum von SiGe/Si- <i>dot molecules</i>	19
2.2.4 Template-basierte Ordnung mittels lokaler anodischer Oxidation .	23
2.2.5 Asymmetrische Korrelationsfunktion	27
2.3 Elastische Relaxation in diskontinuierlichen Benetzungsschichten	36
2.4 Besonderheiten gleichgewichtsfernen Wachstums	41
2.5 Strukturanalytik mittels diffuser Röntgenstreuung	46
2.5.1 Morphologieänderung und Konzentrationsgradient	46
2.5.2 Beugung unter streifendem Ein- und Austritt	55
2.5.3 Geometrisches Aspektverhältnis	67
2.5.4 Untersuchung lateraler Positions korrelation mit Strahlung finiter Kohärenzlänge	72
2.5.5 Diffuse Röntgenstreuung als Funktion chemischer Komposition und Deformation in 0-dimensionalen Heterostrukturen	77
3 GaAs-basierte Heterostrukturen	83
3.1 Kompositionsprofile in InGaAs/GaAs <i>quantum dots</i>	83
3.2 Deformationsfreie GaAs <i>quantum dot molecules</i>	92
3.3 Vertikal gestapelte InGaAs/GaAs <i>quantum rings</i>	96
3.4 Positions korrelierte InGaAs/GaAs <i>step bunches</i>	101
4 SiGe/Si Nanowhisker	107
5 Zusammenfassung	113
Anhang	115
Tabellarischer Lebenslauf	123

Publikationen

Die vorliegende Habilitationsschrift ist in einer kumulativen Form abgefasst. Sie basiert auf Ergebnissen der folgenden, chronologisch geordneten und bereits publizierten Arbeiten.

1. **M. Hanke**, Yu.I. Mazur, E. Marega Jr., Z.Y. AbuWaar, G.J. Salamo, P. Schäfer, M. Schmidbauer
Shape transformation during overgrowth of InGaAs/GaAs(001) quantum rings
Appl. Phys. Lett. **91**, 043103 (2007).
2. **M. Hanke**, C. Eisenschmidt, P. Werner, N. D. Zakharov, F. Syrowatka, F. Heyroth, P. Schäfer, O. Konovalov
Elastic strain relaxation in axial Si/Ge whisker heterostructures
Phys. Rev. B **75**, 161303(R) (2007).
3. **M. Hanke**, T. Boeck
On the various impact of chemical composition and elastic strain in SiGe nanoscale islands to the diffuse x-ray scattering
Physica E **32**, 69 (2006).
4. **M. Hanke**, T. Boeck, A.-K. Gerlitzke, F. Syrowatka, F. Heyroth
Dedicated fabrication of silicon-based ensembles of dot molecules with a specific and unique number of dots
Appl. Phys. Lett. **88**, 063119 (2006).
5. **M. Hanke**, T. Boeck, A.-K. Gerlitzke
Template-based assembling of SiGe/Si(001) dots by local anodic oxidation
Appl. Phys. Lett. **88**, 173106 (2006).
6. **M. Hanke**, T. Boeck, A.-K. Gerlitzke, F. Syrowatka, F. Heyroth
Elastic strain relaxation in discontinuous wetting layers and its impact on lateral ordering of heteroepitaxial dots
Phys. Rev. B **74**, 153304 (2006).
7. **M. Hanke**, M. Schmidbauer, D. Grigoriev, P. Schäfer, R. Köhler, T. H. Metzger, Zh. M. Wang, Yu. I. Mazur, G. J. Salamo
Zero-strain GaAs quantum dot molecules as investigated by x-ray diffuse scattering
Appl. Phys. Lett. **89**, 053116 (2006).
8. **M. Hanke**, T. Boeck, A.-K. Gerlitzke, F. Syrowatka, F. Heyroth
Unidirectional self-assembling of SiGe Stranski-Krastanow islands on Si(113)
Appl. Phys. Lett. **86**, 223109 (2005).

9. **M. Hanke**, T. Boeck, A.-K. Gerlitzke, F. Syrowatka, F. Heyroth, R. Köhler
Size, shape and ordering of LPE-SiGe/Si(001) islands grown under far non-equilibrium growth conditions
Appl. Phys. Lett. **86**, 142101 (2005).
10. M. Schmidbauer, **M. Hanke**, R. Köhler
Asymmetric Correlation Function Describing the Positional Ordering of LPE SiGe Nanoscale Islands
Phys. Rev. B **71**, 115323 (2005).
11. M. Schmidbauer, D. Grigoriev, **M. Hanke**, P. Schäfer, T. Wiebach, R. Köhler
Effects of Grazing Incidence on the X-Ray Diffuse Scattering from Self-Assembled Nanoscale Islands
Phys. Rev. B **71**, 115324 (2005).
12. **M. Hanke**, M. Schmidbauer, R. Köhler
Lateral correlation of SiGe Stranski-Krastanow islands on silicon as probed by high resolution x-ray diffraction
Jour. Appl. Phys. **96**, 1959 (2004).
13. **M. Hanke**, D. Grigoriev, M. Schmidbauer, P. Schäfer, R. Köhler, R. L. Sellin, U. W. Pohl, D. Bimberg
Vertical composition gradient in InGaAs/GaAs alloy quantum dots as revealed by high resolution x-ray diffraction
Appl. Phys. Lett. **85**, 3062 (2004).
14. **M. Hanke**, M. Schmidbauer, D. Grigoriev, R. Köhler
Aspect ratio of LPE-SiGe/Si(001) islands as probed by high resolution x-ray diffraction
Jour. Appl. Phys. **96**, 1447 (2004).
15. **M. Hanke**, M. Schmidbauer, R. Köhler, F. Syrowatka, A.-K. Gerlitzke, T. Boeck
Equilibrium shape of SiGe Stranski-Krastanow islands on silicon grown by liquid phase epitaxy
Appl. Phys. Lett. **84**, 5228 (2004).
16. **M. Hanke**, M. Schmidbauer, R. Köhler, H. Kirmse, M. Pristovsek
Lateral short range ordering of step bunches in MOCVD grown InGaAs/GaAs superlattices
Jour. Appl. Phys. **95**, 1736 (2004).
17. **M. Hanke**, D. Grigoriev, M. Schmidbauer, P. Schäfer, R. Köhler, U. W. Pohl, R. L. Sellin, D. Bimberg, N. D. Zakharov, P. Werner
Diffuse X-Ray Scattering of InGaAs/GaAs Quantum Dots
Physica E **21**, 684 (2004).

18. **M. Hanke**, M. Schmidbauer, D. Grigoriev, H. Raidt, P. Schäfer, R. Köhler, A.-K. Gerlitzke, H. Wawra
SiGe/Si(001) Stranski-Krastanow islands by liquid-phase epitaxy: Diffuse x-ray scattering versus growth observations
Phys. Rev. B **69**, 075317 (2004).
19. **M. Hanke**, H. Raidt, R. Köhler, H. Wawra
Island chain formation during liquid phase epitaxy of SiGe on silicon
Appl. Phys. Lett. **83**, 4927 (2003).

1 Einleitung

1.1 Zielsetzung

Die vorliegende Habilitationsschrift zielt im Kern auf ein besseres Verständnis von Selbstorganisationsmechanismen in niedrigdimensionalen Halbleiterstrukturen. Gut die Hälfte der ausgewählten Veröffentlichungen beschäftigen sich dabei mit sogenannten Stranski-Krastanow Inseln im System SiGe/Si, wobei das Wachstum ausnahmslos aus der Flüssigphase erfolgte. Es ist seit langem bekannt, dass dieser Prozess in vielen Fällen von einer ausgeprägten Positions korrelation begleitet wird. Ein zentraler Punkt war deshalb die Untersuchung der durch die Heteroepitaxie bedingten mechanischen Deformationen in der Umgebung einer bereits bestehenden Insel(formation) und die Frage, inwieweit diese das weitere Nukleationsgeschehen (aber auch die sich ausbildende chemische Komposition und mechanische Deformation) steuern. Darauf aufbauend stellt sich die Frage, ob und wie völlig selbstorganisierte Template in einem mehrstufigen Wachstumsexperiment als Ausgangspunkt für sogenanntes *directed self-assembling* genutzt werden können. Darüber hinaus sollte untersucht werden, wie sich Inselwachstum aus der Flüssigphase auf künstlich (durch lokale anodische Oxidation) strukturierten Substraten vollzieht. Eine Kombination aus Lithographie und selbst-organisiertem Wachstum erlaubt die Herstellung beliebig separierter Nanostrukturen. Der letzte Aspekt ist insofern von großem aktuellen Interesse, als dass sich Nanostrukturphysik zunehmend auf die Untersuchung individueller Objekte konzentriert. Dieser Trend bildet sich u.a. in der zunehmenden Verfügbarkeit hochbrillianter und auf wenige 100 nm fokussierter Röntgenquellen ab, wobei sich die genannten Strukturen als ein ausgezeichnetes Modellsystem anbieten.

Röntgenstreumethoden sind ein Mittel der Wahl, um mechanische Deformationen in Nanostrukturen nachzuweisen. Allerdings lässt sich aufgrund der fehlenden Phaseninformation aus den Streubildern nicht direkt in den Ortsraum zurückrechnen, so dass ein Simulationsverfahren entwickelt werden musste, mit dessen Hilfe indirekt auf die entsprechenden Parameter geschlossen werden kann.

GaAs-basierte Nanostrukturen besitzen (im Gegensatz zu Silizium und Germanium) eine direkte Bandlücke, die sie für opto-elektronische Anwendungen besonders interessant machen. Gleichermassen bestimmen aber auch hier strukturelle Parameter die finalen Eigenschaften. Am Beispiel verschiedener Nanostrukturen wie z.B. *quantum dots*, *quantum dot molecules*, *quantum rings* und *step bunches* wurde deshalb die gegenseitige Wechselbeziehung zwischen Form und Größe einerseits und chemischer Komposition und elastischer Relaxation andererseits genauer untersucht.

1.2 Gliederung der Arbeit

Im Folgenden sind aus dieser Arbeit resultierende (durchweg englischsprachige) Publikationen zusammengestellt. Allerdings sind diesen kurze deutsche Zusammenfassungen als Einleitung vorangestellt, die die Zielsetzung und Schlussfolgerungen der einzelnen

Veröffentlichungen im Gesamtkontext näher erläutern. Die Einteilung erfolgte nach den jeweiligen Materialsystemen der selbstorganisierten Nanostrukturen, die im Zentrum der Veröffentlichung stehen. So behandelt Kap. 2 Stranski-Krastanow Inseln im System SiGe/Si, während Kap. 3 einige Beispiele GaAs-basierter niedrigdimensionaler Halbleiterstrukturen zusammenfasst und Kap. 4 Deformationsrelaxation in axialen SiGe/Si Whiskern vorstellt.

Ausgehend von der Gleichgewichtsform von SiGe/Si(001) Inseln (Kap. 2.1) wird in Kap. 2.2 das *self-assembling* ganzer Inselensembles näher beleuchtet. Im Bereich der mit dem Stranski-Krastanow-Verfahren hergestellten Inseln erscheint derzeit eine Kombination aus lithographischen Verfahren und Selbstorganisation am erfolgversprechendsten, um die Vorteile beider Methoden auszunutzen: die gute Positionskontrolle und Homogenität, die durch Lithographie erreicht werden kann einerseits, und die Möglichkeit, Nanostrukturen defektfrei herzustellen, auf der anderen Seite. Der Einfluss einer stets vorhandenen sehr dünnen Benetzungsschicht für die Ausbildung lateraler Positions korrelation wird in Kap. 2.3 diskutiert. Im Rahmen dieser Arbeit wurden die SiGe/Si Inseln ausnahmslos mittels Flüssigphasenepitaxie (LPE) hergestellt, wobei das Wachstum im Allgemeinen sehr nahe am thermodynamischen Gleichgewicht erfolgt. Durch hohe Abkühl raten lässt sich LPE jedoch auch sehr gleichgewichtsfern betreiben. Unterschiede und Gemeinsamkeiten beider Grenzszenarien werden in Kap. 2.4 erörtert. Eine Reihe von Veröffentlichungen beschäftigt sich mit diffuser Röntgenstreuung zur Aufklärung von Form und Größe sowie mechanischer Deformation und lateraler Positions korrelation von SiGe/Si Stranski-Krastanow Inseln, Kap. 2.5. Dazu wurde ein numerisches Verfahren entwickelt, das ausgehend von dreidimensionalen Deformationsfeldern, wie sie mittels der Methode der Finiten Elemente bestimmt wurden, den Streuvorgang in einem kinematischen bzw. semi-kinematischen Ansatz behandelt. Wegen seiner hohen Perfektion eignen sich in diesem Zusammenhang SiGe/Si Stranski-Krastanow Inseln als Modellsystem in ganz besonderer Weise.

Dieses so etablierte numerische Verfahren wurde dann anschließend auch auf verschiedene GaAs-basierte Nanostrukturen, wie z.B. *quantum dots* (Kap. 3.1), *quantum dot molecules* (Kap. 3.2), *quantum rings* (Kap. 3.3), *step bunches* (Kap. 3.4) sowie axiale SiGe/Si Whiskerstrukturen (Kap. 4) ausgedehnt.

Die wichtigsten Ergebnisse und Schlussfolgerungen der vorliegenden Arbeit werden in Kap. 5 zusammenfassend dargestellt.

2 SiGe/Si Stranski-Krastanow Inseln

Sofern die Bewegung von Ladungsträgern in einem Halbleiter auf Dimensionen unterhalb der de-Broglie Wellenlänge beschränkt ist, führen Quantisierungseffekte im Gegensatz zum unendlich ausgedehnten Festkörper auf diskrete Energieniveaus. Grenzt man die Beweglichkeit in allen drei Dimensionen ein, entstehen sogenannte Quantenpunkte. Neben vergleichsweise aufwändigen lithographischen Verfahren zeigt die Bildung von Stranski-Krastanow Inseln durch elastischen Abbau von Deformationsenergie beim heteroepitaktischen Wachstum einen sehr eleganten Weg zur Herstellung geordneter null-dimensionaler Strukturen auf, die die vorangestellten Forderungen hinreichend gut erfüllen. Dabei kommt dem Gitterparameterunterschied zwischen Schicht und Substrat insofern eine Schlüsselrolle für die erreichbaren Dimensionen der Objekte zu, als dass mit zunehmend unterschiedlichem Gitterparameter die sich ausbildenden Inseln immer kleinere Ausmaße aufweisen. Die während des zunächst planaren Wachstums angesammelte Deformationsenergie kann in einem folgenden Wachstumsstadium über die Bildung von Oberflächenverwellungen und später durch die Ausbildung von teils facettierten Inseln auf Kosten einer erhöhten Oberflächenenergie wieder abgebaut werden. Dabei bleibt die Kohärenz des Kristallgitters an der Phasengrenze unterhalb einer bestimmten Schichtdicke erhalten, und erst in einem späteren Stadium können sich Fehlanpassungsversetzungen bilden. Durch die vermittelnde Wirkung des die Inseln umgebenden Deformationsfeldes können sich Inselensembles außerordentlich hoher lateraler Ordnung herausbilden, die durch das vertikale Abscheiden mehrerer heteroepitaktischer Schichten übereinander noch forciert werden kann.

2.1 Gleichgewichtsform

M. Hanke, M. Schmidbauer, R. Köhler, F. Syrowatka, A.-K. Gerlitzke, T. Boeck
Equilibrium shape of SiGe Stranski-Krastanow islands on silicon grown by liquid phase epitaxy
Appl. Phys. Lett. **84**, 5228 (2004).

Bemerkenswerterweise stoppt das Wachstum pseudomorpher SiGe/Si(001) Inseln stets, sobald ein Aspektverhältnis von etwa 2:1 (Basisbreite versus Inselhöhe) erreicht ist. Dieses ausgezeichnete Verhältnis stellt sich als Konsequenz einer höchst effektiven Oberflächenminimierung - und damit verbundenen Energieabsenkung - bei Vorhandensein von {111} Seiten- und einer (001)-Deckfacette ein. Im übrigen führt die finale Inselform (und insbesondere das Aspektverhältnis) zu speziellen Charakteristika in der diffusen Streuung in der Nähe asymmetrischer Gitterpunkte, die eine hochgenaue Anpassung der Modellform an die Messungen erlaubt, siehe Kap. 2.5.3.

Equilibrium shape of SiGe Stranski–Krastanow islands on silicon grown by liquid phase epitaxy

M. Hanke,^{a)} M. Schmidbauer, and R. Köhler

Institut für Physik, Humboldt-Universität zu Berlin, Newtonstrasse 15, D-12489 Berlin, Germany

F. Syrowatka

Interdisziplinäres Zentrum für Materialwissenschaften, Hoher Weg 8, D-06120 Halle/Saale, Germany

A.-K. Gerlitzke and T. Boeck

Institut für Kristallzüchtung, Max-Born-Strasse 2, D-12489 Berlin, Germany

(Received 10 December 2003; accepted 7 April 2004; published online 10 June 2004)

SiGe Stranski–Krastanow islands coherently grown on Si(001) substrates by liquid phase epitaxy are typically made of truncated pyramids with {111} side facets, whereas the persistent presence of an (001) top facet indicates an energetical disadvantage of complete pyramids compared to truncated ones. We attribute this to a surface minimization process during the island evolution under the assumption of isotropically distributed surface energies and stable island facets. For the presence of {111} side facets we have theoretically derived a final geometrical aspect ratio of island base versus island height of 1.96, which is in excellent agreement with the experimentally derived averaged value of 2.08 ± 0.10 within a concentration window between 9% and 30% germanium.

© 2004 American Institute of Physics. [DOI: 10.1063/1.1759070]

In the last decade, the study of dedicated growth and characterization of low-dimensional structures as quantum dots and quantum wires has attracted exceptional interest.¹ Therein the system SiGe on silicon has been widely used as a model system to study heteroepitaxial growth. Since in general the energy gain as a consequence of elastic strain relaxation can overcompensate for the loss in free surface energy three-dimensional, so-called Stranski–Krastanow² islands, become energetically favorable instead of a coherently strained two-dimensional film. Typically these islands do not grow immediately on the substrate material however on a thin wetting layer.³ Moreover the island positions are very often not randomly distributed. In truth a *self-organization* process can provide lateral^{4,5} and vertical⁶ as well as three-dimensional⁷ positional correlation of dot positions. However, a predictable growth model, the final dot shape, and a high monodispersity become rather desirable key features for any possible device application.

The first report on germanium islands on silicon⁸ as {105} faceted elongated pyramids grown by molecular beam epitaxy has been followed by a variety of impressive theoretical and experimental results concerning final island shapes and corresponding pre-staged during their evolution, e.g., Refs. 9–12. Theoretically the final island shapes are discussed within two limiting ideal cases. Various papers emphasize the importance of kinetic effects^{13,14} for island formation, where deposition, diffusion, and attachment as well as detachment are key features. However, the island *equilibrium* shape has to be seen in a thermodynamical equilibrium picture, where the total free energy tends to minimize. The gain in deformation energy, surface energy, and a contribu-

tion by edge energies summing up the total free energy of an isolated island. Since there is no solely theoretical framework which sufficiently describes all the relevant features most attempts rely on hybrid approaches, e.g., Refs. 15 and 16. This combines density functional theory to calculate microscopic parameters, surface energies, and surface stresses with linear elasticity theory for long-range strain field and strain relaxation in the investigated structures. We will show by a rather simple model that under the presence of stable island facets the surface free energy (and in particular its minimization with respect to a covered island volume) dominates the final shape of SiGe islands grown on silicon.

The samples investigated here have been grown by means of liquid phase epitaxy (LPE)—a growth method which operates rather close to thermodynamical equilibrium compared to techniques as molecular beam epitaxy or metalorganic chemical vapor deposition. Since there are only weak kinetic limitations present in LPE, it approaches the limit of a thermodynamical equilibrium better than any other growth technique and the grown structures show the quasi-equilibrium state. Since known surface energies at the solid–gas interface, e.g., Ref. 16, cannot be assigned for the solid–liquid interface within LPE we have considered the surface energy isotropically distributed. From the first view this assumption seems to be a rather rough one, however, taking this and stable facets into account we could ascribe the observed final aspect ratio between the island base and the final island height to a highly sufficient mechanism on the base of surface minimization during growth.

The scanning electron micrograph, shown in Fig. 1(a) taken on a sample with a comparatively low germanium concentration of 9% depicts various SiGe island stages. Recent investigations¹² show that the island evolution takes place throughout distinct growth stages starting with rather shallow lense-like islands without any faceting via faceted islands,

^{a)}Present address: Fachbereich Physik, Martin-Luther-Universität Halle-Wittenberg, Hoher Weg 8, D-06120 Halle/Saale, Germany; electronic mail: hanke@nist.gov

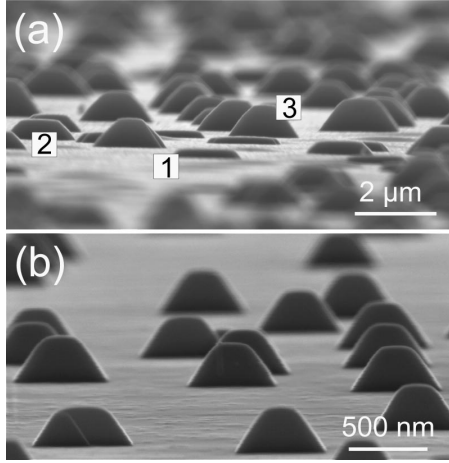


FIG. 1. Scanning electron micrographs of LPE-SiGe islands with nominal germanium content of 9% (a) and 17% (b). Island evolution takes place through various island stages starting from shallow lens like islands via faceted islands (1) and (2), whereas the final island morphology (3) depicts truncated pyramids with {111} side and an (001) top facet. At higher germanium contents (b) only final island stages could be observed.

labeled (1) and (2), and finally results in an island morphology (3) consisting of truncated pyramids with {111} side and an (001) top facet. Independent on the actual lattice mismatch the ensembles show a very narrow size distribution (5% full width at half maximum) for the final island stages. A precise analysis of the sample shown in Fig. 1(a) reveals an averaged island base along the [110] direction of 1660 nm and an averaged final island height of 780 nm resulting in a geometrical aspect ratio $Q=w/h$ of 2.13, where w denotes the island base width and h the final island height. This relationship even holds for higher lattice mismatches, see Fig. 1(b), which depicts islands containing 17% germanium. Here only final stages with a base of 575 nm and a height of 271 nm could be observed yielding $Q=2.12$. Even in case of 30% germanium, thus islands with a base width of 130 nm and a corresponding height of 65 nm an aspect ratio of two has been experimentally confirmed.⁵ Thus, we have found a geometrical aspect ratio of 2.08 ± 0.10 for germanium contents between 9% and 30%.

Generally it is interesting that a *truncated* coherently grown pyramid provides better strain relaxation than a complete one, indicating a rather sufficient mechanism which effectively terminates the growth at a certain island height where a top facet is still present. We trace this to a surface energy minimization. The mean total energy gain per atom is given by

$$\Delta E = \frac{A}{N_A \rho_m} \frac{1}{V} (E_V - E_S), \quad (1)$$

where A is the molar atomic mass, N_A Avogadro constant, ρ_m the mass density, and V the island volume. E_V and E_S are the total gains in strain and surface energy, respectively. Under the assumption that the strain energy is proportional to the enclosed volume and an isotropically distributed surface energy, thus $E_V = c_1 V$ and $E_S = c_2 S$, where S denotes the total surface which has to be minimized with respect to the island volume

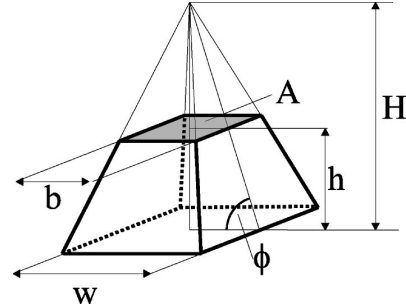


FIG. 2. Schematic model of a truncated pyramid with base length w , height h , and facet angle Φ , whereas a complete pyramid with same w and Φ would reach the final height H .

$$\frac{S}{V} = \text{Min} \quad (2)$$

in order to maximize the total energy gain ΔE . We have to state clearly that in our approach an additional height and shape dependence of the parameter c_1 will be neglected, since we have shown previously¹⁷ by finite element calculations that for truncated LPE-grown SiGe pyramids on silicon with {111} side facets and an (001) top facet the lattice is perfectly elastically relaxed within the upper half. Even rather shallow islands with a height of 15 nm and a base width of 50 nm, resulting in a facet angle of $\Phi=30^\circ$, are fully relaxed at the island apex.¹⁸ Hence, c_1 obviously does not depend on the actual position within the island. Since the lateral island size will be determined during early prestages by the actual lattice mismatch,¹⁹ the growth suspends mainly at the island top,¹² see also the labeled island types of same base however different in height in Fig. 1(a), where a constant c_1 becomes an evident assumption. On the other hand plastically relaxed LPE-SiGe islands are typically made of pyramids with {111} side but without any top facet (not shown here). This shape cannot be explained by our model because the underlying strictly linear dependence between energy gain and enclosed volume of dislocation-free islands becomes invalid for plastically relaxed structures.

For a truncated pyramid as depicted in Fig. 2 (base w , top width b , height h , and a corresponding facet angle Φ) the ratio S/V can be expressed after some simple mathematics:

$$\begin{aligned} \frac{S}{V} &= 6 \frac{w^2 - b^2(1 - \cos \Phi)}{(w^3 - b^3)\sin \Phi} \\ &= \frac{6}{w} \frac{1 - \left(1 - \frac{h}{H}\right)^2 (1 - \cos \Phi)}{\left(1 - \left(1 - \frac{h}{H}\right)^3\right) \sin \Phi}. \end{aligned} \quad (3)$$

A numerical treatment of Eq. (3) as a function of a normalized height h/H , where H denotes the height of a complete pyramid, has been done for various facet angles $\Phi_A = 80^\circ$, $\Phi_B = 54.7^\circ$, and finally $\Phi_C = 30^\circ$. The value Φ_B corresponds to {111} side facets as experimentally observed. As shown in Fig. 3 the minima in S/V are rather flat, however, within the first derivative

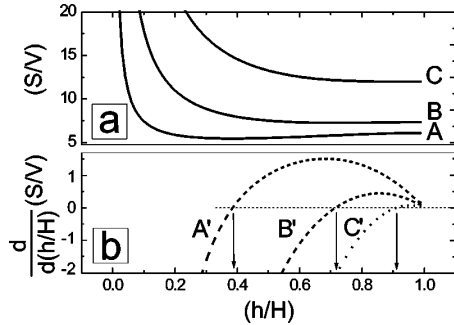


FIG. 3. (a) Calculated ratio S/V and its first derivative (b) as a function of a normalized height h/H for truncated pyramids with various facet angles Φ . $\Phi_A=80^\circ$, $\Phi_B=54.7^\circ$, and $\Phi_C=30^\circ$.

$$\frac{d}{d(h/H)}(S/V) \quad (4)$$

the zero-crossings indicate their exact position which are $(h/H)_{30}=0.91$, $(h/H)_{54.7}=0.72$ and $(h/H)_{80}=0.39$. Thus, pyramids with steeper facets tend to be not as high as those with flat facets. Beside this general tendency we will stress the particular geometrical aspect ratio $Q=w/h=1.96$ derived from $(h/H)_{54.7}$, which is in good agreement with the experimentally observed ratio of 2.08 ± 0.10 .

At the example of LPE-SiGe Stranski–Krastanow islands with a germanium content of 9% and 17% we have shown that the final island stage consists of a truncated pyramid with $\{111\}$ side and an $\{001\}$ top facet, whereas a geometrical aspect ratio of island base versus height of nearly two will be achieved. On the base of isotropically distributed surface energies and stable facets, we could trace this result to a surface minimization process during the growth which will effectively suspend further vertical growth after a certain island height is achieved. Moreover within a concentration range between 9% and 30% germanium a respective averaged aspect ratio of 2.08 ± 0.10 was found which is in excellent agreement with the theoretically derived value of 1.96.

The authors would like to thank H. Wawra from the Institute of Crystal Growth in Berlin for valuable discussions. This work was sponsored by the Deutsche Forschungsgemeinschaft under Project No. KO1510/2.

- ¹D. Bimberg, M. Grundmann, and N. N. Ledentsov, *Quantum Dot Heterostructures* (Wiley, Chichester, 1999).
- ²I. Stranski and L. Krastanow, *Sitzungsber. Akad. Wiss. Wien, Math.-Naturwiss. Kl., Abt. 2B* **146**, 797 (1937).
- ³S. A. Chaparro, Y. Zhang, and J. Drucker, *Appl. Phys. Lett.* **76**, 3534 (2000).
- ⁴M. Meixner, E. Schöll, M. Schmidbauer, H. Raidt, and R. Köhler, *Phys. Rev. B* **64**, 245307 (2001).
- ⁵M. Hanke, H. Raidt, R. Köhler, and H. Wawra, *Appl. Phys. Lett.* **83**, 4927 (2003).
- ⁶Q. Xie, A. Madhukar, P. Chen, and N. Kobayashi, *Phys. Rev. Lett.* **75**, 2542 (1995).
- ⁷G. Springholz, V. Holý, M. Pinczelits, and G. Bauer, *Science* **282**, 734 (1998).
- ⁸Y.-W. Mo, D. E. Savage, B. S. Swartzentruber, and M. G. Lagally, *Phys. Rev. Lett.* **65**, 1020 (1990).
- ⁹V. M. Kaganer and K. H. Ploog, *Phys. Rev. B* **64**, 205301 (2001).
- ¹⁰J. Tersoff, B. Spencer, A. Rastelli, and H. von Känel, *Phys. Rev. Lett.* **89**, 196104 (2002).
- ¹¹A. Rastelli, H. von Känel, B. Spencer, and J. Tersoff, *Phys. Rev. B* **68**, 115301 (2003).
- ¹²M. Hanke, M. Schmidbauer, D. Grigoriev, P. Schäfer, R. Köhler, A.-K. Gerlitzke, and H. Wawra, *Phys. Rev. B* **69**, 075317 (2004).
- ¹³Y. Chen and J. Washburn, *Phys. Rev. Lett.* **77**, 4046 (1996).
- ¹⁴H. Dobbs, D. Vvedensky, A. Zangwill, J. Johansson, N. Carlson, and W. Seifert, *Phys. Rev. Lett.* **79**, 897 (1997).
- ¹⁵Q. K. K. Liu, N. Moll, M. Scheffler, and E. Pehlke, *Phys. Rev. B* **60**, 17008 (1999).
- ¹⁶N. Moll, M. Scheffler, and E. Pehlke, *Phys. Rev. B* **58**, 4566 (1998).
- ¹⁷T. Wiebach, M. Schmidbauer, M. Hanke, H. Raidt, R. Köhler, and H. Wawra, *Phys. Rev. B* **61**, 5571 (2000).
- ¹⁸M. Schmidbauer, F. Hatami, M. Hanke, P. Schäfer, K. Braune, W. Masselink, R. Köhler, and M. Ramsteiner, *Phys. Rev. B* **65**, 125320 (2002).
- ¹⁹W. Dorsch, B. Steiner, M. Albrecht, H. P. Strunk, H. Wawra, and G. Wagner, *J. Cryst. Growth* **183**, 305 (1998).

2.2 Laterale Positionskorrelation

2.2.1 Entstehung lateraler Inselkorrelation auf Si(001)

M. Hanke, H. Raidt, R. Köhler, H. Wawra

Island chain formation during liquid phase epitaxy of SiGe on silicon

Appl. Phys. Lett. **83**, 4927 (2003).

Für eine vergleichsweise große Gitterfehlpassung von 1.26% lässt sich gut die Entstehung lateraler Inselkorrelation¹ im System SiGe/Si(001) *ex-situ* mittels direktabbildender Atomkraftmikroskopie verfolgen. Unterschiedliche Bedeckungsgrade von etwa drei Inseln je μm^2 bis zum vierfachen Wert gestatten die Untersuchung aufeinander folgender Stadien, so dass retrospektiv auf die Entstehung der Korrelation geschlossen werden kann.

Während sich bei der geringsten Bedeckung die meisten Inseln in sogenannten Dimeren entlang einer $\langle 100 \rangle$ Richtung bevorzugt anordnen, treten mit zunehmender Dichte immer längere Ketten entlang $\langle 100 \rangle$ auf. Diese entstehen durch Nukleation an den Enden bereits bestehender Formationen. Interessanterweise wird ein Abknicken dieser Ketten nicht beobachtet, was den Schluss nahelegt, dass die jeweils letzte Insel innerhalb einer Kette sowohl den Deformationseinfluss der direkt benachbarten Insel, aber auch den der vorletzten Insel spüren muss.²

Dieser Befund lässt sich durch vergleichende Finite Elemente Berechnungen zur mechanischen Deformation in der Umgebung einer freistehenden SiGe/Si(001) Insel und eines Inseldimers erhärten. Aufgrund der elastischen Anisotropie fällt die Deformationsenergiedichte entlang der elastisch weicheren $\langle 100 \rangle$ Richtungen stets schneller ab als entlang $\langle 110 \rangle$ - ein Indiz für eine höhere Nukleationswahrscheinlichkeit in einem kleineren Abstand entlang $\langle 100 \rangle$. Auf der anderen Seite fehlt jedoch ein ausgeprägtes Energieminimum, das sich aber ergibt, sofern man einen spannungsinduzierten Abtrag der Benetzungsschicht berücksichtigt, siehe dazu Kap. 2.3. Die vierzählige Symmetrie reduziert sich im Fall eines Dimers, wobei dann die Deformationsenergiedichte schneller entlang der Hauptdiagonalen des Dimers abfällt als senkrecht dazu. Die Richtung einer Kette ist folglich bereits durch die Vorzugsrichtung des Dimers festgelegt.

¹In Kap. 2.5 wird im Gegensatz dazu die Formänderung einzelner Inseln bei kleinen Gitterfehlpassungen von 0.38% diskutiert.

²Andernfalls würde man keine ausgedehnten linearen Anordnungen beobachten. Eine denkbare Vorstrukturierung, ähnlich dem bei kleinen Gitterfehlpassungen beobachteten *rippling* würde ein vergleichbares Ergebnis zur Folge haben, konnte in diesem Fall jedoch nicht nachgewiesen werden.

Island chain formation during liquid phase epitaxy of SiGe on silicon

M. Hanke,^{a)} H. Raidt, and R. Köhler

Institut für Physik, Humboldt-Universität zu Berlin, Newtonstrasse 15, D-12489 Berlin

H. Wawra

Institut für Kristallzüchtung, Max-Born-Strasse 2, D-12489 Berlin

(Received 14 July 2003; accepted 17 October 2003)

We report on the evolution of lateral ordering of SiGe nanoscale islands on Si(001), which have been grown by means of liquid phase epitaxy in the Stranski-Krastanow mode. Applying *post-growth* atomic force microscopy on different sample areas covered by different island densities, we could trace *ex-situ* the development of extended island chains along the ⟨100⟩-directions. The linear alignment happens by further nucleation of islands at the end of an already existing formation. Those direct observations will be discussed in terms of finite element strain energy calculations around various island configurations. © 2003 American Institute of Physics.

[DOI: 10.1063/1.1633028]

Self-organization of low dimensional structures as e.g. quantum dots (QDs) and the physics behind it has been attracted much interest in semiconductor physics during the past decade.¹ One very promising way towards dislocation-free nanoscale islands and QDs takes advantage of strain relief during heteroepitaxial growth. Since the energy gain from elastic relaxation can overcompensate the loss in surface free energy the formation of three-dimensional objects becomes energetically favorable. Very often this so-called Stranski–Krastanow growth mode is accompanied by the formation of lateral,² vertical,³ and even three-dimensional positional correlation.⁴

Previous investigations^{3,5} discuss self-organization in terms of energetics. Thus, one could directly prove a significant influence of spacer layer thickness on the vertical inheritance of QD positions, e.g., in laser stacks, indicating the importance of strain. In this paper we will emphasize its influence on the development of lateral ordering. Besides, an additional path towards extended island chains has been reported, which is based on a self-organized underlying ripple pattern as a precursor in view of further island nucleation.⁶ In the case of $\text{Si}_{1-x}\text{Ge}_x/\text{Si}(001)$ such an initial pattern has been observed only for comparatively small lattice mismatches below 0.6%. However, a pronounced lateral ordering appears within a wide range of concentration x , even where the amplitude of a ripple pattern is believed to be smaller than a lattice parameter.

In this study, we examine a particular sample which has been grown by means of liquid phase epitaxy (LPE) using a slide-boat reactor. In contrast to other growth techniques as molecular beam epitaxy or metalorganic chemical vapor deposition LPE operates comparatively close to thermodynamical equilibrium. Consequently, LPE-grown islands yield a similar shape for an extended concentration range.

To ensure a high purity of the epitaxial layers the entire process has to be performed under a pure hydrogen atmo-

sphere. In a first step Si and Ge will be solved in a Bi-solution which will be homogenized for several hours at growth temperature to equilibrate the system thermodynamically. After *in-situ* desorption of an oxide layer at 930 °C the Si–Ge–Bi solution is brought into contact with the target substrate. To initialize the growth an oversaturation was established by choosing a growth temperature up to 2 K below saturation temperature.

The following observations prove a significant influence of strain energy distribution around an island and multi-island configurations on the self-organization process. For germanium contents smaller than 15% the island growth happens on a time scale which allows a detailed view on different stages by *ex-situ* AFM.⁷ By increasing the lattice mismatch the corresponding final island size will linearly shrink on a double logarithmic scale,⁸ whereas the time necessary to nucleate an island will drastically decrease. Hence, for germanium contents higher than 15% we could not observe different stages of an individual island, however, as an additional subsequent process the formation of island–island correlation could be traced.

The sequence of atomic force micrographs depicted in Fig. 1 were made on a particular sample containing various island densities within the range of 2.6 islands per μm^2 in (a) up to nearly the four-fold value in (c), whereas the individual island shape is not affected by the coverage. Without exception all islands consist of truncated pyramids with {111} side facets and an (001) top facet. It is interesting to note that all of them appear with a constant aspect ratio island base/height $b_{[110]}/h$ of nearly two. All over the sample dust particles P have been deposited incidently after growth. They are visible as larger objects.

Most SiGe islands appear as single objects S in the area of lowest coverage, thus there are no adjacent islands within a given distance and direction, however, even in Fig. 1(a) some dimers D, and, very rarely trimers T have evolved already. Those multi-island configurations follow the elastically soft ⟨100⟩-directions. By increasing the island coverage the absolute amount of single islands will decrease and longer chains made of up to 12 islands in (c) appear.

^{a)}Present address: Fachbereich Physik, Martin-Luther-Universität Halle-Wittenberg, Hoher Weg 8, D-06120 Halle/Saale; electronic mail: hanke@physik.uni-halle.de

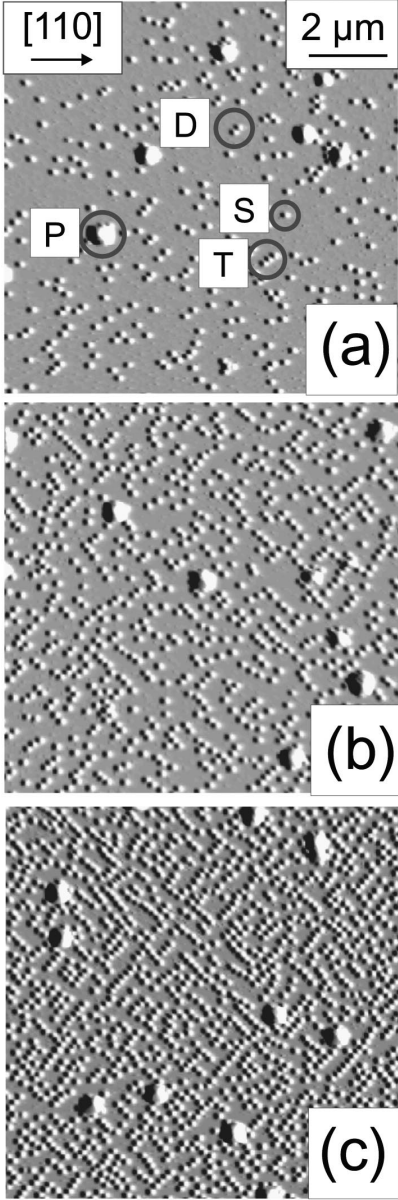


FIG. 1. Atomic force micrographs of a $\text{Si}_{0.7}\text{Ge}_{0.3}$ sample showing different island coverages. (a) 2.6, (b) 6.3 (c) 10.8 islands per μm^2 . All the SiGe islands occur with the same height of approximately 65 nm. Dust particles shown as comparatively large objects have been deposited incidentally *post-growth* all over the sample.

Outgoing from the *post-growth* micrographs we could deduce the path towards extended island chains. In general, this process is based on two distinct steps. Since we have found a near balance between [100]- and [010]-dimers in Fig. 1(a), at the very beginning, it has to remain still open into which particular $\langle 100 \rangle$ direction the subsequent island chain will develop. This behavior can be related to the four-fold symmetry of the strain energy distribution around a single, well separated SiGe island, which favors further nucleation along the island diagonal into all $\langle 100 \rangle$ directions with the same probability, and, on the other hand it effec-

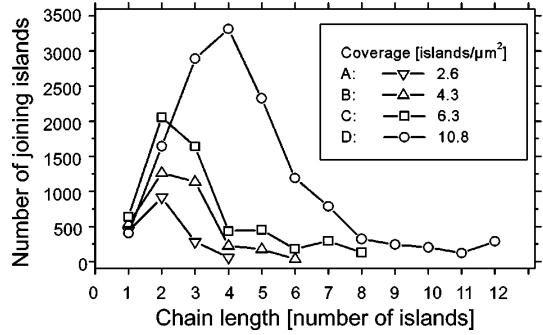


FIG. 2. The total number of islands arranged within chains of a particular length as a function of chain length (abscissa) and island density.

tively suppresses nucleation along $\langle 110 \rangle$ within the immediate environment. After a certain direction has been selected by forming a dimer the symmetry will be reduced down to a two-fold one. Consequently, the growth will proceed along the selected direction by subsequent island nucleation at the end of an already existing chain. This gives us a strong evidence that not only the strain field caused by the outermost island but at least the second to last in a chain considerably enforces the linear alignment. The observed process seems to be highly efficient since there are no zigzag-like configurations in Fig. 1 visible.

A numerical analysis of the island distributions depicted in Fig. 1 plots the total amount of islands accumulated within a certain type of chain as a function of the length for the different coverages. Figure 2 reveals quantitatively that the total amount of single islands does not significantly depend on the island density, whereas the maximum of the distribution shifts towards longer island chains with increasing coverage, and the longest realized chain length increases approximately linearly with coverage.

Since there is no indication of an underlying ripple pattern within the atomic force micrographs we argue that the strain energy distribution around a certain configuration controls to some extend this process. Figure 3 depicts the normalized strain energy at the surface as calculated by the finite element method⁹ around two different configurations. Within the model the islands have been modeled by truncated pyramids bounded by [111] side facets and an (001) top facet with a base length $b_{[110]}$ of 130 nm and an aspect ratio of exactly two. Model (a) considers a single $\text{Si}_{0.7}\text{Ge}_{0.3}$ pyramid, whereas (b) refers to a dimer configuration, wherein the islands' centers are 230 nm apart from each other, regarding the averaged distance revealed from Fig. 1. They have been positioned on top of a flat, thin 2 nm wetting layer of same germanium content which covers a Si(001) substrate material. The elastic constants c_{ijkl} have been applied assuming Vegard's law for the binary compound $\text{Si}_{1-x}\text{Ge}_x$. The strain energy distribution in Fig. 3(a) reflects the typical four-fold symmetry of Young's modulus in the considered configuration, where the different $\langle 100 \rangle$ directions are equivalent, while the distribution (b) shows a reduced symmetry: where the strain energy decreases slightly faster along the main axis than perpendicular to that, $L_{100} < L_{010}$. It is worth noting explicitly that we could neither prove an energy *minimum* along a certain direction nor a local *maximum* along the

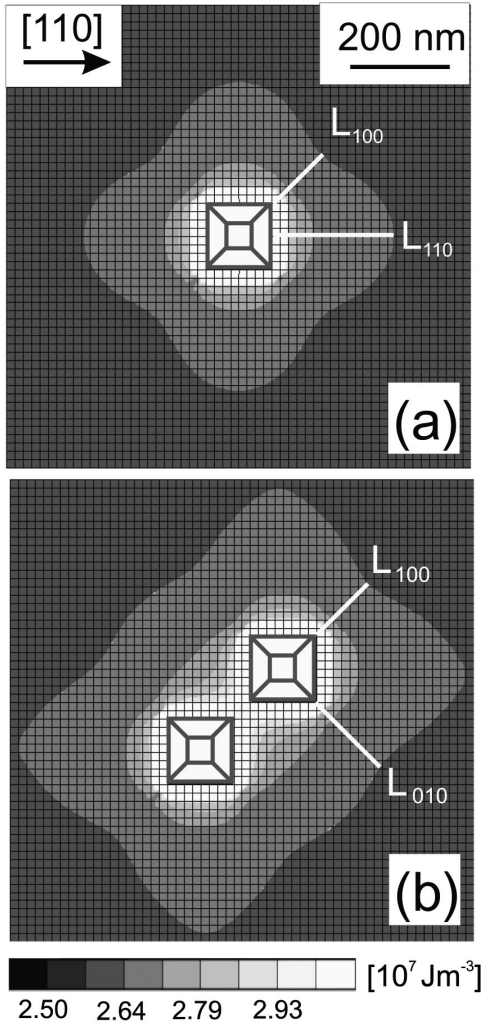


FIG. 3. The strain energy distribution at the surface of the wetting layer around a single island (a) and a dimer (b), respectively. The islands themselves are shown schematically. The energy has been normalized to an atom.

[110] direction which can lead to an averaged flux of adatoms into the elastically soft direction.² Hence, the strain energy as shown in Fig. 3 in view of an anisotropic decay has to be considered only as a weak hint towards self-organization into chains.

On the other hand, this weak indication stresses the importance of another morphological particularity which has not been taken into account yet within the presented FEM simulations. Several papers^{10,11} report on the phenomenon that the strain energy around a Stranski–Krastanow island can overcompensate the driving forces of growth and even can cause a resolving of already grown material. In case of liquid phase epitaxy of SiGe on silicon a wetting layer depletion has been demonstrated,⁷ whose shape follows exactly the strain energy distribution in Fig. 3(a). The unresolved, remaining material path along the island diagonal will elastically relax, since there is no additional material aside. Consequently, a wetting layer depletion, which traces the strain energy distribution, will enforce the energy minimization along the ⟨100⟩-direction.

In conclusion we have monitored *ex-situ* the self-organization of laterally ordered SiGe/Si(001) Stranski–Krastanow nanoscale islands. Atomic force micrographs taken on a sample containing various island coverages point out that the formation of extended island chains along the elastically soft ⟨100⟩-direction happens by subsequent nucleation at the end of an already existing formation. Since there is no indication of an underlying ripple pattern we argue a strong influence of strain energy on the linear alignment.

This project was sponsored by the German Research Society under Project No. KO1510/2.

¹D. Bimberg, M. Grundmann, and N. N. Ledentsov, *Quantum Dot Heterostructures* (Wiley, Chichester, NY, 1999).

²M. Meixner, E. Schöll, M. Schmidbauer, H. Raidt, and R. Köhler, Phys. Rev. B **64**, 245307 (2001).

³Q. Xie, A. Madhukar, P. Chen, and N. Kobayashi, Phys. Rev. Lett. **75**, 2542 (1995).

⁴G. Springholz, V. Holý, M. Pinczelits, and G. Bauer, Science **282**, 734 (1998).

⁵J. Tersoff, C. Teichert, and M. G. Lagally, Phys. Rev. Lett. **76**, 1675 (1996).

⁶W. Dorsch, B. Steiner, M. Albrecht, H. P. Strunk, H. Wawra, and G. Wagner, J. Cryst. Growth **183**, 305 (1998).

⁷M. Hanke, M. Schmidbauer, D. Grigoriev, H. Raidt, P. Schäfer, R. Köhler, A.-K. Gerlitzke, and H. Wawra, submitted to Phys. Rev. B.

⁸W. Dorsch, H. P. Strunk, H. Wawra, G. Wagner, J. Groenen, and R. Carles, Appl. Phys. Lett. **72**, 179 (1998).

⁹Program package MarcMentat™.

¹⁰X. Z. Liao, J. Zou, D. J. H. Cockayne, J. Qin, Z. M. Jiang, X. Wang, and R. Leon, Phys. Rev. B **60**, 15605 (1999).

¹¹U. Denker, O. G. Schmidt, N. Y. Jin-Phillip, and K. Eberl, Appl. Phys. Lett. **78**, 3723 (2001).

2.2.2 Unidirektionale Ordnung auf höherindizierten Siliziumsubstraten

M. Hanke, T. Boeck, A.-K. Gerlitzke, F. Syrowatka, F. Heyroth

Unidirectional self-assembling of SiGe Stranski-Krastanow islands on Si(113)

Appl. Phys. Lett. **86**, 223109 (2005).

Wie im vorangegangenen Kapitel diskutiert, wird auf nicht strukturierten Substraten die Entstehung lateraler Positions korrelation im Wesentlichen durch die elastische Anisotropie des Substrates getrieben. Höherindizierte Substrate weisen im Allgemeinen jedoch eine geringere Oberflächensymmetrie auf, was sie als Ausgangspunkt für die Selbstorganisation niedriger symmetrischer Inselensembles prädestiniert.

Hier wurde eine kombinierter³ Ansatz aus primärer Homo- und subsequenter SiGe Heteroepitaxie auf Si(113) Substraten verfolgt. Die Züchtung reinen Siliziums aus der Flüssigphase auf poliertem Si(113) führt zu alternierenden (111) und (116) Facetten, deren Stufenkanten entlang [110] verlaufen, und somit ein unidirektionales Template bilden. Allerdings erfolgt dieser erste Teilprozess aus einer Indiumschmelze bei vergleichsweise hoher Temperatur zwischen 930°C und 920°C. Um nun die homoepitaktische Oberflächenmorphologie während der folgenden SiGe Heteroepitaxie zu nutzen, muss dieser bei deutlich niedriger Temperatur erfolgen. Hierfür bietet sich eine Bismutschmelze an, die eine Züchtung bei 590°C erlaubt. AFM Aufnahmen belegen, dass die SiGe Insel bevorzugt in den Gräben des homoepitaktischen Templates nukleieren. Bemerkenswerterweise beträgt der Insel-Insel Abstand senkrecht zu den Inselketten jedoch etwa das 1.6-fache des vergleichbaren Stufen-Stufen Abstandes im Template. Offenbar dient nicht jeder der durch die (111) und (116) gebildeten Gräben als Nukleationspunkt.

Verstehen lässt sich die Diskrepanz durch das heteroepitaktisch bedingte Deformati ons feld während des Inselwachstums. Finite Elemente Berechnungen für eine einzelne, in einem solchen Graben positionierte Insel belegen eine lateral nach außen und vertikal nach innen gerichtete Verschiebung des Kristallgitters in benachbarten Gräben - eine energetisch ungünstige Ausgangsposition für Inselnukleation an diesen Stellen. Sobald also eine Insel vorhanden ist, wird Inselnukleation in direkt benachbarten Gräben benachteiligt. Im Ergebnis führt dies zu einem deutlich vergrößerten Insel-Insel Abstand im Vergleich zum Template.

³Mehrstufige Prozesse, die eine (wenn auch selbstorganisierte) Vorstrukturierung beinhalten, werden in der Literatur oft unter dem Begriff 'directed self-assembling' geführt.

APPLIED PHYSICS LETTERS 86, 223109 (2005)

Unidirectional self-assembling of SiGe Stranski-Krastanow islands on Si(113)

M. Hanke^{a)}*Martin-Luther-Universität Halle-Wittenberg, Fachbereich Physik, Hoher Weg 8, D-06120 Halle/Saale, Germany*

T. Boeck and A.-K. Gerlitzke

Institut für Kristallzüchtung, Max-Born-Strasse 2, D-12489 Berlin, Germany

F. Syrowatka and F. Heyroth

Interdisziplinäres Zentrum für Materialwissenschaften, Hoher Weg 8, D-06120 Halle/Saale, Germany

(Received 25 March 2005; accepted 26 April 2005; published online 26 May 2005)

We report on a dedicated two-step liquid phase epitaxy (LPE) experiment yielding ensembles of SiGe/Si(113) nanoscale islands with unidirectional ordering along the [110] direction. Initial homoepitaxy of silicon on a polished Si(113) wafer from an indium solution at 930 °C results in a highly regular pattern consisting of (111) and (116) facets. For the subsequent heteroepitaxy with SiGe the solvent has been exchanged for bismuth since it enables an LPE process at considerably lower temperatures around 590 °C, and thus preserves the initial template which strictly enforces the linear self-assembling of SiGe islands. However, with respect to the initial grooves the established island-island correlation length perpendicular to them has been increased by a factor of about 1.6 indicating that not every groove acts as a nucleation place. This can be explained by finite element calculations on the three-dimensional deformation field which proves energetically favorable nucleation sites in the island vicinity within and unfavorable places in adjacent rows.

© 2005 American Institute of Physics. [DOI: 10.1063/1.1943490]

Well ordered nanoscale objects are suited candidates as a part of optoelectronic device applications as, e.g., 2d-photon crystals.¹ Since most *topdown* approaches are comparatively slow and expensive, the self-formation and hierarchically the self-*assembling* of nanostructures provide an elegant and simple alternative. In that context SiGe/Si widely served as a model system for a better understanding of the underlying phenomena, in particular the mutual impact of strain and shape evolution during heteroepitaxial growth.^{2–4} In view of future device applications, on the other hand, a comprehensive knowledge of the epitaxial process becomes mandatory for any dedicated growth of low-dimensional structures.

At the beginning of the so-called Stranski-Krastanow (SK) growth mode a very thin and planar layer wets the surface. However, with increasing thickness, respectively, ongoing epitaxy, the strain energy stored in a deformed crystal lattice increases as well, and eventually the growth changes from a planar layer by layer to a three-dimensional mode since the energy gain due to elastic relaxation overcompensates the additional free surface energy. In the limit of thermodynamical equilibrium, as it is nearly realized in a liquid phase epitaxy (LPE) experiment, the islands tend to take their equilibrium shape.⁵ Moreover the performance of, e.g., 2d-photon crystals might be reinforced if the dot positions can be controlled to a high degree of precision, whereas the assembling can either be induced by an artificial prepattern,⁶ or in a self-organized way, e.g., Refs. 7–11. In the case of SiGe/Si(001)-LPE the particular fourfold crystallographic symmetry of the substrate causes a pronounced chessboard-like pattern with extended island chains along

{100}.¹² This can be understood in terms of the anisotropic strain field surrounding an initial island which suppresses nucleation along the stiffer {110} direction. However, as soon as an island dimer has been formed the fourfold symmetry of the single island strain field will be locally reduced to a two-fold symmetry favoring nucleation along the main axes of the dimer.¹³

In this letter, we deal with the unidirectional ordering of faceted SiGe islands on Si(113) substrates grown by means of liquid phase epitaxy (LPE) applying a conventional slide-boat reactor. During the entire growth process a pure hydrogen atmosphere ensures an extremely clean environment. The native oxid layer was removed by a thermal treatment at 930 °C for 180 min prior to the actual LPE process. In the first and high temperature regime a homoepitaxial silicon layer was deposited from an indium-silicon solution cooling down from 930 to 925 °C with a gradient of 5 K/h. Originating from step wandering the silicon deposition results in a groove-like topology as depicted in Fig. 1(a). It shows alternating faces inclined by 29.1° and 12.7° which can be attributed to (111) (29.50°) and (116) (11.98°) facets. A lateral period of 125 nm along with an averaged height of about 19 nm preserves the mean Si(113) surface orientation whereas the lateral aspect ratio of groove length (typically 2–3 μm) vs width amounts to 15–25. In contrast to the four-fold symmetry of shallow surface undulations formed during initial stages of SiGe heteroepitaxy on Si(001), e.g., Ref. 14, the pattern in Fig. 1(a) displays a reduced twofold symmetry.

In order to avoid resolving of the template during subsequent heteroepitaxy the initial solvent indium has been exchanged for bismuth since it enables the LPE process at considerably lower temperatures. Subsequent to the mandatory homogenization of the Bi-Si-Ge solution several hours at

^{a)}Electronic mail: hanke@physik.uni-halle.de

223109-2 Hanke et al.

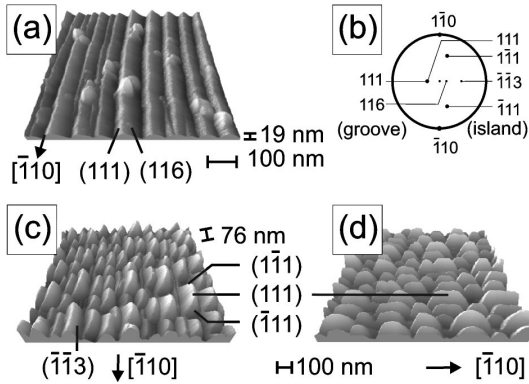


FIG. 1. Detailed atomic force micrograph of the homoepitaxial Si(113) surface (a) depicts a regular groove-like pattern which consists of alternating (111) and (116) facets, whereas the micrographs (c) and (d) were taken after the SiGe heteroepitaxy along and perpendicular to the initial groove structure, respectively. The realized inclination angles indicate the presence of three {111} and a single $\{\bar{1}\bar{1}3\}$ facet; (b) shows a stereographic projection on the (113) surface comprising the relevant crystallographic directions.

10 K above the starting temperature of 590 °C a slow cooling step with 10 K/h initiates the island growth. Hereafter the solution has been removed from the target.

Figure 1 depicts perspective views on the final morphology along (c) and perpendicular (d) to the grooves. Since homoepitaxial pattern and heteroepitaxial SiGe islands have been grown from different solutions the incorporated amount of germanium can be adjusted independently from the lateral periodicity, whereas in the recent experiment the germanium content amounts to 33%. To some extent the island morphology resembles the equilibrium shape of LPE-SiGe islands grown on Si(001) substrates which consists of four {111} and a single (001) top facet.⁵ However, the recent ones are truncated by three adjacent {111} facets, namely $(\bar{1}11)$, $(1\bar{1}1)$ (both inclined by 45.87°) and (111) (29.50°) and a single $(\bar{1}\bar{1}3)$ (50.48°) facet. The latter one does not flip open towards a fourth $(\bar{1}11)$ facet (which would be inclined by 79.98°) indicating an energetical drawback to form very steep facets due to the additional free surface energy. In contrast to SiGe/Si(001) islands there is no evidence for an (001) oriented facet. Since nucleation on the (111) facet of the initial pattern in Fig. 1(a) is energetically rather unlikely it presumably starts on the (116) facets. Moreover the smooth and step-less (111) island facets in Fig. 1(c) prove an efficient lateral self-limitation of the island growth which eventually yields a unidirectional self-assembling into chains of up to 4 μm length, see Fig. 2(c). The inset in Fig. 1(b) summarizes in a stereographic projection on the (113) plane the occurring groove and island facets.

Figure 2 depicts top view atomic force micrographs of the homo- (a) and heteroepitaxial (c) surface topology and corresponding fast Fourier transformations (FFT) of respective sample areas (b) and (d). During overgrowth the periodicity perpendicular to the groove structure has obviously been increased by a factor of ~ 1.6 , whereas usually the period of a prepattern will be taken over during a subsequent overgrowth with quantum dots, e.g., Ref. 10. Consequently, the correlation peak P1 within the corresponding FFT image shifts from 0.051 nm^{-1} for the initial surface [Fig. 1(b)], towards 0.031 nm^{-1} (P2). However, since the SiGe islands

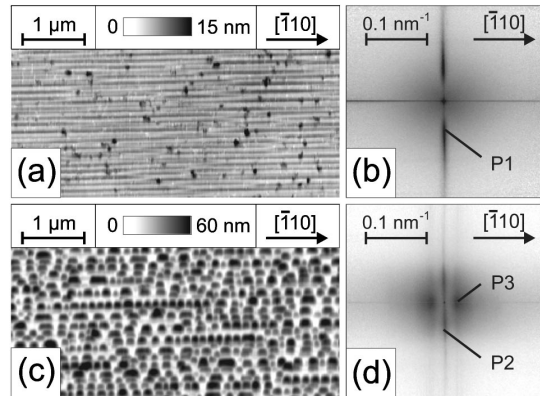
Appl. Phys. Lett. **86**, 223109 (2005)

FIG. 2. Linear pattern of the homoepitaxial Si(113) surface (a) enforces the unidirectional self-assembling of subsequently grown SiGe islands along the $[\bar{1}10]$ direction (c); respective fast Fourier transformations are shown in (b) and (d). The correlation peak P1 proves lateral self-assembling of alternating facets whereas satellite P2 shifts toward smaller values, respectively, larger island-island distances *perpendicular* to the grooves compared with the initial surface. Since the islands moreover self-assemble into the grooves, an additional satellite P3 appears.

self-assemble into extended chains along the $[\bar{1}10]$ direction an additional correlation peak P3 appears in Fig. 1(d) at a distance of 0.023 nm^{-1} which refers to a mean island-island separation of 273 nm within the chains.

Both findings, a unidirectional self-assembling within chains and second an increased periodicity perpendicular to them indicates a growth scenario which comprises a favored nucleation nearby an already existing island within a groove, which has been observed in other systems as well, e.g., Ref. 10. However, it additionally proves decreased nucleation probability within adjacent rows, and consequently not every single groove serves as a starting point for island nucleation.

To estimate the impact of elastic strain on the nucleation probability we have performed numerical finite element (FEM) calculations on the relaxation behaviour around a single island. The respective FEM model consists of a vertically extended Si(113) substrate covered by alternating (111) and (116) facets, whereas the lateral period of 100 nm has been adjusted to the morphology depicted in Fig. 1(a). Additionally a single $\text{Si}_{0.7}\text{Ge}_{0.3}$ island has been placed in the central groove. Generally a heteroepitaxial lattice mismatch acts as the driving force building up elastic strain. Its particular three-dimensional distribution is strongly influenced by the morphology and crystallographic orientation of the system. Both vector fields, the normalized lateral and vertical displacements, $\Delta x/a_{\text{Si}}$ and $\Delta z/a_{\text{Si}}$, are shown in Figs. 3(a) and 3(b). Obviously the crystal lattice will be nearly symmetrically compressed in lateral direction within adjacent grooves, where $\Delta x/a_{\text{Si}}$ is negative left and positive right of the island. Consequently elastic constraints in lateral direction are reduced along the central groove as well. Thus, in this location the lattice can expand vertically, which results in a positive value of $\Delta z/a_{\text{Si}}$ throughout the central groove, whereas the lattice will be compressed inwards along both adjacent grooves ($\Delta z/a_{\text{Si}} < 0$).

Since larger unit cells, those appearing respectively during the heteroepitaxial growth, preferably nucleate on locally expanded areas subsequent island nucleation will be favored within the grooves where an island already exists and hence

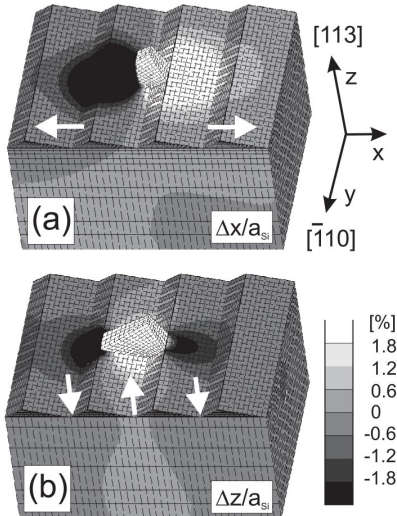


FIG. 3. Finite element calculation of the normalized lateral (a) and vertical (b) displacement field in the vicinity of a SiGe island placed on a faceted Si(113) substrate. The lateral displacement shows nearly a symmetric behavior with respect to the central groove (a). Consequently the lattice relaxes outwards ($\Delta z/a_{\text{Si}} > 0$) within the central row and will be depressed inwards within the adjacent rows (b).

yields extended chains along the $[\bar{1}10]$ direction. On the other hand the nucleation probability decreases in adjacent rows due to the locally compressed lattice. Generally this results in an increased island-island distance perpendicular to the grooves compared with the periodicity of the homoepitaxial prepattern.

Applying a dedicated two-step LPE process we have shown unidirectional ordered SiGe/Si(113) Stranski-Krastanow islands self-assembling into extended chains along the $[\bar{1}10]$ direction. An initial silicon homoepitaxy

from indium solution at 930 °C provides a highly regular and unidirectional faceting of the Si(113) surface, which serves as a template for the subsequent island nucleation. However, the SiGe heteroepitaxy has been performed from bismuth solution at a distinctly lower temperature in order to preserve the initial pattern. We attribute the development of extended chains to the particular strain distribution as confirmed by finite element method which favors island nucleation aside an already existing island within the groove and effectively decreases nucleation probability in adjacent rows.

The authors appreciate helpful discussions with H. Wawra, Institute of Crystal Growth, Berlin and H.-R. Höche, Department of Physics, Martin-Luther-University, Halle-Wittenberg.

- ¹S. David, M. Elkurd, P. Boucaud, A. Chelnokov, V. L. Thanh, D. Bouchier, and J.-M. Lourtioz, *Appl. Phys. Lett.* **83**, 2509 (2003).
- ²U. Denker, M. Stoffel, and O. G. Schmidt, *Phys. Rev. Lett.* **90**, 196102 (2003).
- ³E. Sutter, P. Sutter, and J. E. Bernard, *Appl. Phys. Lett.* **84**, 2262 (2004).
- ⁴M. Hanke, M. Schmidbauer, D. Grigoriev, P. Schäfer, R. Köhler, A.-K. Gerlitzke, and H. Wawra, *Phys. Rev. B* **69**, 075317 (2004).
- ⁵M. Hanke, M. Schmidbauer, R. Köhler, F. Syrowatka, A.-K. Gerlitzke, and T. Boeck, *Appl. Phys. Lett.* **84**, 5228 (2004).
- ⁶J. Liang, H. Luo, R. Beresford, and J. Xu, *Appl. Phys. Lett.* **85**, 5974 (2004).
- ⁷Q. Xie, A. Madhukar, P. Chen, and N. Kobayashi, *Phys. Rev. Lett.* **75**, 2542 (1995).
- ⁸G. Springholz, V. Holy, M. Pinczelits, and G. Bauer, *Science* **282**, 734 (1998).
- ⁹M. Meixner, E. Schöll, M. Schmidbauer, H. Raidt, and R. Köhler, *Phys. Rev. B* **64**, 245307 (2001).
- ¹⁰I. Berbezier, A. Ronda, A. Portavoce, and N. Motta, *Appl. Phys. Lett.* **83**, 4833 (2003).
- ¹¹T. van Lippen, R. Nötzel, G. J. Hamhuis, and J. H. Wolter, *J. Appl. Phys.* **97**, 044301 (2005).
- ¹²J. Zhu, K. Brunner, and G. Abstreiter, *Appl. Phys. Lett.* **73**, 620 (1998).
- ¹³M. Hanke, H. Raidt, R. Köhler, and H. Wawra, *Appl. Phys. Lett.* **83**, 4927 (2003).
- ¹⁴C. S. Ozkan, W. D. Nix, and H. Gao, *Appl. Phys. Lett.* **70**, 2247 (1997).

2.2.3 Straininduziertes Wachstum von SiGe/Si-dot molecules

M. Hanke, T. Boeck, A.-K. Gerlitzke, F. Syrowatka, F. Heyroth

Dedicated fabrication of silicon-based ensembles of dot molecules with a specific and unique number of dots

Appl. Phys. Lett. **88**, 063119 (2006).

In jüngster Zeit werden lokale Anordnungen einiger weniger Quantenpunkte, sogenannte *dot molecules*, u.a. als Bausteine zukünftiger Quantencomputer und für Einzelphotonenanwendungen diskutiert. Wenngleich die minimalen Strukturgrößen den Exzitonenradius im System Ge/Si aufgrund des vergleichsweise kleinen Gitterparameterunterschiedes von nur 4.2% deutlich übersteigen, so lassen sich doch an diesem Modellsystem einige grundlegende Mechanismen der Selbstorganisation von *dot molecules* studieren.⁴

Selbstorganisierte SiGe/Si *dot molecules* lassen sich in einem zweistufigen LPE Prozess herstellen, wobei zunächst eine sehr germaniumarme $\text{Si}_{0.985}\text{Ge}_{0.015}$ Schicht aufgebracht wird. Dieses Wachstum erfolgt anfangs planar, jedoch führt eine partielle Rücklösung zu Vertiefungen mit vierzähliger Symmetrie, die an invertierte Pyramiden erinnern. AFM Aufnahmen belegen, dass deren Seitenflächen durch {111} Facetten gebildet werden. Dieses selbstorganisierte Template kann dann in einem zweiten Schritt als Vorlage für die eigentliche Inselnukleation dienen. Aufgrund der sehr geringen Abkühlrate und der damit verbundenen Nähe zum thermodynamischen Gleichgewicht lassen sich subsequente Stadien der *dot molecules* (Einzelinseln, Dimere, Trimere und vollständige Quadruplets) beobachten. Dimere mit direkt gegenüberliegenden Inseln scheinen gegenüber solchen mit direkt benachbarten Inseln bevorzugt. Offenbar führt die Nukleation einer ersten Insel zu einer stärkeren Deformation des Kristallgitters in direkt benachbarten Gebieten, so dass zunächst der gegenüberliegende Platz präferiert wird.

Finite Elemente Berechnungen zum Deformationsfeld in der Nähe einer vierzähligen Kavität in SiGe/Si(001) zeigen in Übereinstimmung mit dem beobachteten Nukleationsszenario Minima entlang ⟨110⟩. Unterdrückt man in der Simulation die aufgezwungene vierzählige Symmetrie und betrachtet stattdessen eine rotationssymmetrische Kavität, so führt dies zu Energieminima entlang der elastisch weicheren ⟨100⟩ Richtung.⁵ Folglich ist die Symmetrie des *dot molecules* nur indirekt, durch die spezielle Symmetrie der Kavität, mit der elastischen Anisotropie der beteiligten Materialien verknüpft.

⁴Im Gegensatz dazu werden in Kap. 3.2 GaAs *dot molecules* besprochen, die durch Tröpfchenepitaxie (*droplet epitaxy*) hergestellt wurden. Bei dieser Wachstumsmethode entstehen die Quantenpunkte nicht wie beim Stranski-Krastanow Prozess üblich durch den heteroepitaktischen Gitterparameterunterschied. Dies bietet u.a. die hochinteressante Möglichkeit, deformationsfreie Quantenpunkte bzw. *dot molecules* zu erzeugen.

⁵In diesem Zusammenhang sei an das Deformationsfeld um eine SiGe/Si(001) Insel erinnert, das im Wesentlichen die elastische Anisotropie des Substrates wiedergibt. Ein Energieminimum lässt sich auf planaren Substraten ohne Berücksichtigung einer partiell abgetragenen Benetzungs schicht jedoch nicht nachweisen.

APPLIED PHYSICS LETTERS 88, 063119 (2006)

Dedicated fabrication of silicon-based ensembles of dot molecules with a specific and unique number of dots

M. Hanke^{a)}*Martin-Luther-Universität Halle-Wittenberg, Fachbereich Physik, Hoher Weg 8, D-06120 Halle/Saale, Germany*

T. Boeck and A. -K. Gerlitzke

Institut für Kristallzüchtung, Max-Born-Straße 2, D-12489 Berlin, Germany

F. Syrowatka and F. Heyroth

Interdisziplinäres Zentrum für Materialwissenschaften, Hoher Weg 8, D-06120 Halle/Saale, Germany

(Received 14 October 2005; accepted 29 December 2005; published online 10 February 2006)

We have performed a two-step liquid phase epitaxy yielding ensembles of SiGe/Si(001) dot molecules with a specific and unique number of dots. An undersaturation of the initial bismuth solution causes strain-induced pits in the epitaxial $\text{Si}_{0.985}\text{Ge}_{0.015}$ layer which are effectively preserved during subsequent $\text{Si}_{0.68}\text{Ge}_{0.32}$ dot growth at considerably lower temperatures. Since the latter process happens extremely close to thermodynamic equilibrium, we are able to interrupt it after the formation of ensembles of dimers, trimers or quadruplets, respectively. The crosslike ensemble symmetry is discussed in terms of strain energy distribution as revealed by finite element calculations. © 2006 American Institute of Physics. [DOI: [10.1063/1.2173216](https://doi.org/10.1063/1.2173216)]

Self-assembling of three-dimensional semiconductor dots following the Stranski–Krastanow (SK) growth mode has been widely demonstrated as a suitable pathway towards nanoscale dots.^{1,2} Those are suitable candidates to form artificial atoms or so-called quantum dot molecules, e.g., Refs. 3 and 4. The possibility to self-assemble collections of dots with desired shape and inherent symmetry opens a variety of interesting applications. Dot molecules are frequently discussed as building blocks for quantum computational systems,⁵ single-electron,⁶ and single-photon devices.⁷ In the framework of SK mode both, self-formation of an individual dot, and subsequently self-assembling of them into laterally and/or vertically ordered ensembles are ruled by the mutual impact of heteroepitaxially caused elastic strain plus its release on the one hand and evolution of dot shape and ordering on the other.

Since the evolution of dot molecules in a kinetically restricted growth regime as approached by, e.g., molecular-beam epitaxy (MBE) has been previously investigated^{4,8} there is comparatively less knowledge about dot molecule formation in a near-equilibrium growth environment. In most cases, liquid phase epitaxy (LPE) serves as a growth method which approximates thermodynamic equilibrium better than any other technique as MBE or molecular organic chemical vapor deposition.

In this letter, we describe a near-equilibrium two-step LPE from bismuth solvents subsequently using two different temperature windows. Finally, this process yields equilibrium-shaped⁹ dots which self-assemble into highly symmetric dot molecules. Since a horizontal slide boat technique is applied we can perform both growth steps directly one after another. To ensure a high purified environment, the entire process has been performed under a pure hydrogen atmosphere. While the solvent bismuth (50 g) is fully saturated¹⁰ with silicon at 1073 K, 28 mg germanium were

added to establish a nominal composition of $\text{Si}_{0.985}\text{Ge}_{0.015}$ in the solid layer. Hereafter, the solution was homogenized for 2 h at 1023 K to approach a near-equilibrium situation, and after a mandatory *in situ* desorption of the natural oxide layer at 1203 K, the solvent was brought into contact with the target substrate. A cooling step from 1023 K to 1013 K with a rate of 0.5 K/min results in a surface morphology as shown in Fig. 1(a). The scanning electron micrograph depicts a surface with randomly distributed pits (P) with a typical

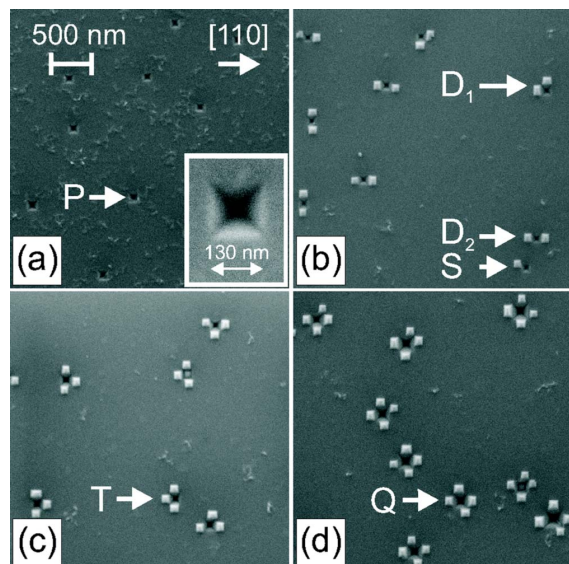


FIG. 1. The scanning electron micrographs show a growth sequence starting with the surface after an initial growth of a $\text{Si}_{0.985}\text{Ge}_{0.015}$ layer (a). It is decorated with randomly distributed pits (P) which serve as nucleation points for the subsequent $\text{Si}_{0.68}\text{Ge}_{0.32}$ dot growth. Depending on the actual growth time single (S) SiGe dots, dimers D_1 and D_2 (b), (c) triplets (T), and eventually (d) quadruplets (Q) appear.

^{a)}Electronic mail: hanke@physik.uni-halle.de

lateral dimension of 130 nm, a density of approximately $1 \mu\text{m}^{-2}$ and a four-fold symmetry. A closer inspection reveals four adjacent facets forming an inverse pyramid which will be of high importance for the final symmetry of the dot molecules. Atomic force microscopy (not shown) yields an inclination angle of approximately 53.5° with respect to the surface which nearly corresponds to $\{111\}$ facets (54.7°). It is noteworthy that both—a bismuth solvent which contains only a very small amount of silicon, and second a disproportional high incorporation of silicon—results in a rapid undersaturation of the solvent. Thus, the already grown SiGe layer will be locally resolved resulting in the observed morphology.

To preserve the initial self-formed template during the actual dot nucleation, lower growth temperatures are required. As in the previous step, the solved amount of germanium (166.8 mg) within 50 g bismuth determines the final dot composition ($\text{Si}_{0.68}\text{Ge}_{0.32}$) while the solution is silicon saturated¹⁰ at 848 K. A cooling step from 848 K to 846 K with a very slow rate of 0.01 K/min initiates the dot growth. Single dots and ensembles of dot molecules consisting of either two, three, or four dots and distinct inherent symmetry occur, Figs. 1(b)–1(d). Different stages allow a retrospective reconstruction of their evolution. In the very beginning, single dots nucleate aside the pits. This initial step happens with the same probability along all four $\langle 110 \rangle$ directions (not shown here). Subsequently dimers (dot molecules containing two dots) appear in two different morphologies D_1 and D_2 , see Fig. 1(b). Since a single dot aside a pit compresses the lattice at adjacent edges (not shown), the opposite edge remains comparatively unpersuaded. Consequently, dimers of type D_1 are less likely than dimers with opposite dots. If the dot density increases further, dot molecules with three dots appear, and finally highly symmetric quadruplets assemble. Interestingly we have never observed various dot stages, thus we conclude that the actual dot nucleation and growth happens on an essentially faster time scale than the lateral self-formation of dot molecules. Moreover, dot molecules consisting of two, three, or four dots are more likely at higher dot-coverage.

Figure 2 depicts two comparative finite element (FE) calculations of the strain energy distribution. Both models consist of a silicon substrate and a $\text{Si}_{0.985}\text{Ge}_{0.015}$ layer, however they consider different cavity geometries. In Fig. 2(a), we have calculated for an inverted pyramid as experimentally observed, Fig. 1(a), while Fig. 2(b) bases on a hypothetical round-shaped inverted cone. Due to symmetry reasons of the FE calculation (quasi-periodic boundary conditions), a quarter of a model provides sufficient information. Distribution Fig. 2(a) proves surface areas around an inverted pyramid—denoted $R_{\langle 110 \rangle}$ —under less strained condition compared with the rest of the surface. In contrast to that Fig. 2(b) for an inverted cavity predicts a completely different dot molecule growth scenario. Obviously, the elastic anisotropy of the $\text{Si}(001)$ surface, which claims crystallographic softer $\langle 100 \rangle$ and stiffer $\langle 110 \rangle$ directions, determines the symmetry properties of the strain energy density. Consequently, one could expect quadruplets with preferential $\langle 100 \rangle$ direction for $\text{Si}(001)$ templates with cone-shaped cavities. Thus, we conclude that for the system SiGe/Si, the particular dot allocation is rather determined by the initial cavity ge-

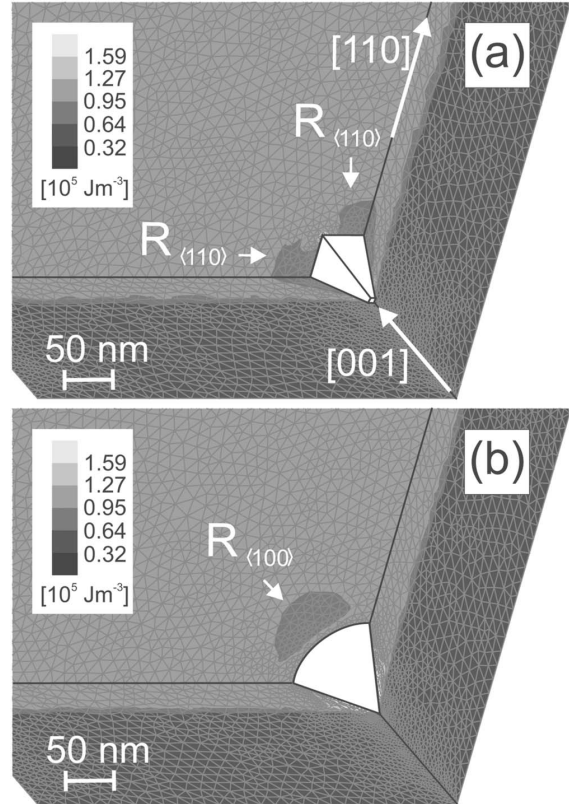


FIG. 2. FE calculations of the elastic strain energy density around an inverted pyramidlike (a) and a cone-shaped (b) cavity. Due to symmetry reasons only a quarter of a model has been considered. The particular geometry (a) with a four-fold symmetry promotes an efficient lattice relaxation along $\langle 110 \rangle$ while, on the other hand, a hypothetical cone-shaped cavity yields an area of lower strain energy density—denoted $R_{\langle 100 \rangle}$ — 45° azimuthally off, thus along $\langle 100 \rangle$. This finding directly refers to different stiffnesses within the surface. The particular strain distribution (a) energetically favors dot nucleation as shown in Fig. 1.

ometry than by the crystallographic anisotropy of the surface.

Figure 3 shows a scanning electron micrograph of a quadruplet. The image was taken under an angle of 85° and reveals the near-equilibrium dot shape⁹ which consists of four adjacent $\{111\}$ -type facets and a single (001) top facet. The finally realized dot size with an averaged base width of 110 nm and a height of 58 nm does not fully exceed the

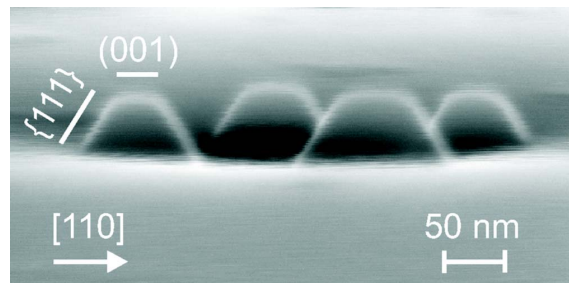


FIG. 3. Scanning electron micrograph of squarelike formation taken at a very glancing angle of 85° . The dots clearly show their near-equilibrium shape consisting of four adjacent $\{111\}$ and a single (001) top facet.

063119-3 Hanke *et al.*Appl. Phys. Lett. **88**, 063119 (2006)

lateral pit size nor does it reach its equilibrium size of approximately 130 nm as observed for free standing SiGe dots of equal concentration.¹¹ This indicates that the strain distribution around a cavity can favor dot dimensions smaller than the equilibrium size which is attractive for further dot shrinking.

In conclusion, we have demonstrated a two-fold liquid phase epitaxy which provides ensembles of dot molecules with a specific and unique number of individual SiGe/Si dots, namely either two, three or four. During the first high-temperature growth step a strain driven and locally restricted resolving of the SiGe layer yields pits with $\langle 110 \rangle$ -type edges whereas those cavities serve as nucleation spots during the subsequent low-temperature dot growth. Since we have only observed fully developed dots of equilibrium shape with four adjacent $\{111\}$ facets and a single (001) top facet, but dot molecules with different numbers of dots, we conclude that the actual dot growth happens on a considerably faster time scale than the lateral self-formation of the molecules. FE calculations of the strain energy distribution around a pit of four-fold symmetry prove a relaxed lattice along $\langle 110 \rangle$ and thus indicate favorable nucleation spots. Consequently, the dot allocations exhibit a preferential $\langle 110 \rangle$ direction. However, a cone-shaped cavity yields favorable nucleation spots along $\langle 100 \rangle$ which can be directly attributed to the crystallographic anisotropy.

The authors appreciate helpful discussions with Herbert Wawra, Institute for Crystal Growth, Berlin, and Rolf Köhler, Humboldt-Universität zu Berlin. The work was financially supported by the federal state of Sachsen-Anhalt within the cluster of excellence (CoE) *Nanostructured materials* project NW3, and the Deutsche Forschungsgemeinschaft Contract No. HA3495/3.

¹D. Bimberg, M. Grundmann, and N. N. Ledentsov, *Quantum Dot Heterostructures* (Wiley, Chichester, NY, 1999).

²V. A. Shchukin, N. N. Ledentsov, and D. Bimberg, *Epitaxy of Nanostructures* (Springer, New York, 2004).

³R. Songmuang, S. Kiravittaya, and O. G. Schmidt, Appl. Phys. Lett. **82**, 2892 (2003).

⁴J. L. Gray, R. Hull, and J. A. Floro, Appl. Phys. Lett. **81**, 2445 (2002).

⁵A. Imamoglu, D. D. Awschalom, G. Burkard, D. P. DiVincenzo, D. Loss, M. Sherwin, and A. Small, Phys. Rev. Lett. **83**, 4204 (1999).

⁶R. J. Warburton, C. Schaflein, D. Haft, F. Bickel, A. Lorke, K. Karrai, J. M. Garcia, W. Schoenfeld, and P. M. Petroff, Nature (London) **405**, 926 (2000).

⁷P. Michler, A. Kiraz, C. Becher, W. V. Schoenfeld, P. M. Petroff, L. D. Zhang, E. Hu, and A. Imamoglu, Science **290**, 2282 (2000).

⁸J. L. Gray, S. Atha, R. Hull, and J. A. Floro, Nano Lett. **4**, 2447 (2004).

⁹M. Hanke, M. Schmidbauer, R. Köhler, F. Syrowatka, A.-K. Gerlitzke, and T. Boeck, Appl. Phys. Lett. **84**, 5228 (2004).

¹⁰The solubility of silicon within a bismuth solution of 50 g accounts for 3.074 mg at 1073 K and 0.156 mg at 848 K, respectively.

¹¹W. Dorsch, H. P. Strunk, H. Wawra, G. Wagner, J. Groenen, and R. Carles, Appl. Phys. Lett. **72**, 179 (1998).

2.2.4 Template-basierte Ordnung mittels lokaler anodischer Oxidation

M. Hanke, T. Boeck, A.-K. Gerlitzke

Template-based assembling of SiGe/Si(001) dots by local anodic oxidation

Appl. Phys. Lett. **88**, 173106 (2006).

Während sich, wie in Kap. 2.2.2 gezeigt, durch die geeignete Wahl höherindizierter Substrate eine unidirektionale Ordnung bzw. in Kap. 2.2.3 durch einen zweistufigen Wachstumsprozess spezielle lokale Anordnungen erreichen lassen, so scheint eine *aktive* Vorstrukturierung für beliebige Inselformationen unverzichtbar. Da der eigentlichen Züchtung aus der Flüssigphase stets eine Desorption des natürlichen Siliziumoxids vorausgeht, mag ein Ansatz mittels lokaler anodischer Oxidation auf den ersten Blick überraschen.

Im Wesentlichen wurde mit zwei strukturell verschiedenen Templates gearbeitet: einem linearen und einem quadratischen Muster mit jeweils 500 nm Periode.⁶ Die mittlere Breite der entlang $\langle 110 \rangle$ orientierten oxidischen Stege betrug 100 nm. Ganz offenbar wird das Inselwachstum durch die Stege effektiv unterdrückt. Es bilden sich Inselreihen auf dem linearen Muster bzw. einzelne Inseln innerhalb des quadratischen Musters. In beiden Fällen weichen die Größen der Inseln stark von dem für die eingestellte Germaniumkonzentration erwarteten Gleichgewichtswert nach oben ab. Dies deutet auf ein durch die Vorstrukturierung effektiv verringerten Gitterparameterunterschied zwischen Substrat und Schicht. Es ließ sich zeigen, dass dieser Effekt mit der Dimensionalität des Templates zunimmt.

Die im Artikel diskutierten SiGe/Si Inseln eignen sich bestens als Modellsystem für Untersuchungen zur kohärenten Röntgenstreuung.⁷ Nanostrukturphysik fokussiert sich zunehmend auf die Erzeugung, Manipulation und Charakterisierung *individueller* nanoskaliger Objekte. Für die Röntgenanalytik bildet sich dieser Trend in der Verfügbarkeit immer besser fokussierter Quellen ab. So sind im Rahmen des Ausbaus von PETRAIII am DESY, diverse Messstationen mit Mikro- und Submikrofokus geplant, während die ESRF bereits einige Experimentierplätze mit Mikrofokus anbietet. Eine detaillierte Charakterisierung dreidimensionaler Deformationsfelder innerhalb und in der Umgebung *einzelner* Inselstrukturen zielt sowohl auf zugrunde liegende Wachstumsmechanismen als auch auf ein tieferes Verständnis eines vollständig kohärenten Streuprozesses. Neben einer Vermessung des Deformationsfeldes mittels Planwellentopographie, ermöglichen bis auf wenige 100 nm Spotgröße fokussierbare Quellen die Untersuchung individueller nanoskaliger Objekte auch mittels hochauflöster diffuser Röntgenbeugung, einer Methode die bislang nur Inselensembles vorbehalten war.

⁶ Atomkraftmikroskopie im *contact mode* mit elektrisch leitenden Platin-Iridium Spitzen dient dabei als Lithographietechnik. Dissozierte Hydroxidionen innerhalb eines kleinen, auf der Oberfläche stets vorhandenen Wasserfilms bewegen sich durch Anlegen einer negativen Spannung zum Substrat und erzeugen dort ein lokales Oxid.

⁷ Dem Autor wurde in diesem Zusammenhang vor kurzem eine DFG Sachbeihilfe zum Thema *Kohärente Röntgenstreuung an individuellen SiGe/Si Nanostrukturen*, HA3495/6-1, gewährt.

APPLIED PHYSICS LETTERS 88, 173106 (2006)

Template-based assembling of SiGe/Si(001) islands by local anodic oxidation

M. Hanke^{a)}*Martin-Luther-Universität Halle-Wittenberg, Fachbereich Physik, Hoher Weg 8,
D-06120 Halle/Saale, Germany*

T. Boeck and A.-K. Gerlitzke

Institut für Kristallzüchtung, Max-Born-Straße 2, D-12489 Berlin, Germany

(Received 21 December 2005; accepted 9 March 2006; published online 26 April 2006)

Template-based SiGe/Si(001) island formation has been performed by a combination of local anodic oxidation and liquid phase epitaxy. In case of unidirectional stripes the island pattern directly follows along the trenches, whereas a squarelike stripe pattern enforces island nucleation within the oxide-free cavities. The final island size significantly probes an effectively lowered lattice mismatch, thus a locally expanded crystal lattice in noncovered areas of the silicon substrate. © 2006 American Institute of Physics. [DOI: [10.1063/1.2198099](https://doi.org/10.1063/1.2198099)]

Due to their outstanding physical properties semiconductor quantum dots have attracted a tremendous interest during the last decade, e.g., see Refs. 1–3. However, besides applications which solely address the effective carrier confinement in all three dimensions and hence discrete energy states, quantum dots have recently been embedded within photonic crystal structures^{4–6}—an implementation which essentially relies on a precise spatial and spectral overlap.

Besides template-based efforts to establish an appropriate lateral and/or vertical positional arrangement of semiconductor islands self-organization provides an elegantly simple alternative which refers to the heteroepitaxial Stranski-Krastanow growth process. Thereby the accumulated elastic strain energy decreases after the formation of an initial very thin wetting layer, which eventually yields pseudomorphically strained nanoscale islands. Lateral island dimensions can be adjusted since the applied lattice mismatch determines the final island size.⁷ Moreover the self-formation of individual Stranski-Krastanow islands is often accompanied by a pronounced lateral and/or vertical assembling referring to energetically favorable nucleation places due to strain energy anisotropy, thus, e.g., SiGe/Si(001) islands self-assemble into extended island chains along the ⟨100⟩ direction.⁸ On the other hand, the morphology of a homoepitaxial Si(113) surface can serve as a self-formed unilateral template for subsequent island nucleation along particular directions.⁹ Nevertheless arbitrary island patterning on the exclusive base of self-formation mechanisms remains a challenging issue.

Artificially created template structures created by electron beam lithography¹⁰ and focused ion beam¹¹ enable island growth at particular positions. A more direct approach¹² towards a tip-induced creation of nanoscale islands relies on a modified atomic force microscope (AFM) applying a locally restricted electrical current through a conducting tip. Generally the obtained oxide features exhibit an excellent resolution since the AFM tip can be controlled on the surface at nanometer accuracy. On silicon substrates typical thicknesses of the oxide features, depending on humidity, actual

electric current, and tip geometry, may vary between 1 and 8 nm Refs. 13 and 14 along a width as narrow as 10 nm.¹⁵ Although the recently reported experiment¹² enables a *direct* tip-induced island growth, it suffers, on the other hand, by its restriction to metal-oxide-semiconductor islands. In this letter we describe a dedicated method which combines tip-induced oxide patterning and subsequently performed nucleation of SiGe/Si islands in order to intentionally control island assembling into arbitrary lateral patterns.

For the lithographical setup, shown in Fig. 1, we have used electrically conducting platinum-iridium coated tips with a typical diameter of 7 nm in a standard atomic force microscope (AutoProbe CP, Veeco). Under ambient conditions a thin water film covers the surface which forms a tiny water droplet around the tip during contact mode. Thus, dissociated ions are able to move at the presence of an external electric field. In case of a negatively charged tip hydroxide ions move towards the substrate and can eventually establish silicon oxide patterns of arbitrary shape. The morphologies discussed here have been evolved for an impressed voltage of 9.0 V and show a one-dimensional periodic arrangement of silicon oxide stripes Fig. 2(a), and a two-dimensional squarelike pattern Fig. 3(a), respectively. Both templates exhibit a lateral periodicity of 500 nm with typical stripe widths of 100 nm.

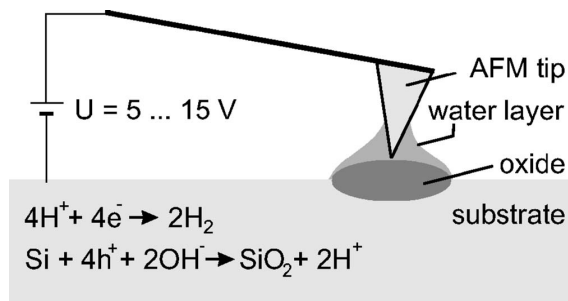


FIG. 1. A platinum-iridium coated negatively charged tip in an ambient AFM causes a local anodic oxidation of the silicon surface. The electric field within the tiny water droplet around the tip enables ion movement which eventually yields oxide features of arbitrary shape.

^{a)}Electronic mail: michael.hanke@physik.uni-halle.de

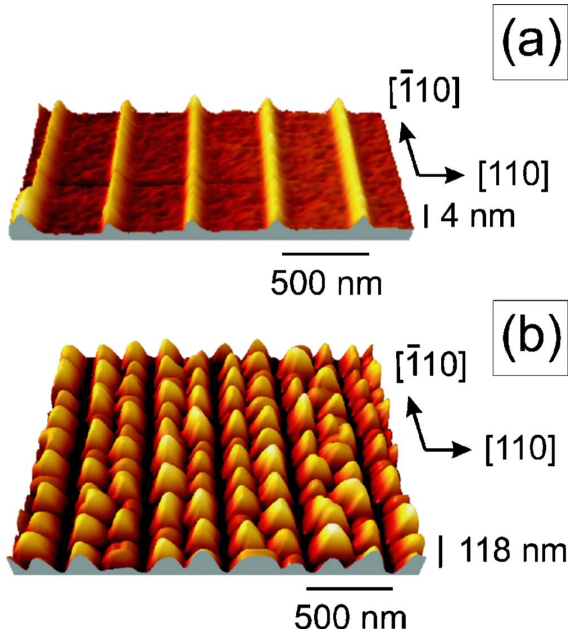


FIG. 2. (Color online) The atomic force micrograph (a) depicts the surface morphology after anodic oxidation consisting of regularly arranged silicon oxide lines. (b) shows the template-based unidirectional SiGe island assembling.

It is noteworthy that at the absence of a prepatterning SiGe/Si(001) islands self-assembling along the crystallographically softer $\langle 100 \rangle$ directions.^{8,16} In order to ensure a directed island assembling, and thereby to probe the template-based impact, both stripe systems point along the $\langle 110 \rangle$ direction which is 45° azimuthally off.

The actual SiGe island growth has been performed from the liquid phase very close to thermodynamic equilibrium. Compared with molecular beam epitaxy the driving forces are weak due to an up to four orders higher diffusion rate of solved components. We have used a horizontal slide boat technique, an implementation of liquid phase epitaxy (LPE) where a graphite boat containing the liquid solution can horizontally be moved. For the sake of highly purified growth environment the entire process is performed under a pure hydrogen flow. In a first step the liquid bismuth solution is fully saturated with silicon, whereas the amount of solved germanium corresponds to the final germanium concentration in the solid state, 30% for the overgrowth of pattern Fig. 2(a) and 35% for pattern Fig. 3(a). However, previous to the actual island growth the overall natural silicon oxide has to be removed by thermal annealing at 1200 K for 30 min. The comparatively large widths of the tip-induced stripes of about 100 nm ensure a preservation during annealing. Subsequently the temperature of the target substrate is adjusted towards the starting temperature of 870.5 K. A 15 min growth step with a linear cooling rate of 0.16 K/min finally results in the morphology as shown in Fig. 2(b).

Obviously, the island nucleation at the stripe locations is effectively hampered due to the presence of the artificial oxide stripes. The islands are formed by four adjacent facets inclined by approximately 53° which can be attributed to $\{111\}$ side facets (54.7°). Moreover the islands self-assemble pairwise along the $\langle 110 \rangle$ direction. Since the LPE regime

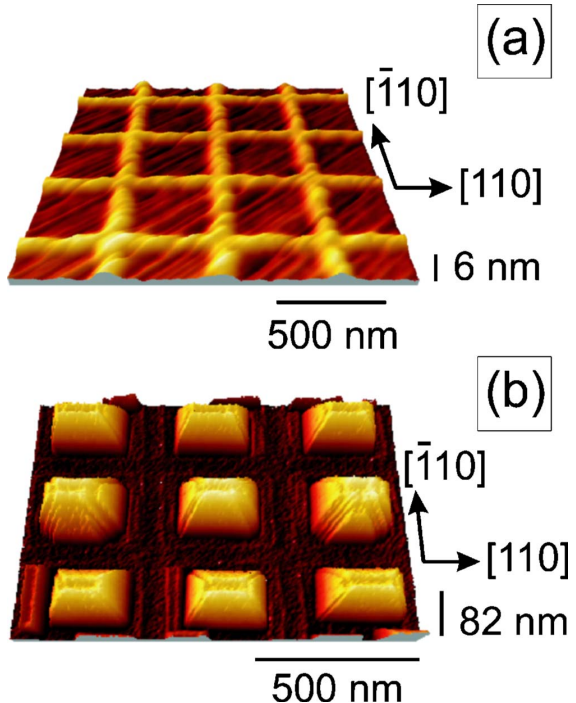


FIG. 3. (Color online) (a) shows a squarelike pattern of intersecting silicon oxide stripes which serve as an artificial template for the subsequent SiGe nucleation (b).

operates close to thermodynamic equilibrium one can consider the actual island width w as a measure of the effective lattice mismatch f . Both quantities are interrelated by $w \propto f^{-2.03}$ (Ref. 7), which yields an equilibrium size of approximately $w_{\text{equ}} = 130$ nm for $\text{Si}_{0.7}\text{Ge}_{0.3}/\text{Si}(001)$ islands. However, the experimentally observed mean size accounts for $w_{\text{exp}} = 205$ nm along with a maximum height of 118 nm, Fig. 2(b). Obviously the oxide stripes modify the strain field in the nonpatterned areas in a way that the crystal lattice is laterally expanded. Consequently, the lattice mismatch between the prestrained substrate and the heteroepitaxial SiGe islands is *effectively* decreased by approximately $(w_{\text{equ}}/w_{\text{exp}})^{-2} = 1.26$ which motivates enlarged island widths.

An even stronger prestrained crystal lattice at the uncovered areas has to be presumed due the squarelike nature of pattern Fig. 3(a). In order to compensate this effect a higher germanium content of 35% has been chosen. The growth was performed between 865 and 862 K applying a linear growth rate of 0.16 K/min. Surprisingly only single islands appear within uncovered areas, Fig. 3(b). The pyramidal islands are made of four adjacent $\{111\}$ and a single $\{001\}$ top facet developing the near equilibrium shape.¹⁷ However, the lateral island size accounts for 240 nm although an increased lattice mismatch generally yields smaller islands. The increased island size proves, on the other hand, that a two-dimensional squarelike pattern of same periodicity as an unidirectional template increases the template-related strain within noncovered areas and hence further reduces the effective lattice mismatch.

In conclusion, we have performed a dedicated twofold process towards template-based nucleation of SiGe islands on Si(001) substrates. First, local anodic oxidation by a

173106-3 Hanke, Boeck, and Gerlitzke

Appl. Phys. Lett. **88**, 173106 (2006)

modified atomic force microscope yields oxide pattern of arbitrary shape which serve during the subsequently performed liquid phase epitaxy as templates. Both unidirectional and squarelike island assembling along the $\langle 110 \rangle$ directions have been demonstrated. The observed island dimensions, with respect to the nonpatterned nucleation under equivalent conditions, subsequently increase with the dimensionality of the pattern which indicates a decreased effective lattice mismatch at noncovered areas.

The authors thank G. Schadow, Institute for Crystal Growth, Berlin for the assistance during the LPE experiments. The work was financially supported by the federal state of Sachsen-Anhalt within the Cluster of Excellence (CoE) *Nanostructured materials*, Project No. NW3.

¹V. A. Shchukin, N. N. Ledentsov, and D. Bimberg, *Epitaxy of Nanostructures* (Springer, New York, 2004).

²M. S. Skolnik and D. J. Mowbray, Annu. Rev. Mater. Res. **34**, 181 (2004).

³J. Stangl, V. Holý, and G. Bauer, Rev. Mod. Phys. **76**, 725 (2004).

⁴K. H. A. Badolato, M. Atature, J. Dreiser, E. Hu, P. M. Petroff, and A.

İmamoğlu, Science **308**, 1158 (2005).

⁵K. Hennessy, C. Reese, A. Badolato, C. F. Wang, A. İmamoğlu, P. M. Petroff, E. Hu, G. Jin, S. Shi, and D. W. Prather, Appl. Phys. Lett. **83**, 3650 (2003).

⁶C. Reese, C. Becher, A. İmamoğlu, E. Hu, B. D. Gerardot, and P. M. Petroff, Appl. Phys. Lett. **78**, 2279 (2001).

⁷W. Dorsch, B. Steiner, M. Albrecht, H. P. Strunk, H. Wawra, and G. Wagner, J. Cryst. Growth **183**, 305 (1998).

⁸M. Hanke, H. Raidt, R. Köhler, and H. Wawra, Appl. Phys. Lett. **83**, 4927 (2003).

⁹M. Hanke, T. Boeck, A.-K. Gerlitzke, F. Syrowatka, and F. Heyroth, Appl. Phys. Lett. **86**, 223109 (2005).

¹⁰S. Kiravittaya and O. G. Schmidt, Appl. Phys. Lett. **86**, 206101 (2005).

¹¹J. L. Gray, S. Atha, R. Hull, and J. A. Floro, Nano Lett. **4**, 2447 (2004).

¹²X. N. Xie, H. J. Chung, C. Sow, and A. T. S. Wee, Appl. Phys. Lett. **86**, 023112 (2005).

¹³P. Avouris, T. Hertel, and R. Martel, Appl. Phys. Lett. **71**, 285 (1997).

¹⁴E. S. Snow, G. G. Jernigan, and P. M. Campbell, Appl. Phys. Lett. **76**, 1782 (2000).

¹⁵E. S. Snow and P. M. Campbell, Appl. Phys. Lett. **64**, 1932 (1994).

¹⁶M. Meixner, E. Schöll, M. Schmidbauer, H. Raidt, and R. Köhler, Phys. Rev. B **64**, 245307 (2001).

¹⁷M. Hanke, M. Schmidbauer, R. Köhler, F. Syrowatka, A.-K. Gerlitzke, and T. Boeck, Appl. Phys. Lett. **84**, 5228 (2004).

2.2.5 Asymmetrische Korrelationsfunktion

M. Schmidbauer, M. Hanke, R. Köhler

Asymmetric Correlation Function Describing the Positional Ordering of LPE SiGe Nanoscale Islands

Phys. Rev. B **71**, 115323 (2005).

Der vorliegende Artikel diskutiert, inwieweit laterale Positions korrelation im System SiGe/Si(001) Lage und Form von Überstruktursatelliten in der diffusen Streuung prägt.⁸ Obwohl in der diffusen Streuung eine ganze Reihe von Korrelationssatelliten in der Nähe des symmetrischen 004 Reflexes nachweisbar sind, lässt sich dieser Befund im reziproken Raum nicht notwendigerweise mit einer auf großen Längenskalen bestehenden Korrelation im Ortsraum erklären. Das mag auf den ersten Blick überraschen, wird jedoch klar, sobald man in einem sogenannten *short-range order* Modell einen nach unten begrenzten, minimalen, nach oben jedoch offenen Insel-Insel-Abstand innerhalb der Inselketten annimmt. Diese Bedingung führt im Ortsraum zu einer Korrelationsfunktion mit asymmetrischem Peakprofil, im reziproken Raum zu nicht-äquidistanten Korrelationssatelliten, deren Halbwertsbreite mit zunehmendem lateralen Impulsübertrag zudem ansteigt.

Dass der Inselabstand nach unten beschränkt ist, stützt die in Kap. 2.2.1 formulierte These, nach der die Inselketten durch subsequente Nukleation am Ende einer bestehenden Formation entstehen. Ganz offenbar wird die Nukleation in der unmittelbaren Umgebung einer Insel sehr effektiv unterdrückt. Der (der Form des Deformationsfeldes folgende) Abtrag der Benetzungsschicht forciert diesen Effekt noch weiter, siehe Kap. 2.3.

⁸Er könnte damit auch in Kap.2.5, *Strukturanalytik mittels diffuser Röntgenstreuung*, gehören. Eine weitere Arbeit, die sich mit Positions korrelation und deren Einfluss auf die diffuse Streuung beschäftigt, findet sich in Kap. 2.5.4. Dort liegt jedoch der Schwerpunkt auf der numerischen Implementierung, wobei verschiedene Aspekte einer endlichen Kohärenzlänge der genutzten Synchrotronstrahlung im Detail diskutiert werden.

PHYSICAL REVIEW B 71, 115323 (2005)

Asymmetric correlation function describing the positional ordering of liquid-phase-epitaxy Si–Ge nanoscale islands

M. Schmidbauer, M. Hanke,* and R. Köhler

Institut für Physik, Humboldt-Universität zu Berlin, Newtonstraße 15, 12489 Berlin, Germany

(Received 16 January 2004; revised manuscript received 21 December 2004; published 25 March 2005)

Liquid-phase-epitaxy grown SiGe nanoscale islands on (001)Si form extended chains which are aligned along the $\langle 100 \rangle$ directions. The positional ordering within the island chains was studied by x-ray diffuse scattering. The results can be interpreted by a short-range order model. The corresponding correlation function exhibits an asymmetric peak profile. The asymmetry leads to nonequidistantly spaced satellite peaks that disperse outward slightly with increasing lateral momentum transfer. The observed asymmetric island-island correlation is caused by the successive growth of the islands within a chain, while the new island position is influenced by depletion of the wetting layer around the island.

DOI: 10.1103/PhysRevB.71.115323

PACS number(s): 68.65.-k, 61.10.-i, 81.16.Dn

I. INTRODUCTION

Semiconductor nanoscale islands have been extensively investigated in the last decade.¹ Technological applications of these systems require dense arrays of monodisperse structures of identical shape. Initially, the most widely followed approach to forming nanoscale islands was through electron-beam lithography of suitably small featured patterns. However, besides the fact that the spatial resolution of typically 30 nm is often not small enough, there is still a problem with the large amount of damage introduced during the fabrication process itself. Therefore, self-organized growth mechanisms, such as the Stranski-Krastanow growth mode,² have attracted considerable interest. Here, a heteroepitaxial film can release its elastic energy by forming small dislocation-free three-dimensional islands.

Depending on the growth conditions often a well-defined lateral positional ordering of self-assembled nanoscale islands can be observed.^{3–6} Type and strength of this ordering can be described by a pair-correlation function. At free-standing islands positional ordering can be investigated by real-space imaging techniques, such as scanning probe microscopy or scanning electron microscopy. Those methods probe the structure locally with high spatial resolution but often with insufficient statistical significance. Therefore, an accurate determination of the pair-correlation function from, e.g., atomic force micrographs, seems to be not feasible. By contrast—owing to typical spot sizes in the range of a few square millimeters—x-ray scattering techniques average statistically over rather large ensembles of islands, and the data are very reliable concerning statistics.

As a result of positional ordering, significant interference of scattered waves from the individual islands may occur and satellite peaks can be observed in the diffuse x-ray scattering. The angular positions of these satellites are related to the mean lateral island distances while the peak widths contain information about a lateral correlation length. Moreover, since the diffuse intensity distribution of the satellite peaks is related to the Fourier transform of the pair-correlation function, a detailed quantitative analysis enables one to distinguish between different types of ordering. Among them are the two limiting cases of short-range order (SRO) and long-

range order (LRO), which have been already discussed for positional ordering of quantum dots.⁷ In both cases, the satellite peaks are equidistantly spaced in reciprocal space and they vary only in intensity and peak width.

In this paper we discuss the lateral ordering of free-standing $\text{Si}_{1-x}\text{Ge}_x$ islands, which were grown on (001)Si by means of liquid-phase epitaxy (LPE). A description of the LPE growth procedure can be found elsewhere.⁸ Owing to growth conditions close to thermodynamic equilibrium these samples contain highly monodisperse islands of uniform shape and, at sufficiently large island coverage, high positional correlation is observed.^{3,9} As an example, atomic force micrographs of $\text{Si}_{0.70}\text{Ge}_{0.30}$ nanoscale islands are shown in Figs. 1(a) and 1(b). It is very interesting to track the evolution of positional ordering as a function of island coverage. At very low island coverage, there is already a large fraction of islands that are clustered.^{3,10} These clusters consist mainly of island dimers, with a small fraction of linear three-island trimers that are oriented along the elastically soft $\langle 100 \rangle$ directions. When the island coverage is increased, the dimers and trimers develop into extended rows of islands oriented along $\langle 100 \rangle$.¹¹

The observed clustering is a clear indication of short-range ordering and suggests that during the growth phase, the nucleation of an island is strongly influenced by already existing islands. However, we will demonstrate that the q dependence of experimental satellite peak positions in the x-ray diffuse scattering indicates that the above-mentioned random-walklike SRO model as used by Stangl *et al.*⁷ is not appropriate to correctly describe the lateral ordering of our samples.

II. X-RAY SCATTERING FROM A CORRELATED ENSEMBLE

The investigation of mesoscopic structures by means of x-ray diffuse scattering implies averaging over the illuminating spot size of typically a few square millimeters on the sample. When a single layer of islands with spacings of 100–1000 nm is considered, the number of scattering mesoscopic objects is of order 10^6 – 10^8 , which is a statistically

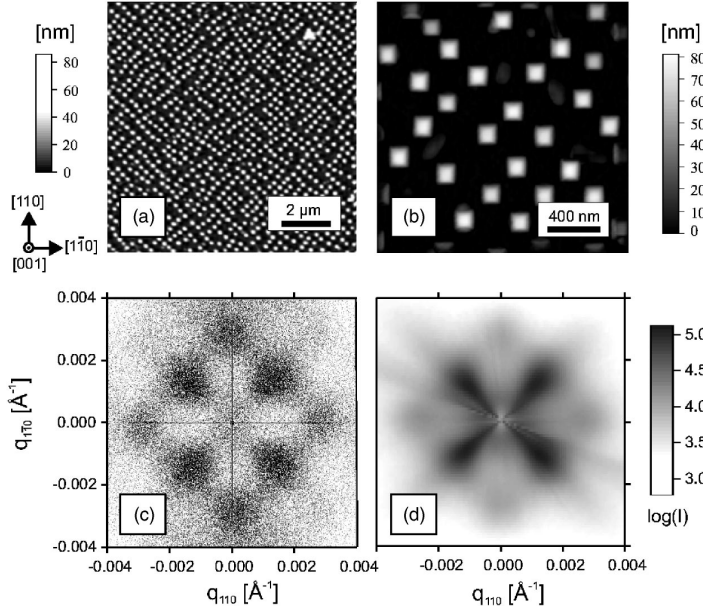


FIG. 1. (a,b) Atomic force micrographs of $\text{Si}_{0.70}\text{Ge}_{0.30}$ nanoscale islands grown on (001) Si by LPE. The islands are of truncated pyramidal shape with {111} side facets and a (001) top facets. Island base width and height are 130 nm and 65 nm, respectively. The island area coverage is approximately 16%. (c) In-plane AFM power spectrum, (d) GISAXS in-plane intensity distribution.

significant large number. In the case of an ensemble of monodisperse islands of identical shape the diffuse intensity from each individual island is identical. However, the positions of these islands in the ensemble can be correlated, resulting in significant interference of the diffusely scattered waves from the individual islands. Depending on the strength of the positional correlation, this could lead to more or less pronounced and sharp satellite peaks in the diffuse scattering. The distances Δq in reciprocal space between the satellites and the coherent Bragg peak are related to corresponding mean distances $\langle d \rangle$ in real space via

$$\langle d \rangle = \frac{2\pi}{\Delta q}. \quad (1)$$

This equation can be applied to both vertical and horizontal correlation and is very helpful for quickly evaluating experimental data. However, this relationship does not provide information about the details of the correlation function that determines the scattered intensities. Here, we describe how to take account of positional correlation in the framework of kinematical theory. The diffraction from an ensemble of nanoscale islands can be treated such that the scattered amplitudes A_m^{diffuse} from single islands at positions \mathbf{R}_m are (coherently) summed

$$\mathbf{A}_{\text{total}}^{\text{diffuse}}(\mathbf{q}) = \sum_m A_m^{\text{diffuse}}(\mathbf{q}) e^{i\mathbf{q} \cdot \mathbf{R}_m}, \quad (2)$$

where \mathbf{q} denotes the scattering vector. Note, however, that this expression is valid only if the strain fields of neighboring islands do not remarkably overlap, which is true for the sample discussed here.

For practical reasons, it is impossible to extract useful information about the individual objects when they are different in size, shape, and chemical composition. Extracting information is only possible if all of them are sufficiently similar, i.e., they must have the same shape (including orientation) and at least a narrow size distribution. In the case of identical islands at positions \mathbf{R}_m , the amplitudes $A_m^{\text{diffuse}}(\mathbf{q})$ are also identical and Eq. (2) transforms into

$$\mathbf{A}_{\text{total}}^{\text{diffuse}}(\mathbf{q}) = \mathbf{A}^{\text{diffuse}}(\mathbf{q}) \sum_m e^{i\mathbf{q} \cdot \mathbf{R}_m}. \quad (3)$$

The diffuse intensity from the entire island ensemble can be then written as

$$I(\mathbf{q}) = I(\mathbf{q})_{\text{single}} G(\mathbf{q}), \quad (4)$$

where the interference function is defined as

$$G(\mathbf{q}) = \left| \sum_m e^{i\mathbf{q} \cdot \mathbf{R}_m} \right|^2 = \sum_{m,n} e^{i\mathbf{q} \cdot (\mathbf{R}_m - \mathbf{R}_n)}. \quad (5)$$

In Eq. (5), the summation is performed over the entire ensemble of mesoscopic structures. This requires a knowledge of all island positions \mathbf{R}_m , which is practically impossible. Equation (5) should therefore read

$$G(\mathbf{q}) = \left\langle \sum_{m,n} e^{i\mathbf{q} \cdot (\mathbf{R}_m - \mathbf{R}_n)} \right\rangle, \quad (6)$$

where the brackets $\langle \rangle$ denote averaging over all possible configurations of the mesoscopic ensemble.

To a certain extent the positions \mathbf{R}_m can be determined by imaging techniques, such as atomic force microscopy (AFM). Here, a sufficiently large area in real space has to be considered. However, the result obtained has to be adapted to the experimental conditions, i.e., the finite coherence of the x-ray beam has to be taken into account. This means that the

ASYMMETRIC CORRELATION FUNCTION DESCRIBING...

PHYSICAL REVIEW B 71, 115323 (2005)

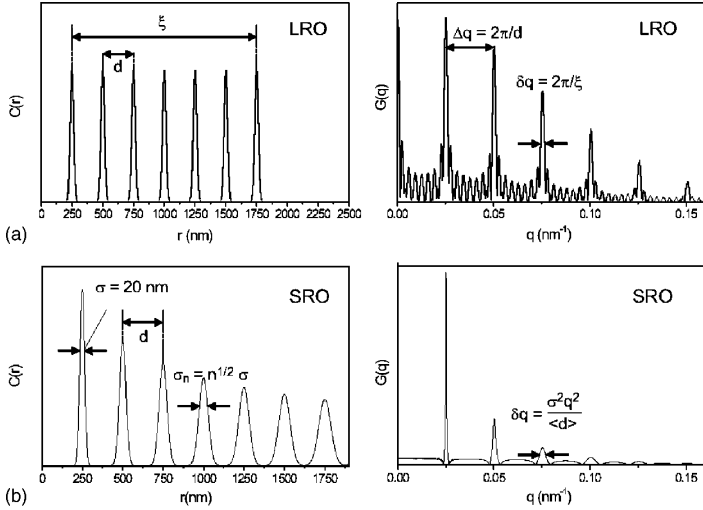


FIG. 2. Autocorrelation function $C(\mathbf{r})$ in real space and the corresponding interference function $G(\mathbf{q})$ in reciprocal space for (a) long-range ordering (LRO), and (b) short-range ordering (SRO) using a random-walklike behavior. For LRO the peak widths and peak spacings of $C(\mathbf{r})$ and $G(\mathbf{q})$ are constant, whereas for SRO the peak widths increase with the peak index. A mean lateral distance of $\langle d \rangle = 250$ nm has been assumed.

coherent sum in (5) has to be taken over those islands that are inside the coherence volume. This sum has then to be averaged over all islands. In other words, the total intensity is calculated by partly coherent and partly incoherent averaging over different subensembles. Recently, this procedure has been successfully applied to SiGe islands.¹²

Equation (4) shows that, as a result of spatial correlation, the diffuse intensity of a single island is modulated by the interference function $G(\mathbf{q})$. Note that $G(\mathbf{q})$ is defined in reciprocal space, whereas the correlation function $C(\mathbf{r})$ is defined in real space. There exists, however, an interesting relationship between $C(\mathbf{r})$ and $G(\mathbf{q})$, which can be obtained by expressing the positions \mathbf{R}_m of the islands in terms of the “island density” through

$$\varrho(\mathbf{r}) = \sum_m \delta(\mathbf{r} - \mathbf{R}_m). \quad (7)$$

Here, the extended size of the mesoscopic structures is neglected and only the mean positions \mathbf{R}_m are considered. By using this relationship for calculating the correlation function

$$C(\mathbf{r}) = \int \varrho(\mathbf{r}') \varrho(\mathbf{r} + \mathbf{r}') dV', \quad (8)$$

we obtain

$$G(\mathbf{q}) = \int C(\mathbf{r}) e^{i\mathbf{q} \cdot \mathbf{r}} dV. \quad (9)$$

Thus, the interference function in reciprocal space $G(\mathbf{q})$ is the Fourier transform of the correlation function in real space $C(\mathbf{r})$ and vice versa.

Ordering phenomena are usually discussed in the framework of two limiting models—short-range order (SRO) and long-range order (LRO). For LRO [Fig. 2(a)], the correlation is assumed to be perfect within coherent domains of size ξ [i.e., $C(\mathbf{r})$ exhibits (sharp) peaks of constant width indepen-

dent of \mathbf{r}]. In this case $G(\mathbf{q})$ also shows correlation peaks with constant widths, which are given by Scherrer's formula,¹³

$$\delta q = \frac{2\pi}{\xi}. \quad (10)$$

The domain size ξ can then be interpreted as a correlation length that quantitatively describes the length scale up to which positional correlation is present.

For SRO, the ordering disappears gradually at large distances [Fig. 2(b)]. Therefore the peaks in $C(\mathbf{r})$ become broader and are damped with increasing relative distance r . For the rms peak widths of $C(\mathbf{r})$, Stangl *et al.*⁷ have assumed that they behave similar to a random-walk, i.e.,

$$\sigma_n = \sqrt{n}\sigma. \quad (11)$$

Here σ is the rms standard deviation of the mean distance $\langle d \rangle$ between two adjacent islands and is, thus, identical to the peak width of the first correlation peak of $C(\mathbf{r})$. As a consequence of Eq. (11), the peak widths of $G(\mathbf{q})$ also increase with the peak index. They can be expressed as

$$\delta q = \frac{(\sigma q)^2}{\langle d \rangle}, \quad (12)$$

with a correlation length

$$\xi = \frac{\langle d \rangle^3}{2\sigma^2}. \quad (13)$$

Stangl *et al.*⁷ have proven the validity of the “random-walk” SRO model for SiGe and PbSe/PbEuTe quantum-dot superlattices. In these systems the degree of ordering is remarkably high, but the SRO behavior is still evident.

The qualitative difference between SRO and LRO is sketched in Fig. 2. In both models the peaks in $G(\mathbf{q})$ are damped for larger q and are equally spaced. Please note that the LRO model employs a finite domain size ξ leading to a

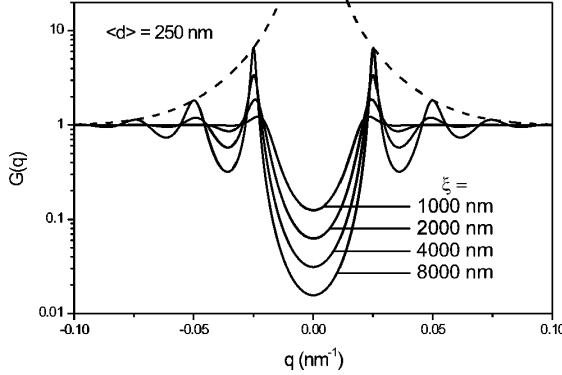


FIG. 3. Calculated interference function $G(q)$ obtained using Eq. (14) for $\langle d \rangle = 250 \text{ nm}$ and various values of the correlation length ξ . The dashed line is the envelope function of the satellite peaks for $\xi = 8000 \text{ nm}$.

finite, constant peak width of $\delta q = 2\pi/\xi$. By contrast, according to Eq. (12), the peak widths get larger with increasing q for the SRO model.

For the random-walk SRO model as described by Eq. (11), an analytical expression for the interference function $G(\vec{q})$ exists and is given by

$$G(q) = \frac{1 - e^{-\sigma^2 q^2}}{1 + e^{-\sigma^2 q^2} - 2e^{-\sigma^2 q^2/2} \cos(q\langle d \rangle)}. \quad (14)$$

This expression was developed by Hosemann^{14,15} in order to describe scattering in the framework of the so-called paracrystal model. This model attempts to account for both the liquid-like (amorphous) SRO scattering and the sharp diffraction maxima from an LRO structure. The Hosemann function as given in Eq. (14) has been already applied for describing in-plane correlation of free-standing quantum dots.^{16,17} Here $\langle d \rangle$ and σ were used as free-fitting parameters. They were treated as anisotropic in real space, since a generalized two-dimensional (in q -space) analytical expression for $G(\vec{q})$ does not exist yet.

A very interesting point is the interrelation between $C(\mathbf{r})$ and $G(\mathbf{q})$. What qualitative information can be obtained from the functional behavior of $G(\mathbf{q})$? In the literature (e.g., Ref. 18), the statement can often be found that the presence of many peaks in $G(\mathbf{q})$, i.e., the presence of high-order correlation peaks, can be interpreted as very high correlation. This statement is, however, not generally correct and will be discussed now in more detail. It is certainly true that the degree of ordering is related to the peak width of the first correlation peak, and the corresponding correlation length is given by Eq. (10). This behavior can be inspected in Fig. 3, where calculated values of the interference function $G(q)$ given by Eq. (14) are plotted for different values of ξ . The width of the first correlation peak, indeed, inversely scales with the correlation length ξ . In addition to that behavior, the correlation peaks decay with increasing values of q . The intensity decay can be quantified by an envelope function of the form $(1 + e^{-\sigma^2 q^2/2})/(1 - e^{-\sigma^2 q^2/2})$. The smaller ξ is, the stronger the de-

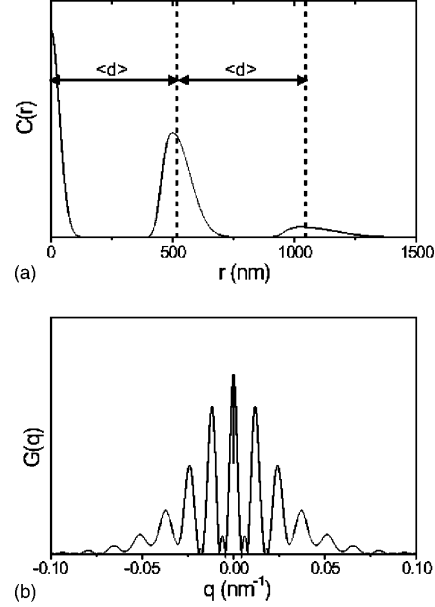


FIG. 4. Calculated autocorrelation (a) and corresponding interference (b) functions $C(\mathbf{r})$ and $G(\mathbf{q}_{\parallel})$, for a special SRO model, exhibiting only next-neighbor correlations. A mean distance of $\langle d \rangle = 500 \text{ nm}$ has been assumed. The line shape in $C(\mathbf{r})$ is asymmetric. As a consequence, many high-order correlation peaks are present in $G(\mathbf{q})$ that are not equidistantly spaced but disperse outward slightly with increasing q .

cay of the correlation peaks. In the SRO model as used in Eq. (11), the appearance of many orders of satellite peaks is thus a sign of high correlation.

The behavior of SRO discussed above is, however, not generally valid. In Fig. 4, an SRO model where only next-neighbor correlation is present is depicted. When an *asymmetric* peak profile is used for $C(\mathbf{r})$ [Fig. 4(a)] instead of a symmetrical Gaussian distribution, interesting features in the resulting intensity distribution $G(\mathbf{q})$ [Fig. 4(b)] are obtained: (i) Many orders of correlation peaks are present, although rather SRO is present. (ii) The position of the first correlation peak in $G(\mathbf{q})$ is given by $q = (2\pi/\langle d \rangle)$, however, the spacing between neighboring peaks disperse slightly outward. This is a direct consequence of the asymmetric peak profile of $C(\mathbf{r})$.

III. EXPERIMENT

X-ray diffuse scattering intensity distributions were measured in order to probe the interference function $G(q)$ originating from lateral island-island correlation. Two different scattering geometries have been employed, namely, high-resolution x-ray diffraction (HRXRD) and grazing-incidence small-angle x-ray scattering (GISAXS). While GISAXS is solely sensitive to morphological details, such as island shape, size, and spatial correlation, HRXRD additionally probes the lattice strains inside and in the vicinity of the

ASYMMETRIC CORRELATION FUNCTION DESCRIBING...

PHYSICAL REVIEW B 71, 115323 (2005)

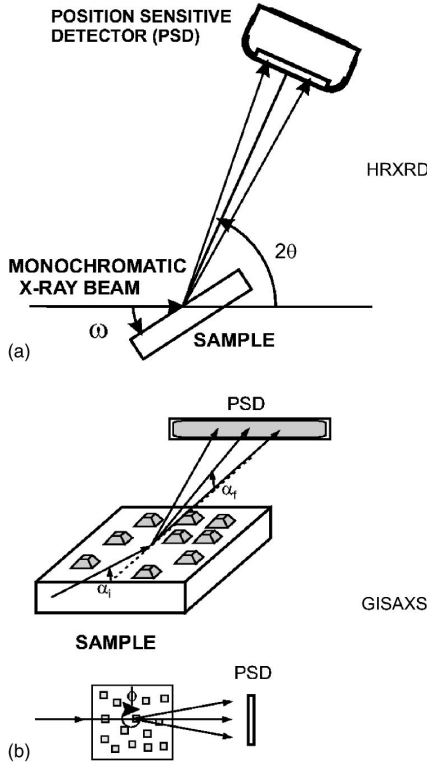


FIG. 5. Experimental scattering geometry for (a) HRXRD and (b) GISAXS. The use of a linear position sensitive detector (PSD) ensures rapid data acquisition.

SiGe islands. Intense synchrotron radiation as provided by the BW2 wiggler station at HASYLAB/DESY has been used in the x-ray scattering experiments. An x-ray wavelength of $\lambda=1.54 \text{ \AA}$ was selected by a Si(111) double-crystal monochromator with a typical bandwidth of $\Delta\lambda/\lambda=10^{-4}$. A multidetection scattering scheme has been employed in that a linear position-sensitive detector (PSD) was placed at a distance of about 750 mm behind the sample. By using a small spot size of the x-ray beam (typically 100–200 μm) on the sample, each channel of the PSD corresponds to a certain scattering angle.

With HRXRD the PSD is aligned along the 2θ direction [see Fig. 5(a)]. A two-dimensional mapping of the diffusely scattered intensity distribution in reciprocal space can be performed by a single rocking scan (ω scan) of the sample. This procedure ensures fast data acquisition with medium resolution in the scattering plane of typically $\Delta q=4\times 10^{-4} \text{ \AA}^{-1}$. This value—although being definitely worse than the high resolution provided by a crystal analyzer—turned out to be sufficient to clearly resolve satellite peaks in the diffuse scattering. In the direction perpendicular to the scattering plane the resolution is determined by a narrow collimating slit system and amounts to $\Delta q=3\times 10^{-3} \text{ \AA}^{-1}$.

With GISAXS the in-plane diffuse intensity distribution was measured by using a PSD oriented horizontally to the sample surface and by performing azimuthal scans of the

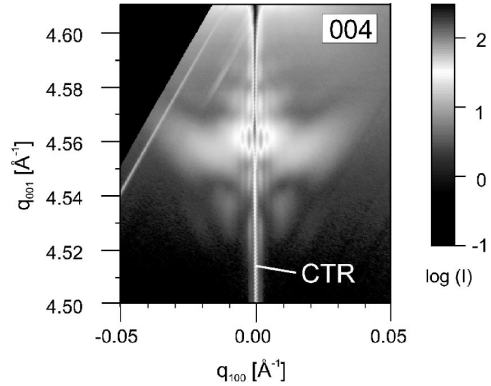


FIG. 6. Measured reciprocal space map ($q_{100}-q_{001}$ -plane) in the vicinity of the symmetrical 004 reciprocal lattice point. The Si 004 substrate reflection appears at $q_{001}=4.628 \text{ \AA}^{-1}$ and is not shown here.

sample [Fig. 5(b)]. The measurements have been carried out at glancing angles close to the critical angle of total external reflection. The in-plane resolution typically amounts to $\Delta q=4\times 10^{-4} \text{ \AA}^{-1}$.

The experimental setup and a more detailed description of GISAXS and HRXRD can be found in Refs. 3 and 8, respectively.

IV. RESULTS AND DISCUSSION

For the sample as presented in Figs. 1(a) and 1(b), the two-dimensional nature of the in-plane interference function $G(\mathbf{q})$ can be inspected in Fig. 1(c), where the Fourier transform (power density spectrum) of the AFM height profile [Fig. 1(a)] is displayed. As further discussed in Ref. 3 this spectrum may be directly compared to the GISAXS in-plane intensity distribution, which is depicted in Fig. 1(d). Both AFM and GISAXS clearly show fourfold symmetry with correlation peaks along both the $\langle 100 \rangle$ and $\langle 110 \rangle$ directions. According to Eq. (1) the corresponding mean spacings fulfill the relationship $\langle d_{100} \rangle / \langle d_{110} \rangle = 294/214 \text{ nm} \approx \sqrt{2}$, which demonstrates the development of a square island pattern in real space. However, owing to the low number of islands contributing to the power density spectrum, the AFM investigations suffer from insufficient statistical significance. As a consequence, only the first-order satellite peaks can be detected. This implies that the AFM data cannot be further used for a quantitative evaluation of the interference function $G(\mathbf{q})$. By contrast, X-rays statistically average over a rather large ensemble of islands, making the data very reliable concerning statistics.

In Fig. 6 the measured diffuse intensity (HRXRD) in the vicinity of the symmetrical Si 004 reciprocal lattice point is shown. Here, the scattering plane contains the $[100]$ axis, i.e., the interference function is probed along this direction. The diffuse scattering consists of a rather sharp peak located at about $q_{001}=4.56 \text{ \AA}^{-1}$, which is surrounded by a characteristic butterfly shaped diffuse feature. The characteristic shape of the intensity distribution is determined by the complex

interplay of strain, local tilts of the atomic planes inside the island, and the island shape function. Comparison to respective x-ray diffuse scattering simulations using elasticity theory could be used to establish the identity of an abrupt vertical Ge composition jump inside the SiGe island.^{8,19} In the following we will focus on the lateral positional island correlation and its impact on the diffusely scattered intensity.

In Fig. 6 strong satellite peaks (rods) up to third order are clearly resolved in the immediate proximity of the 00ℓ crystal truncation rod (CTR) of the Si substrate. The q dependence of the satellite peaks is given by the interference function $G(\mathbf{q})$ as defined in Eq. (6). However, as can be inspected in Figs. 1(c) and 1(d), for the AFM in-plane power spectrum and the GISAXS intensity, the interference function $G(\mathbf{q})$ is of a two-dimensional nature, and integration over one direction, as performed by the finite experimental resolution, might affect the experimental intensity distribution. As described in Sec. III the experimental resolution in the q_{100} direction (i.e., perpendicular to the scattering plane) is given by $\Delta q_{100}=3\times 10^{-3}\text{ \AA}^{-1}$. This is still smaller than the distance of the first-order correlation peaks in q_{100} direction, which is given by $\Delta q_{100}=4.3\times 10^{-3}\text{ \AA}^{-1}$. Thus, the intensity distribution as shown in Fig. 1 should not be substantially affected by the experimental integration along q_{100} .

A linear section at $q_{001}=4.560\text{ \AA}^{-1}$ through the experimental intensity distribution shown in Fig. 6 is presented in Fig. 7(a) as open squares. In order to evaluate our data in more detail we have performed a line-shape analysis of our experimental data using Gaussian profiles. Hereby, the smooth strain and shape-induced diffuse scattering has been taken into account by using a broad Gaussian. From this analysis the experimental peak positions of first-, second-, and third-order satellites can be derived with high accuracy as $q_{100}=\pm 0.00215\text{ \AA}^{-1}$, $\pm 0.0045\text{ \AA}^{-1}$, and $\pm 0.0069\text{ \AA}^{-1}$, respectively. Using Eq. (1) the peak position of the first-order satellite corresponds to a mean island-island distance of about $\langle d_{100} \rangle = 292\text{ nm}$, which fits excellently to the values obtained by GISAXS ($\langle d_{100} \rangle = 294\text{ nm}$). Comparison to the corresponding AFM micrograph [Fig. 1(a)] shows that this value of $\langle d_{100} \rangle$ corresponds to the island-island distance *within* a chain but is not related to the distance *between* chains.

It is important to mention that, depending on the order, the satellite peaks are not equidistantly spaced but disperse outward slightly with increasing horizontal momentum transfer q_{100} . The observed dispersion cannot be explained within a LRO model or the random-walk SRO model as presented in Fig. 3, where the satellite peak spacings would remain constant. Consequently, the Hosemann function [Eq. (14)] cannot be employed to fit our data.

In order to extract “pure” correlation-related information from the experimental data we have subtracted the shape and strain-induced diffuse scattering, approximated as being Gaussian, from the experimental profile. Also the strong crystal truncation rod at $q_{100}=0$ has been subtracted. The remaining data are then Fourier transformed, and the resulting correlation function $C(r)$ is depicted in Fig. 7(b). Please

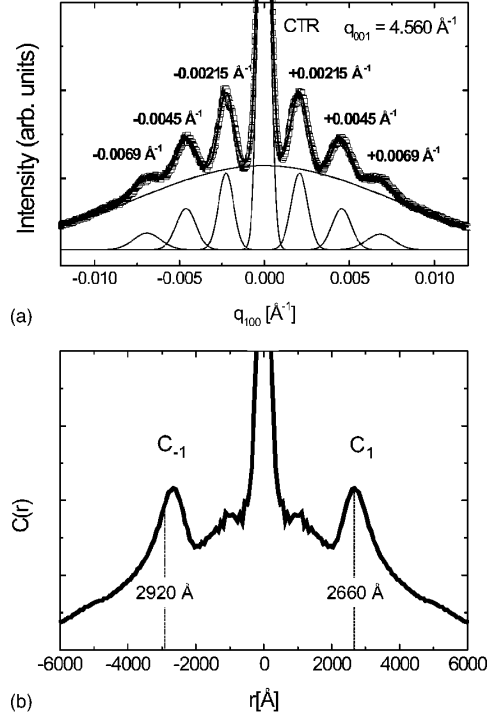


FIG. 7. Measured diffuse intensity of SiGe islands in the vicinity of the 004 reciprocal lattice point: (a) Linear section at $q_{001}=4.560\text{ \AA}^{-1}$ through the experimental intensity distribution shown in Fig. 6. Experimental data are presented as open squares. The solid line represents the best fit to the experimental data using Gaussian line profiles. (b) Corresponding autocorrelation function $C(r)$ in real space. The peak position ($r=266\text{ nm}$) and the “center of mass” ($r=292\text{ nm}$) of the first correlation peaks $C_{\pm 1}$ are marked as dashed lines.

note that, $C(r)$ exhibits only first-order peaks, labeled as $C_{\pm 1}$, indicating the presence of SRO.

The peak positions of $C_{\pm 1}$ can be evaluated as $r=\langle d_{100} \rangle = \pm 266\text{ nm}$, respectively, indicating a somewhat smaller mean island distance as evaluated from the first-order satellite peak positions in $G(q)$ and using Eq. (1), which gives $r=\langle d_{100} \rangle = \pm 292\text{ nm}$. This deviation is caused by the *asymmetric* line profiles of the first-order peaks $C_{\pm 1}$. While the peak positions are given by $r=\pm 266\text{ nm}$, the respective “centers of mass” of $C_{\pm 1}$ are located slightly more outward and their positions agree well with $r=\pm 292\text{ nm}$. Both values for r are marked in Fig. 7(b) as dashed lines.

How can we explain the asymmetric line profile in the autocorrelation function? We would like to emphasize again that the islands are formed *successively*: At early stages of growth dimers and linear trimers of islands are formed, which, at later stages of growth, develop into extended linear island chains oriented along $\langle 100 \rangle$.^{3,10} The linear alignment, thus, takes place by consecutive nucleation of additional islands at the end of an already existing chain. The generation of chains can be explained in terms of minimization of the elastic strain energy during growth¹¹ and by corresponding

ASYMMETRIC CORRELATION FUNCTION DESCRIBING...

kinetic Monte Carlo simulations.¹⁰ However, these calculations of the elastic strain energy of fully evolved islands do not show any energy minimum along $\langle 100 \rangle$ nor any local maximum along the $\langle 110 \rangle$ direction, which can lead to an averaged flux of adatoms into the elastically soft direction.¹¹ However, several papers^{20,21} report on the phenomenon that the strain energy around a Stranski Krastanow island can overcompensate the driving forces of growth and even can cause an ablation of deposited material. Indeed, a wetting-layer depletion has been found for LPE SiGe islands, where the depleted area follows exactly the symmetry of strain energy density in the wetting layer.¹⁹ The depletion of the wetting layer impedes adatom nucleation in the immediate vicinity of the island. It is, however, noteworthy that, the depletion for the sample discussed here is so small that it cannot be observed in the AFM image (Fig. 1).

The growth scenario discussed here leads to a strong “island-island repulsion” at distances similar to the island base width, which prevents a growing island to “touch” a fully evolved adjacent island. This can be observed in Figs. 1(a) and 1(b) where the island-island distance within an island chain does not fall below values of about $r \approx 220$ nm, although the island base diagonal width would allow values down to $r=180$ nm. On the other hand, much larger distances than $\langle d_{100} \rangle = 266$ nm are possible; from the AFM images distances up to about 400 nm are observed, which corresponds to the distance between adjacent island chains. As a consequence of this behavior, an asymmetric distribution of the island-island distances is induced and the profile of the first-order peak in the autocorrelation function becomes asymmetric. The values $r=220$ nm (minimum island distance) and $r=400$ nm (maximum island distance) observed in the atomic force micrograph are also found in the experimental autocorrelation function [Fig. 7(b)]. At these r values the correlation vanishes. There is thus direct agreement between AFM and corresponding x-ray results.

PHYSICAL REVIEW B 71, 115323 (2005)

V. CONCLUSIONS

In conclusion, we have discussed the lateral ordering of SiGe islands grown by LPE on (001)Si. At sufficiently large island area coverage, rows of SiGe islands are formed that extend along the $\langle 100 \rangle$ directions. The positional correlation within the island chains has been studied by x-ray diffuse scattering and atomic force microscopy. Although high orders of satellite peaks can be observed, the results can be explained by a short-range order model. The corresponding correlation function shows an asymmetric peak profile. This, in addition, leads to nonequidistantly spaced satellite peaks, which disperse outward slightly with increasing q .

The observed asymmetric island-island correlation is caused by the successive growth of the islands within a chain. This means that the next island is always formed at the end of an already existing chain. The position of the new island is presumably determined by depletion of the wetting layer around the islands, which exactly follows the shape of the strain energy density. Therefore, the distribution of the islands around the most probable value $\langle d_{100} \rangle = 266$ nm is asymmetric. The distances within the chains cannot be smaller than about $r \approx 220$ nm, however, much larger values up to $r=400$ nm are possible.

ACKNOWLEDGMENTS

We thank our co-workers H. Raidt and P. Schäfer for valuable discussions and assistance with the experiment. We are also thankful to H. Wawra (Institut für Kristallzüchtung, Berlin) for providing us with the SiGe sample. Finally, we gratefully acknowledge technical support by the HASYLAB staff. This work was partly supported by “Deutsche Forschungsgemeinschaft” within the framework of Sfb 296.

*Present address: Fachbereich Physik, Martin-Luther-Universität Halle-Wittenberg, Hoher Weg 8, D-06120 Halle/Saale, Germany.

¹D. Bimberg, M. Grundmann, and N. N. Ledentsov, *Quantum Dot Heterostructures* (Wiley, Chichester, NY, 1999).

²I. Stranski and L. Krastanow, *Sitzungsber. Akad. Wiss. Wien, Math.-Naturwiss. Kl., Abt. 2B* **146**, 797 (1937).

³M. Schmidbauer, T. Wiebach, H. Raidt, M. Hanke, R. Köhler, and H. Wawra, *Phys. Rev. B* **58**, 10 523 (1998).

⁴F. Hatami, U. Müller, H. Kissel, K. Braune, R.-P. Blum, S. Rogaschewski, H. Niehus, H. Kirmse, W. Neumann, M. Schmidbauer *et al.*, *J. Cryst. Growth* **216**, 26 (2000).

⁵G. Springholz, V. Holý, M. Pinczolits, and G. Bauer, *Science* **282**, 734 (1998).

⁶Y. I. Mazur, W. Q. Ma, X. Wang, Z. M. Wang, G. J. Salamo, M. Xiao, T. D. Mishima, and M. B. Johnson, *Appl. Phys. Lett.* **83**, 987 (2003).

⁷J. Stangl, T. Roch, V. Holý, M. Pinczolits, G. Springholz, G. Bauer, I. Kegel, T. H. Metzger, J. Zhu, K. Brunner *et al.*, *J. Vac.*

Sci. Technol. B **18**, 2187 (2000).

⁸T. Wiebach, M. Schmidbauer, M. Hanke, H. Raidt, R. Köhler, and H. Wawra, *Phys. Rev. B* **61**, 5571 (2000).

⁹M. Schmidbauer, T. Wiebach, H. Raidt, M. Hanke, R. Köhler, and H. Wawra, *J. Phys. D* **32**, 230 (1999).

¹⁰M. Meixner, E. Schöll, M. Schmidbauer, H. Raidt, and R. Köhler, *Phys. Rev. B* **64**, 245307 (2001).

¹¹M. Hanke, H. Raidt, R. Köhler, and H. Wawra, *Appl. Phys. Lett.* **83**, 4927 (2003).

¹²M. Hanke, M. Schmidbauer, and R. Köhler, *J. Appl. Phys.* **96**, 1959 (2004).

¹³A. Guinier, *X-Ray Diffraction* (Freeman, San Francisco, 1968).

¹⁴R. Hosemann, *Z. Phys.* **128**, 1 (1950).

¹⁵R. Hosemann and S. N. Bagchi, *Direct Analysis of Diffraction by Matter* (North-Holland, Amsterdam, 1963).

¹⁶I. Kegel, T. H. Metzger, J. Peisl, P. Schittenhelm, and G. Abstreiter, *Appl. Phys. Lett.* **74**, 2978 (1999).

¹⁷V. Chamard, T. H. Metzger, E. Bellet-Amalric, B. Daudin, C.

SCHMIDBAUER, HANKE, AND KÖHLER

PHYSICAL REVIEW B 71, 115323 (2005)

- Adelmann, H. Mariette, and G. Mula, *Appl. Phys. Lett.* **79**, 1971 (2001).
- ¹⁸K. Zhang, C. Heyn, W. Hansen, T. Schmidt, and J. Falta, *Appl. Phys. Lett.* **76**, 2229 (2000).
- ¹⁹M. Hanke, M. Schmidbauer, D. Grigoriev, H. Raidt, P. Schäfer, R. Köhler, A.-K. Gerlitzke, and H. Wawra, *Phys. Rev. B* **69**, 075317 (2004).
- ²⁰X. Z. Liao, J. Zou, D. J. H. Cockayne, J. Qin, Z. M. Jiang, X. Wang, and R. Leon, *Phys. Rev. B* **60**, 15 605 (1999).
- ²¹U. Denker, O. G. Schmidt, N. Y. Jin-Phillip, and K. Eberl, *Appl. Phys. Lett.* **78**, 3723 (2001).

2.3 Elastische Relaxation in diskontinuierlichen Benetzungsschichten

M. Hanke, T. Boeck, A.-K. Gerlitzke, F. Syrowatka, F. Heyroth

Elastic strain relaxation in discontinuous wetting layers and its impact on lateral ordering of heteroepitaxial dots

Phys. Rev. B **74**, 153304 (2006).

Es wurde bereits mehrfach in Kap. 2.2 auf die Bedeutung des Deformationsfeldes für die Ausprägung lateraler Korrelation hingewiesen. Abgesehen von dem in Kap. 2.2.3 diskutierten Prozess zur Entstehung sogenannter Dotmoleküle, der primär auf einem lokalen Abtrag einer zuvor abgeschiedenen sehr germaniumarmen Schicht beruht, wurden jedoch nur Systeme mit kontinuierlicher Benetzungsschicht besprochen. Im vorliegenden Kapitel wird dagegen der allgemeinere Fall einer diskontinuierlichen Benetzungsschicht behandelt.

Bei der für die LPE angewandten Schiebeboot-Technik⁹ befindet sich die metallische Schmelze innerhalb eines kleinen Graphittiegels, welcher horizontal über das zu bewachsende Substrat geschoben werden kann. Dieses Setup erlaubt eine Verschiebung während der Abkühl- bzw. Wachstumsphase, so dass auf der Probe nebeneinander subsequente Wachstumsstadien beobachtet werden können.

Im vorliegenden Fall erfolgte die SiGe Heteroepitaxie aus einer Indiumschmelze über einen Temperaturgradienten von 0.16 K/min zwischen 930°C und 920°C, wobei nach 6, 9 und 12 min (korrespondierend zu partiellen Temperaturrampen ΔT von 1, 1.5 und 2K) die Schmelze um etwa 3 mm lateral auf dem Si(001) Zielsubstrat verschoben wurde.

Initialstadien zeigen flache Oberflächenverwellungen mit Tendenz zur Stufenbildung an den Flanken. Später entwickeln sich aus diesen kleinere vierzählige Inseln, die von kreisförmigen Ringen umgeben sind. Diese Strukturen weisen eine steilen Abfall nach innen bei flachen Außenflanken auf. Durch einen partiellen Abtrag entstehen aus zunächst kreisrunden Inseln steilere, {111} facettierte Inseln, wobei im Zuge der Morphologieänderung die Benetzungsschicht zwischen Insel und Ring vollständig abgetragen wird, wie energiedispersive Röntgenspektroskopie an diesen Bereichen belegt. Ermöglicht man weitere Abscheidung, so dienen die Ringinnenkanten aufgrund des fehlenden lateralen Confinements und der damit einhergehenden elastischen Relaxation, günstige Nukleationsbedingungen. Dabei startet die Dekoration zunächst entlang der elastisch weicheren $\langle 100 \rangle$ Richtungen. Berechnungen mittels der Methode der Finiten Elemente zum Deformationszustand belegen nicht nur einen schnelleren Abfall der Deformationsenergieladung entlang $\langle 100 \rangle$, wie im Fall kontinuierlicher Benetzungsschichten (Kap. 2.2.1), sondern zeigen zudem ein *Energieminimum* in dieser Richtung. Offenbar führt erst eine Kombination aus Diskontinuität in der Benetzungsschicht und elastischer Anisotropie zu diesem Effekt.

⁹Eine andere sogenannte Kipptiegel-Technik nutzt drehbar gelagerte Tiegel, in denen das Substrat an einer Seite befestigt wird. Verkippt man nun diesen Tiegel, so kann die flüssige Schmelze sehr schnell vom Substrat fließen, was u.a. sehr kurze Wachstumszeiten ermöglicht. Allerdings lassen sich auf diese Weise verschiedene Zonen auf derselben Probe nicht herstellen.

Elastic strain relaxation in discontinuous wetting layers and its impact on lateral ordering of heteroepitaxial dots

M. Hanke,¹ T. Boeck,² A.-K. Gerlitzke,² F. Syrowatka,³ and F. Heyroth³

¹*Martin-Luther-Universität Halle-Wittenberg, Fachbereich Physik, Hoher Weg 8, D-06120 Halle/Saale, Germany*

²*Institut für Kristallzüchtung, Max-Born-Straße 2, D-12489 Berlin, Germany*

³*Interdisziplinäres Zentrum für Materialwissenschaften, Hoher Weg 8, D-06120 Halle/Saale, Germany*

(Received 30 August 2006; published 10 October 2006)

We discuss morphological changes of strained SiGe/Si(001) dots grown from an indium solution. In the course of a particular depletion scenario initial, lenslike dots transform into truncated pyramids of fourfold symmetry inside circular rims of rising height and steep inner edge. Further dot nucleation performs close to the rim indicating elastically relaxed lattice sites. The observations made are supported by numerical finite element calculations on the strain energy distribution.

DOI: 10.1103/PhysRevB.74.153304

PACS number(s): 68.65.-k, 68.37.Hk, 81.15.Lm

Condensed matter at zero dimensionality has promoted an overwhelming research effort comprising a zoo of fabrication techniques and analytical tools.^{1–4} In many cases self-formation of semiconductor dots^{5,6} can provide a suitable alternative to expensive and time-consuming template based approaches.⁷ Within the Stranski-Krastanow process a heteroepitaxial layer initially wets the surface and the strain energy increases with thickness. Beyond a critical value planar wetting becomes, however, unstable in favor of three-dimensional growth as the energy gain due to elastic relief overcompensates additional free surface.⁸ Since molecular beam epitaxy (MBE) approaches a more kinetically restricted regime, dot nucleation from a metallic solution during liquid phase epitaxy (LPE), cooling rates of less than 0.2 K/min provided, enables growth studies extremely close to thermodynamic equilibrium. Shape transformation^{9–13} and assembling phenomena^{14–19} of heteroepitaxial dots are frequently discussed within these limits, whereas SiGe on silicon has widely served as a model system. One of the most obvious, however, hardly recognized differences manifest in the dot orientation. Since MBE based SiGe/Si(001) dots form {10l} side facets,^{20,21} respective LPE dots depict {11l} facets.^{22,23} Elastic strain, caused by buried dots and mediated by subsequent spacer layers, supports vertical positional replication^{14,15} and may also improve lateral assembling within subsequent layers of dot stacks.¹⁹ Strain propagation within a single heteroepitaxial layer, on the other hand, remains a surface-mediated process, which strongly relates dot assembling to the particular relaxation behavior within the wetting layer.

Here we discuss the formation of a discontinuous, nonuniform wetting layer and its implications for the lateral self-formation of heteroepitaxial dots. Samples have been grown by means of LPE applying a slide-boat setup. There a target substrate is placed underneath a horizontally movable graphite frame which contains the liquid solution. In a first step the indium solution has been fully saturated with silicon at 930 °C whereas the amount of germanium (3.551 g) added to 50-g indium corresponds to 10% germanium in the solid state. In order to ensure a clean growth environment the entire LPE process performs under a pure hydrogen flux. After a mandatory annealing step at 930 °C for 1 h to remove the

natural oxide layer and a homogenization of the solution for 3 h, the frame is placed on top of the Si(001) substrate. Then a constant gradient of 0.16 K/min is applied during an overall temperature ramp from 930 to 920 °C, which initiates the heteroepitaxial growth. However, to get an *ex situ* access to initial and intermediate growth stages the frame (containing the liquid solution) was moved forward by approximately 3 mm after 6, 9, and 12 min. Thus adjacent sample positions provide stages according to temperature ramps ΔT of 1, 1.5, 2, and 10 K which enables a detailed reconstruction of the growth scenario later on. Therefore we have applied a field emission scanning electron microscope (Philips XL30) operated at primary electron energies of 2 and 12 kV for top view and side view images, respectively.

Incipient heteroepitaxial stages have been revealed by stripping the solution after an applied ramp from 930 to 929 °C. Tiny surface undulations, Fig. 1(a), provide elastic relief at the expense of additional free surface. It is noteworthy that the developing pattern tends to step bunching whereas the step density subsequently increases on the slopes. Eventually the wetting layer shrinks between initial stages resulting in lenslike SiGe dots with an average height of 410 nm along a base diameter of 1.7 μ m, Fig. 1(b). The inset displays an intermediate quadruplet with preferential ⟨100⟩ orientation. Lateral assembling, mediated by prior surface undulations, inherently happens before the final dot shape evolves. The nucleation of dots with increased lattice mismatch, on the other hand, performs on a much faster time scale than the evolution of lateral ordering.^{16,17}

During the following growth sequence the temperature was lowered to 928.5 °C. Circular dots split into a central truncated pyramid (d1) with {11l} side facets and an asymmetrically shaped rim (w) enclosing uncovered silicon substrate (sub), Fig. 1(c). This process is obviously supported by further strain relaxation at the free-standing side facets. Typical widths and heights of walls surrounding individual dots are 270 nm and about 45 nm, respectively. Even more extended rings, inset of Fig. 1(c), have been observed, e.g., around quadruplets of fully developed dots. LPE relies on a finite material reservoir, so that the liquid solution becomes undersaturated in the course of dot nucleation. Strain induced material transport from the wetting layer as well as from the

BRIEF REPORTS

PHYSICAL REVIEW B 74, 153304 (2006)

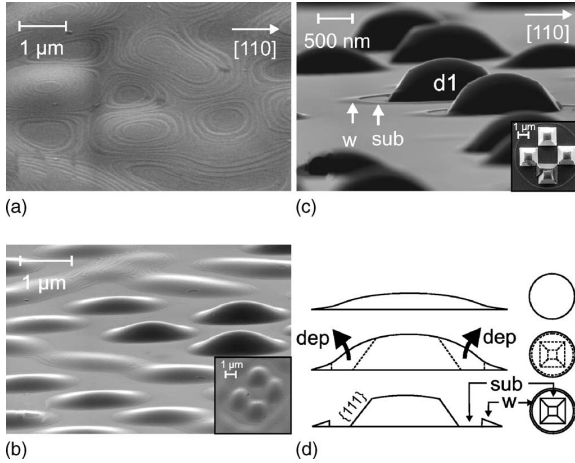


FIG. 1. The initial growth sequence starts with surface undulations which are formed by discrete vertical steps (a). Individual lenslike dots subsequently appear (b) with preferential $\langle 100 \rangle$ direction (inset therein). They transform during later stages (c) into truncated pyramids (d1) with four adjacent $\{111\}$ side and a single (001) top facet. Strain induced depletion (dep) yields uncovered silicon substrate (sub) and asymmetrically shaped walls (w) surrounding single dots and dot ensembles (inset). (d) depicts the subsequent stages (a) through (c) in side and top view.

dots back into the liquid solution becomes very likely since the nucleation performs close to equilibrium. Figure 1(d) illustrates the observed depletion (dep) which transfers round-shaped dots into fourfold pyramids surrounded by asymmetrically shaped rims. Moreover, the fourfold symmetry of the depletion inside the rim indicates a strain mediated shape transformation. Trench formation near MBE grown SiGe dots²⁴ is also strain mediated. However, the material moves from the substrate into the dot.

Due to the subsequently performed cooling to 928 °C the solution becomes oversaturated which causes further nucleation. Small dots (d2) in Fig. 2(b) indicate favorable nucleation sites along $\langle 100 \rangle$ near the rim. However, their distribution eventually becomes quite uniform, Fig. 2(a). Obviously the discontinuity at the rim provides elastic relief due to the lack of lateral mechanical confinement.

Nucleation at the rim and the observed occupation sequence can be explained by numerical finite element calculations on the strain energy density $(E/V)_{\text{strain}}$, which is given by $2c_{44}(c_{11}+2c_{12})/c_{11}[(\epsilon_{xx}^2+\epsilon_{yy}^2+\epsilon_{zz}^2)+1/2(\epsilon_{xy}^2+\epsilon_{xz}^2+\epsilon_{yz}^2)]$. c_{ij} and ϵ_{ij} are the elastic constants within a cubic system and calculated strain components, respectively. Note that only a quarter of the actual models in Figs. 3(a) and 3(b) is considered due to quasiperiodic boundary conditions applied to the outer edges. Both calculations consider a germanium content of 10% within the wetting layer and the dot, which refers to a lattice mismatch of 0.42%. A truncated pyramid with $\{111\}$ side and a single (001) top facet placed on a planar wetting layer of 30 nm, Fig. 3(a), results in a strain energy density, Fig. 3(c), which basically expresses Young's modulus.^{17,24} Figure 3(b) shows, on the other hand, a more lifelike model similar to the experimentally observed

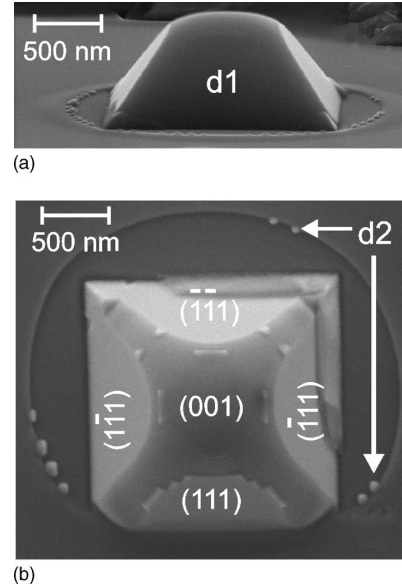


FIG. 2. Inclined (a) and top view scanning electron micrographs (b) of individual dots (d1) surrounded by circular walls which are decorated with considerably smaller dots (d2).

in Fig. 1(c). It considers a depleted area surrounded by an asymmetrically shaped wall. A nonuniform wetting layer tremendously alters the elastic behavior. Figure 3(d) indicates an elastically relaxed wall due to the discontinuity, however, diverse energy minima develop. Related areas inside the depleted region, denoted $M_{[110]}$ and $M_{[\bar{1}10]}$, approach the silicon lattice, hence they are not suitable candidates for an ongoing nucleation. However, another type of minima appears within the rim itself, $M_{[100]}$, which indicates initial decoration along the $\langle 100 \rangle$ direction.

The nucleation scenario around a single dot, comprising wetting layer depletion and subsequent dot decoration at the rim, applies for dot dimers and longer formations as well. Figure 4(a) displays chains of dots still joining the rim around an initial dimer. The main orientation of the rim along the mechanically softer $\langle 100 \rangle$ directions refers to the dimer axis, which itself results from the orientation of the prior surface undulations as shown in Fig. 1(a). Thus as soon as the fourfold symmetry of a separated single dot (d1), Fig. 2, is reduced to a twofold symmetry of a linear dimer (d1-d1), Fig. 4(a), succeeding dots (d2) are subject to linear self-assembling into chains along the $\langle 100 \rangle$ direction. After an overall growth time of 60 min, corresponding to a temperature gradient of 10 K the dot size and the average distance between them increase and eventually leads to dots (d3) which are distinctly apart from the wetting layer, Fig. 4(b).

Both types, initial (d1) and succeeding dots (d2) have been formed due to elastic strain relaxation. However, diverse morphologies suppose different growth conditions. An undersaturated indium solution, caused by the extensive incorporation of silicon within the initial $\text{Si}_{0.9}\text{Ge}_{0.1}$ dots and the strain-induced partial depletion of the wetting layer, implies different thermodynamic conditions for both. This will affect

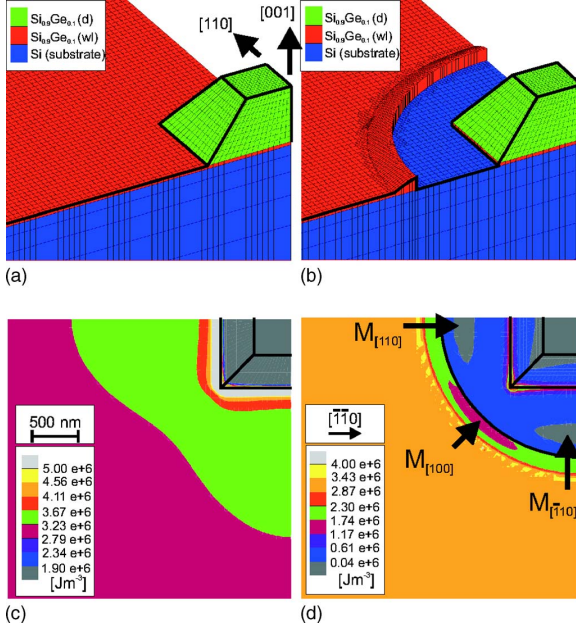


FIG. 3. (Color online) The strain energy distribution around a single $\text{Si}_{0.9}\text{Ge}_{0.1}/\text{Si}(001)$ dot on a continuous and planar wetting layer (a) results in the well-known (Ref. 24) distribution (c) where the lattice relaxes more sufficient along the elastically softer $\langle 100 \rangle$ direction. However, a wetting layer which is partially depleted and confined by an asymmetrically shaped wall (b), as experimentally observed in Fig. 1(c), yields an absolute energy minimum $M_{[100]}$ along $\langle 100 \rangle$. The other indicated minima $M_{[110]}$ and $M_{[\bar{1}10]}$ figure in the depleted area.

the incorporation of germanium and hence the dot size. Energy dispersive x-ray (EDX) microanalysis yields a measure of the averaged dot composition and vice versa probes the local growth conditions. The applied EDX parameters ensure an effective suppression of the underlying silicon substrate due to a neglectable penetration depth. Electrons with a comparatively low primary energy of 5 keV illuminate the sample under a very glancing angle of 5° and hence restrict the probed volume mainly to the dots themselves. Nevertheless the EDX values account for a lower limit of the germanium content in the dot. Figure 5 shows three spectra taken out of depleted areas of the silicon substrate (sub), out of a single parental dot (d1) and from a single dot at the rim (d3). Evaluating the intensity ratios of the Si-K and Ge-L edges results in germanium contents of $c_{\text{sub}} < 1\%$, $c_{\text{d}1} = 8.3\%$, and $c_{\text{d}3} = 19.6\%$, respectively. Since $c_{\text{d}1}$ corresponds well with the aspired content of 10%, the smaller dots incorporate more than twice the relative amount. Strain-induced resolving of wetting layer material obviously enables further dot growth, however, the operating point in the phase diagram has been shifted towards higher germanium contents.

In conclusion, we have discussed strain-mediated morphological changes during heteroepitaxial growth of SiGe/Si(001) dots. Further on the impact of a nonuniform, discontinuous wetting layer on the lateral assembling of heteroepitaxial dots has been studied. The experimental results

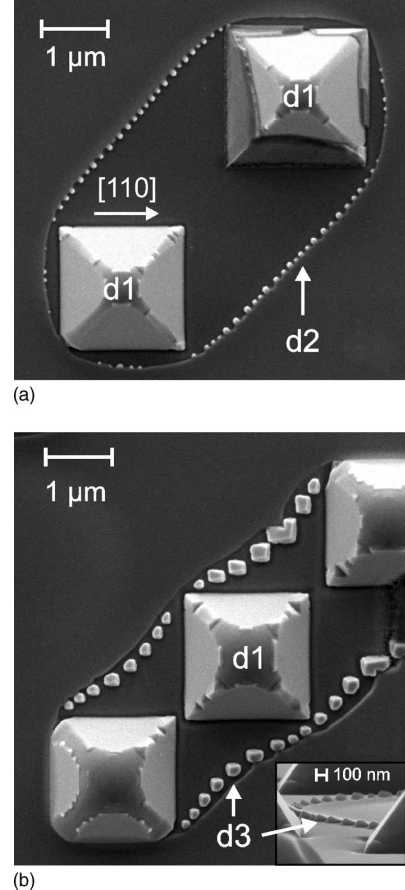


FIG. 4. A partially straight wall (a) around dimers (d1-d1) yields linearly self-assembled dots (d2). Further growth results in detached dots (d3) along the inner rim path (b) whereas the dot size increases with respect to those which are still connected to the wetting layer. The inset (b) proves a vertical extent beyond the average wetting layer plateau.

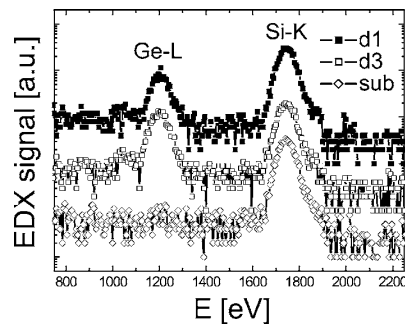


FIG. 5. Energy dispersive x-ray spectroscopy yields approximately $\text{Si}_{0.917}\text{Ge}_{0.083}$ within the initial dots (d1), a considerably higher germanium content of approximately 19.6% within the subsequently formed, separated dots (d3) and nearly pure silicon ($>99\%$) at depleted areas. Curves are vertically shifted for better view.

BRIEF REPORTS

PHYSICAL REVIEW B 74, 153304 (2006)

from low misfit liquid phase epitaxy are supported by numerical finite element calculations on the strain energy density. Initial elastic strain relief induces surface undulations, which transform into lenslike SiGe dots. The subsequent transition into faceted dots of fourfold symmetry is accompanied by a partial wetting layer depletion forming asymmetrically shaped, circular rims of rising height and a steep inner edge. In general, areas close to the rim provide an elastically relaxed lattice due to the lack of lateral mechanical confinement, which is confirmed by further dot decora-

tion and finite element calculations. Our calculations imply different relaxation behaviors on uniform and discontinuous wetting layers.

M.H. acknowledges funding by the Federal State of Sachsen-Anhalt, Germany, within the Cluster of Excellence (CoE) *Nanostructured Materials*, project NW3 and the German Research Foundation, Grant No. HA3495/3. We thank Rolf Köhler, Humboldt-University, Berlin, for continuous support and interest.

-
- ¹V. A. Shchukin, N. N. Ledentsov, and D. Bimberg, *Epitaxy of Nanostructures* (Springer, New York, 2004).
- ²M. A. Herman, W. Richter, and H. Sitter, *Epitaxy, Physical Principles and Technical Implementations* (Springer, Berlin, 2004).
- ³J. Stangl, V. Holý, and G. Bauer, Rev. Mod. Phys. **76**, 725 (2004).
- ⁴M. S. Skolnick and D. J. Mowbray, Annu. Rev. Mater. Sci. **34**, 181 (2004).
- ⁵D. J. Eaglesham and M. Cerullo, Phys. Rev. Lett. **64**, 1943 (1990).
- ⁶Y.-W. Mo, D. E. Savage, B. S. Swartzentruber, and M. G. Lagally, Phys. Rev. Lett. **65**, 1020 (1990).
- ⁷S. Kiravittaya, A. Rastelli, and O. G. Schmidt, Appl. Phys. Lett. **88**, 043112 (2006).
- ⁸D. J. Srolovitz, Acta Metall. **37**, 621 (1989).
- ⁹M. Hanke, M. Schmidbauer, D. Grigoriev, H. Raidt, P. Schäfer, R. Köhler, A.-K. Gerlitzke, and H. Wawra, Phys. Rev. B **69**, 075317 (2004).
- ¹⁰P. Sutter, P. Zahl, and P. Sutter, Appl. Phys. Lett. **82**, 2003 (2003).
- ¹¹M. Meixner, E. Schöll, V. A. Shchukin, and D. Bimberg, Phys. Rev. Lett. **87**, 236101 (2001a).
- ¹²E. Sutter, P. Sutter, and J. E. Bernard, Appl. Phys. Lett. **84**, 2262 (2004).
- ¹³M. Hanke, T. Boeck, A.-K. Gerlitzke, F. Syrowatka, F. Heyroth, and R. Köhler, Appl. Phys. Lett. **86**, 142101 (2005).
- ¹⁴J. Tersoff, C. Teichert, and M. G. Lagally, Phys. Rev. Lett. **76**, 1675 (1996).
- ¹⁵G. Springholz, V. Holý, M. Pinczelits, and G. Bauer, Science **282**, 734 (1998).
- ¹⁶M. Meixner, E. Schöll, M. Schmidbauer, H. Raidt, and R. Köhler, Phys. Rev. B **64**, 245307 (2001).
- ¹⁷M. Hanke, H. Raidt, R. Köhler, and H. Wawra, Appl. Phys. Lett. **83**, 4927 (2003).
- ¹⁸M. Hanke, T. Boeck, A.-K. Gerlitzke, F. Syrowatka, and F. Heyroth, Appl. Phys. Lett. **88**, 063119 (2006).
- ¹⁹M. Schmidbauer, S. Seydmohamadi, D. Grigoriev, Z. M. Wang, Y. I. Mazur, P. Schäfer, M. Hanke, R. Köhler, and G. J. Salamo, Phys. Rev. Lett. **96**, 066108 (2006).
- ²⁰J. Tersoff, B. J. Spencer, A. Rastelli, and H. von Känel, Phys. Rev. Lett. **89**, 196104 (2002).
- ²¹A. Rastelli, M. Stoffel, J. Tersoff, G. S. Kar, and O. G. Schmidt, Phys. Rev. Lett. **95**, 026103 (2005).
- ²²P. O. Hansson, M. Albrecht, W. Dorsch, H. P. Strunk, and E. Bauser, Phys. Rev. Lett. **73**, 444 (1994).
- ²³W. Dorsch, H. P. Strunk, H. Wawra, G. Wagner, J. Groenen, and R. Carles, Appl. Phys. Lett. **72**, 179 (1998).
- ²⁴U. Denker, O. G. Schmidt, N. Y. Jin-Phillip, and K. Eberl, Appl. Phys. Lett. **78**, 3723 (2001).

2.4 Besonderheiten gleichgewichtsfernen Wachstums

M. Hanke, T. Boeck, A.-K. Gerlitzke, F. Syrowatka, F. Heyroth, R. Köhler

Size, shape and ordering of LPE-SiGe/Si(001) islands grown under far non-equilibrium growth conditions

Appl. Phys. Lett. **86**, 142101 (2005).

Mit Hilfe der Flüssigphasenepitaxie lassen sich kinetische Limitierungen weitestgehend minimieren, so dass sich das Wachstum vergleichsweise nah am thermodynamischen Gleichgewicht vollzieht. Die bislang diskutierten Strukturen wurden ausnahmslos in diesem Grenzregime (mit geringen Abkühlraten) gezüchtet und zeigen im Finalstadium im Wesentlichen die Gleichgewichtsform, siehe Kap. 2.1. Unter diesen Umständen, und wie auch in vielen MBE Experimenten, korreliert die finale Inselgröße mit dem eingestellten Gittermisfit. Aus dem bei einem konkreten heteroepitaktischen System resultierenden maximalen Misfit folgt somit eine Beschränkung der Inselgröße nach unten, die für reine Germaniuminseln auf Silizium etwa 20 .. 30 nm beträgt.

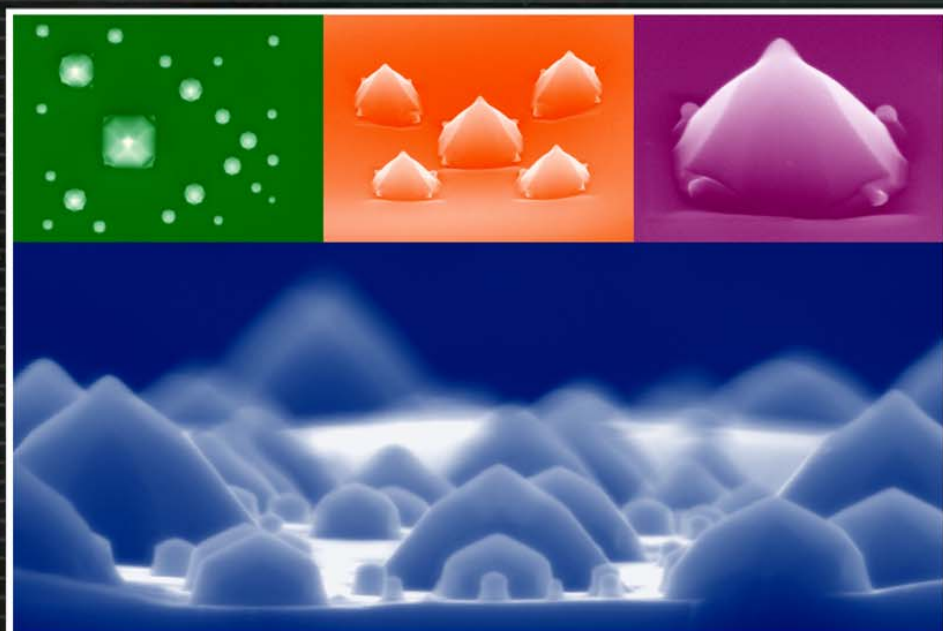
Gelänge es nun, das Kristallwachstum vor Ausbildung der Gleichgewichtsform zu stoppen, hätte man damit eine Möglichkeit in der Hand, gezielt das primär durch den Gitterparameterunterschied vorgegebene Limit weiter zu unterschreiten. Der Inset der folgenden Abbildung zeigt von uns untersuchte SiGe/Si(001) Inselstrukturen, die infolge einer sehr hohen Abkühlrate von 10 K/min und damit sehr fern vom Gleichgewicht gezüchtet wurden. Wie man an dem grünen Inset erkennt, ändert sich das Ordnungsverhalten der Inseln gänzlich im Vergleich zu gleichgewichtsnahen LPE-Prozessen, bei denen lange Inselketten mindestens eine Wechselwirkung (durch mechanische Spannungen in Substrat und Benetzungsschicht) zwischen übernächsten Nachbarn voraussetzen, siehe dazu Kap. 2.2.1, hin zu einem Mechanismus, der ausschließlich auf einer Wechselwirkung zwischen nächsten Nachbarn basiert. Die zentrale Insel favorisiert durch ihr in das Substrat eingetragene Deformationsfeld weitere Nukleation entlang $\langle 100 \rangle$. Allerdings deuten die Positionen der darauf folgenden dritten Inselgeneration auf einen fehlenden direkten Zusammenhang zur Zentralinsel, so dass sich für kleine Bereiche auf der Probe selbstähnliche Inselanordnungen herausbilden.

Auch die Entstehung einer individuellen Insel (blauer Inset) vollzieht sich grundlegend verschieden von der in gleichgewichtsnahen Experimenten, siehe Kap. 2.5.1, von zunächst sehr steilen, whisker-artigen Inselstadien hin zu flacher facettierten Objekten.

Schließlich vollzieht sich das Wachstum derartig rasch, dass die Inseln nicht ihre Gleichgewichtsform und -größe ausbilden können. Ganz konkret äußert sich das an finalen Inseldimensionen, die um bis einen Faktor zwei kleiner ausfallen als man aus dem mittels energiedispersiver Röntgenspektroskopie bestimmten Germaniumgehalt - respektive Gittermisfit - schließen würde. Darüber hinaus hängt der Germaniumgehalt in bestimmten Grenzen nicht von der Inselgröße ab.

04 APRIL 2005
Volume 86 Number 14

APPLIED PHYSICS LETTERS



0003-6951(20050404)86:14;1-Q

Available online—
See apl.aip.org

AMERICAN
INSTITUTE
OF PHYSICS

APPLIED PHYSICS LETTERS 86, 142101 (2005)

Size, shape, and ordering of SiGe/Si(001) islands grown by means of liquid phase epitaxy under far-nonequilibrium growth conditions

M. Hanke^{a)}*Martin-Luther-Universität Halle-Wittenberg, Fachbereich Physik, Hoher Weg 8, D-06120 Halle/Saale*

T. Boeck and A.-K. Gerlitz

Institut für Kristallzüchtung, Max-Born-Straße 2, D-12489 Berlin

F. Syrowatka and F. Heyroth

Interdisziplinäres Zentrum für Materialwissenschaften, Hoher Weg 8, D-06120 Halle/Saale

R. Köhler

Humboldt-Universität zu Berlin, Institut für Physik, Newtonstraße 15, D-12489 Berlin

(Received 17 December 2004; accepted 16 February 2005; published online 28 March 2005)

Applying scanning electron microscopy, we have studied the evolution of shape and lateral positional correlation of $\text{Si}_{1-x}\text{Ge}_x/\text{Si}(001)$ Stranski-Krastanov islands grown by means of liquid phase epitaxy (LPE). However, in contrast to conventional near-equilibrium LPE, a distinctly higher cooling rate of 10 K/min ensures extremely nonequilibrium growth conditions. The facet inclination of subsequent island stages decreases from nearly vertical sidewalls toward {111}- and {101}-type facets. Energy dispersive x-ray microanalysis yields a size-independent germanium content of 8.9% within islands between 760 and 1700 nm base width which is—by more than a factor of 2—smaller than islands of the same concentration grown in a near-equilibrium LPE process. Square-like formations of subsequently smaller islands around a large central island indicate only next to island interactions during the lateral self-assembling. © 2005 American Institute of Physics.

[DOI: 10.1063/1.1895476]

In nowadays optoelectronic device applications low-dimensional structures such as quantum dots (QDs) became increasingly important during the last decade, e.g., Refs. 1 and 2. A very promising *bottom-top* attempt toward perfectly ordered monodisperse ensembles of QDs relies on the so-called Stranski-Krastanov (SK) growth mode³ whereby the strain energy rising during heteroepitaxy relieves by the formation of dislocation-free three-dimensional structures on top of a thin wetting layer. Regardless of great efforts dedicated to a more comprehensive description of the underlying mechanisms, an active debate about various growth scenarios is still ongoing where SiGe/Si has been widely utilized as a model system.^{4–8} From an applicational point of view a strong localization of carriers in discrete states of QDs is most favorable since it will enhance the optical recombination efficiency of electron hole pairs in indirect semiconductors as Si and Ge. However, the maximum lattice mismatch of a particular heteroepitaxial system generally restricts the minimal island size.⁹ Consequently, many attempts are devoted to decrease the QD size further, e.g., by a subsequent overgrowth which yields broader QDs of smaller height.¹⁰ On the other hand, a considerable interdiffusion during the overgrowth can change the initial chemical composition^{10,11} and thus the final optical properties. Surfactant-mediated growth has been applied in order to control the size of ultrasmall Ge QDs.^{12,13}

In this letter, we report on liquid phase epitaxy (LPE) of SiGe/Si(001) which has been intentionally performed under far nonequilibrium conditions in order to grow SiGe SK islands which are distinctly smaller than determined by the

applied lattice mismatch. Usually LPE serves as the prototype of a near-equilibrium technique. This yields highly monodisperse and pseudomorphic islands of near-equilibrium shape.⁸ Recently we have shown that the final aspect ratio of base width versus height at LPE-SiGe/Si(001) islands in the presence of {111}-side facets and an (001) top facet results from a local energy minimum in surface energy.¹⁴ Moreover, island ensembles often exhibit a high degree of lateral positional correlation^{15,16} resulting in extended island chains—a phenomenon which can be explained by the particular strain energy distribution around a single island or a configuration of them, respectively.^{17,18}

Samples were grown in a conventional slide boat reactor from a metallic In solution. Since the solubility of Si within In amounts to two orders of magnitude smaller than that of Ge, the solution has been fully saturated with Si. Thus, the final Ge concentration of 10% within the islands was adjusted through the amount of Ge (1.5 g) added to the Si-saturated In solution (25 g). First, the native oxide layer on the Si(001) substrate was removed by a thermal treatment for 30 min at 930 °C under a pure hydrogen atmosphere. In order to ensure a quasithermodynamic equilibrium prior to the growth, thus to establish a homogenized system, the solution stays at 930 °C for 3 h. Hereafter, the temperature has been decreased with a rate of 10 K/min down to 920 °C. This represents an extremely high cooling rate which accounts typically for 0.2 K/min in a conventional LPE process.

Since the growth of $\text{Si}_{0.9}\text{Ge}_{0.1}$ islands occurs significantly slower than in the case of pure Ge dots, different stages can be observed indicating the process of island formation. The scanning electron micrograph in Fig. 1 taken along a ⟨110⟩ direction depicts subsequent island stages, marked (1)–(7) which are schematically drawn in the inset.

^{a)}Author to whom correspondence should be addressed; electronic mail: hanke@physik.uni-halle.de

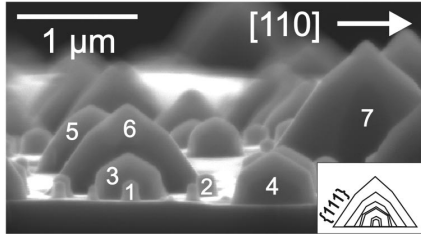


FIG. 1. The scanning electron micrograph shows different island stages during the evolution. The process starts with steep dome-like islands with nearly vertical sidewalls which grow predominantly in lateral direction. Eventually, when they reach an aspect ratio base width vs height of 1.7, the shape changes significantly forming shallower {111} facets at the bottom.

In contradiction to near-equilibrium LPE where the islands evolve from very shallow surface undulations⁸ the initial islands form steep mounds (1), (2) with an aspect ratio of island base versus height of approximately 0.8 indicating a prevalent vertical growth at initial stages. At this point the islands are bounded by nearly vertical sidewalls at the bottom and shallow facets at the apex. Subsequently the islands grow laterally faster than in a vertical direction whereby the initial inclination angles are preserved. Eventually, when an aspect ratio of about 1.7, e.g., island (4), has been accomplished, shallower facets inclined by 55.2° appear at the island bottom (5) which we attribute to facets of type {111} (54.7°), however, those are vertically not completed. Additional {101} facets appear azimuthally 45° off. Recently observed SiGe/Si(001) islands grown by means of molecular beam epitaxy exhibit a similar barn-like shape, however they have been evolved from shallow pre-stages, thus by increasing the facet angle toward {111}-type facets at the island bottom.⁵ Figure 2 shows an enlarged micrograph of the final shape which clearly reveals {101}-type facets in addition to the {111} ones. Every corner at the island bottom carries thin spikes (s) and another one figures on the island top. A strain driven wetting layer depletion in the vicinity of larger islands can be observed (d).

Figure 3 depicts a top view scanning electron micrograph of islands which form a square-like pattern around a central island (a). Since the various islands differ by more than a factor of 5 in size, they provide subsequent snapshots of both the individual island growth *and* the formation of lateral ordering. The largest island (a) with a base of $b_1=1380$ nm shown in the center of Fig. 3 appears first and determines the positions for further island nucleation. Subsequently, a second island generation, e.g., (c), with a mean

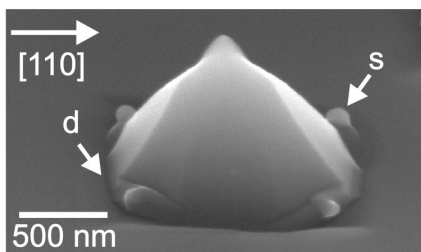


FIG. 2. Final island stages are bounded by {111}- and {101}-type side facets without any top facet. At the island bottom characteristic spikes (s) in ⟨101⟩ direction appear. Moreover, every island causes a strain driven trench formation (d) in the closest lateral vicinity.

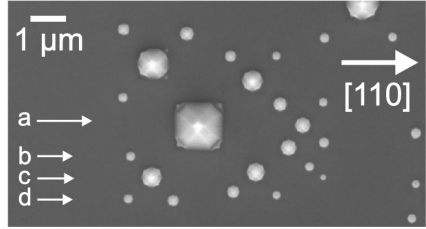


FIG. 3. The SiGe/Si(001) islands arrange themselves into a square-like pattern around a central island. This process indicates only next to island interactions.

base width of $b_2=545$ nm, appears in ⟨100⟩-direction around the central island. Different island sizes can be explained by the very high cooling rate. Thus, the system does not allow to equilibrate and the growth stops before the islands could establish their equilibrium size. Despite this, a third generation of SiGe islands with a final base of $b_3=240$ nm, e.g. (b) and (d), starts to grow around the four previously evolved islands. Both second and third generation islands are located on squares with base length $d_1=2950$ nm and $d_2=1270$ nm, thus the size ratio (b_1/b_2) nearly equals the distance ratio (d_1/d_2) indicating a linear dependence of the inter-island distance on the island size of the parental generation. Moreover, the islands marked (b) and (d) in Fig. 3 are fully symmetric with respect to the central one (c) which proves that the third generation does not directly probe the strain impact of first generation island. This is in clear contradiction to near-equilibrium LPE where the development of extended island chains along the ⟨100⟩ direction can only be explained by the strain influence of a next to neighbor island which defines the linear one-dimensional character of self-assembling.¹⁸

Various sizes raise the question about the incorporated Ge content. The size b of islands grown under near-equilibrium conditions follow a well established scaling law $b \propto f^{-2.03}$ depending on the heteroepitaxial misfit f .⁹ Since the performed growth regime obviously changes the process of lateral self-assembling only next to island interaction (Fig. 3), and restricts the final island size depending on the individual time to grow (Figs. 1 and 3) it offers the chance to conceive islands which are smaller than solely determined by the established misfit f . Different island sizes generally prevent the application of, e.g., diffuse x-ray scattering in combination with kinematical scattering simulations in order to measure the three-dimensional chemical composition in nanoscale islands. Thus, energy dispersive x-ray (EDX) microanalysis has been applied to probe the averaged chemical composition within individual islands of various sizes. Figure 4 depicts three EDX spectra taken at islands with base widths $b_1=760$ nm, $b_2=1340$ nm, and $b_3=1700$ nm. On the base of the scaling law given in Ref. 9 the corresponding equilibrium Ge contents are $c_1^{\text{eq}}=14.9\%$, $c_2^{\text{eq}}=11.5\%$ and $c_3^{\text{eq}}=10.0\%$. However, evaluating the intensity ratios of the Ge-L edge and Si-K edge as shown in Fig. 4 we found clear evidence of a size-independent Ge content which accounts for $c_1=8.6\%$, $c_2=9.2\%$ and $c_3=8.9\%$. In order to ensure exclusively island related signal all EDX spectra were taken at a primary electron energy of 8 keV. Moreover, to determine the absolute precision of the applied EDX system, we have investigated $\text{Si}_{1-x}\text{Ge}_x$ bulk material (not shown here) for $x_{\text{nominal}}=\{0.055, 0.096\}$ which yields experimental values

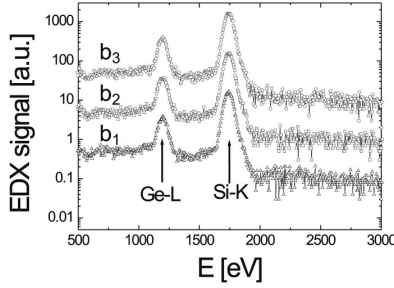


FIG. 4. Energy dispersive x-ray microanalysis at islands of base widths $b_1=760$ nm, $b_2=1340$ nm and $b_3=1700$ nm yielding germanium concentrations $c_1=8.6\%$, $c_2=9.2\%$ and $c_3=8.9\%$, respectively. Each spectra has been vertically shifted by a factor of 10 for the sake of clearance.

$x_{\text{experimental}}=\{0.060, 0.106\}$, respectively, defining the accuracy to about $\pm 0.5\%$ Ge.

Applying scanning electron microscopy and energy dispersive x-ray microanalysis we have investigated SiGe/Si(001) Stranski–Krastanov islands grown by means of liquid phase epitaxy. However, a very high cooling rate of 10 K/min provides extreme nonequilibrium growth conditions. The resulting islands are smaller than determined by the applied lattice mismatch. Moreover, the incorporated Ge content does not depend on the island size. Initial island stages bounded by nearly vertical sidewalls transform into multifaceted islands with shallower {111}- and {101}-type facets clearly indicating a growth scenario with decreasing facet angles. Eventually, lateral self-assembling occurs exclusively by next to island interactions.

The authors thank H. Riemann, Institute of Crystal Growth Berlin for the preparation of $\text{Si}_{1-x}\text{Ge}_x$ bulk crystals

which have been used as references for the EDX calibration. Financial support by the German Research Foundation within Project No. KO1510/2 is gratefully acknowledged.

- ¹D. Bimberg, M. Grundmann, and N. N. Ledentsov, *Quantum Dot Heterostructures* (Wiley, Chichester, 1999).
- ²V. A. Shchukin, N. N. Ledentsov, and D. Bimberg, *Epitaxy of Nanostructures* (Springer, New York, 2004).
- ³I. Stranski and L. Krastanov, Sitzungsber. Akad. Wiss. Wien, Math.-Naturwiss. Kl., Abt. 2B **146**, 797 (1937).
- ⁴S. A. Chaparro, Y. Zhang, and J. Drucker, Appl. Phys. Lett. **76**, 3534 (2000).
- ⁵E. Sutter, P. Sutter, and J. E. Bernard, Appl. Phys. Lett. **84**, 2262 (2004).
- ⁶P. Sutter, P. Zahl, and P. Sutter, Appl. Phys. Lett. **82**, 2003 (2003).
- ⁷U. Denker, M. Stoffel, and O. G. Schmidt, Phys. Rev. Lett. **90**, 196102 (2003).
- ⁸M. Hanke, M. Schmidbauer, D. Grigoriev, P. Schäfer, R. Köhler, A.-K. Gerlitzke, and H. Wawra, Phys. Rev. B **69**, 075317 (2004).
- ⁹W. Dorsch, H. P. Strunk, H. Wawra, G. Wagner, J. Groenen, and R. Carles, Appl. Phys. Lett. **72**, 179 (1998).
- ¹⁰A. Hesse, J. Stangl, V. Holý, T. Roch, G. Bauer, O. Schmidt, U. Denker, and B. Struth, Phys. Rev. B **66**, 085321 (2002).
- ¹¹G. Patriarche, I. Sagnes, P. Boucaud, V. L. Thanh, D. Bouchier, C. Hernandez, Y. Campidelli, and D. Bensahel, Appl. Phys. Lett. **77**, 370 (2000).
- ¹²I. Berbezier, A. Ronda, A. Portavoce, and N. Motta, Appl. Phys. Lett. **83**, 4833 (2003).
- ¹³A. Beyer, E. Müller, H. Sigg, S. Stutz, D. Grützmacher, O. Leitfeld, and K. Ensslin, Appl. Phys. Lett. **77**, 3218 (2000).
- ¹⁴M. Hanke, M. Schmidbauer, R. Köhler, F. Syrowatka, A.-K. Gerlitzke, and T. Boeck, Appl. Phys. Lett. **84**, 5228 (2004).
- ¹⁵M. Schmidbauer, T. Wiebach, H. Raidt, M. Hanke, R. Köhler, and H. Wawra, Phys. Rev. B **58**, 10523 (1998).
- ¹⁶M. Hanke, M. Schmidbauer, and R. Köhler, J. Appl. Phys. **96**, 1959 (2004).
- ¹⁷M. Meixner, E. Schöll, M. Schmidbauer, H. Raidt, and R. Köhler, Phys. Rev. B **64**, 245307 (2001).
- ¹⁸M. Hanke, H. Raidt, R. Köhler, and H. Wawra, Appl. Phys. Lett. **83**, 4927 (2003).

2.5 Strukturanalytik mittels diffuser Röntgenstreuung

Zur Bestimmung von Form, Größe, chemischer Zusammensetzung und damit verbundenem Deformationszustand in mesoskopischen SiGe/Si Strukturen sowie zur Charakterisierung von Positions korrelation wurde die diffuse Röntgenstreuung in der Nähe qualitativ verschiedener reziproker Gitterpunkte detektiert und analysiert. Sogenannte *reciprocal space maps* wurden dabei an den Synchrotronmeßplätzen ID1, ID10B und ID11 der European Synchrotron Radiation Facility (ESRF) in Grenoble sowie BW2 und W1 am Hamburger Synchrotronstrahlungslabor (HASYLAB) vermessen. Für Details der Instrumentierung sei insbesondere auf die aktuellen Homepages des ESRF und des HASYLAB verwiesen. Abgesehen vom konkreten Setup, das sich für jeden Experimentierplatz anders gestaltet und auf das hier nicht eingegangen wird, werden Spezifika der benutzten Streumethoden in den einzelnen Kapiteln diskutiert: hochauflöste Weitwinkelbeugung¹⁰ (Kap. 2.5.1, 2.5.3, 2.5.4, 2.5.5), Kleinwinkelstreuung¹¹ (Kap. 2.5.2) sowie die Beugung unter kleinen Ein- und Austrittswinkeln¹² (Kap. 2.5.2). Darüber hinaus sei auf den kurzen Anhang und die beiden Folgekapitel 3 und 4 verwiesen, in denen ebenfalls Strukturaufklärung mittels diffuser Röntgenstreuung (jedoch an GaAs basierten niedrigdimensionalen Objekten bzw. SiGe/Si Whiskern) diskutiert wird.

2.5.1 Morphologieänderung und Konzentrationsgradient

M. Hanke, M. Schmidbauer, D. Grigoriev, H. Raidt, P. Schäfer, R. Köhler, A.-K. Gerlitzke, H. Wawra

SiGe/Si(001) Stranski-Krastanow islands by liquid-phase epitaxy: Diffuse x-ray scattering versus growth observations

Phys. Rev. B **69**, 075317 (2004).

Sofern nach Abschluss des Wachstums noch verschiedene Inselstadien auf der Probe vorliegen, lässt sich aus diesen ein mögliches Wachstumsszenario ableiten. Eine Probe mit einer Vielzahl unterschiedlicher Inselmorphologien ist dafür ein idealer Kandidat. Im vorliegenden Fall liegen neben sehr flachen Inseln, die sich kaum vom unterliegenden Ripplermuster abheben, Pyramidenstümpfe im Finalstadium mit einer (001) Deck- und {111} Seitenfacetten vor. Dabei erfolgt der Übergang von flachen zu abgestumpften Inseln keineswegs kontinuierlich sondern über diskrete, strukturell klar unterscheidbare Zwischenstadien.

Bis zu einer kritischen Höhe h_k erfolgt das Wachstum durch zunehmend steilere Seitenfacetten hin zu {115}, gefolgt von einem extrem schnellen Übergang zu Pyramidenstümpfen. Gemessen an der Gesamthöhe h des finalen Pyramidenstumpfes erfolgt der Übergang etwa bei $h/3$. Es bleibt zunächst im unklaren, wie sich dieser Übergang im Detail gestaltet, wobei zwei Grenzszenarien denkbar erscheinen: entweder

¹⁰HRXRD - high resolution x-ray diffraction

¹¹GISAXS - grazing incidence small angle x-ray scattering

¹²GID - grazing incidence diffraction

erfolgt der Übergang durch weiteres Aufklappen der $\{115\}$ Seitenfacetten bis $\{111\}$ oder aber das Wachstum vollzieht sich entlang $[001]$. Da für beide Prozesse die lokalen Wachstumsgeschwindigkeiten (und damit auch der den Germaniumeinbau bestimmende Segregationskoeffizient k) unterschiedlich ausfallen, sollte eine Unterscheidung anhand des Germaniumprofils in den Inseln möglich sein.

Da bei Germaniumgehalten größer 15% ausschließlich Ensembles mit Inseln im Finalstadium (Pyramidenstumpf mit $\{111\}$ Seiten- und einer (001) Deckfacette) beobachtet wurden, besteht hier keine direkte Möglichkeit, über verschiedene Stadien auf den Entstehungsprozess zu schließen. Andererseits eignen sich derart monodisperse Ensembles ideal für die Untersuchung mittels diffuser Röntgenstreuung.

Um solche Messungen auch quantitativ zu analysieren, wurde ein Verfahren entwickelt, mit dessen Hilfe auf Basis kinematischer Streurechnungen entsprechende Verteilungen simuliert werden können. In einem zweistufigen Prozess wird zunächst das Deformationsfeld in einer Insel numerisch mit Hilfe der Finiten Elemente bestimmt, das dann anschließend als Grundlage für die eigentliche Streurechnung dient.

Wenngleich für eine Vielzahl verschiedener Germaniumprofile die diffuse Streuung berechnet wurde, wird hier exemplarisch nur für zwei bereits sehr realitätsnahe Germaniumverteilungen die hohe Empfindlichkeit der Methode diskutiert. Die äußerlich identischen Modelle basieren für die oberen zwei Drittel des Pyramidenstumpfes auf einer konstanten Germaniumkonzentration von 30%. Während jedoch in dem einen Modell der untere Teil vollständig aus $\text{Si}_{0.75}\text{Ge}_{0.25}$ besteht, berücksichtigt das andere eine vergrabene Pyramide dieser Verteilung. Der qualitative Unterschied besteht also im unteren Drittel zwischen $\{115\}$ - und den (finalen) $\{111\}$ -Seitenfacetten, reflektiert mithin auf die beiden angesprochenen Wachstumsszenarien für den charakteristischen Umschlag bei $h/3$. Abgesehen von Effekten, die durch die laterale Positions korrelation der Inseln entstehen und in Kap. 2.5.4 diskutiert werden, ähneln beide Simulationen der gemessenen Verteilung. Man kann jedoch numerisch zeigen, dass die Annahme eines Konzentrationssprunges bei $h/3$ am besten die gemessene diffuse Streuung wiedergibt. Dieser Befund legt den Schluss nahe, dass bis zur Ausprägung von $\{111\}$ Seitenfacetten das Wachstum durch sukzessiv steilere Facetten erfolgt.

PHYSICAL REVIEW B 69, 075317 (2004)

SiGe/Si(001) Stranski-Krastanow islands by liquid-phase epitaxy: Diffuse x-ray scattering versus growth observations

M. Hanke, M. Schmidbauer, D. Grigoriev, H. Raidt, P. Schäfer, and R. Köhler
Institut für Physik, Humboldt-Universität zu Berlin, Newtonstrasse 15, D-12489 Berlin

A.-K. Gerlitzke and H. Wawra

Institut für Kristallzüchtung, Max-Born-Strasse 2, D-12489 Berlin, Germany

(Received 6 May 2003; revised manuscript received 3 November 2003; published 26 February 2004)

Ex situ observed growth stages of LPE-SiGe/Si(001) Stranski-Krastanow islands with a germanium content of 10% give clear evidence of a rapid shape transition at one third of the final island height. The island shape changes from a lenslike type without a top facet to truncated pyramids with {111} side facets and an (001) top facet. High-resolution x-ray diffraction has been applied to islands with higher germanium content of about 30%. Experimental results are compared with respective kinematical scattering simulations based on finite element calculations for the strain field. From these simulations the three-dimensional germanium composition profile inside the islands can be extracted and it substantiates a similar growth scenario with a distinct shape transition at one third of the final island height also for this germanium concentration range. We attribute the observed finite island size to a distinct nucleation problem at the island bottom caused by exceptional high strain energy around the island corners in combination with a strain driven wetting layer depression.

DOI: 10.1103/PhysRevB.69.075317

PACS number(s): 68.65.-k, 61.10.-i, 81.15.Lm

I. INTRODUCTION

In the past decade ambitious efforts have been undertaken for the fabrication and investigation of low-dimensional semiconductor structures. As soon as a charge carrier is spatially confined to lateral dimensions smaller than the DeBroglie wavelength the according density of states will drastically change with respect to bulk material, which promises new fascinating electronical and optical properties. In principle, the confinement can be obtained in one, two, or even three dimensions. Quantum dots (QD) with zero-dimensional properties represent the outmost degree of confinement predestinating them for exceptional optoelectronical devices as quantum dot lasers,¹ single electron transistors,² or single electron memory devices.³

For the fabrication of zero-dimensional structures of high density along with outstanding degree of uniformity the Stranks-Krastanow (SK) growth mode⁴ has been widely used for different material combinations. The accumulated deformation energy during heteroepitaxial growth can be partially relieved by forming three-dimensional dislocation-free islands on top of a wetting layer because the energy reduction associated with elastic relaxation exceeds the increase in surface energy.

A purposeful fabrication and application requires a detailed understanding of the growth process. Therefore there is a practical need for precise characterization of morphological properties as shape, size, chemical composition, and strain profile. A large variety of direct and indirect methods have been applied, among them scanning probe techniques as atomic force microscopy (AFM) (Refs. 5 and 6) and scanning tunneling microscopy. Furthermore scanning electron microscopy (SEM) as well as transmission electron microscopy (Ref. 7) can reveal reliable structural properties. Further on Raman scattering can provide information concerning composition and strain in free standing and capped islands.⁸

However, all the direct methods can provide structural information only for a comparatively limited number of objects. Indirect methods are able to compensate this lack in a complementary way, although reliable information regarding a particular individual type will be available only in case of a monodisperse distribution.

High-resolution x-ray diffraction (HRXRD) has been widely used for strain analysis in QD's, e.g.,^{9–16} which confirms the important role of interdiffusion as an effective way of elastic relaxation during growth. Previously, different germanium profiles within free standing SiGe SK islands have been proposed: a linear increase of germanium for islands on a Si(111) substrate,¹⁴ a quadratic increase in case of SiGe/Si(001) islands¹⁷ and a stepped germanium profile.^{10,18} Recently, Denker *et al.*¹⁹ have reported on a lateral composition profile inside self-assembled SiGe dots on Si(001). By selective etching technique the authors observed a strong silicon intermixing in the island corners, whereas the edges, the island top and the inner part of the island remain germanium rich. Lateral transport governed by three-dimensional strain distribution and local incorporation probabilities have been discussed in addition as further key parameters for the final concentration profile within SK islands.²⁰

In the present paper we will reconstruct how island evolution in the system SiGe/Si(001) takes place in detail. We got evidence for a characteristic growth transition at $h/3$, which can be directly interconnected to a certain germanium profile depending on the particular growth mode. We could trace the island evolution by different growth stages only in case of comparatively low germanium contents. Since islands with a higher lattice mismatch with respect to the substrate material grow increasingly faster, there is no direct access to different stages of growth. From HRXRD experiments along with various kinematical scattering simulations, which reveal a certain germanium profile we argue that even in that case the proposed growth scenario remains the same.

M. HANKE *et al.*

Furthermore we will focus on the rather frequently discussed question why the observed only misfit dependent final island size²¹ keeps finite. We will explain this in terms of a sustainable nucleation problem at the island bottom along with a wetting layer depression.

The present paper is organized as follows. An introduction to the simulation procedure will be given in the following section. Section III briefly describes sample preparation. Section IV refers to the experimental setup and the applied scattering techniques, whereas in Sec. V concentration profiles revealed by respective simulations will be discussed versus direct growth observations. Finally, in Sec. VI we will present our conclusions.

II. THEORY

Kinematical scattering simulations have been performed in order to evaluate the diffusely scattered intensity patterns. Although different groups pursue analytical methods to calculate the strain field, e.g., within buried²² and freestanding quantum wires,²³ hut clusters,¹⁷ QD's with rotational symmetry,²⁴ and buried SiGe/Si QD's neglecting the elastic anisotropy²⁵ there is still a lack of analytical solutions for the strain field within mesoscopic structures taking into account the elastic properties. Alternatively, numerical finite element method (FEM) is as a very powerful tool for strain analysis. It has been widely used for mesoscopic structures.^{7,18,26,27}

Island shape and size serve as input parameters for FEM calculation²⁸ as well as composition profile, corresponding lattice parameters and the elastic constants c_{ijkl} for $\text{Si}_{1-x}\text{Ge}_x$ assuming Vegard's law.²⁹ Shape and size have been previously determined by direct methods. A wetting layer of constant 2 nm thickness has been considered within the FEM model. Previous investigations confirm a strong elastic interaction between substrate and island. It has been shown that there is a remarkable influence to the strain profile into the substrate at least down to a depth equivalent to the island height.³⁰ Thus, according to the concrete geometry of the investigated islands lateral and vertical dimensions of the entire model are 260 nm and 100 nm, respectively, which ensure a realistic elastic behavior. To establish quasiperiodic boundary conditions the FEM nodes within the outermost planes of the substrate have the freedom to exclusively relax within those planes.

Since finite element method is a continuum theory it remains still impossible to take an atomistic structure of mesoscopic objects correctly into account. Consequently, we have to simplify the model defining FEM cells with typical dimensions between 5 Å and 50 Å. Usually the grid has to be arranged more dense in areas with high strain energy, e.g., at the interface island/wetting layer and near the edges. In an intermediate step the deformation field has to be interpolated onto a regular grid of a mesh size d which is usually still larger than an interatomic distance corresponding to supercells. However, this treatment is only valid under the assumption that the local displacement \vec{u} within a supercell is negligible with respect to the displacement of the supercell itself, thus

PHYSICAL REVIEW B **69**, 075317 (2004)

$$\vec{u}(\vec{R}_i + \vec{r}_k) \approx \vec{u}(\vec{R}_i), \quad (1)$$

where \vec{R}_i is the position of the i th supercell. \vec{r}_k denotes the position of the k th atom in the supercell. In general the diffusely scattered amplitude A_{diffuse} can be calculated as a coherent sum over all illuminated scatterers,

$$A_{\text{diffus}}(\vec{q}) \propto \sum_i \sum_k \{ \varrho^{\text{ideal}}(\vec{R}_i + \vec{r}_k) \exp[i\vec{q}[(\vec{R}_i + \vec{r}_k) \\ + \vec{u}(\vec{R}_i + \vec{r}_k)] - \varrho^{\text{ref}}(\vec{R}_i + \vec{r}_k) \exp[i\vec{q}(\vec{R}_i + \vec{r}_k)]], \quad (2)$$

where ϱ^{ref} and ϱ^{ideal} are electron densities of an *ideal* and a *reference* lattice, respectively. It has to be noted that most of the intensity has to be treated dynamically. Whereas only a small fraction—the scattering by highly distorted parts of the crystal—can be calculated kinematically. It was shown³¹ that in our case the chemical composition within an island de-facto exclusively enters the diffuse scattering via a certain strain profile $\vec{u}(\vec{R})$ and not directly by the atomic form amplitudes. A detailed discussion of this treatment has been published elsewhere.¹⁸

III. SAMPLE PREPARATION

The samples were grown with liquid phase epitaxy (LPE) using a slide-boat reactor. In contrast to other growth techniques as molecular beam epitaxy (MBE) or metal organic chemical vapor deposition LPE operates comparatively closer to thermodynamical equilibrium. Consequently, LPE-grown islands exhibit a similar shape for an extended concentration range which consists of truncated pyramids with {111} side facets and an (001) top facet with a nearly constant aspect ratio of island base along [110] to island height of two.

To ensure a high purity of the epitaxial layers the entire growth process has to be performed under a pure hydrogen atmosphere. In a first step the components Si and Ge are solved in a Bi-solution which will be homogenized for several hours at growth temperature of 973 K to equilibrate the system thermodynamically. Averaged germanium contents of 9% (sample shown in Fig. 4) and 30% [for diffuse scattering see Fig. 5(b)] in the solid phase correspond to germanium mol fractions of 0.0046 and 0.0103 in the liquid phase, respectively. After *in situ* desorption of the natural oxid layer at 930 °C the Si-Ge-Bi solution is brought into contact with the substrate material. To initialize the growth an oversaturation was established by choosing a growth temperature up to 2 K below saturation temperature.

IV. EXPERIMENT

Direct imaging techniques as AFM and SEM have been applied to characterize morphological properties like island size and shape. HRXRD and grazing incidence small angle x-ray scattering have been used to get access to inherent properties as concentration and strain profiles. X-ray scattering experiments were performed by using synchrotron radia-

SiGe/Si(001) STRANSKI-KRASTANOW ISLANDS BY . . .

PHYSICAL REVIEW B 69, 075317 (2004)

tion as provided by BW2 station at Hasylab (DESY) using a monochromatized well collimated beam with an x-ray energy of 8 keV and a typical energy band width of $\Delta\lambda/\lambda = 10^{-4}$. Typical beam spots are 0.5 mm by 2 mm with respective beam divergences within and perpendicular the scattering plane of 50 μrad and 200 μrad . A linear position sensitive detector with a spatial resolution of 80 μm was placed 750 mm behind the sample, whereas the resolution perpendicular to the scattering plane amounts to $4 \times 10^{-3} \text{ \AA}^{-1}$.

V. RESULTS AND DISCUSSION

A. Island evolution

Elastic lattice relaxation during heteroepitaxial growth may occur through the transition from a flat surface to an undulated surface. In case of $\text{Si}_{1-x}\text{Ge}_x/\text{Si}(001)$ the originating pattern exhibits preferential directions along the elastically soft $\langle 100 \rangle$ directions of the cubic diamond lattice. It has been shown that during later growth stages separated islands appear exactly at the crest of the ripple pattern. Thus, the final island positions have been discussed in terms of a ripple pattern.³² However, positional correlation could also be found in case of high Ge content ($x > 0.15$)—within a concentration window without a proof of a ripple pattern.

Since at lower Ge contents a variety of different island stages remain at the surface a *postgrowth* analysis opens a detailed morphological view to the island evolution. The reconstructed sequence can be subdivided into three main stages, Fig. 1. At the very beginning initial island stages (a) arise from a tiny surface undulation by increasingly steeper boundary planes up to an inclination angle of $\approx 16.9^\circ$, which nearly corresponds to $\{115\}$ -type facets (15.8°). During this first step no top facets are present and the islands exhibit a lenslike shape. Once $\{115\}$ facets are present the island shape undergoes a rapid change by forming truncated pyramids with an (001) top facet, $\{111\}$ side facets, and a quadratic base. With respect to the final island height h the growth mode alters exactly at $h/3$. However, this transition happens as fast as nonintermediate stage could be observed. There are two conceivable scenarios: (i) either the growth performs by different side facets down to $\{111\}$ or (ii) there is vertical growth along (001) filling up the volume between previous $\{115\}$ and final $\{111\}$. In the following section we will present results clearly indicating path (ii). At the end of transition ($a \Rightarrow b$) truncated pyramids with $\{111\}$ side facets and an (001) top facet have evolved. It should be mentioned that the island base width slightly decreases during this step. Finally—after an (001) facet is present—the growth almost exclusively takes place vertically. However, there is also a lateral island broadening, whose microscopic nature throw light to the phenomenon of a finite island size.

The characteristic scaling law²¹ for the final island size $w \propto x^{-2.03}$ is frequently discussed in terms of an inverse quadratic strain dependence. Regions of comparatively high strain energy tend to be resolved during subsequent growth and can serve as a monitor of strain distribution. Figure 2 shows a typical cloverleaflike wetting layer depression in the vicinity of a $\text{Si}_{0.9}\text{Ge}_{0.1}$ island, whose particular shape reflects the fourfold symmetry of the strain energy distribution, see

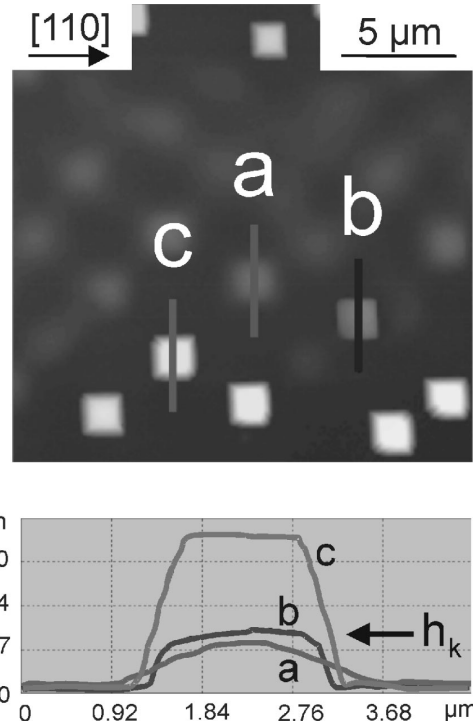


FIG. 1. Atomic force micrograph (top) and corresponding height profiles (bottom) taken on a sample with a comparatively low germanium content of 10%. A large variety of different island shapes and sizes has been recognized at special growth conditions. At a critical height the shape changes rapidly from a flat lens type (a) to truncated pyramids (b). Afterwards the growth happens along (001) (c).

Fig. 3(b). Strain induced wetting layer depression has also been observed for MBE and other material systems.^{5,33–36} Figure 4 depicts a fully developed $\text{Si}_{0.91}\text{Ge}_{0.09}$ island with a final aspect ratio island base/height of nearly two. The image clearly reveals the microstructure of the $\langle 101 \rangle$ edges, which are made of small $\{111\}$ -type facets.

Thus, the lateral island dimension still increases after formation of a truncated pyramid due to additional $\{111\}$ slabs. Because there is no two-dimensional nucleation at $\{111\}$ subsequent slabs exclusively nucleate at the island bottom. However, they do not grow into spatially complete facets since they stop in the island's corners at the bottom. FEM calculations predict a strongly enhanced strain energy nearby these corners, see Fig. 3(a), indicating a reason that the growth process initially suspends around these points. Later on nucleation will be completely suppressed after a strain induced wetting layer depression. For MBE grown islands it has been shown⁵ that the depth of a wetting layer depression linearly scales with island diameter and self-limits after a certain island size is achieved. Taking both, the observed wetting layer depression and the calculated enhanced strain energy around the island corners, into account the final island size can be explained rather in terms of a kinetically caused nucleation problem than a transport phenomenon. We pre-

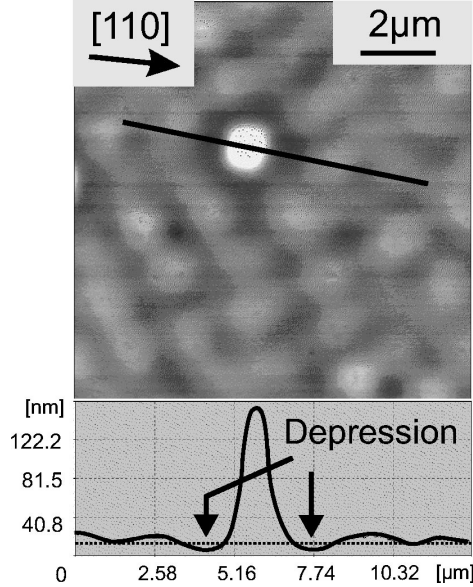


FIG. 2. Atomic force micrograph of a sample containing 10% germanium. Due to high strain energy in the vicinity of an island the wetting layer was depressed. Lateral dimension of this depression is in the order of the island size itself.

sume that the absence of further nucleation even holds as a key argument to a finite SK-island size in case of other growth techniques.

B. High-resolution x-ray diffraction

In the preceding section we have proposed a three-step island nucleation process reconstructed from *direct* imaging. There is a strong indication that at $\approx h/3$ the growth mechanism distinctly changes from a rough growth mode (corresponding to lenslike island shapes) towards a faceted one (truncated pyramids). In case of $x > 0.15$ a direct view to temporary morphological stages gets impossible, because an individual island passes extremely fast through subsequent stages, inducing island ensembles of high monodispersity.

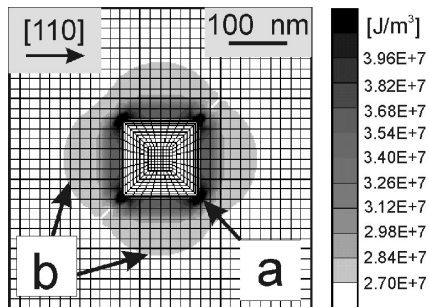


FIG. 3. Finite element calculation of the strain energy density in vicinity of a $\text{Si}_{0.7}\text{Ge}_{0.3}/\text{Si}(001)$ island, (a) denotes regions of an increased strain energy density and (b) the typical fourfold symmetry of the far field.

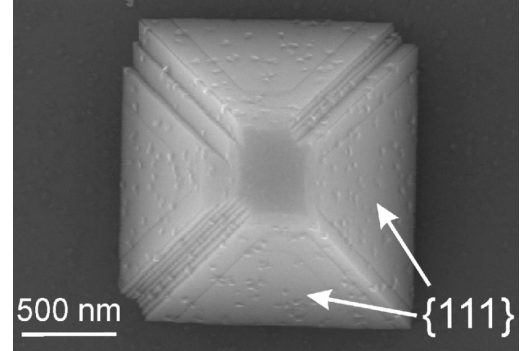


FIG. 4. Scanning electron micrograph of a $\text{Si}_{0.91}\text{Ge}_{0.09}/\text{Si}(001)$ island. The $\langle 101 \rangle$ -edges show a pronounced dissection indicating to a suspended nucleation at the island bottom.

However, diffuse x-ray scattering can be applied as an excellent tool to reveal structural details of the island evolution. Since the actual growth mechanism significantly influences the amount of germanium incorporated a growth scenario could be deduced from a certain concentration profile. Further reasons for an inhomogeneous germanium profile could be an anisotropic incorporation probability, strain dependent lateral transport, and an impact of the actual moment of evolution, which directly refers to a time-dependent composition within the solution. Namely, the last point attracts particular interest since atomic force micrographs of a sample containing locally different island densities prove a sequential nucleation, where the islands appear one after another in chains along $\langle 100 \rangle$ directions at the end of an already existing formation.³⁷

We investigated two-dimensional intensity distributions around symmetrical as well as asymmetrical reciprocal lattice points applying HRXRD. Figure 5(b) shows the measured intensity distribution around the $\text{Si}(004)$ reciprocal lattice point, which will actually appear out of the measured area (at $q_{001}=4.628 \text{ Å}^{-1}$), whereas the cloud of diffuse intensity originates mainly from the scattering at coherently strained SiGe islands. It contains information regarding island size and shape as well as strain state, chemical composition, and positional correlation.

Lateral ordering satellites nearby the crystal truncation rod have been observed up to third order indicating a high degree of island correlation along the $\langle 100 \rangle$ direction. The averaged peak distance of $\Delta q=0.0022 \text{ Å}^{-1}$ corresponds to $\Lambda=285 \text{ nm}$, which coincides with the island-island spacing within an island chain detected by AFM. The convolution theorem states that the diffusely scattered intensity by an ensemble of equivalent objects gets a simple product of diffuse scattering by a single individual times an interference function. Thus, regardless of correlation effects, scattering from an island ensemble can be treated exactly the same way as a single individual scattering process.

As a final outcome of an iterative evaluation process considering various island shapes and concentration profiles we will present two kinematical scattering simulations [Figs. 5(a) and 5(c)] which basically refer to exactly the same is-

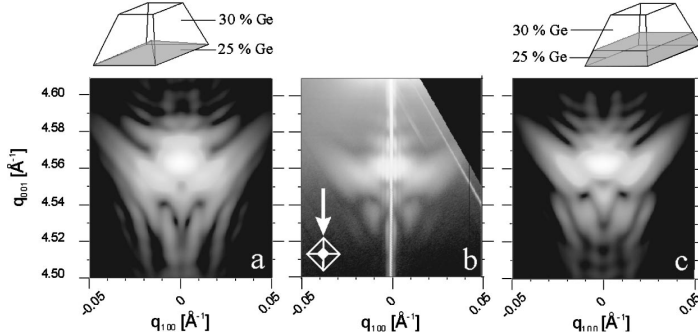


FIG. 5. Diffusely scattered intensity around 004 reflection (a) and (c) kinematical simulations for different models and (b) respective measurement. The strong feature on the right-hand side in (b) is caused by a detector artefact.

land shape revealed by AFM: a truncated pyramid with {111} side facets and an (001) top facet with a base width along [110] and height of 130 nm and 65 nm, respectively. However, the considered Ge distributions slightly differ regarding the two possible scenarios for the microscopical nature of transition ($a \Rightarrow b$) at $h/3$ as proposed in the preceding section.

Since the islands may elastically relax during their evolution increasing lattice parameter towards the apex will be favored in general. However, a linear increase of germanium concentration could be excluded by comparison with respective simulations indicating a discrete concentration profile. In order to prove whether the growth transition ($a \Rightarrow b$) (the change from {115} towards {111}-type facets, respectively) performs similar to the preceding *nonfaceted* or to the subsequent *faceted* growth mechanism the particular germanium content has been used as a sensitive probe. Both models assume a fixed germanium content of 30% within $h \geq h/3$.

The simulation shown in Fig. 5(c) considers a truncated pyramid of 25% Ge covered by $\text{Si}_{0.7}\text{Ge}_{0.3}$ —a linear and only height-dependent germanium gradient, which has been already proposed for LPE-SiGe islands.¹⁰ However, in the present paper we compare this with a more sophisticated germanium distribution shown in Fig. 5(a) an embedded pyramid of 25% within the island bottom surrounded by a $\text{Si}_{0.7}\text{Ge}_{0.3}$ matrix. The recently reported three-dimensional concentration profile inside MBE-grown SiGe islands on Si(001) obtained by selective etching technique proves a higher germanium content around the island apex (compared with that in the island corners) as well.¹⁹ *A priori* this particular distribution does not exclude the two models proposed here because crystal growth from the liquid phase provides different growth conditions rather close to thermodynamic equilibrium. This leads to—as the most obvious feature—different planar island orientations and corresponding faceting for MBE- and LPE-SiGe islands, which could motivate various concentration profiles as well.

Due to the models' particular inner structure the respective averaged germanium contents \bar{x} hold $\bar{x}^a > \bar{x}^c$. Consequently, the center of diffuse intensity shifts from around $q_{001}^a = 4.555 \text{ \AA}^{-1}$ towards $q_{001}^c = 4.560 \text{ \AA}^{-1}$.

In order to avoid any subjectivism when comparing experiment and respective simulations, a quantitative correlation analysis has been used. First of all it is noteworthy to state that simulations due to the finite size of our finite ele-

ment models, will be unable to reproduce a narrow crystal truncation rod. Also the ratio between the integrated intensities of x-ray scattering from the islands and substrate is not accessible by our calculations. Moreover, the most distinctive features of the diffuse scattering from islands are located apart from the substrate Bragg peak. Therefore, we have defined a range of interest for the correlation analysis. Taking into account the symmetry of reciprocal space intensity distribution for the 004 reflection with respect to the q_{001} axis, we have limited ourselves to a rectangular region defined by $q_{001} = 4.52 \dots 4.56 \text{ \AA}^{-1}$ and $q_{100} = 0.006 \dots 0.030 \text{ \AA}^{-1}$.

The correlation coefficients have been calculated according to the conventional definition,

$$K(\xi, \eta) = \frac{\text{cov}(\xi, \eta)}{\sqrt{V\xi}\sqrt{V\eta}} = \frac{E((\eta - E\eta)(\xi - E\xi))}{\sqrt{E(\eta - E\eta)^2}\sqrt{E(\xi - E\xi)^2}}, \quad (3)$$

where ξ and η are the experimental and simulation datasets, respectively, $\text{cov}(\eta, \xi)$ denotes the covariance, and finally V and E are the variance and mathematical expectation value, respectively. Basically, the modulus of the correlation coefficient K is equal to one in the case of a linear dependence between datasets and is equal to zero in the case of purely independent datasets. Additionally, the correlation coefficient, due to the generic properties of mathematical expectations, is a noise proof. So, the correlation analysis could be performed on the raw data without any scaling adjustment. In order to reveal the minor features of the reciprocal space intensity distribution, intensities should be, naturally, represented in a logarithmic scale. However, the dynamical range of the experimental data is rather limited. The weak diffusely scattered intensities are superimposed by a background intensity, while the simulations are free of this experimental feature. This fact enforces us to shift the calculated intensity maximum to the experimental one in the region of interest, and to add a smooth experimental background. The given procedure was absolutely identical for both island models, including scaling coefficient and background level. Corresponding correlation coefficients were calculated, line by line along the q_{001} direction in the mentioned range of interest. Standard subroutines of two-dimensional interpolation, with averaging over q_{001} range, and vice versa were used.

M. HANKE *et al.*

PHYSICAL REVIEW B 69, 075317 (2004)

Finally, we obtained K values of 0.84 for the model in Fig. 5(c) and a distinctly smaller value of 0.60 for the model in Fig. 5(a).

This difference is mainly caused by regions at q_{001} smaller than 4.54 \AA^{-1} , which are comparatively far away from diffuse maxima, and are sensitive for the particular three-dimensional germanium distribution. For these regions alone the corresponding K values are 0.78 [Fig. 5(c)] and 0.32 [Fig. 5(a)]. This result indicates a growth mode for the transition ($a \rightarrow b$), which is rather similar to the growth via different side facets up to {115}.

In order to estimate the absolute accuracy of our treatment two-dimensional reciprocal space maps (RSM) based on objects similar to model Fig. 5(c) have been calculated, however, taking into account slightly different germanium contents. The final intensity distribution arising from a coherent summation of various RSM's shows a significant change with respect to the measured distribution only in case the absolute germanium content changes more than $\pm 1\%$. Thus, there is no indication to a concentration spread along different islands within the island ensemble.

VI. CONCLUSION

LPE grown self-organized $\text{Si}_{1-x}\text{Ge}_x/\text{Si}(001)$ islands have been investigated by means of direct imaging techniques as well as diffuse x-ray scattering.

Scanning electron micrographs address the well-known

phenomenon of a finite island size during SK-growth mode to a twofold nucleation problem at the island bottom: (i) areas of exceptional high strain energy in vicinity of the island corners predicted by FEM calculations acts as a lateral nucleation barrier for the outmost {111}-type slabs, and finally, (ii) a strain driven wetting layer depression completely prevents ongoing nucleation at the island bottom.

Various growth stages observed by *ex situ* AFM at germanium contents below 15% reveal a three-step island nucleation process, wherein the island shape undergoes a significant change at one third of the final height from a lenslike type towards faceted islands. Since the incorporated germanium content probes the particular growth mode we applied HRXRD along with kinematical scattering simulations at samples where temporary growth stages could not be observed. From a discrete concentration change at exactly $h/3$ we conclude that the proposed island nucleation process remains the same even in case of higher concentrations.

ACKNOWLEDGMENTS

We would like to thank W. Drube and H. Schulte-Schrepping for their experimental assistance at beamline BW2 (HASYLAB). The scanning electron micrograph has been prepared by U. Jahn (Paul-Drude-Institut, Berlin). This project was sponsored by the German Research Society in the framework of the Sonderforschungsbereich 296.

-
- ¹D. Bimberg, M. Grundmann, F. Heinrichsdorff, N.N. Ledentsov, Ch. Ribbat, R. Sellin, Zh. Alferov, P.S. Kopev, M.V. Maximov, V.M. Ustinov, A.E. Zhukov, and J.A. Lott, in *Nanoscale Linear and Nonlinear Optics*, edited by M. Bertolotti, C. M. Bowden, and C. Sibilia, AIP Conf. Proc. No. **560** (AIP, Melville, NY, 2001), p. 178.
²H. Ishikuro and T. Hiramoto, Appl. Phys. Lett. **71**, 3691 (1997).
³H. Okada and H. Hasegawa, Jpn. J. Appl. Phys., Part 1 **40**, 2797 (2001).
⁴I. Stranski and L. Krastanow, Sitzungsber. Akad. Wiss. Wien, Math.-Naturwiss. Kl., Abt. 2B **146**, 797 (1937).
⁵S.A. Chaparro, Y. Zhang, and J. Drucker, Appl. Phys. Lett. **76**, 3534 (2000).
⁶C.J. Huang, Y.H. Zuo, D.Z. Li, B.W. Cheng, L.P. Luo, J.Z. Yu, and Q.M. Wang, Appl. Phys. Lett. **78**, 3881 (2001).
⁷S. Christiansen, M. Albrecht, H.P. Strunk, and H.J. Maier, Appl. Phys. Lett. **64**, 3617 (1994).
⁸M. Cazayous, J. Groenen, F. Demangeot, R. Sirvin, M. Caumont, T. Remmeli, M. Albrecht, S. Christiansen, M. Becker, H.P. Strunk, and H. Wawra, J. Appl. Phys. **91**, 6772 (2002).
⁹A.A. Darhuber, P. Schittenhelm, V. Holý, J. Stangl, G. Bauer, and G. Abstreiter, Phys. Rev. B **55**, 15 652 (1997).
¹⁰T. Wiebach, M. Schmidbauer, M. Hanke, H. Raidt, R. Köhler, and H. Wawra, Phys. Rev. B **61**, 5571 (2000).
¹¹I. Kegel, T.H. Metzger, A. Lorke, J. Peisl, J. Stangl, G. Bauer, J.M. Garcia, and P.M. Petroff, Phys. Rev. Lett. **85**, 1694 (2000).
¹²K. Zhang, C. Heyn, W. Hansen, T. Schmidt, and J. Falta, Appl. Phys. Lett. **76**, 2229 (2000).
¹³M. Rauscher, R. Paniago, H. Metzger, Z. Kovats, J. Domke, J. Peisl, H.D. Pfannes, J. Schulze, and I. Eisele, J. Appl. Phys. **86**, 6763 (1999).
¹⁴Z. Kovats, M. Rauscher, H. Metzger, J. Peisl, R. Paniago, H.D. Pfannes, J. Schulze, I. Eisele, F. Boscherini, and S. Ferrer, Phys. Rev. B **62**, 8223 (2000).
¹⁵J. Stangl, A. Daniel, V. Holý, T. Roch, G. Bauer, I. Kegel, T.H. Metzger, T. Wiebach, T. Schmidt, and O.G. Eberl, Appl. Phys. Lett. **79**, 1474 (2001).
¹⁶R. Paniago, H. Metzger, M. Rauscher, Z. Kovats, J. Peisl, J. Schulze, I. Eisele, and S. Ferrer, J. Appl. Crystallogr. **33**, 433 (2000).
¹⁷A.J. Steinfort, P.M.L.O. Scholte, A. Etterna, F. Tuinstra, M. Nielsen, E. Landemark, D.-M. Smilgies, R. Feidenhans'l, G. Falkenberg, L. Seehofer, and R.L. Johnson, Phys. Rev. Lett. **77**, 2009 (1996).
¹⁸M. Schmidbauer, M. Hanke, and R. Köhler, Cryst. Res. Technol. **37**, 3 (2002).
¹⁹U. Denker, M. Stoffel, and O.G. Schmidt, Phys. Rev. Lett. **90**, 196102 (2003).
²⁰N. Liu, J. Tersoff, O. Baklenov, A.L. Holmes, and C.K. Shih, Phys. Rev. Lett. **84**, 334 (2000).
²¹W. Dorsch, H.P. Strunk, H. Wawra, G. Wagner, J. Groenen, and R. Carles, Appl. Phys. Lett. **72**, 179 (1998).
²²D.A. Faux, J.R. Downes, and E.P. O'Reilly, J. Appl. Phys. **82**, 3754 (1997).
²³Q. Shen and S. Kycia, Phys. Rev. B **55**, 15 791 (1997).

SiGe/Si(001) STRANSKI-KRASTANOW ISLANDS BY . . .

PHYSICAL REVIEW B **69**, 075317 (2004)

- ²⁴V.M. Kaganer and K.H. Ploog, Phys. Rev. B **64**, 205301 (2001).
- ²⁵G.S. Pearson and D.A. Faux, J. Appl. Phys. **88**, 730 (2000).
- ²⁶T. Benabbas, P. Francios, Y. Androussi, and A. Lefebvre, J. Appl. Phys. **80**, 2763 (1996).
- ²⁷M. Grundmann, O. Stier, and D. Bimberg, Phys. Rev. B **52**, 11 969 (1995).
- ²⁸Program package MarcMentat®.
- ²⁹L. Vegard, Z. Phys. **5**, 17 (1921).
- ³⁰S. Christiansen, M. Albrecht, H.P. Strunk, P.O. Hansson, and E. Bauser, Appl. Phys. Lett. **66**, 574 (1995).
- ³¹M. Hanke, Ph.D. thesis, Humboldt-Universität zu Berlin, Mensch & Buch Verlag, ISBN 3-89820-398-0, 2002.
- ³²W. Dorsch, B. Steiner, M. Albrecht, H.P. Strunk, H. Wawra, and G. Wagner, J. Cryst. Growth **183**, 305 (1998).
- ³³X.Z. Liao, J. Zou, X.F. Duan, D.J.H. Cockayne, R. Leon, and C. Lobo, Phys. Rev. B **58**, R4235 (1998).
- ³⁴U. Denker, O.G. Schmidt, N.Y. Jin-Phillip, and K. Eberl, Appl. Phys. Lett. **78**, 3723 (2001).
- ³⁵X.Z. Liao, J. Zou, D.J.H. Cockayne, J. Qin, Z.M. Jiang, X. Wang, and R. Leon, Phys. Rev. B **60**, 15 605 (1999).
- ³⁶X.Z. Liao, J. Zou, D.J.H. Cockayne, Z.M. Jiang, X. Wang, and R. Leon, Appl. Phys. Lett. **77**, 1304 (2000).
- ³⁷M. Hanke, H. Raidt, R. Köhler, and H. Wawra, Appl. Phys. Lett. **83**, 4927 (2003).

2.5.2 Beugung unter streifendem Ein- und Austritt

M. Schmidbauer, D. Grigoriev, **M. Hanke**, P. Schäfer, T. Wiebach, R. Köhler
Effects of Grazing Incidence on the X-Ray Diffuse Scattering from Self-Assembled Nanoscale Islands
Phys. Rev. B **71**, 115324 (2005).

Bei der Beugung unter kleinem Einfalls- und Austrittswinkel (GID) besitzt der Beugungsvektor nur eine sehr kleine Komponente senkrecht zur Oberfläche. Daraus folgt, dass man in dieser Geometrie insbesondere auf Gitterparameterunterschiede parallel zur Oberfläche (in-plane) empfindlich ist. Zusätzlich bewirkt der Effekt der externen Totalreflexion einen raschen Abfall der einfallenden Welle in den Kristall hinein, so dass GID eine oberflächensensitive, bei Benutzung verschiedener Einfallswinkel in gewissen Grenzen¹³ auch tiefenselektive Methode ist. Wegen der im Vergleich zur Weitwinkelbeugung (im Sinne von Reflexen (hkl) ; $l > 0$) stärkeren Unterdrückung von Streubeiträgen des Substrates eignet sich GID gut für die Untersuchung kleiner und damit weniger stark streuernder, in Oberflächennähe befindlicher Objekte. Vergleichbare Oberflächenempfindlichkeit erreicht man bei der Röntgenkleinwinkelstreuung (GISAXS). Hier verliert man jedoch im Gegensatz zu GID aufgrund des sehr kleinen Streuvektors die Deformationsempfindlichkeit.

In beiden Fällen hängt die diffuse Streuung sehr stark vom konkreten Einfallswinkel ab, so dass eine rein kinematische Behandlung des Streuprozesses versagt. Im Rahmen eines störungstheoretischen Ansatzes, der sogenannten Distorted-Wave-Born Approximation (DWBA), lassen sich jedoch Effekte durch den streifenden Ein- und Austritt berücksichtigen, wobei das untersuchte Modellsystem SiGe/Si(001) die besten Voraussetzungen bietet, da die Inseln nur sehr wenig in Größe, Form und chemischer Komposition variieren.

¹³Eine tiefenaufgelöste Untersuchung im Sinne eines kontinuierlichen Durchstimmens der Informationstiefe Λ erweist sich als ausgesprochen schwierig, da sich diese in der Nähe des kritischen Winkels der Totalreflexion sehr rasch über mehrere Größenordnungen ändert.

PHYSICAL REVIEW B 71, 115324 (2005)

Effects of grazing incidence conditions on the x-ray diffuse scattering from self-assembled nanoscale islands

M. Schmidbauer, D. Grigoriev, M. Hanke,* P. Schäfer, T. Wiebach, and R. Köhler

Institut für Physik, Humboldt-Universität zu Berlin, Newtonstraße 15, 12489 Berlin, Germany

(Received 5 April 2004; revised manuscript received 21 December 2004; published 25 March 2005)

Grazing incidence small-angle x-ray scattering and grazing incidence x-ray diffraction from SiGe nanoscale islands grown on Si(001) substrate were investigated. Experiments and corresponding theoretical simulations based on the distorted-wave Born approximation were carried out. The strain field inside and in the vicinity of the SiGe islands was calculated in the framework of linear elasticity theory using the numerical finite element method. The diffuse intensity pattern in reciprocal space reveals a well-resolved fine structure with prominent maxima and a complicated fringe pattern. The distribution of diffuse intensity in reciprocal space strongly depends on the angle of incidence with respect to the sample surface. The results obtained substantiate the important role of basically five (grazing incidence small-angle x-ray) and nine (grazing incidence diffraction) scattering channels that have to be considered for a complete understanding of the scattering scenario. A refined island model concerning shape, size, and Ge composition was elaborated.

DOI: 10.1103/PhysRevB.71.115324

PACS number(s): 68.65.-k, 61.10.-i, 81.16.Dn, 81.15.Lm

I. INTRODUCTION

Semiconductor nanoscale islands have been extensively investigated in the past decade because of their novel electronic and optical properties related to quantum confinement.^{1,2} Self-organized growth mechanisms, such as the Stranski-Krastanow growth mode,³ have attracted considerable interest. Here, a heteroepitaxial film can release its elastic energy by forming small dislocation free three-dimensional islands. Structural properties as strain, shape, size, composition, and positional correlation are essential for device properties and require accurate analysis. On the other hand, knowledge of structural details allows a valuable insight into the island formation process, which has not been completely understood yet.

X-ray scattering methods are widely used for the nondestructive structural characterization of materials systems and have been recently applied to semiconductor nanoscale systems.⁴ Among the most widely used x-ray scattering techniques for the investigation of self-assembled nanoscale islands are grazing incidence small-angle x-ray scattering (GISAXS)^{5,6} and grazing incidence diffraction (GID).⁷⁻⁹ At GISAXS, electron density fluctuations averaged over the atomistic structure are probed, making this method sensitive mainly to morphological properties of the sample, e.g., island size, shape, composition and positional correlation of islands. All these features can be also probed by GID, which, additionally, is sensitive to the lattice strains inside the sample.

GID and GISAXS have been successfully applied to nanoscale structures.¹⁰⁻¹² However, further use of these techniques still suffers from the lack of convenient approaches that can explain the mechanisms and distribution of scattered intensity formation in reciprocal space. This especially holds for nanoscale islands with a well-developed facet structure where the deformation field cannot be calculated analytically within the framework of linear elasticity theory. Although enhanced surface and interface sensitivity is achieved in a

grazing incidence and/or exit scattering experiment, there is the principal problem that the kinematical scattering theory in its simplest form cannot be used. On one hand, refraction effects lead to a significant change of the wave vector's direction outside and inside the sample. On the other hand, owing to the small glancing angles of incidence, there is a large fraction of x rays that are reflected at the surface, and below a critical angle total external reflection occurs. Consequently, the reflected wave takes part in the scattering process and a considerable impact of the angle of incidence on the distribution of diffuse intensity in reciprocal space can be expected. Owing to the reciprocity theorem this holds also for the dependence of intensity on the exit angle. This means that preferentially "out-of-plane" measurements in GISAXS or GID geometry are influenced. These effects complicate the interpretation of the x-ray scattering data and makes the use of the distorted-wave Born approximation (DWBA) inevitable.

The implementation of the specular beam was introduced by Kaganer *et al.*¹³ for the evaluation of interface roughness. Later, the theory was further developed for GISAXS by Rauscher *et al.*¹⁰ and for GID by Kegel *et al.*^{9,11} and Grigoriev *et al.*¹⁴ for interpreting scattering from free-standing nanoscale islands. However, though the x-ray reflectivity critically depends on the angle of incidence, a systematic study of the influence on the x-ray diffuse scattering has not yet been performed in detail.

In this paper we will explicitly demonstrate the impact of the reflected wave on the scattered diffuse intensity distribution. In order to visualize this influence the model system SiGe islands grown on Si(001) by means of liquid-phase epitaxy (LPE) has been chosen. These islands are especially suitable, owing to their high perfection regarding uniform shape and size. Moreover, they are large enough to give a sufficiently high scattering signal.

Since both the island shape and the internal strain field are three-dimensional (3D) in nature we would like to point out that it is not sufficient to probe the diffuse intensity by

SCHMIDBAUER *et al.*

PHYSICAL REVIEW B 71, 115324 (2005)

simple one-dimensional rocking scans; it has to be probed at least within two-dimensional (2D) sections in reciprocal space, although a 3D data acquisition would be most advantageous. Reciprocal-space mapping has to be carried out with sufficiently high angular resolution. Precise determination of the scattering vector can be performed by a triple crystal setup, with the principal advantage to map reciprocal space with extremely high resolution. However, the corresponding large data collection time represents a serious disadvantage and makes this technique less feasible for recording the 2D or 3D intensity distribution of diffuse scattering from nanoscale islands, even if a very intense x-ray source is available. This difficulty of long data collection times can be overcome by exploiting modern multidetection techniques through the use of x-ray area detectors or a linear position-sensitive detector (PSD).

X-ray diffuse scattering intensity patterns were measured in GISAXS and GID scattering geometry for a set of different angles of incidence. Comparison to respective theoretical simulations enables one to qualitatively and quantitatively prove the validity of the DWBA approach.

This paper is organized as follows. In Sec. II the DWBA approach as further used for GISAXS and GID will be introduced. This is followed by a short description on how the strain field will be incorporated into the x-ray diffuse scattering simulations. In a short experimental part (Sec. III), the samples and details of the experimental setup are presented. Finally, in Sec. IV, results of experiments and simulations will be compared and discussed.

II. THEORY

In the framework of the distorted-wave Born approximation the amplitude of the scattered wave can be written as¹³

$$A(\mathbf{q}) = \frac{k^2}{4\pi} \int \mathbf{E}^{\text{out}}(\mathbf{r}) \delta\chi(\mathbf{r}) \mathbf{E}^{\text{in}}(\mathbf{r}) dV. \quad (1)$$

$\mathbf{E}^{\text{in}}(\mathbf{r})$ and $\mathbf{E}^{\text{out}}(\mathbf{r})$ are the wave fields in the scattering object produced by x-ray plane waves incoming in the incident direction and incoming from the observation point. They correspond to the perfect “undisturbed” dynamical solutions of the diffraction problem, while $\delta\chi(\mathbf{r})$ is the disturbance of the dielectric polarizability and k is the modulus of the wave vector in vacuum. Please note that the amplitudes of all participating wave fields are normalized with respect to the incoming wave field, i.e., the amplitude of the incoming vacuum wave is set to unity.

The DWBA can be described as follows: The incident vacuum plane wave produces a wave field inside and outside the sample. This wave field is treated as being the exact solution for the undisturbed sample. It is thus created by dynamical scattering from the undisturbed potential. In the next step this wave field is (diffusely) scattered by the disturbance provided by the sample. After the scattering process, the resulting scattered waves leave the crystal.

The DWBA represents first-order perturbation theory. The exact solutions of the undisturbed system are calculated dynamically, whereas the diffuse scattering from the disturbed

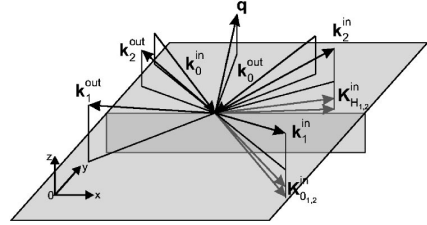


FIG. 1. Definition of wave vectors for incoming (in) and outgoing (out) waves for grazing incidence diffraction. The indices 0, 1, and 2 correspond to incoming, reflected, and diffracted waves, respectively.

system is simply calculated kinematically. For a detailed description of DWBA, see Ref. 15.

In the most general case, the solution of the dynamical problem supplies us with three plane waves in vacuum. These are the incoming wave, the specularly reflected wave, and—for GID—also the diffracted wave, with amplitudes E_m^{in} and wave vectors \mathbf{k}_m^{in} . For these incoming (in) wave fields, inverted outgoing (out) wave fields can be constructed with amplitudes E_n^{out} and wave vectors $\mathbf{k}_n^{\text{out}}$. The indices m and n label the incident wave ($m,n=0$), the specularly reflected wave ($m,n=1$), and the diffracted wave ($m,n=2$), respectively. Please bear in mind that these waves are the solutions for the perfect undisturbed crystal.

Mutual combinations of \mathbf{k}_m^{in} and $\mathbf{k}_n^{\text{out}}$ give a set of scattering vectors \mathbf{q}_{mn} through

$$\mathbf{q}_{mn} = -(\mathbf{k}_m^{\text{in}} + \mathbf{k}_n^{\text{out}}). \quad (2)$$

According to dynamical theory each of the incident plane waves with wave vectors \mathbf{k}_0^{in} and $\mathbf{k}_0^{\text{out}}$ creates a corresponding wave field inside the crystal, which consists of a pair of coupled plane waves with wave vectors $\mathbf{K}_{0(1,2)}^{\text{in,out}}$ and $\mathbf{K}_{h(1,2)}^{\text{in,out}}$ (Fig. 1) and corresponding amplitudes. The components of the vectors $\mathbf{K}_{0(1,2)}^{\text{in,out}}$ and $\mathbf{K}_{h(1,2)}^{\text{in,out}}$ are found from the dispersion equation.¹⁶ The corresponding amplitudes E_m^{in} and E_n^{out} for the vacuum solution and $D_{0(1,2)}^{\text{in,out}}$ and $D_{h(1,2)}^{\text{in,out}}$ for the solutions inside the medium are calculated by solving a system of boundary equations.¹⁷ Thus, the calculation of scattering from the semi-infinite substrate requires the consideration of four waves inside the crystal, and the DWBA coupling scheme provides us with 16 channels into which scattering can occur.¹⁸ However, when the diffuse scattering from free-standing islands is calculated, only three vacuum waves have to be taken into account: the incident, the specularly reflected, and the diffracted wave. In this case, the total amplitude can be expressed as

$$A(\mathbf{q}) = \frac{k^2}{4\pi} \sum_{m=0}^2 \sum_{n=0}^2 \int E_m^{\text{in}} E_n^{\text{out}} \delta\chi_{mn}(\mathbf{r}) e^{i\mathbf{q}_{mn}\cdot\mathbf{r}} dV, \quad (3)$$

where $\delta\chi_{mn}(\mathbf{r})$ is given by

EFFECTS OF GRAZING INCIDENCE CONDITIONS ON...

PHYSICAL REVIEW B 71, 115324 (2005)

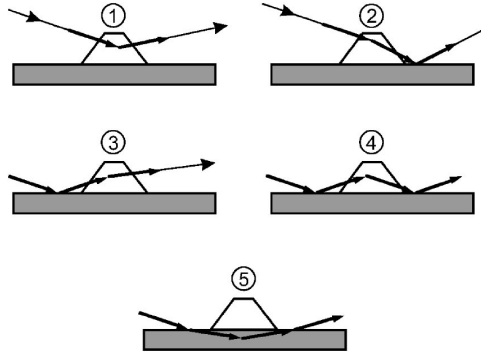


FIG. 2. Schematic view of the five-channel scattering process at free-standing islands and surrounding substrate.

$$\delta\chi_{mn}(\mathbf{r}) = \begin{cases} \chi_0(\mathbf{r}) & \text{for } \frac{|\mathbf{k}_m^{\text{in}} \cdot \mathbf{k}_n^{\text{out}}|}{|\mathbf{k}_m^{\text{in}}||\mathbf{k}_n^{\text{out}}|} \approx 1 \\ \chi_h(\mathbf{r}) & \text{for } \frac{|\mathbf{k}_m^{\text{in}} \cdot \mathbf{k}_n^{\text{out}}|}{|\mathbf{k}_m^{\text{in}}||\mathbf{k}_n^{\text{out}}|} \approx \cos(2\theta_B), \end{cases} \quad (4)$$

and θ_B is the Bragg angle of the chosen reflection. Here, the disturbance $\delta\chi(\mathbf{r})$ is assumed to be the polarizability of the island and $\chi_0(\mathbf{r})$ and $\chi_h(\mathbf{r})$ are its zeroth and h th Fourier components. They still depend on \mathbf{r} , taking into account a possible composition gradient inside the island. Please be aware that the expressions as given in Eqs. (3) and (4) are strictly valid only for centrosymmetric structures, where $\chi_h(\mathbf{r}) = \chi_{-h}(\mathbf{r})$ holds.

A. GISAXS at free-standing islands

Equation (3) is a general expression, which holds for both GID and GISAXS. However, in the case of GISAXS the amplitudes of the diffracted wave $E_2^{\text{in},\text{out}}$ can be set to zero and only the incident (direct) and specularly reflected waves have to be considered for scattering from the islands. Consequently, the following four scattering channels, depicted in Fig. 2 (processes 1–4) are relevant: (i) direct diffuse scattering from the island, (ii) diffuse scattering from the island followed by specular reflection from the surface, (iii) specular reflection from the surface followed by diffuse scattering from the island, (iv) specular reflection from the surface followed by diffuse scattering from the island followed by specular reflection from the surface. In addition to these four contributions we may also consider scattering from the underlying substrate leading to an additional fifth scattering channel: (v) penetration into substrate followed by diffuse scattering inside substrate followed by transmission into the vacuum as depicted in Fig. 2 (process 5). The diffuse scattering from the substrate originates from the penetrating strain field generated by the island. Although somehow surprising, we found that this strain field will remarkably contribute to the GISAXS intensity.

In case of GISAXS the amplitudes $E_n^{\text{in},\text{out}}$ of the participating wave fields can be easily calculated by using the Fresnel equations. For small angles of incidence compared to

the Brewster angle, the Fresnel reflection and transmission coefficients r and t , respectively, are independent of the polarization state of the x rays and can be expressed as a function of the glancing incident angle α and the complex refractive index n_0

$$r(\alpha) := \frac{E_1}{E_0} = \frac{\sin \alpha - \sqrt{n_0^2 - \cos^2 \alpha}}{\sin \alpha + \sqrt{n_0^2 - \cos^2 \alpha}}, \quad (5a)$$

$$t(\alpha) := \frac{E_t}{E_0} = \frac{2 \sin \alpha}{\sin \alpha + \sqrt{n_0^2 - \cos^2 \alpha}}, \quad (5b)$$

where E_t is the amplitude of the transmitted wave inside the crystal. By using these expressions we can write for the differential diffuse scattering cross section (r_0 : classical electron radius)

$$\frac{d\sigma}{d\Omega}(\mathbf{q}_{\parallel}, \alpha_i, \alpha_f) = r_0^2 |A_1 + A_2 + A_3 + A_4 + A_5|^2, \quad (6)$$

with the four amplitudes from the scattering from the island

$$A_1(\mathbf{q}) = \frac{k^2}{4\pi} \int_{\text{island}} \chi_0(\mathbf{r}) e^{i(\mathbf{q}_{\parallel} + \mathbf{q}_1^{\perp}) \cdot \mathbf{r}} dV, \quad (7a)$$

$$A_2(\mathbf{q}_{\parallel}, \alpha_f) = r(\alpha_f) \frac{k^2}{4\pi} \int_{\text{island}} \chi_0(\mathbf{r}) e^{i(\mathbf{q}_{\parallel} + \mathbf{q}_2^{\perp}) \cdot \mathbf{r}} dV, \quad (7b)$$

$$A_3(\mathbf{q}_{\parallel}, \alpha_i) = r(\alpha_i) \frac{k^2}{4\pi} \int_{\text{island}} \chi_0(\mathbf{r}) e^{i(\mathbf{q}_{\parallel} + \mathbf{q}_3^{\perp}) \cdot \mathbf{r}} dV, \quad (7c)$$

$$A_4(\mathbf{q}_{\parallel}, \alpha_i, \alpha_f) = r(\alpha_i) r(\alpha_f) \frac{k^2}{4\pi} \int_{\text{island}} \chi_0(\mathbf{r}) e^{i(\mathbf{q}_{\parallel} + \mathbf{q}_4^{\perp}) \cdot \mathbf{r}} dV, \quad (7d)$$

and the amplitude from scattering from the substrate

$$A_5(\mathbf{q}_{\parallel}, \alpha_i, \alpha_f) = t(\alpha_i) t(\alpha_f) \frac{k^2}{4\pi} \int_{\text{substrate}} \delta\chi_0(\mathbf{r}) e^{i(\mathbf{q}_{\parallel} + \mathbf{q}_5^{\perp}) \cdot \mathbf{r}} dV, \quad (8)$$

where $\delta\chi_0$ is the disturbance inside the substrate.

Two important properties have to be mentioned:

(i) The diffuse intensities given by Eqs. (7) and (8) depend on the Fresnel reflection and transmission coefficients $r(\alpha_{i,f})$ and $t(\alpha_{i,f})$, respectively, where the subscripts i and f refer to the incoming and outgoing waves. These coefficients strongly depend on the angle of incidence and/or exit $\alpha_{i,f}$ with respect to the sample surface. However, while the reflection coefficient equals to unity below the critical angle of total external reflection α_c , the transmission coefficient exhibits a pronounced maximum at α_c . This leads to the so-called Yoneda wings in the diffuse intensity.

(ii) According to Eq. (2) the vertical momentum transfers q^{\perp} are different for the four amplitudes. They are summarized in Table I.

The diffuse intensity is, thus, a function of both \mathbf{q} and the angles of incidence (α_i) and exit (α_f). The reflectivities $r(\alpha_{i,f})$ have the largest impact on the diffuse intensities when

TABLE I. Vertical momentum transfer q_j^\perp for the five different scattering amplitudes as used in Eqs. (7) and (8).

Index	q_j^\perp
$j=1$	$-k_{0,z}^{\text{out}} - k_{0,z}^{\text{in}}$
$j=2$	$+k_{0,z}^{\text{out}} - k_{0,z}^{\text{in}}$
$j=3$	$-k_{0,z}^{\text{out}} + k_{0,z}^{\text{in}}$
$j=4$	$+k_{0,z}^{\text{out}} + k_{0,z}^{\text{in}}$
$j=5$	$-K_{0,z}^{\text{out}} - K_{0,z}^{\text{in}}$

$\alpha_{i,\text{rf}}$, are chosen close to the critical angle of total external reflection, α_c . At higher angles the reflectivities are small and can be neglected. In this case only the first term on the right-hand side of Eq. (6) has to be considered, and the same result as predicted by the kinematical approach is obtained.

Rauscher *et al.*¹⁰ have derived a similar expression. They were treating GISAXS from free-standing islands grown on a homogeneous substrate, i.e., they neglected scattering from the strained substrate. In this case only the direct and reflected waves need to be considered, and the amplitude A_5 vanishes.

B. Grazing incidence diffraction at free-standing islands

As already pointed out, all four waves inside the crystal have to be considered in the most general case. However, when diffuse scattering from the free-standing islands is calculated, only three vacuum waves have to be taken into account and the expression as given in Eq. (3) can be used. This double sum consists of nine terms (i.e., nine scattering channels), which correspond to all possible types of coupling between \mathbf{k}_m^{in} and $\mathbf{k}_n^{\text{out}}$. An accurate account of the diffracted waves is needed, however, only for a restricted area in reciprocal space, when either the incident “in” or “out” waves satisfy the dynamical (!) Bragg condition for the substrate and corresponding E_2^{in} and E_2^{out} become essential. But in the case when the scattering signal far from the substrate reflection is considered (i.e. the diffuse scattering from the island), only four of the nine terms are expected to be essential: the incident and specularly reflected waves for each \mathbf{k}_m^{in} and $\mathbf{k}_n^{\text{out}}$. The corresponding four scattering channels are sketched in Fig. 2 (processes 1–4) with corresponding vertical momentum transfers q_j^\perp as given in Table I. We will, however, demonstrate in Sec. IV B that the nine-channel approach yields considerably better agreement with experiment as compared to the four-channel approach.

In the case of GID—especially for incident angles larger than the critical angle of total external reflection—the amplitudes of the specular beams depend on the azimuthal (in-plane) direction defined by the $\theta-\theta_B$ value. The only reliable way to evaluate them correctly is to solve the boundary equations at the surface using the dynamical wave model in the substrate body, i.e., introducing the dispersion corrections. This means that the Fresnel equations [see Eq. (5)]—as common for GISAXS—must not be used anymore.

C. Calculation of the strain field by the finite element method

In recent years, the use of the numerical finite element method (FEM) to calculate the strain field in mesoscopic

structures has become successfully established (e.g., Refs. 19–22). The FEM is based on linear continuum elasticity theory; it includes the full elastic anisotropy and has proven to be applicable down to structure sizes of a few tens of nanometers. For the systems under consideration here, linear elasticity theory is valid.

The results obtained by FEM can be used for x-ray diffuse scattering simulations. Wiebach *et al.*²⁰ have developed the following iterative approach for data evaluation of nanoscale islands: (i) creation of a specific structure model in real space that includes island size, shape, and chemical composition; (ii) FEM calculation of the three-dimensional strain field inside the island and the surrounding substrate and wetting layer; (iii) numerical calculation of diffuse scattering using the formula described in the previous sections; (iv) comparison to experimental data; and (v) further improvement of the model (i) and calculation of diffuse intensities from a new model until satisfactory agreement is achieved.

The components of the displacement field $\mathbf{u}(\mathbf{r}) = (u_1, u_2, u_3)$ that is used in the x-ray simulations are related to the (symmetrical) elastic strain tensor components ε_{ij} through

$$\varepsilon_{ij} = \frac{1}{2} \left(\frac{\partial u_i}{\partial x_j} + \frac{\partial u_j}{\partial x_i} \right), \quad i, j = 1, 2, 3. \quad (9)$$

In general, this approach cannot be used as a true “fitting” procedure because there are too many free parameters in the model (shape, size, chemical composition, and spatial correlation). Therefore, it is necessary to include knowledge obtained by other methods, e.g., information on the shape and size obtained by AFM (see Sec. III A). The calculation is done for a single island and its environment. The subsequent simulation of the diffuse intensity is performed numerically, i.e., on a regular grid consisting of *base cells*. Thus, the integrals in Eq. (3) have to be replaced by a discrete sum over all base cells of the regular grid. If necessary, the dimensions of the base cells can be chosen as small as that of the crystal unit cells; however, depending on the actual sample they can also be chosen larger. The numerical procedure has to be carried out for some 100 000 to 1 million base cells and more than 10 000 values of \mathbf{q} .

Different types of islands were created exhibiting either a homogenous Ge content or an abrupt change of the Ge atomic concentration at about one-third of the island height. In particular, Fig. 3 depicts the calculated strain field for a SiGe island (base width 140 nm, height 70 nm, {111} facets) in the case of $x=24\%$ in the lower third of the island and $x=29\%$ in the upper part. This model is in accordance with recent investigations obtained with high-resolution diffraction using coplanar 004 and 224 reflections.²³ Please note that the *total* strain is employed, i.e., the lattice parameter of the underlying substrate is used as the reference. This is advantageous because the diffuse scattering is sensitive to the atomic displacement with respect to the ideal lattice of the substrate.

In this work the finite element method was used to calculate the strain field inside mesoscopic structures. It is worth mentioning that a different approach, called *isostrain scattering*, has been developed by Kegel *et al.*^{9,11,24} This method is

EFFECTS OF GRAZING INCIDENCE CONDITIONS ON...

PHYSICAL REVIEW B 71, 115324 (2005)

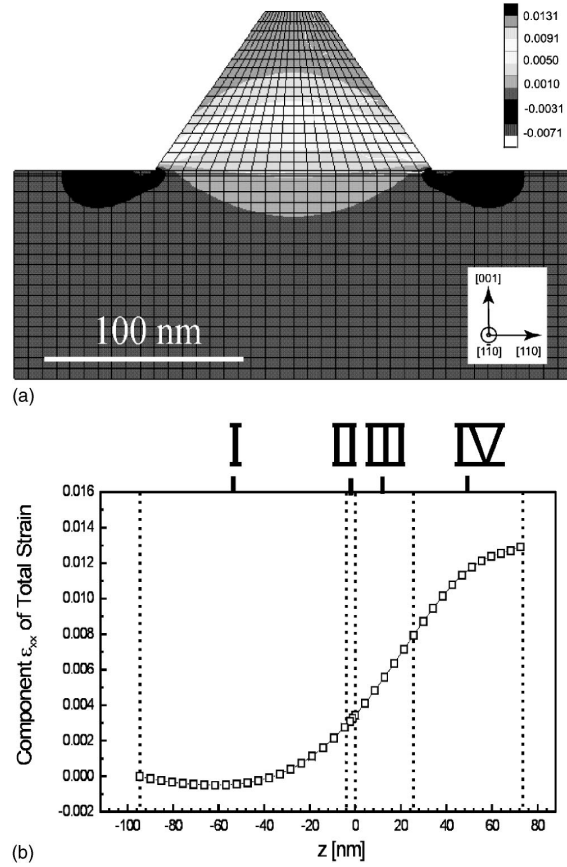


FIG. 3. Finite element calculation of a SiGe pyramid grown coherently on Si(001). The island base width and height are 140 nm and 70 nm, respectively. The side faces are of type {111}. The Ge content passes through an abrupt change from $x=24\%$ to $x=29\%$ at one-third of the island height ($z=22\text{ nm}$). (a) Horizontal component ε_{xx} of total strain in the (110) plane through the central axis of the pyramid. (b) Section of ε_{xx} along vertical symmetry axis (z axis). Region I corresponds to substrate, II to the wetting layer, III to the island bottom ($x=24\%$), and IV to the island top ($x=29\%$).

more direct, in the sense that the chemical composition can be directly deduced from the scattered intensities. However, this approach works for cylindrically symmetric islands only and can, thus, not be applied to truncated pyramids with a square base. Though the authors make use of the four-channel scattering process, scattering from the substrate is omitted.

III. EXPERIMENTAL

A. Description of samples

In order to quantitatively prove the validity of the theoretical approach as described in Sec. II, a single layer of highly regular free-standing $\text{Si}_{1-x}\text{Ge}_x$ islands with a nominal Ge atomic concentration of $x=30\%$ has been chosen that are grown coherently on Si(001). The sample preparation has

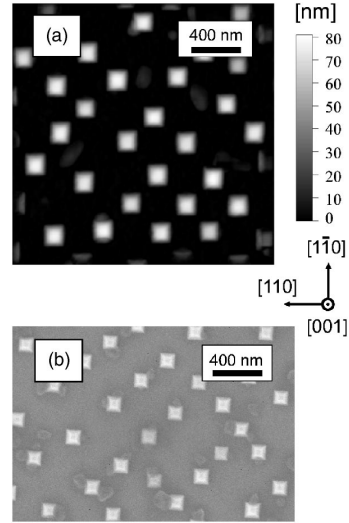


FIG. 4. Atomic force (a) and scanning electron (b) micrographs of SiGe nanoscale islands grown on Si(001) by LPE.

been described in a previous paper, in detail.⁶ Briefly, the $\text{Si}_{1-x}\text{Ge}_x$ islands were grown by liquid-phase epitaxy (LPE)²⁵ using a Bi solution. The epitaxial layers are deposited in a horizontal solution growth system that is kept under pure hydrogen. In order to ensure that the system is in thermodynamical equilibrium before growth starts, the solution is homogenized at the growth temperature ($600\text{ }^\circ\text{C}$) for several hours. A low cooling rate of about 10 K/h was chosen in order to achieve a low growth rate.

The surface morphology was investigated by atomic force microscopy (AFM) and scanning electron microscopy (SEM) such that the exact shape and size of the islands could be determined with high accuracy. As depicted in Fig. 4 the $\text{Si}_{1-x}\text{Ge}_x/\text{Si}(001)$ islands are shaped like truncated pyramids with {111} side facets and a (001) top facet. The resulting samples consist of coherent, highly monodisperse islands with uniform shape and a base width-to-height aspect ratio of approximately 2.²⁶ They are particularly perfect when the growth conditions are chosen close to thermodynamic equilibrium. The island size distribution is rather narrow with a mean value of $w=140\text{ nm}$ for the island base width. This value is in accordance to the observed relationship $w \propto f^{-2.03}$ between the island base width w and the lattice mismatch f between $\text{Si}_{1-x}\text{Ge}_x$ and Si.²⁷

The islands form a planar system of extended rows aligned along the $\langle 100 \rangle$ directions. The origin of these rows is discussed elsewhere.^{28,29}

B. X-ray scattering experiment

The x-ray scattering investigations were carried out at the European Synchrotron Radiation Facility (ESRF) in Grenoble. The GISAXS experiment was performed at the beamline ID11 using a very well-collimated and narrow incident beam. Monochromatic x-rays with a wavelength of $\lambda=1.28\text{ \AA}$ were employed. The x-ray beam was reduced to a

SCHMIDBAUER *et al.*

PHYSICAL REVIEW B 71, 115324 (2005)

size of approximately $50 \mu\text{m} \times 50 \mu\text{m}$. A charge-coupled device (CCD) detector with a pixel size of $60 \mu\text{m} \times 60 \mu\text{m}$ was placed at a distance of more than 4 m from the sample. The entire beam path between the sample and detector was evacuated. Behind the sample the strong primary beam and the specular reflected beam were attenuated by a narrow metal wire in order to avoid saturation of the CCD detector. These experimental conditions ensured very good resolution and counting statistics. Typical data acquisition times for a single CCD frame were of order of 300 s. To further improve counting statistics a set of different CCD frames were recorded under identical experimental conditions. In good approximation, the intensity of a CCD frame corresponds to a planar 2D section of reciprocal space.

The GID experiment was carried out at ID10B station at a wavelength of $\lambda = 1.54 \text{ \AA}$ using a triple-crystal setup: The direction of the diffracted beam was analyzed by a three-bounce Si(111) crystal within the diffraction plane (within the sample surface) and normal to the surface (out-of-plane) by a linear position sensitive detector. Using this setup the entire 3D intensity distribution around in-plane reciprocal lattices points of the type $(hk0)$ was recorded with high resolution.

IV. RESULTS AND DISCUSSION

A. Grazing incidence small-angle x-ray scattering

A set of different experimental GISAXS intensity patterns recorded at different angles of incidence is shown in Figs. 5 and 6. A clear dependence of the experimental GISAXS intensity distributions on the angle of incidence α_i can be seen. The experimentally observed behavior can be excellently reproduced by calculations using the five channel DWBA approach as given by Eqs. (7) and (8). In particular, the diffuse scattering in the vicinity of the specular beam is clearly reproduced in the simulations.

At low angles of incidence (Fig. 5) the diffuse scattering in the vicinity of the Yoneda wing and the diffuse intensity around the specular beam overlap and cannot be clearly separated. With increasing angle of incidence (Fig. 6) the diffuse intensity that is related to the specular beam moves to higher values of q_{001} (relative to the Yoneda wing). Both the specular peak and the Yoneda wing show $\{111\}$ truncation rods (CTR), which correspond to the side facets of the islands. These facet CTRs are modulated by fringes, which are related to the finite size of the islands. Owing to refraction effects, the Yoneda CTR is bowed and crosses the q_{001} axis at a finite value of q_{001} (not at $q_{001}=0$ as expected from kinematical scattering theory). In contrast, the CTRs from the specular beam appear at an angle of about $\pm 55^\circ$. This value approximately fits to the angle between $\{111\}$ and $\{001\}$ planes.

The experimental and respective theoretical data shown here are in very good correspondence with each other, and only slight deviations can be observed:

(i) It is noticeable that the 00ℓ CTR is rather broad, while the experimental CTR (which has been attenuated by a metal wire in the experiment) is very sharp. This finite-size effect is due to the restricted volume of the sample that was used in

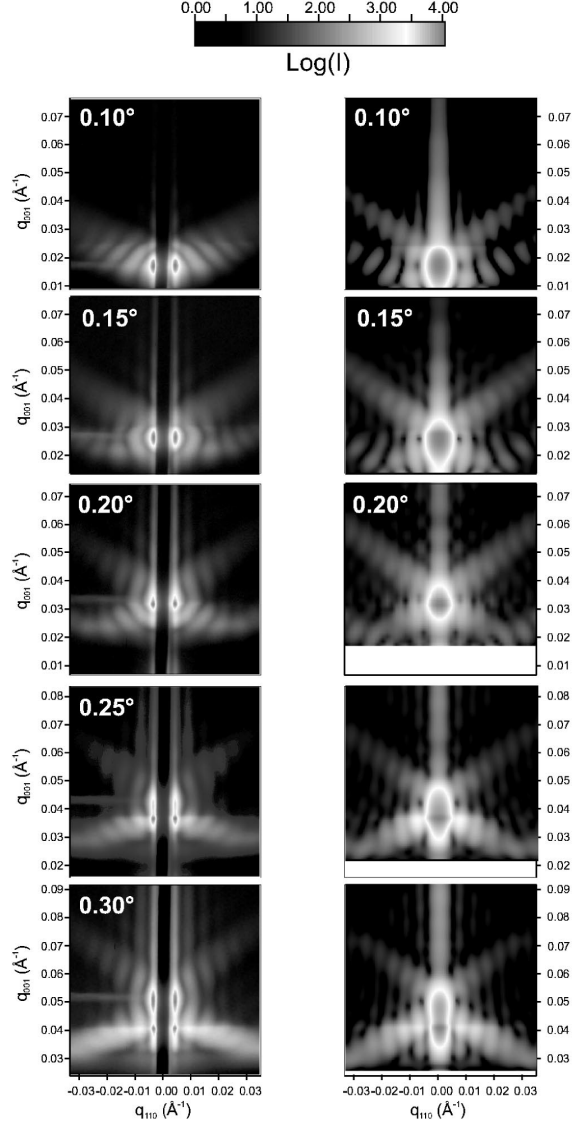


FIG. 5. Experimental measurements (left) and corresponding theoretical simulations (right) of the GISAXS diffuse intensity from SiGe islands ($w=140 \text{ nm}$, $h=70 \text{ nm}$) at different angles of incidence ($\alpha_i=0.1^\circ-0.3^\circ$). The measurements were performed with the use of a CCD detector at $\lambda=1.28 \text{ \AA}$ (critical angle: $\alpha_c=0.18^\circ$). The specular beam and the strong 00ℓ CTR at $q_{110}=0$ were attenuated by a thin metal wire. The simulations were carried out in the framework of the distorted-wave Born approximation Eq. (7) and do not take into account spatial correlation between the islands.

the simulations. In the simulations, the horizontal substrate dimensions were three times the island base width and the vertical dimension was similar to the island height.

(ii) Note that only the diffuse scattering was calculated by the DWBA. Therefore, a sharp specular beam is missing in the simulations.

EFFECTS OF GRAZING INCIDENCE CONDITIONS ON...

PHYSICAL REVIEW B 71, 115324 (2005)

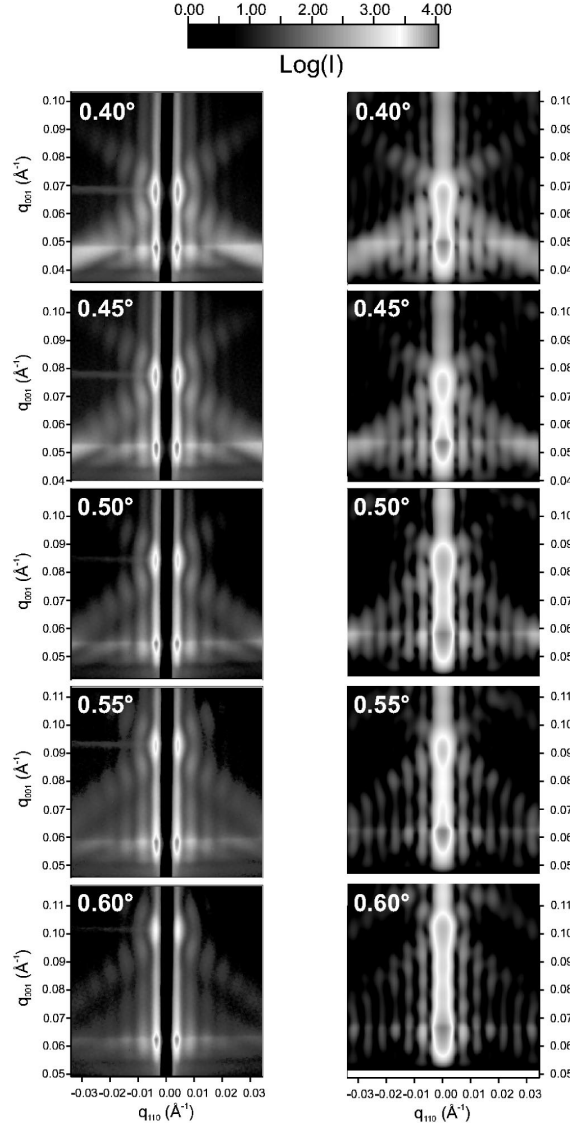


FIG. 6. Experimental measurements (left) and corresponding theoretical simulations (right) of the GISAXS diffuse intensity from SiGe islands ($w=140$ nm, $h=70$ nm) at different angles of incidence of ($\alpha_i=0.4^\circ-0.6^\circ$). The measurements were performed with the use of a CCD detector at $\lambda=1.28$ Å (critical angle: $\alpha_c=0.18^\circ$). The specular beam and the strong 00ℓ CTR at $q_{110}=0$ were attenuated by a thin metal wire. The simulations were carried out in the framework of the distorted-wave Born approximation Eq. (7) and do not take into account spatial correlation between the islands.

(iii) Sharp satellite rods at about $q_{110}=0.003$ Å⁻¹ are visible in the experimental data. These rods are created by spatial correlation between neighboring islands and imply a mean distance along $\langle 110 \rangle$ of about $\langle d_{110} \rangle=210$ nm. Spatial correlation was, however, not considered in the simulations. For more details concerning spatial correlation between adjacent islands, see Refs. 28–30.

(iv) The experimental intensity pattern is, in a sense, washed out as compared to the simulations, which are more rich in detail. This could be induced by a finite island size distribution. However, since the island array is rather dense, effects of multiple refraction and/or scattering could also be responsible. The picture schematically sketched in Fig. 2 represents an idealized case. In reality, the scattered and/or reflected beams have to pass through other, additional islands before they can leave the sample. This may lead to absorption and multiple-refraction effects.

The problems as addressed in the first item can, in principle, be solved by using smaller cell sizes in the numerical calculations and by increasing the sample volume, i.e., the volume of the substrate. However, each of the calculations as shown here requires ~ 6 h of computing time for a Pentium IV processor with a clock frequency of 1 GHz. Using half the cell size and double the substrate dimensions would lead to unfeasible computing times on the order of several hundreds of hours.

The last item is still under investigation. Recent experiments with samples with a lower island area coverage have not substantially changed the results as shown in Figs. 5 and 6.

B. Grazing incidence diffraction

Let us first focus on experimental data on the in-plane diffuse intensity in the vicinity of the 220 reciprocal lattice point, which has been recorded at incidence angles close to the critical angle of total external reflection. The experimental intensity pattern displayed in Fig. 7(a) looks very complicated and is indeed determined by a complex interplay between shape, size, and strain field inside and in the proximity of the SiGe island. In the radial direction, i.e., in the direction along the scattering vector, three strong peaks can be observed at about $q_{\text{radial}}=3.259$ Å⁻¹, 3.247 Å⁻¹, and 3.239 Å⁻¹. These are related to horizontally dilated areas inside the island. At decreasing values of q_{radial} increasing horizontal strain is probed. As can be seen in Fig. 3 the horizontal strain component ε_{xx} is a strictly monotonic function of the height z inside the island. Therefore, the diffuse scattering at low values of q_{radial} can be related to regions close to the top of the island, whereas at high values of q_{radial} scattering from the base of the island is found. This is also substantiated by the pronounced fringes that are generated by the finite horizontal size of the island. At low values of q_{radial} , the distance between the fringes is large, thus implying a small horizontal extension in real space, i.e., the top of the island is probed. In contrast, the distance between the fringes decreases on going to larger values of q_{radial} , thus, implying a large horizontal extension in real space. The corresponding areas are located at the island base.

It is interesting to distinguish between the scattering signal from the island itself and the signal originating from diffuse scattering inside the underlying substrate. It has been pointed out that scattering from free-standing islands requires the consideration of two waves (the incident and specularly reflected waves), whereas all four waves that are present inside the crystal are necessary to treat diffuse scat-

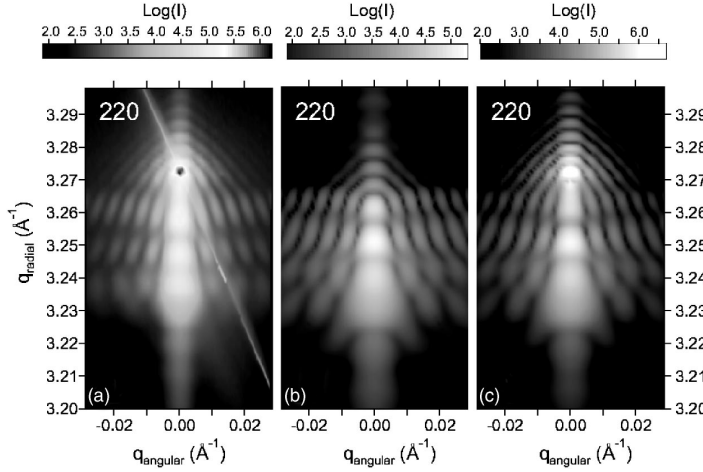


FIG. 7. Diffuse intensity in the vicinity of the 220 in-plane reciprocal lattice point: (a) experiment, (b) simulation (island only), (c) simulation (island and substrate). The angle of incidence $\alpha_i = 0.25^\circ$ was chosen to be slightly above the critical angle of total external reflection (for Si, $\alpha_c = 0.22^\circ$ at $\lambda = 1.542 \text{ \AA}$). The simulations were based on the DWBA and used the island model as shown in Fig. 3. The simulated intensity was integrated vertically over $\Delta q_z = 0.02 \text{ \AA}^{-1}$.

tering from the substrate. As can be seen in Figs. 7(b) and 7(c), the diffuse intensities from island and substrate are almost separated in reciprocal space. At low values of q_{radial} the scattering signal arises from strained areas inside the island, whereas the diffuse intensity from the substrate is mainly concentrated at values around $q_{\text{radial}} = 3.272 \text{ \AA}^{-1}$. Note that the frequencies of the fringe pattern at large values of q_{radial} are different for the different calculations. The fringes are determined not by the actual horizontal size of the island but by the lateral extension of the strain field inside the substrate. This fact should enable future investigation of the strain field that is penetrating from the island into the underlying substrate.

Although the lateral strain tensor component ε_{xx} is a smooth function of z , three distinct peaks are seen in the diffuse scattering along q_{radial} . The origin of these peaks is a phase effect and can be explained simply. Let us first restrict ourselves to the direct scattering channel, which is dominant at high angles of incidence. On the basis of Eq. (3), the exponential function has maxima when the Bragg condition is locally fulfilled in-plane and the local horizontal atomic period can be evaluated accordingly. On the other hand, the exponential function gives additional maxima for $q_{\perp} = q_z = q_{001} = 2\pi(n/z)$, where n is an integer value and z the height inside the island. For reasons of simplicity, a linear increase of the lateral lattice spacings with increasing values of z [Fig. 8(a)] is assumed. This is certainly a rather coarse approximation, since the lateral strain tensor component ε_{xx} is not a linear function of z . Moreover, ε_{xx} does not depend on z only, but also depends on x and y (see Fig. 3). However, the smooth, monotonic behavior of ε_{xx} as a function of z may justify the linear approximation. For a 220 reflection the positions $(q_z, q_{\text{radial}}) = (q_{001}, q_{110})$ of the maxima in reciprocal space are then given by

$$q_{001} = \frac{2\pi n(a_{\parallel}^{\text{top}} - a_{\parallel}^{\text{bot}})}{h} \left[\frac{2\pi\sqrt{8}}{q_{110}} - a_{\parallel}^{\text{bot}} \right]^{-1}. \quad (10)$$

The quantities $a_{\parallel}^{\text{top}}$ and $a_{\parallel}^{\text{bot}}$ are the horizontal lattice spacings at the top and the bottom of the island, respectively, and h is

the island height. Since the island is grown coherently on the substrate, $a_{\parallel}^{\text{bot}}$ is identical to the Si lattice parameter.

The expression given in Eq. (10) is displayed in Fig. 8(b). From this figure, it is clear that the number of maxima along q_{110} that are visible in x-ray diffuse scattering increases with increasing q_{001} . The maxima—at a given value of q_{001} —are equidistantly spaced with respect to q_{110} . [From Eq. (10) the spacings of the maxima are constant for $\varepsilon_{\parallel}^{\text{max}} := (a_{\parallel}^{\text{top}} - a_{\parallel}^{\text{bot}})/a_{\parallel}^{\text{bot}} \ll q_{001}(2\pi/h)$.] This is a direct consequence of the linearly increasing horizontal strain inside the island depicted in Fig. 8(a). Any deviation from this linear law should thus lead to nonequidistantly spaced maxima positions. Indeed, the complex strain tensor field inside a three-dimensional island does not justify the assumption of a linear increase. This can be seen in Fig. 3. Therefore, the diffuse scattering

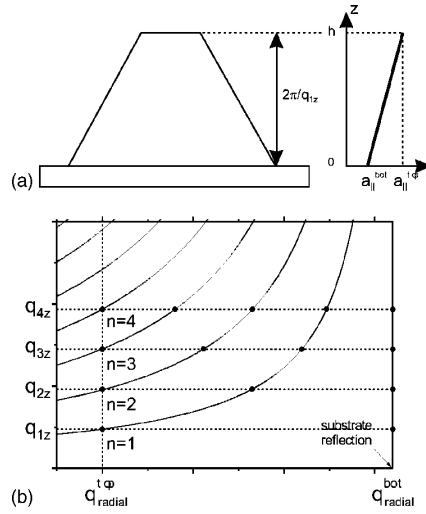


FIG. 8. Effect of (a) a linear increase of the horizontal lattice parameter a_{\parallel} with z on (b) the positions (q_{radial}, q_z) of the maxima in reciprocal space. The lines are given by Eq. (10). The substrate reflection appears at $q_{\text{radial}} = 2\pi/8/a_{\parallel}^{\text{bot}}$. The dots indicate the maximum intensity at fixed values of q_z .

EFFECTS OF GRAZING INCIDENCE CONDITIONS ON...

PHYSICAL REVIEW B 71, 115324 (2005)

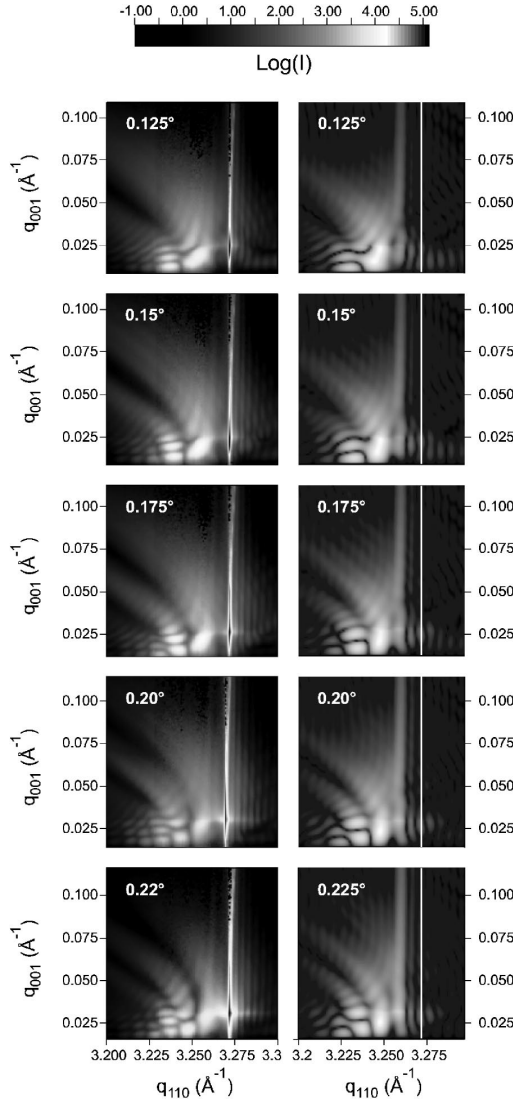


FIG. 9. Experimental measurements (left) and corresponding theoretical simulations (right) of the diffuse intensity (GID, 220) of SiGe islands at different angles of incidence ($\alpha_i=0.125^\circ-0.225^\circ$). The scattering plane contains the $\langle 110 \rangle$ direction. The simulations were carried out in the framework of the distorted-wave Born approximation. They contain the scattering signal from the island only and use the island model as shown in Fig. 3. The positions of the substrate peak and CTR are marked by vertical white lines.

from a free-standing island should show a somehow different behavior for the peak positions from the simple formula given in Eq. (10).

In Figs. 9 and 10 experimental and simulated x-ray diffuse scattering maps in the $q_{110}-q_{001}$ plane are shown. Note that, in the simulations, only the scattering from the island itself is depicted and diffuse scattering from the substrate has been omitted. The data set shows a pronounced influence of α_i on the diffuse intensity pattern. Let us first discuss large

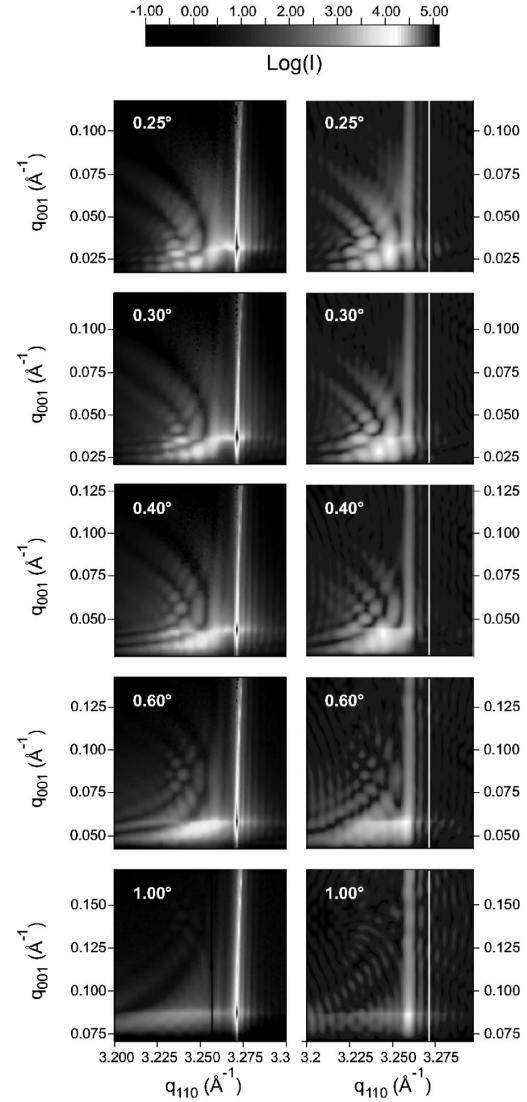


FIG. 10. Experimental measurements (left) and corresponding theoretical simulations (right) of the diffuse intensity (GID, 220) of SiGe islands at different angles of incidence ($\alpha_i=0.25^\circ-1.00^\circ$). The scattering plane contains the $\langle 110 \rangle$ direction. The simulations were carried out in the framework of the distorted-wave Born approximation. They contain the scattering signal from the island only and use the island model shown in Fig. 3. The positions of the substrate peak and CTR are marked by vertical white lines.

angles of incidence, e.g., $\alpha_i=0.60^\circ$. In both the experimental data and the simulations, the shape of diffuse intensity is similar to the iso-intensity lines sketched in Fig. 8, proving the qualitative correctness of the simple model described as given by Eq. (10). At large angles α_i the corresponding q_{001} values are large, and according to Fig. 8(b) narrow peaks along q_{110} appear. These are visible in the simulation, but cannot be resolved further in the experiment.

SCHMIDBAUER *et al.*

For decreasing values of α_i the peaks along q_{110} shift outward until only two peaks are present at $\alpha_i=0.125^\circ$. In addition CTRs of the island $\{111\}$ facets become strong, leading to a characteristic tail that is inclined by about 55° with respect to the q_{001} axis. Moreover, at smaller angles of incidence, not only direct scattering from the island but also all other scattering channels become important. This leads to additional structure in the diffuse scattering. The entire pattern of x-ray diffuse scattering now becomes very complicated and cannot be interpreted by a simple picture. However, there is very good agreement between the experiment and the theoretical simulations in Figs. 9 and 10, which proves the excellent quality of the DWBA for describing the actual scattering scenario for free-standing islands.

The calculations presented in Figs. 7, 9, and 10 are based on the nine-channel scattering approach as given by Eqs. (3) and (4). As can be seen in Figs. 7(b) and 7(c), the diffuse intensities from island and substrate are almost separated in reciprocal space. Therefore, one might expect that the restriction to only four scattering channels yields a very similar diffuse intensity pattern. In Figs. 11(a) and 11(b) calculations performed in the framework of the four-channel and nine-channel approach, respectively, are compared. Here we restrict ourselves to scattering from the free-standing islands only. Qualitatively, all features of diffuse scattering that are related to the islands are visible in both figures. However, distinct differences are still observed, and the nine-channel approach yields much better agreement with the corresponding experimental data [Fig. 11(c)].

V. CONCLUSIONS

In summary, we have investigated the x-ray diffuse scattering (GISAXS, GID) from free-standing LPE grown SiGe islands under conditions of grazing incidence. In both, GISAXS and GID, a complicated fine structure is observed in the diffuse intensity pattern. For GID a semiquantitative approach could explain the particular influence of the island size and lateral strain on the formation of the diffraction pattern. However, a more detailed, quantitative analysis requires the use of theoretical simulations. In particular, we investigated the dependence of the diffuse intensity pattern as a function of the incidence angle α_i . For that purpose, x-ray scattering simulations were carried out in the framework of the distorted-wave Born approximation, and excellent agreement is found with experiment. Comparison with experiment allows for obtaining valuable information about island size, shape, and Ge content within the island.

For GID, the validity of the (“kinematical”) four-channel approach versus the (“dynamical”) nine-channel approach was discussed. In the present case of strongly strained free-standing islands where the corresponding substrate and island reflections are clearly separated in reciprocal space, the simple kinematical approach seems to be almost sufficient. However, still much better agreement with experiment is achieved by applying the nine-channel approach. On the

PHYSICAL REVIEW B 71, 115324 (2005)

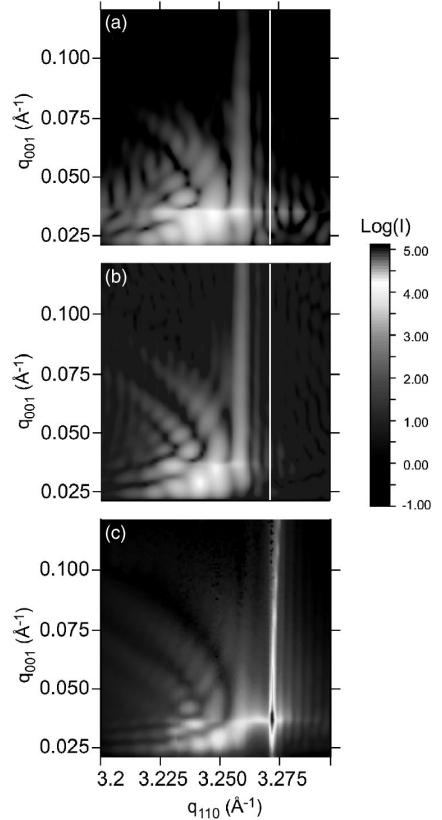


FIG. 11. Theoretical simulations (GID, 220, $\alpha_i=0.30^\circ$) of SiGe islands based on the (a) four-channel and (b) nine-channel DWBA along with (c) corresponding experimental intensity distribution. The calculations contain the scattering signal from the island only and they use the island model shown in Fig. 3. The positions of the substrate peak and CTR are marked by vertical white lines.

other hand, our intention was to create a flexible DWBA program that is able to cover not only the present rather specific case of grazing incidence diffraction from free-standing islands, but more critical cases of disturbances located in the crystal volume as well. The recursive matrix formalism permits us to derive correct values of amplitudes in the vicinity of a strong reflection, what is obviously important if island and substrate are close by their lattice periods.

ACKNOWLEDGMENTS

We are thankful to H. Wawra (Institut für Kristallzüchtung, Berlin) for providing us with the SiGe sample. We gratefully acknowledge technical support by G. Vaughan, B. Struth, and O. Konovalev (ESRF). This work was supported by “Deutsche Forschungsgemeinschaft” within the framework of Sfb 296.

EFFECTS OF GRAZING INCIDENCE CONDITIONS ON...

PHYSICAL REVIEW B **71**, 115324 (2005)

- *Present address: Fachbereich Physik, Martin-Luther-Universität Halle-Wittenberg, Hoher Weg 8, D-06120 Halle/Saale, Germany.
- ¹D. Bimberg, M. Grundmann, and N. N. Ledentsov, *Quantum Dot Heterostructures* (Wiley, Chichester, NY, 1999).
- ²V. Shchukin, N. N. Ledentsov, and D. Bimberg, *Epitaxy of Nanostructures, Nanoscience and Technology* (Springer, Berlin, 2003).
- ³I. Stranski and L. Krastanow, Sitzungsber. Akad. Wiss. Wien, Math.-Naturwiss. Kl., Abt. 2B **146**, 797 (1937).
- ⁴M. Schmidbauer, *X-Ray Diffuse Scattering from Self-Organized Mesoscopic Semiconductor Structures*, Springer Tracts in Modern Physics Vol. 199 (Springer, Berlin, 2004).
- ⁵J. R. Levine, J. B. Cohen, Y. W. Chung, and P. Georgopoulos, *J. Appl. Crystallogr.* **22**, 528 (1989).
- ⁶M. Schmidbauer, T. Wiebach, H. Raidt, M. Hanke, R. Köhler, and H. Wawra, *Phys. Rev. B* **58**, 10 523 (1998).
- ⁷V. Holý, A. A. Darhuber, J. Stangl, S. Zerlauth, F. Schäffler, G. Bauer, N. Darowski, D. Lübbert, U. Pietsch, and I. Vávra, *Phys. Rev. B* **58**, 7934 (1998).
- ⁸I. Kegel, T. H. Metzger, J. Peisl, P. Schittenhelm, and G. Abstreiter, *Appl. Phys. Lett.* **74**, 2978 (1999).
- ⁹I. Kegel, T. H. Metzger, A. Lorke, J. Peisl, J. Stangl, G. Bauer, J. M. Garcia, and P. M. Petroff, *Phys. Rev. Lett.* **85**, 1694 (2000).
- ¹⁰M. Rauscher, R. Paniago, H. Metzger, Z. Kovats, J. Domke, J. Peisl, H.-D. Pfannes, J. Schulze, and I. Eisele, *J. Appl. Phys.* **86**, 6763 (1999).
- ¹¹I. Kegel, T. H. Metzger, A. Lorke, J. Peisl, J. Stangl, G. Bauer, K. Nordlund, W. V. Schoenfeld, and P. M. Petroff, *Phys. Rev. B* **63**, 035318 (2001).
- ¹²Z. Zhong, O. Ambacher, A. Link, V. Holý, J. Stangl, R. T. Lechner, T. Roch, and G. Bauer, *Appl. Phys. Lett.* **80**, 3521 (2002).
- ¹³V. M. Kaganer, S. A. Stepanov, and R. Köhler, *Phys. Rev. B* **52**, 16 369 (1995).
- ¹⁴D. Grigoriev, M. Hanke, M. Schmidbauer, P. Schäfer, O. Konov, alov, and R. Köhler, *J. Phys. D* **36**, A225 (2003).
- ¹⁵U. Pietsch, V. Holý, and T. Baumbach, *High Resolution X-Ray Scattering from Thin Films and Multilayers*, Advanced Texts in Physics (Springer, Berlin, 2004).
- ¹⁶T. Jach, P. L. Cowan, S. Qun, and M. J. Bedzyk, *Phys. Rev. B* **39**, 5739 (1989).
- ¹⁷A. M. Afanasyev and M. K. Melkoyan, *Acta Crystallogr., Sect. A: Found. Crystallogr.* **39**, 207 (1983).
- ¹⁸S. A. Stepanov and R. Köhler, *J. Appl. Phys.* **76**, 7809 (1994).
- ¹⁹S. Christiansen, M. Albrecht, H. P. Strunk, and H. J. Maier, *Appl. Phys. Lett.* **64**, 3617 (1994).
- ²⁰T. Wiebach, M. Schmidbauer, M. Hanke, H. Raidt, R. Köhler, and H. Wawra, *Phys. Rev. B* **61**, 5571 (2000).
- ²¹T. Benabbas, P. Francios, Y. Androussi, and A. Lefebvre, *J. Appl. Phys.* **80**, 2763 (1996).
- ²²M. Grundmann, O. Stier, and D. Bimberg, *Phys. Rev. B* **52**, 11 969 (1995).
- ²³M. Hanke, M. Schmidbauer, D. Grigoriev, H. Raidt, P. Schäfer, R. Köhler, A.-K. Gerlitzke, and H. Wawra, *Phys. Rev. B* **69**, 075317 (2004).
- ²⁴I. Kegel, T. H. Metzger, P. Fratzl, J. Peisl, A. Lorke, J. M. Garcia, and P. M. Petroff, *Europhys. Lett.* **45**, 222 (1999).
- ²⁵E. Bauser, *Crystal Growth of Electronic Materials* (Elsevier, New York, 1985), p. 41.
- ²⁶M. Hanke, M. Schmidbauer, R. Köhler, F. Syrowatka, A. K. Gerlitzke, and T. Boeck, *Appl. Phys. Lett.* **84**, 5228 (2004).
- ²⁷W. Dorsch, H. P. Strunk, H. Wawra, G. Wagner, J. Groenen, and R. Carles, *Appl. Phys. Lett.* **72**, 179 (1998).
- ²⁸M. Hanke, H. Raidt, R. Köhler, and H. Wawra, *Appl. Phys. Lett.* **83**, 4927 (2003).
- ²⁹M. Meixner, E. Schöll, M. Schmidbauer, H. Raidt, and R. Köhler, *Phys. Rev. B* **64**, 245307 (2001).
- ³⁰M. Schmidbauer, M. Hanke, and R. Köhler, *Phys. Rev. B* **71**, 115323 (2005).

2.5.3 Geometrisches Aspektverhältnis

M. Hanke, M. Schmidbauer, D. Grigoriev, R. Köhler

Aspect ratio of LPE-SiGe/Si(001) islands as probed by high resolution x-ray diffraction
Jour. Appl. Phys. **96**, 1447 (2004).

Im Fall der Flüssigphasenepitaxie bestimmt sich die finale Form von Stranski-Krastanow Inseln im Wesentlichen durch eine Balance zwischen Energiegewinn aus elastischer Relaxation und einer daraus resultierenden vergrößerten Oberflächenenergie. Eine numerische Betrachtung führt unter der Annahme isotroper Oberflächenenergien für SiGe/Si(001) zu {111} facettierte Pyramidenstümpfen mit (001) Deckfacette und einem geometrischen Aspektverhältnis Inselbasis versus -höhe von etwa 2, siehe Kap. 2.1. Inwieweit nun das Aspektverhältnis (bei ansonsten unveränderten weiteren Parametern) die diffuse Streuung beeinflusst, wird im vorliegenden Kapitel besprochen.

Dazu wurde die diffuse Streuung in der Umgebung des asymmetrischen (404) Reflexes hochauflöst vermessen. In der Intensitätsverteilung lassen sich tetragonale und kubische Gitteranteile und damit Bereiche am Inselboden von denen im Apex unterscheiden. Entsprechende Simulationen der diffusen Streuung auf Basis unterschiedlicher Aspektverhältnisse zeigen zudem, dass auch über sehr große Probenbereiche die Inseln in der in Kap. 2.1 gefundenen Gleichgewichtsform vorliegen.

Aspect ratio of liquid phase epitaxial SiGe/Si(001) islands as probed by high resolution x-ray diffraction

M. Hanke^{a)}

Fachbereich Physik, Martin-Luther-Universität Halle-Wittenberg, Hoher Weg 8, D-06120 Halle/Saale, Germany

M. Schmidbauer, D. Grigoriev, and R. Köhler

Institut für Physik, Humboldt-Universität zu Berlin, Newtonstraße 15, D-12489 Berlin, Germany

(Received 25 March 2004; accepted 27 April 2004)

X-ray diffuse scattering is used to probe size, shape, and strain distribution of self-organized SiGe/Si(001) islands, which were grown by liquid phase epitaxy. The SiGe islands show a truncated pyramidal shape with {111} side facets and a (001) top facet and they are highly uniform in size. With an averaged island base width of 130 nm and a corresponding height of 65 nm all the islands have a characteristic geometrical *base-to-height* aspect ratio of about 2. X-ray diffuse scattering is used to locally probe the elastically relaxed regions inside the island apex and the strongly strained regions near the substrate-island interface. It is found that the geometrical aspect ratio has a large impact on the x-ray diffuse intensity pattern in reciprocal space. By performing corresponding kinematical x-ray simulations this fact can be utilized to determine the aspect ratio with high sensitivity. © 2004 American Institute of Physics. [DOI: 10.1063/1.1763994]

I. INTRODUCTION

Owing to their exceptional physical properties low-dimensional semiconductor structures (e.g., quantum dots) have attracted considerable interest. While *top-bottom* approaches to generate quantum dots mostly rely on highly sophisticated masking and etching techniques, both self-formation and spatial orientation during heteroepitaxy can provide an interesting alternative. On the other hand, heteroepitaxial growth exhibits a widespread complexity, whose details are not completely understood yet. Therefore, model systems as, e.g., SiGe/Si(001) have been extensively investigated to attain a more comprehensive knowledge of crystal growth (see, e.g., Refs. 1–5).

Heteroepitaxial growth inherently implies the formation of elastic strain owing to the different lattice parameters of the epitaxial layer and the substrate. In the Stranski-Krastanow mode⁶ the growth initially starts by wetting the substrate with a thin planar layer. This process is accompanied by the formation of strain energy, which increases with enhancing layer thickness. When approaching a critical thickness, which amounts to typically a few monolayers, the formation of three-dimensional island growth becomes energetically favorable since the gain in energy due to elastic strain relaxation is larger than the total amount of surface free energy.

For liquid phase epitaxial (LPE) grown SiGe islands the scaling law $w \propto f^{-2.03}$ has been found⁷ which interrelates the island base width w and the lattice mismatch f between island and the underlying substrate. This scaling behavior addresses strain as the key property which restricts the final

island size, and it represents a very useful tool to adjust the island size by choosing an appropriate atomic composition in layer.

During evolution the island shape and strain distribution inside the islands may alter. This is also significantly affected by the specific growth conditions. Pure germanium islands grown by molecular beam epitaxy (MBE) evolve by hut clusters⁸ via pyramids resulting finally in domes.⁹ While MBE grown SiGe islands exhibit {10m}-type facets,^{8,10,11} SiGe islands generated by LPE consist of truncated pyramids with {11m}-type facets.^{12–14} Thus, they are azimuthally 45° off their MBE counterparts. It is interesting to note that for both individual methods the respective growth sequences do not qualitatively depend on the lattice mismatch at a certain concentration window.^{15,16}

Although providing high resolution in real space direct imaging techniques give information on a restricted number of objects only and thus suffer from low statistics. On the other hand, scattering techniques yield information on the basis of large ensembles and thus represent a statistically relevant measure. Among these techniques x-ray diffuse scattering has turned out to be a very powerful tool to investigate mesoscopic and nanoscale semiconductor structures. This includes the determination of shape, size, chemical composition, strain profile, and positional correlation (e.g., Refs. 16–22). In this work we apply high resolution x-ray diffraction combined with corresponding scattering simulations. These are based on kinematical scattering theory and use the strain field within SiGe/Si(001) nanoscale islands as determined by finite element calculations based on linear elasticity theory.¹⁶

II. SAMPLE

Respective samples were grown by liquid phase epitaxy which operates rather close to thermodynamical equilibrium.

^{a)}Present address: National Institute of Standards and Technology, 100 Bureau Drive, Gaithersburg, MD 20899.

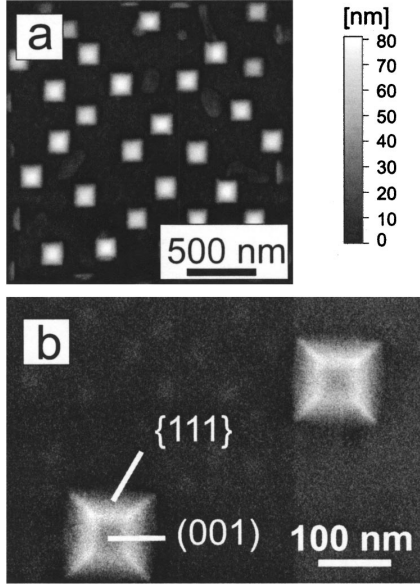


FIG. 1. Atomic force (a) and a scanning electron micrograph (b) of the sample surface. Typically, the islands consist of truncated pyramids with {111}-type side facets and a (001) top facet.

As compared to germanium, silicon is at least two orders of magnitude less soluble within bismuth. Consequently, the bismuth solvent can be saturated with silicon, whereas a germanium mol fraction of 0.0103 within the solution has to be carefully adjusted in order to give 30% germanium in the solid state. To ensure that growth takes place at conditions close to thermodynamical equilibrium a homogenization procedure of several hours at the growth temperature ($600\text{ }^{\circ}\text{C}$) was performed. After an *in situ* desorption of the natural silicon oxide at $930\text{ }^{\circ}\text{C}$ the actual growth temperature was adjusted 2 K below the saturation temperature to initiate the growth process.

Figure 1 represents an atomic force (a) and scanning electron micrograph (b) of the resulting sample surface. Nearly all islands are of uniform shape and size and they consist of truncated pyramids defined by four {111} side facets and a (001) top facet. A geometrical aspect ratio $Q=w/h$ of ≈ 2 is found, where $w=130\text{ nm}$ denotes the island base width along the [110] direction and $h=65\text{ nm}$ is the final island height. This result can be explained by equilibrium shape calculations. Here different ratios Q at fixed {111} side and a (001) top facet have been considered and a local minimum in total energy has been found for $Q=2$ (Ref. 23).

III. EXPERIMENT

In order to determine the island shape and residual strain distribution we have evaluated the diffusely scattered intensity around various reciprocal lattice points. However, we will take particular advantage of asymmetrical reflections, which probe both the horizontal and vertical lattice spacings independently, and thus enable a clear distinction between a

tetragonally distorted lattice and a cubic lattice referring to different areas inside the islands. The scattering experiments were carried out at BW2 station at HASYLAB/DESY applying highly collimated x-rays with an energy of 8 keV and an energy band width of $\Delta E/E=10^{-4}$. A position sensitive detector (PSD) with an inherent resolution of $80\text{ }\mu\text{m}$ was placed 750 mm behind the sample. By utilizing a small x-ray spot at the sample, each channel of the PSD corresponds to a certain scattering angle. Thus, a PSD simultaneously records the diffuse intensity distribution along a (curved) line in reciprocal space, and a 2D reciprocal space map can be recorded by a single rocking scan of the sample. Although the resolution is definitely worse than with a triple crystal arrangement this multidetection setup ensures fast data acquisition at medium resolution of typically $\Delta q=5\times 10^{-4}\text{ \AA}^{-1}$ which is sufficient to detect the rather broad diffuse intensity. Perpendicular to the scattering plane a pair of 1 mm slits is used thus intergrating the x-ray diffuse intensity in reciprocal space within $\Delta q=8\times 10^{-3}\text{ \AA}^{-1}$.

IV. RESULTS AND DISCUSSION

The chemical composition inside the islands, the resulting strain distribution, positional correlation, and the island shape itself contribute in a very complex way to the diffuse scattering, generally preventing a direct access to those parameters. Hence, scattering simulations are an essential part of data evaluation. We have treated the scattering process within the kinematical approximation where the scattered amplitudes sum up coherently without taking into account absorption, extinction, and multiple scattering processes. Consequently, our approach is less useful for treating the scattering from the Si substrate, where multiple scattering processes cannot be neglected. However, kinematical theory is a rather good approximation as long as the structures are comparatively strongly distorted and restricted in size. This holds for the small and strongly strained islands as discussed in this work. For more details concerning the simulations see Ref. 14.

Despite the limits of kinematical theory, one has to take into account the substrate underneath the island and wetting layer in order to correctly calculate the extended strain field in the surrounding areas of the island. The calculation of the three-dimensional strain field was numerically performed in the framework of the finite element method (FEM), which is based on linear elasticity theory and which takes into account both the three dimensional Ge composition profile and the elastic anisotropy. FEM requires some initial information concerning the island shape and size, which can be provided by scanning probe microscopy, see Fig. 1. Then, throughout subsequent iterations of the simulation procedure the impact of various parameters as the Ge composition profile and the island shape/size to the diffuse scattering can be tested and, if necessary, further improved until satisfactory agreement with experiment is achieved.

Figure 2(a) depicts the diffusely scattered intensity around the asymmetrical 404 reciprocal lattice point. The diffuse intensity from the Si substrate is mainly concentrated in a cloud around the coherent substrate peak (marked as

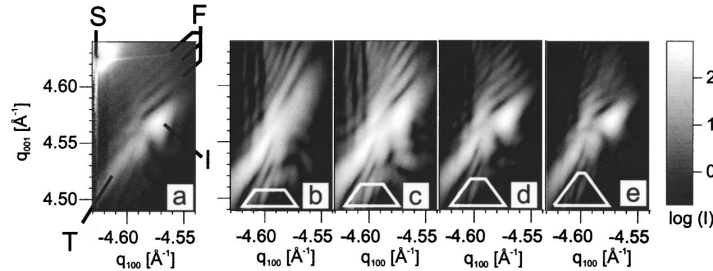


FIG. 2. Diffusely scattered intensity in the proximity of the asymmetric 404 silicon reciprocal lattice point S. (a) experimental data, (b)–(e) corresponding simulations. The intensity cloud I at $-q_{100}=q_{001}=4.57 \text{ \AA}^{-1}$ is related to the scattering at elastically relaxed parts in the island top, whereas the feature T corresponds to strained parts at the island bottom. A set of parallel fringes F appears tilted 45° off the [001] direction. The simulations assume islands of 130 nm base width but with different heights: (b) 39 nm, (c) 52 nm, (d) 65 nm, and (e) 78 nm.

“S”). It can be well distinguished from the diffuse scattering from the SiGe islands which is distributed around a bright maximum (marked as “I”). This feature can be attributed to the island apex consisting of an elastically relaxed lattice of cubic symmetry.²⁰ Additionally, the comparatively broad and weak tail (T) originates from the strongly strained regions close to the island-substrate interface. Here, the horizontal lattice spacings are close to that of the substrate; however, the lattice is vertically elongated.

While there are {111}-type facets present within the [110] zone there are no facets existing in the [100] zone [see Fig. 1(b)]. Nevertheless we find a bundle of parallel fringes (F) in close vicinity of the island peak (I) in Fig. 2(a). They are tilted 45° off the [001] direction. This might be indicative of a mean surface (i.e., facet) of the type {101}. A detailed inspection of the scanning electron micrograph in Fig. 1(b) supposes somewhat coarsened {101} island edges. At comparable islands containing 10% germanium and with a base width of around $w=1500 \text{ nm}$ the {101} edges are found to consist of small {111} facets locally forming a {101} mean surface, see Fig. 4 in Ref. 16. However, as we will demonstrate in this work, the observed fringes are *not created* by {101} surfaces. They are, instead, basically caused by the strain distribution inside the island, which is, nevertheless, sensitive to the island shape.

Figures 2(b)–2(e) show results of simulations of x-ray diffuse intensity patterns that can be compared to the experimental results displayed in Fig. 2(a). The FEM strain calculations were used as input for respective x-ray simulations. In all simulations the islands are composed of four {111} sides and a (001) top facet. The islands have been placed on a silicon substrate with lateral dimensions of twice the island base. While the island height changes from $h=39 \text{ nm}$ (b) via $h=52 \text{ nm}$ (c) and $h=65 \text{ nm}$ (d) finally up to $h=78 \text{ nm}$ (e) the corresponding lateral width of $w=130 \text{ nm}$ at the island bottom was kept fixed, thus resulting in different aspect ratios Q (see the schematic insets). According to previous investigations a steplike vertical germanium profile inside the islands has been assumed.¹⁶ In this case, the composition changes from $\text{Si}_{0.75}\text{Ge}_{0.25}$ at the island bottom towards $\text{Si}_{0.7}\text{Ge}_{0.3}$ at $h=22 \text{ nm}$ (b-d) and 26 nm (e). However, the interface width is defined within an accuracy of about 4 nm accounting for a

calculation grid with a lattice parameter four times larger than that of silicon and considering the interface by at least one node on both sides.

Since scattering from the silicon substrate has been completely omitted in the simulations there is no contribution of scattering from a pure silicon lattice. However, the simulations prove a significant impact of the island aspect ratio Q on the diffuse intensity distribution: Most obviously, the inclination angle of the fringes with respect to the [001] direction monotonically decreases from about 60° (b) via 54°(c) to 45° (d) meeting the experimental value. When the island height approaches 78 nm (e) the fringe pattern is even partly washed out. Although all angles defined by adjacent facets are kept fixed for different aspect ratios Q , it is generally not possible to address this observation exclusively to a shape phenomenon since an altered aspect ratio correspondingly modifies the strain field inside the island. In fact, the intensity distribution as shown in Fig. 2 is determined by a complex interplay of both the island shape and size and the strain distribution inside the island. On the other hand feature (I) appears more and more pronounced on decreasing the aspect ratio Q . This clearly proves that islands with small aspect ratio Q —and therein regions close to the apex—can relax more efficiently than shallow islands. For the simulations (d, e) using $h=65 \text{ nm}$ and 78 nm the intense spot I is in good agreement with experiment indicating a cubic, nearly perfectly relaxed lattice at the island top, which is also evident in the FEM strain calculations (not shown here). Consequently, an increasing island height does not further modify feature I. Finally, the tail-like diffuse intensity pattern (T), which horizontally appears close to the substrate position, indicates a tetragonally distorted lattice close to the substrate-island interface. Thus, its particular shape and position in reciprocal space does not depend on the island aspect ratio Q . The simulation (d)—referring to an island height of 65 nm and corresponding aspect ratio of $Q=2$ —clearly gives the best agreement with the experimental data. This result is confirmed by scanning electron micrographs, see Fig. 1(b). However, it provides a statistically relevant quantity since the x-ray scattering experiment averages over an ensemble of $\approx 3 \times 10^7$ islands taking an island density of $3 \times 10^9 \text{ cm}^{-2}$ and an illuminated sample area of 1 mm^2 into account.

V. CONCLUSION

In conclusion, we investigated LPE grown $\text{Si}_{0.7}\text{Ge}_{0.3}/\text{Si}(001)$ nanoscale islands. Scanning probe micrographs indicate islands of uniform shape forming truncated pyramids with $\{111\}$ side facets and a (001) top facet. The island ensemble exhibits a very narrow size distribution with an averaged island base width of $w=130$ nm and an island height of $h=65$ nm, resulting in a geometrical aspect ratio base vs height of 2. The SiGe islands were investigated by x-ray diffuse scattering. Experimental diffuse intensity distributions were compared to corresponding kinematical scattering simulations. These simulations use the strain field as calculated by the finite element method. The diffuse scattered intensity in the vicinity of the asymmetrical Si 404 reflection indicates a fully relaxed lattice in the island top. The scattering simulations show that the island aspect ratio significantly influences the scattering pattern. This, finally, enabled us to determine very accurately the island shape.

ACKNOWLEDGMENTS

We wish to thank H. Wawra (Institut für Kristallzüchtung, Berlin) for sample growth and U. Jahn, (Paul-Drude-Institut, Berlin) for the scanning electron micrograph. The valuable help of P. Schäfer and W. Drube (HASYLAB, Hamburg) during experiment is gratefully acknowledged. This work was financially supported by the Deutsche Forschungsgemeinschaft under Contract No. KO1510/2 and the Sonderforschungsbereich 296.

¹P. Sutter and M. G. Lagally, Phys. Rev. Lett. **84**, 4637 (2000).

²V. B. Shenoy, C. V. Ciobanu, and L. B. Freund, Appl. Phys. Lett. **81**, 304

- (2002).
³P. Sutter, P. Zahl, and E. Sutter, Appl. Phys. Lett. **82**, 3454 (2003).
⁴J. Tersoff, B. Spencer A. Rastelli, and H. von Känel, Phys. Rev. Lett. **89**, 196104 (2002).
⁵R. Tromp, F. M. Ross, and M. Reuter Phys. Rev. Lett. **84**, 4641 (2000).
⁶I. N. Stranski and L. Krastanow, Sitzungsberichte d. Akademie d. Wissenschaften in Wien, Abt. III, 146, 797 (1937).
⁷W. Dorsch, H. P. Strunk, H. Wawra, G. Wagner, J. Groenen, and R. Carles, Appl. Phys. Lett. **72**, 179 (1998).
⁸Y.-W. Mo, D. E. Savage, B. S. Swartzentruber, and M. G. Lagally, Phys. Rev. Lett. **65**, 1020 (1990).
⁹F. M. Ross, M. C. Reuter, and R. M. Tromp, Science **286**, 193 (1999).
¹⁰M. Kästner and B. Voigtländer, Phys. Rev. Lett. **82**, 2745 (1999).
¹¹A. Rastelli, H. von Känel, B. J. Spencer, and J. Tersoff, Phys. Rev. B **68**, 115301 (2003).
¹²J. Groenen, R. Carles, S. Christiansen, M. Albrecht, W. Dorsch, H. P. Strunk, H. Wawra, and G. Wagner, Appl. Phys. Lett. **71**, 3856 (1997).
¹³M. Schmidbauer, T. Wiebach, H. Raidt, M. Hanke, R. Köhler, and H. Wawra, Phys. Rev. B **58**, 10523 (1998).
¹⁴M. Schmidbauer, M. Hanke, and R. Köhler, Cryst. Res. Technol. **37**, 3 (2002).
¹⁵J. Floro, G. Lucadamo, E. Chason, L. Freund, M. Sinclair, R. Twesten, and R. Hwang, Phys. Rev. Lett. **80**, 4717 (1998).
¹⁶M. Hanke, M. Schmidbauer, D. Grigoriev, P. Schäfer, R. Köhler, A.-K. Gerlitzke, and H. Wawra, Phys. Rev. B **69**, 075317 (2004).
¹⁷R. Lechner, T. Schülli, V. Holý, G. Springholz, J. Stangl, A. Raab, G. Bauer, and T. Metzger, Appl. Phys. Lett. **84**, 885 (2004).
¹⁸T. Schülli, J. Stangl, Z. Zhong, R. Lechner, M. Sztucki, T. Metzger, and G. Bauer, Phys. Rev. Lett. **90**, 066105 (2003).
¹⁹I. Kegel, T. H. Metzger, A. Lorke, J. Peisl, J. Stangl, G. Bauer, J. M. Garcia, and P. M. Petroff, Phys. Rev. Lett. **85**, 1694 (2000).
²⁰T. Wiebach, M. Schmidbauer, M. Hanke, H. Raidt, R. Köhler, and H. Wawra, Phys. Rev. B **61**, 5571 (2000).
²¹J. Stangl *et al.*, Appl. Phys. Lett. **79**, 1474 (2001).
²²M. Schmidbauer, *X-Ray Diffuse Scattering From Self-Organized Mesoscopic Semiconductor Systems*, Springer Tracts in Modern Physics, Vol. 199 (Springer, Berlin, 2004).
²³M. Hanke, M. Schmidbauer, R. Köhler, F. Syrowatka, A. K. Gerlitzke, and T. Boeck, Appl. Phys. Lett. **84**, 5228 (2004).

2.5.4 Untersuchung lateraler Positions korrelation mit Strahlung finiter Kohärenzlänge

M. Hanke, M. Schmidbauer, R. Köhler

Lateral correlation of SiGe Stranski-Krastanow islands on silicon as probed by high resolution x-ray diffraction

Jour. Appl. Phys. **96**, 1959 (2004).

Die in den zurückliegenden Kapiteln zur Strukturanalytik mittels diffuser Röntgenstreuung gemachten Ausführungen basieren ausnahmslos auf der (für die verwendeten Proben durchaus gerechtfertigten) Annahme homogener Inselensembles. Dabei erstreckt sich die Uniformität nicht nur auf die Form sondern auch auf die chemische Komposition innerhalb der Inseln. Aus diesem Grund kann man (abgesehen von den Beiträgen zur diffusen Streuung durch die Positions korrelation) in den meisten Fällen bei den Streusimulationen von einer einzigen Insel ausgehen.

Mit der Annahme nur eines Insel types lässt sich das anschaulich leicht verstehen. Ein solch geartetes Ensemble Ω kann im Ortsraum als Faltung einer Positions funktion, die den Ort der einzelnen Inseln enthält, mit einer Inselformfunktion aufgefasst werden. Misst man die diffuse Streuung, so entspricht diese im Wesentlichen der Fouriertransformierten von Ω , die sich infolge des Faltungstheorems im reziproken Raum aber gerade als einfaches Produkt der Streuung an einer einzelnen Insel und einer Korrelationsfunktion darstellt. Somit lassen sich die Streubeiträge einer einzelnen Insel gut (multiplikativ) von solchen aus Positions korrelation separieren.

Hier soll untersucht werden, inwieweit sich unter Berücksichtigung einer endlichen Kohärenzlänge die Insel-Insel-Korrelation in den Streuprozess integrieren lässt. Ausgehend von einem idealen, kaum realistischen Grenzfall eines vollständig kohärenten Szenarios werden noch zwei weitere Modelle diskutiert. Die Berücksichtigung einer finiten Kohärenzlänge erweist sich als essentiell, jedoch gelingt eine realistische Beschreibung nur in einem zweistufigen Streuprozess. In diesem werden zunächst auf Längenskalen kleiner der Kohärenzlänge die Streuamplituden (unter vollständiger Berücksichtigung der Phase) kohärent summiert. Andererseits geht auf größeren Längenskalen die Phaseninformation generell verloren, so dass hier die Summation rein inkohärent erfolgt.

Lateral correlation of SiGe Stranski-Krastanow islands on silicon as probed by high resolution x-ray diffraction

M. Hanke,^{a)} M. Schmidbauer, and R. Köhler

Institut für Physik, Humboldt-Universität zu Berlin, Newtonstraße 15, D-12489 Berlin, Germany

(Received 20 January 2004; accepted 23 May 2004)

We describe a procedure to consider the impact of lateral positional correlation of SiGe nanoscale islands onto the diffuse scattering within a high resolution x-ray diffraction experiment. The samples have been grown by means of liquid phase epitaxy which provides monodisperse island ensembles containing up to 10^9 equivalent objects. It is shown that a proper numerical simulation of the x-ray diffuse scattering pattern requires careful consideration of the partial coherence of x rays. An appropriate numerical procedure consists of coherent summation over sample areas with lateral dimensions as given by the coherence properties of the radiation and subsequent incoherent summation over a large enough number of such areas. For the given case an effective lateral coherence length of $\approx 1 \mu\text{m}$ has been used, which is derived taking into account also the detector resolution. The according simulation is in good agreement with the experimentally observed x-ray diffuse intensity pattern. © 2004 American Institute of Physics. [DOI: 10.1063/1.1772883]

I. INTRODUCTION

Low-dimensional structures, as, e.g., quantum dots (QDs) have attracted an overwhelming interest during the last years.¹ Many dedicated device applications require highly uniform ensembles of such structures. Thus, different routes towards perfectly ordered nanoscale objects have been employed. Self-organization during crystal growth via the so-called Stranski-Krastanow growth mode is one of the most promising approaches. Here, the elastic energy present at heteroepitaxial strained layer growth is decreased by the formation of nanoscale islands allowing for elastic strain relaxation. This process is often accompanied by lateral,^{2,3} vertical,⁴ or even three-dimensional⁵ positional correlation.

Structural investigations of QDs usually start with direct imaging techniques such as scanning electron microscopy, atomic force microscopy and transmission electron microscopy. Those are excellent analytical tools to study shape, size and in case of TEM even chemical composition profiles of usually a few individual objects.⁶ To a limited extent they can also provide information regarding positional correlation. However, while the mentioned imaging techniques excel in a high spatial resolution, they usually probe small ensembles as compared to x-ray scattering techniques as grazing incidence small angle x-ray scattering (GISAXS), grazing incidence diffraction (GID), and high resolution x-ray diffraction (HRXRD). GISAXS does not provide any information about the strain state, however, in a QD it can be applied to exclusively probe shape, size, and positional correlation.^{7,8} Compared to that HRXRD and GID additionally probe small lattice distortions which—in combination with scattering simulations—makes a three-dimensional determination of strain and chemical composition feasible, e.g., Refs. 9–11. Generally the diffusely scattered intensity is af-

fected by both vertical *and* lateral positional correlation. Consequently the cited x-ray scattering techniques contain information on positional correlation in both spatial directions.^{12–17} Recently a very promising attempt employs anomalous x-ray scattering to enhance the chemical contrast of buried quantum dots in order to investigate ordering properties.¹⁸ Usually theoretical approaches either restrict themselves to the completely coherent case [see Eq. (1) below] or additionally indicate averaging. In the latter case averaging is then often implicitly part of an analytical correlation function, see, e.g., Ref. 13.

II. SAMPLE

Here we will demonstrate the influence of the partial coherence of the applied radiation on x-ray diffuse scattering. For that purpose we have utilized SiGe islands on Si(100), which serve as a model system with an outstanding degree of conformity in terms of island size, shape, and orientation. The respective samples have been grown by means of liquid phase epitaxy, which operates comparatively close to the thermodynamical equilibrium providing highly monodisperse ensembles, which contain only a single type of dislocation-free nanoscale islands. Almost all of them are made of truncated pyramids with {111} side facets and an (001) top facet. Atomic force microscopy of the sample under consideration reveals an averaged island base width w of 130 nm and a corresponding averaged height h of 65 nm, see Fig. 1(a). The resulting geometrical aspect ratio w/h of ≈ 2 indicates a very effective surface minimization during island growth from a liquid phase.¹⁹ Nearly all islands arrange themselves laterally into island chains that are oriented along the crystallographic soft ⟨100⟩ directions. Recently we have demonstrated that the strain energy distribution in the vicinity of a single island and an island dimer enforces the self-assembling into extended chains.³ Eventually with increasing island density a chessboard like arrangement is observed [see, e.g., the square to the lower left in Fig. 1(a)]. In case of

^{a)}Present address: Fachbereich Physik, Martin-Luther-Universität Halle-Wittenberg, Hoher Weg 8, D-06120 Halle/Saale, Germany; electronic mail: hanke@physik.uni-halle.de

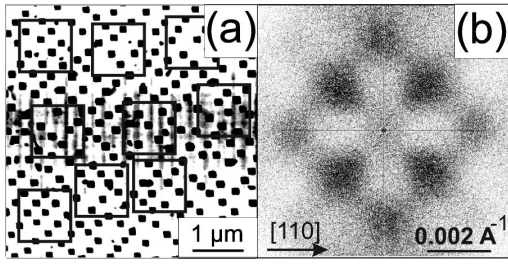


FIG. 1. (a) Atomic force micrograph of the investigated sample. The squares enclose various subensembles containing nine to ten islands. (b) Fourier transform (power spectrum) as derived from the micrograph.

low germanium content this type of arrangement can be directly attributed²⁰ to a prepattern called rippling, which consists of shallow surface undulations along the $\langle 100 \rangle$ directions. However, we could not detect any initial growth stage and only the final island morphology can be observed. In Fig. 1(b) the peaks in the Fourier transform (power spectrum) of the atomic force micrograph in Fig. 1(a) clearly reveal lateral positional correlation along both the $\langle 110 \rangle$ and the $\langle 100 \rangle$ directions.

III. EXPERIMENT

The scattering experiment has been performed at BW2 station (HASYLAB) using monochromatic x rays ($\lambda = 1.54 \text{ \AA}$) and a linear position sensitive detector (PSD) for analyzing the direction of the scattered radiation. The wavelength resolution of $\Delta\lambda/\lambda = 10^{-4}$ results in a longitudinal coherence length $\Lambda_{long} = \lambda^2/2\Delta\lambda$ of $\approx 750 \text{ nm}$. Usually, the spatial coherence length of the incoming beam is determined by calculating the effective aperture seen when looking from a fixed point of the sample back to the source. Analogously the detector aperture, that is, the effective aperture seen when looking from a fixed point of the sample at the smallest resolution element of the PSD (which plays the role of an effective source size) has to be taken into account. In both cases the effective spatial coherence length is given by $\Lambda_{spat} = R\lambda/d$, where d is given either by the x-ray source size or the smallest resolution element of the PSD, and R is the distance between sample and source/detector. In the experimental setup used here the spatial coherence length is mainly determined by the detector spatial resolution. Using a spatial resolution of the PSD of $100 \mu\text{m}$ finally results in an effective spatial coherence length of $\approx 1500 \text{ nm}$, which is considerably smaller than the source-related coherence length of synchrotron radiation.

IV. RESULTS AND DISCUSSION

Figure 2(e) depicts the measured diffusely scattered intensity in the vicinity of the 004 reciprocal lattice point within a scattering plane, which contains the $[100]$ direction. Hence pronounced facet truncation rods originating from the island $\{111\}$ facets do not contribute to the plotted distribution. The entire cloud of diffuse intensity is related to the scattering from a particular island type. However, a remarkable impact of the positional correlation becomes obvious

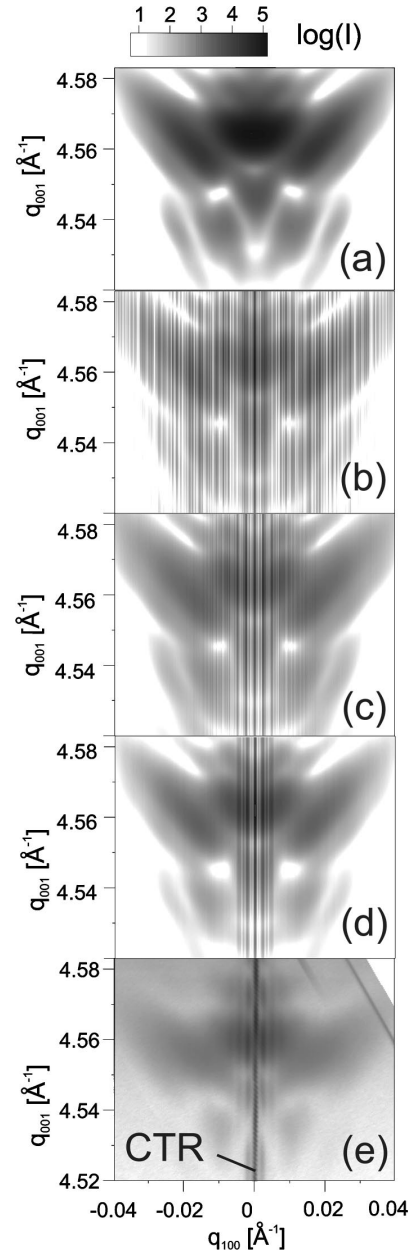


FIG. 2. Simulated diffusely scattered intensity around the symmetrical 004 reciprocal lattice point of a single island (a) and out of various island ensembles (b–d) compared with measurement (e).

through the presence of distinct correlation satellites up to third order in the nearest vicinity of the Si(001) crystal truncation rod (CTR). The averaged separation between them amounts to 0.0022 \AA^{-1} . Direct scanning probe techniques as AFM suffer from comparatively less statistics, thus only the first order satellites appear in the power spectrum [Fig. 1(b)]. Corresponding peak separations amount to $\Delta q_{\langle 100 \rangle} = 0.0020 \text{ \AA}^{-1}$ and $\Delta q_{\langle 110 \rangle} = 0.0027 \text{ \AA}^{-1}$, which roughly confirms the relationship $\sqrt{2} \times \Delta q_{\langle 100 \rangle} = \Delta q_{\langle 110 \rangle}$ due to the par-

ticular cross-like pattern. These values correspond to mean lateral island-island distances of $d_{\langle 110 \rangle} = 233$ nm and $d_{\langle 100 \rangle} = 314$ nm.

Details of the underlying simulation procedure for the scattering by a single island have been described elsewhere¹¹ and will be reported here only in brief. The numerical treatment considers the elastic strain field of the structure as calculated by the finite element method and the diffuse scattering is then simulated within the kinematical scattering approximation. We have demonstrated that a vertical germanium profile with a germanium content of 25% within the lower third of an island and 30% germanium above fits the experimentally observed features very well [see Fig. 2(a)] except for the lateral correlation peaks on both sides of the CTR, which are missing in the simulation for a single island. Here we will mainly focus on lateral positional island correlation and its impact on the diffusely scattered intensity.

For a particular island ensemble E with m equivalent objects the diffusely scattered intensity I_E can be expressed as a simple product

$$I_E \propto \left| A^{diff}(\mathbf{q}) \sum_{m \in E} e^{i\mathbf{q}\mathbf{R}_m} \right|^2 = |A^{diff}(\mathbf{q})|^2 G(\mathbf{q}), \quad (1)$$

where $A^{diff}(\mathbf{q})$ denotes the diffusely scattered amplitude caused by a single object, \mathbf{R}_m points to its actual position and $G(\mathbf{q})$ refers to the in-plane interference function. Thus, the calculation of the diffusely scattered intensity from an island ensemble E requires adding over the index m referring to the actual island positions therein. However, this coherent summation presumes perfect lateral coherence of the x-ray beam and complete information on island positions.

For the following simulations island positions are taken from AFM micrographs as depicted in Fig. 1(a). With an ensemble containing 33 islands—corresponding to a sample area of $2 \times 2 \mu\text{m}^2$ —and coherent summation the simulation in Fig. 2(b) shows extremely pronounced speckles. Moreover, since all island positions are within a plane, the interference function does not depend on q_{001} . Even if the scattering of several thousand islands is considered the simulated intensity distribution (not shown here) still exhibits a complicated speckle pattern.

Obviously, the finite experimental coherence length has to be taken into account. This can be done by a partially coherent summation over areas corresponding with the experimental lateral coherence length Λ and a subsequent incoherent (intensity) summation over many of those coherent summations:

$$I_E \propto |A^{diff}(\mathbf{q})|^2 \sum_{\forall n} \left| \sum_{m \in E_n} e^{i\mathbf{q}\mathbf{R}_m} \right|^2, \quad (2)$$

m subscribes the position within a coherently illuminated ensemble and n indicates the different ensembles.

For the simulation in Fig. 2(c) square areas of $1 \times 1 \mu\text{m}^2$, each enclosing nine to ten islands, have been chosen from Fig. 1(a) as indicated there. In accordance with Eq. (2) amplitudes are summed coherently within those areas and the corresponding intensities of all these areas are added. Indeed, the speckle pattern appears significantly suppressed as compared with Fig. 2(b). However, remarkable differences

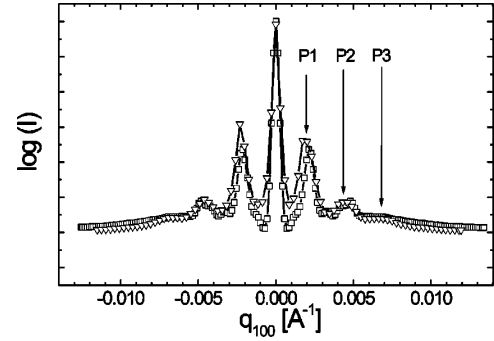


FIG. 3. Sections of the simulated (squares) and measured (triangles) intensity distribution shown in Figs. 2(d) and 2(e) at $q_{001}=4.560 \text{ \AA}^{-1}$.

between measurement and simulation remain. This is related to the comparatively small number of different ensembles.

In principle, it would be possible to extract much more ensembles from a sufficiently large number of AFM micrographs. There is, however, a simpler way to improve simulations. We have numerically generated child-ensembles from those in Fig. 1(a) by adding an offset Ω along the $\langle 100 \rangle$ directions to each island position randomly distributed within a range of ± 50 nm. With a total number of only 1000 child ensembles the speckle pattern can be completely suppressed, Fig. 2(d). Figure 3 depicts one-dimensional intensity cuts at $q_{001}=4.560 \text{ \AA}^{-1}$ through measurement and the theoretically derived distributions in Figs. 2(e) and 2(d), respectively. The numerical treatment reproduces both positions as well as corresponding intensity ratios of the satellites P1 through P3.

To implement a certain, even though small size distribution, amplitudes of two more similar island types (123.5 and 136.5 nm in island base) have been considered. Despite this, the resulting diffuse scattering from a single island (not shown here) does not show a significant impact of the finite size distribution. However, the interference function $G(\mathbf{q})$ becomes dependent on q_{001} .

V. CONCLUSIONS

In summary, the investigated SiGe nanoscale islands grown by means of liquid phase epitaxy on Si(001) are made of truncated pyramids with {111} side and an (001) top facet forming exclusively a single island type. Moreover they exhibit a pronounced lateral positional correlation along the $\langle 100 \rangle$ and $\langle 110 \rangle$ directions. In order to probe this self-organized lateral arrangement we have applied both, direct imaging by atomic force microscopy as well as high resolution x-ray diffraction. We have demonstrated that a detailed analysis of the x-ray diffuse scattering pattern requires careful consideration of the coherence properties of x rays. Although the diffraction experiment probes a sample area of about one mm², thus an ensemble which contains $\approx 10^7$ equivalent islands, the scattering has to be considered coherent within much smaller areas defined by the experimental coherence length. A numerical method has been developed to implement the impact of lateral positional correlation onto the scattering pattern. This approach takes the finite experi-

mental coherence length correctly into account by applying a partially coherent and partially incoherent superimposition of scattering amplitudes of single islands.

ACKNOWLEDGMENTS

The authors would like to thank W. Drube and H. Schulte-Schrepping from BW2 station (HASYLAB) for the assistance during measurements. The sample preparation by H. Wawra at the Institut für Kristallzüchtung in Berlin is gratefully acknowledged. This work was financially supported by the Deutsche Forschungsgemeinschaft under contract No. KO1510/2 and the Sonderforschungsbereich 296.

- ¹D. Bimberg, M. Grundmann, and N. N. Ledentsov, *Quantum Dot Heterostructures* (Wiley, Chichester, NY, 1999).
- ²M. Meixner, E. Schöll, M. Schmidbauer, H. Raidt, and R. Köhler, Phys. Rev. B **64**, 245307 (2001).
- ³M. Hanke, H. Raidt, R. Köhler, and H. Wawra, Appl. Phys. Lett. **83**, 4927 (2003).
- ⁴Q. Xie, A. Madhukar, P. Chen, and N. Kobayashi, Phys. Rev. Lett. **75**, 2542 (1995).
- ⁵G. Springholz, V. Holý, M. Pinczelits, and G. Bauer, Science **282**, 734 (1998).
- ⁶A. Rosenauer, *Transmission Electron Microscopy of Semiconductor Nanostructures: Analysis of Composition and Strain State*, Springer Tracts in Modern Physics, Vol. 182 (Springer, Berlin, 2003).
- ⁷M. Schmidbauer, T. Wiebach, H. Raidt, M. Hanke, R. Köhler, and H. Wawra, Phys. Rev. B **58**, 10523 (1998).
- ⁸M. Rauscher, R. Paniago, H. Metzger, Z. Kovats, J. Domke, J. Peisl, H. D. Pfannes, J. Schulze, and I. Eisele, J. Appl. Phys. **86**, 6763 (1999).
- ⁹A. Hesse, J. Stangl, V. Holý, T. Roch, G. Bauer, O. Schmidt, U. Denker, and B. Struth, Phys. Rev. B **66**, 085321 (2002).
- ¹⁰J. Stangl, A. Hesse, V. Holý, Z. Zhong, G. Bauer, U. Denker, and O. G. Schmidt, Appl. Phys. Lett. **382**, 2251 (2003).
- ¹¹M. Hanke, M. Schmidbauer, D. Grigoriev, P. Schäfer, R. Köhler, A.-K. Gerlitzke, and H. Wawra, Phys. Rev. B **69**, 075317 (2004).
- ¹²A. A. Darhuber, P. Schittenhelm, V. Holý, J. Stangl, G. Bauer, and G. Abstreiter, Phys. Rev. B **55**, 15652 (1997).
- ¹³I. Kegel, T. H. Metzger, J. Peisl, P. Schittenhelm, and G. Abstreiter, Appl. Phys. Lett. **74**, 2978 (1999).
- ¹⁴K. Zhang, C. Heyn, W. Hansen, T. Schmidt, and J. Falta, Appl. Phys. Lett. **76**, 2229 (2000).
- ¹⁵V. Chamard, T. H. Metzger, E. Bellet-Amalric, B. Daudin, C. Adelmann, H. Mariette, and G. Mula, Appl. Phys. Lett. **79**, 1971 (2001).
- ¹⁶V. Holý, T. Roch, J. Stangl, A. Daniel, G. Bauer, T. H. Metzger, Y. H. Zhu, K. Brunner, and G. Abstreiter, Phys. Rev. B **63**, 205318 (2001).
- ¹⁷M. Hanke, M. Schmidbauer, R. Köhler, H. Kirmse, and M. Pristovsek, J. Appl. Phys. **95**, 1736 (2004).
- ¹⁸R. T. Lechner, T. U. Schülli, V. Holý, G. Springholz, J. Stangl, A. Raab, G. Bauer, and T. H. Metzger, Appl. Phys. Lett. **84**, 885 (2004).
- ¹⁹M. Hanke, M. Schmidbauer, R. Köhler, F. Syrowatka, A.-K. Gerlitzke, and T. Boeck, Appl. Phys. Lett. **84**, 5228 (2004).
- ²⁰W. Dorsch, B. Steiner, M. Albrecht, H. P. Strunk, H. Wawra, and G. Wagner, J. Cryst. Growth **183**, 305 (1998).

2.5.5 Diffuse Röntgenstreuung als Funktion chemischer Komposition und Deformation in 0-dimensionalen Heterostrukturen

M. Hanke, T. Boeck

On the various impact of chemical composition and elastic strain in SiGe nanoscale islands to the diffuse x-ray scattering

Physica E **32**, 69 (2006).

Aus der kinematischen Streutheorie folgt, dass diffuse Streuung neben dem konkreten Ort der Streuer (Deformationsfeld) auch noch von der Strukturamplitude (mithin von der Chemie der einzelnen Streuer) abhängt. Bei Energien von etwa 8 keV liegen die Absorptionskanten von Silizium und Germanium energetisch hinreichend weit entfernt, um die Beträge der Strukturamplituden proportional zu den Kernladungszahlen der entsprechenden Atomspezies anzusetzen. Auf der anderen Seite erstreckt sich das jeweils für einen bestimmten Reflex abgetastete Gebiet im reziproken Raum nur über einen sehr kleinen Bereich, so dass man die explizite Abhängigkeit vom Streuvektor vernachlässigen kann.

Im Rahmen von Simulationen lässt sich numerisch untersuchen, inwieweit die einzelnen Beiträge (Deformationsfeld und unterschiedlich starkes Streuvermögen der Silizium- und Germaniumatome) die spezielle Form der diffusen Streuung prägen. Vergleichende Rechnungen mit gleichen Streuamplituden bzw. unter Berücksichtigung der unterschiedlichen Streuvermögen zeigen interessanterweise nur marginale Unterschiede. Dies belegt sehr schön, dass entfernt von Absorptionskanten diffuse Streuung direkt mit dem Deformationsfeld in niedrigdimensionalen Strukturen koppelt, die konkrete chemische Zusammensetzung jedoch nur mittelbar (nämlich als Ursache der Deformation) einen Beitrag liefert.

Available online at www.sciencedirect.comSCIENCE @ DIRECT[®]

Physica E 32 (2006) 69–72

PHYSICA Ewww.elsevier.com/locate/physce

On the various impact of chemical composition and elastic strain in SiGe nanoscale islands to the diffuse X-ray scattering

M. Hanke^{a,*}, T. Boeck^b^a*Martin-Luther-Universität Halle-Wittenberg, Fachbereich Physik, Hoher Weg 8, D-06120 Halle/Saale, Germany*^b*Institut für Kristallzüchtung, Max-Born-Straße 2, D-12489 Berlin, Germany*

Available online 25 January 2006

Abstract

High-resolution X-ray diffraction in combination with kinematical scattering simulations based on finite element calculations for the elastic strain field has been utilized to investigate the chemical composition of SiGe/Si(001) Stranski–Krastanov islands. Therefore, the intensity distribution in the vicinity of the symmetric (004) reflection has been three dimensionally measured and compared with respective simulations. Around an asymmetrical reflection, e.g. Si(113), the impact of lateral and vertical strain tensor components on the diffraction pattern decouples. This allows to distinguish between tetragonally distorted regions at the island bottom and elastically relaxed unit cells of cubic shape at the island apex in accordance with finite element calculations. Artificially switching off and on the various scattering abilities of silicon and germanium in otherwise equivalent simulations yields practically no difference in the resulting scattering. Thus, at X-ray energies far from absorption edges, the diffuse scattering is dominated by elastic strain which is caused by the chemical profile.

© 2006 Elsevier B.V. All rights reserved.

PACS: 68.65.-k; 61.10.-i; 81.15.Lm

Keywords: X-ray scattering; SiGe/Si; Finite element method

1. Introduction

For a large variety of material combinations the Stranski–Krastanov growth mode provides an elegantly simple way to self-form and further self-assemble highly ordered arrays of low-dimensional structures, e.g. Ref. [1]. The strain energy which will be initially accumulated during the heteroepitaxy of the very first amount of material can be accommodated in the crystal lattice resulting in a two-dimensional layer growth. However, after a critical thickness, depending on the actual lattice mismatch, the formation of three-dimensional islands is achieved, which becomes energetically favorable instead of further layer growth. Thus, the energy gain due to elastic relaxation overbalances the additional free surface energy. Moreover, in a near-equilibrium growth environment the final island size inversely scales with the accommodated

strain energy [2]. Liquid phase epitaxy (LPE) of SiGe/Si serves as a suitable model system to achieve a more comprehensive understanding of the observed phenomena and the underlying mechanisms. In a complementary way to direct analytical techniques highly resolved X-ray scattering techniques can provide statistically relevant information concerning elastic strain and morphology, e.g. Refs. [3–5].

2. Experiment

LPE operates very close to thermodynamical equilibrium and hence yields a near-equilibrium island morphology. In case of SiGe/Si(001) it consists of truncated pyramids made of four adjacent {111} and a single (001) top facet [6]. An averaged island base of 130 nm along a mean island height of 65 nm yields a geometric aspect ratio base vs. height of two. Moreover, the islands self-assemble in a strain-driven process into extended chains along the elastically soft ⟨100⟩ directions [7].

*Corresponding author.

E-mail address: hanke@physik.uni-halle.de (M. Hanke).

Naturally scattering from nanoscale objects is expected to appear rather weak in contrast to bulky objects. Moreover, the smaller the objects the more extended the diffuse intensity in reciprocal space whose detection generally requires highly brilliant X-ray sources. Thus, the measurements we present here have been performed at the BW2 synchrotron station at HASYLAB, Hamburg using an X-ray energy of 8 keV. A positional-sensitive detector (PSD) placed in a distance of 1000 mm from the sample position records the diffusely scattered intensity along a (curved) line in reciprocal space. Either by rocking the sample (Ω -scan) or moving sample and detector in a certain ratio ($\Omega/2\Theta$ -scan) two-dimensional intensity distributions were recorded. Thereby, the entrance slit (1 mm) in front of the PSD restricts the resolution perpendicular to the scattering plane to about 0.006 \AA^{-1} .

In order to quantitatively evaluate the measured distributions we have performed kinematical scattering simulations based on a two-step iterative procedure. Thereby, the finite element method (FEM) serves to calculate numerically the three-dimensional strain field within mesoscopic objects of most different shapes and various chemical compositions. However, this method remains restricted to some 10^6 nodes and hence an intermediate refinement procedure becomes necessary where the strain field will be extrapolated on a regular grid with an inter-node distance of typically four times the lattice constant of silicon. Subsequently, this deformation field serves as input for a kinematical scattering routine where the scattering amplitudes arising from all participating scatterers are summed up in a coherent way. Usually only those scatterers residing within the island are taken into account in order to avoid scattering artefacts due to the finite size effect. In general, the diffusely scattered amplitude A_d can be calculated as follows:

$$A_d(\mathbf{q}) \propto \sum_i \sum_k \varrho(\mathbf{r}_{i,k}) \exp[i\mathbf{q}(\mathbf{r}_{i,k} + \mathbf{u}(\mathbf{r}_{i,k}))], \quad (1)$$

with $\mathbf{r}_{i,k} = \mathbf{R}_i + \mathbf{r}_k$, ϱ is the electron density of the crystal lattice, \mathbf{R}_i gives the position of the i th supercell, \mathbf{r}_k denotes the positions of the k th atom within the unit cell and \mathbf{u} denotes the displacement vector.

3. Results and discussion

Generally, the SiGe islands can elastically relax during the growth process and hence an incorporation of a higher germanium content, respectively unit cells with a larger lattice constant, becomes energetically favorable towards the islands apex. However, there are a variety of different conceivable germanium profiles which will fulfil this obvious energetic condition, e.g. a linear concentration gradient in growth direction, a discrete concentration step at a certain island height or a combination of a linear gradient and a homogeneous part.

The distributions in Fig. 1 depict the measured (a) and simulated (b) intensities around the symmetrical 004

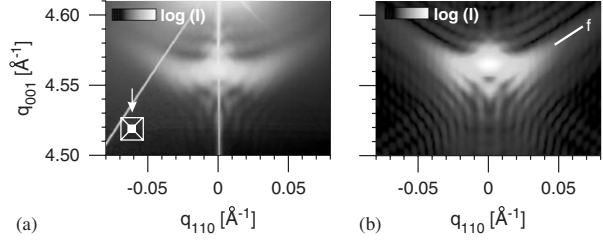


Fig. 1. Experimental (a) and simulated (b) intensity distributions around the symmetric 004 reflection within the [1 1 0] zone referring to a scattering plane containing the island base.

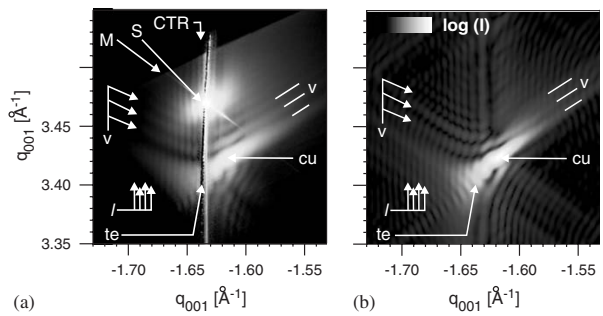


Fig. 2. Both distributions show the diffusely scattered intensity around the asymmetrical 113 reflection as measured (a) and simulated (b).

reflection within the [1 1 0] zone. All scattering simulations discussed here were done for the same island morphology (not shown here) which consists of a truncated pyramid confined by {1 1 1} side and an (0 0 1) top facet with base width and height of 130 and 65 nm, respectively. The island is placed on a 2 nm wetting layer on top of an extended 260 nm \times 260 nm \times 100 nm silicon substrate.

The actual substrate peak has been omitted. It appears outside the depicted area at $q_{001} = 4.628 \text{ \AA}^{-1}$. On the other hand, the butterfly-shaped pattern at smaller q_{001} is influenced by the islands themselves and in particular by elastic strain and thus indirectly (as we will show later) serves as a fingerprint of the chemical profile. Within the present plane it is mainly dominated by the particular island shape resulting in facet rods (f) which are inclined by approximately 54.7°. Due to the finite size effect extended facets in real space, e.g. the {1 1 1}-type island facets, cause intense features which appear in reciprocal space perpendicular to the respective planes in real space. Moreover, those facet rods are superimposed by size oscillations whose lateral period inversely scales with the island size.

Since lateral and vertical strain tensor components are not separable in a symmetric geometry an asymmetrical reflection as e.g. Si(1 1 3), Fig. 2, allows to distinguish between scattering from tetragonally distorted unit cells (te) which figure at the island bottom and scattering by a cubic lattice (cu) at the island apex where the elastic impact of the substrate almost vanishes. However, there is also a prominent contribution due to shape resulting in lateral

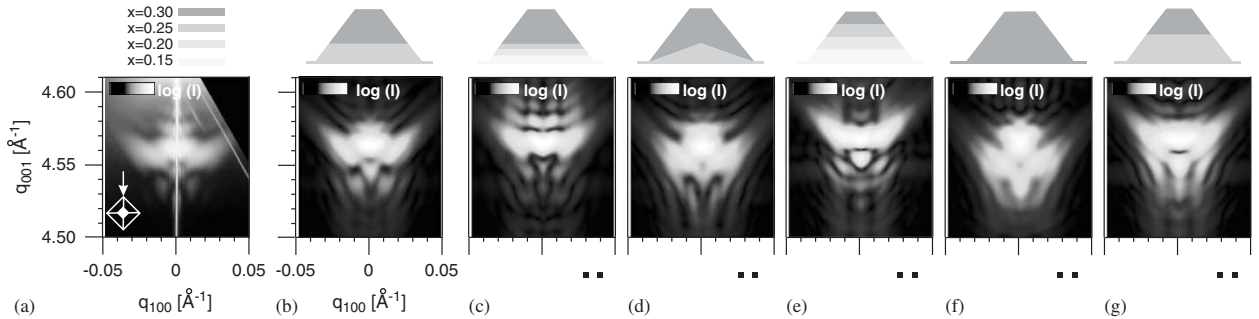


Fig. 3. (a) Shows the measured intensity distributions around the symmetric 004 reflection along the [100] direction, and, in comparison scattering simulations (b–g) on the base of various chemical profiles as depicted.

(l) and vertical (v) size oscillations. A highly intense crystal truncation rod (CTR) and the monochromator artefact (M) intersect the Si(113) substrate reflection (S).

Suitable candidates to probe strain and hence chemical composition with a minimum shape influence are crystallographic zones where no or only small island facets are present. Fig. 3(a) shows the measured intensity distribution in the [100] plane. Except the intense CTR along q_{001} there are no size oscillations as in Fig. 1. Corresponding simulations (b)–(g) probe the influence of strain and chemical composition as sketched in the schemes above.

Further it allows to estimate the spatial and chemical resolution. The overall shape of the diffuse scattering on the very first model, e.g. considering a homogeneous germanium content of 30% (f) clearly differs from the experiment and appears at comparatively small q_{001} , indicating that the averaged germanium content has to be decreased in the model. Thus, the remaining simulations prove a vertical shift of the diffuse intensity towards the silicon reflection. The most appropriate approximation (b) results from an island with a discrete concentration step at $h/3$ from 25% germanium at the island bottom towards 30% above, whereas a linear gradient (e)—approximated by four equally spaced slices of 15%, 20%, 25% and 30%—does not meet the measurement. Thus, we have conceived additional models with *discrete* concentration steps at $h/3$ separating a linear gradient at the island bottom and a homogeneous region above (c) or considering an incorporated pyramid (d). Both models show a slightly worse agreement with respect to simulation (b). Finally, to estimate the spatial resolution in vertical direction we have shifted the interface (25/30)% from $h/3$ (model b) towards $h/2$ (model g) which clearly rejects the latter ones and results in an accuracy of about 5 nm for the interface position.

The simulations in Fig. 3 have been performed taking the different scattering abilities of germanium and silicon into account which enter the scattering process via the electron densities in Eq. (1). Since the X-ray diffraction was performed at an X-ray energy of 8 keV which is far away from relevant absorption edges, the corresponding atomic numbers Z_i equal the absolute value of the respective

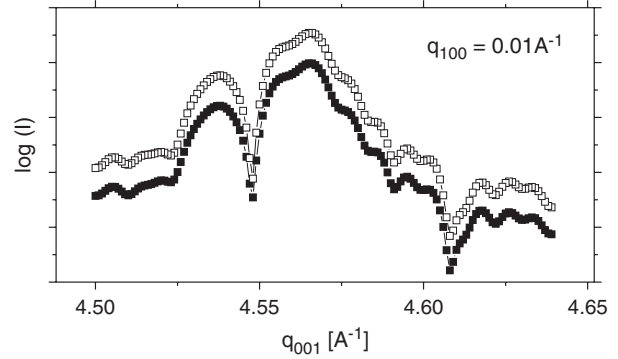


Fig. 4. Simulated vertical sections through the distributions Fig. 3(a) and (b) at a constant $q_{100} = 0.01 \text{ \AA}^{-1}$ taking the appropriate form factors of silicon and germanium into account (open squares) and assuming equivalent scattering abilities (full squares). Both profiles have been vertically shifted by a factor of 5 for better clarity.

structure amplitudes, and consequently there is a more intense contribution to the scattering signal out of areas with a higher germanium content (island apex), whereas the island bottom with a smaller germanium content less contributes to scattering. Assuming only two regions with different concentrations, we can define a factor which describes the ratio of both form factors:

$$a = \left(\frac{x_1 Z_{\text{ge}} + (1-x_1) Z_{\text{si}}}{x_2 Z_{\text{ge}} + (1-x_2) Z_{\text{si}}} \right)^2, \quad (2)$$

which numerically results in a value of 1.08 for $x_1 = 0.25$ and $x_1 = 0.3$ as it was assumed for model Fig. 3(b). Up to this point it is still open which parameter in Eq. (1) dominates the scattering process, the displacement field and/or the chemical profile. Therefore, we have exemplarily performed a simulation similar to that shown Fig. 3(b), however, without any direct chemical influence which was done by having the scattering abilities of germanium and silicon on the same level. Since the overall distribution (not shown) looks the same as Fig. 3(b) two equivalent sections through both distributions at q_{100} are shown in Fig. 4. Both are vertically shifted with respect to each other, however,

no difference was identified. This observation clearly proves the interesting fact that a chemical profile within SiGe/Si islands influences the diffuse scattering only by the resulting strain distribution and not directly through the different structure factors of silicon and germanium.

We have investigated the diffuse X-ray scattering of pseudomorphic SiGe/Si(001) Stranski-Krastanov islands which have been grown by means of liquid phase epitaxy. Respective scattering simulations on the base of finite element calculations for the elastic strain distribution prove a discrete horizontal concentration step at $h/3$. Comparing simulations taking the various scattering abilities of germanium and silicon into account and, on the other hand, assuming same form factors for both materials, clearly demonstrate that elastic strain dominates the diffuse scattering at X-ray energies far away from absorption edges. Consequently, the chemical profile influences the scattering process almost exclusively via a modified strain.

Acknowledgments

The authors thank W. Drube, BW2 at HASYLAB, Hamburg for experimental assistance. Discussions with M. Schmidbauer and R. Köhler, Humboldt-Universität zu Berlin are appreciated.

References

- [1] V.A. Shchukin, et al., *Epitaxy of Nanostructures*, Springer, New York, 2004.
- [2] W. Dorsch, et al., *Appl. Phys. Lett.* 72 (1998) 179.
- [3] M. Schmidbauer, *X-Ray Diffuse Scattering from Self-Organized Mesoscopic Semiconductor Structures*, Springer, Berlin, 2004.
- [4] J. Stangl, et al., *Rev. Mod. Phys.* 76 (2004) 725.
- [5] U. Pietsch, et al., *High Resolution X-Ray Scattering from Thin Solid Films to Lateral Nanostructures*, Springer, Berlin, 2004.
- [6] M. Hanke, et al., *Appl. Phys. Lett.* 84 (2004) 5228.
- [7] M. Meixner, et al., *Phys. Rev. B* 64 (2001) 245307.

3 GaAs-basierte Heterostrukturen

3.1 Kompositionsprofile in InGaAs/GaAs *quantum dots*

M. Hanke, D. Grigoriev, M. Schmidbauer, P. Schäfer, R. Köhler, R. L. Sellin, U. W. Pohl, D. Bimberg

Vertical composition gradient in InGaAs/GaAs alloy quantum dots as revealed by high resolution x-ray diffraction

Appl. Phys. Lett. **85**, 3062 (2004).

M. Hanke, D. Grigoriev, M. Schmidbauer, P. Schäfer, R. Köhler, U. W. Pohl, R. L. Sellin, D. Bimberg, N. D. Zakharov, P. Werner

Diffuse X-Ray Scattering of InGaAs/GaAs Quantum Dots

Physica E **21**, 684 (2004).

Die beiden folgenden Artikel sind inhaltlich sehr verwandt und beschäftigen sich mit der Analyse vertikal gestapelter, in einer GaAs Matrix eingebetteter $\text{In}_{0.6}\text{Ga}_{0.4}\text{As}$ *quantum dots*. Die Proben entstanden am Lehrstuhl von Prof. Bimberg am Institut für Festkörperphysik der Technischen Universität Berlin.

Es wurde zunächst die diffuse Streuung sowohl in der Nähe asymmetrischer Reflexe als auch in GID Geometrie mittels hochbrillianter Synchrotronstrahlung (BW2, HASYLAB und ID10B, ESRF) hochauflöst vermessen. Allerdings verhindert die komplexe Form der diffusen Streuung (aufgrund der vertikalen Überstruktur) direkte Rückschlüsse auf die Form und chemische Komposition der *quantum dots*, so dass als Ausgangspunkt für numerische Streusimulationen Strukturinformationen aus transmissionselektronenmikroskopischen Abbildungen benutzt wurden. Diese zeigen keine ausgeprägte laterale Korrelation, jedoch eine deutliche vertikale Vererbung.¹⁴

Das Streuverhalten verschiedener *quantum dot* Formen (linsenförmig, invertierte Pyramide) zeigt kaum Unterschiede, was vor dem Hintergrund der durch TEM gefundenen Formvarianz wenig überrascht. Allerdings deuten die Simulationen auf eine Indiumsegregation während des Wachstums hin, da im Fuß der *quantum dots* der Indiumgehalt deutlich vom nominellen Wert abweicht. Die beste Übereinstimmung wurde für rotationssymmetrische, linsenförmige $\text{In}_{0.6}\text{Ga}_{0.4}\text{As}$ *quantum dots* erreicht, die im unteren Bereich nur eine Indiumkonzentration von 45% aufweisen und auf einer dünnen (zwei Atomlagen dicken) $\text{In}_{0.37}\text{Ga}_{0.63}\text{As}$ Benetzungsschicht positioniert sind.

Es sei auf Parallelen im System SiGe/Si, Kap. 2, hingewiesen. Dort führte die elastische Relaxation der Stranski-Krastanow Inseln während des Wachstums zu einem vertikalen Kompositionsprofil mit größerem Germaniumgehalt im Inselpex.

¹⁴Das Vorhandensein eines *quantum dots* in der ersten Lage verändert durch das von ihm verursachte Deformationsfeld die Nukleationswahrscheinlichkeit in darauf folgenden Lagen. Sofern die Zwischenschicht nicht zu dick gewählt wird (im vorliegenden Fall 20 nm), lässt sich auf diese Weise eine nahezu vollständige vertikale Korrelation erzeugen.

Vertical composition gradient in InGaAs/GaAs alloy quantum dots as revealed by high-resolution x-ray diffraction

M. Hanke^{a)}

Martin-Luther-Universität Halle-Wittenberg, Hoher Weg 8, D-06120 Halle(Saale), Germany

D. Grigoriev, M. Schmidbauer, P. Schäfer, and R. Köhler

Institut für Physik, Humboldt-Universität zu Berlin, Newtonstraße 15, D-12489 Berlin, Germany

R. L. Sellin,^{b)} U. W. Pohl, and D. Bimberg

Institut für Festkörperphysik, Technische Universität Berlin, Hardenbergstraße 36, D-10623 Berlin, Germany

(Received 6 July 2004; accepted 9 August 2004)

Shape and composition profiles of self-organized $\text{In}_{0.6}\text{Ga}_{0.4}\text{As}/\text{GaAs}$ quantum dots (QDs) were investigated using diffuse x-ray scattering of a fivefold QD stack. To reveal the QD morphology, numerical scattering simulations of QDs with different morphologies were performed based on three-dimensional strain fields calculated by the finite element methods. Comparing our simulations to the data, we proved that the In concentration increases from the wetting layer to the top of the quantum dots. Moreover, we conclude that the In concentration of the wetting layers is significantly lower than the average value in the QDs. © 2004 American Institute of Physics.

[DOI: 10.1063/1.1803938]

Self-organized InGaAs/GaAs quantum dots (QDs) as formed in the Stranski-Krastanow growth mode are zero-dimensional electronic systems,^{1,2} which are highly interesting for both the study of new physical phenomena and device applications, such as lasers and semiconductor optical amplifiers (SOAs).³ Recent studies on the electronic and optical properties of QDs have outlined the impact of QD shape, chemical composition and strain profile on the alignment of confined electron and hole wave functions,⁴ as well as the dependence of the polarization of emitted photons on the QD aspect ratio.⁵ While the morphological properties of QDs were thus shown to be decisive for the design of QD devices, such as polarization-insensitive SOAs, the debate on the In distribution within InGaAs alloy QDs, as well as the exact shape of such QDs, is still ongoing.

Various techniques have been applied to reveal both QD strain and composition profiles. High-resolution transmission electron microscopy (HRTEM) is mostly applied to monitor chemical and strain contrast. The technique allows for atomic resolution, but a clear separation of strain and chemical composition contrast is difficult. Moreover, only columns of atoms are imaged, which average compositional variations along the direction of projection. Cross-sectional tunneling microscopy (XSTM) enables to image strain contrast and compositional profiles with atomic resolution on cleaved surfaces across buried QDs. Using XSTM, different morphologies of InGaAs/GaAs QDs have been identified, including reverse-trapezoidal⁶ and reverse-pyramidal^{7,8} In-rich cores.

Direct imaging techniques, such as HRTEM or XSTM, require sample preparation which alters the shape and strain profile of the investigated QDs. Furthermore, these techniques provide data on only a few selected objects which do

not necessarily represent the QD ensemble. In this letter we show that diffuse x-ray scattering, accompanied by numerical scattering simulations,^{9,10} can likewise be used to reveal inhomogeneous composition profiles in InGaAs/GaAs QDs. The technique is nondestructive and leaves QDs in their original strain environment. Moreover, data are collected on entire QD ensembles, thereby avoiding characterization of potentially unrepresentative QDs.

The sample investigated here was grown on a GaAs(001) substrate by metalorganic chemical-vapor deposition using trimethylgallium, trimethylindium, and arsine as precursors. Each QD layer was grown at 500 °C, whereas the temperature was increased during GaAs overgrowth to 600 °C. In order to stack subsequent layers closely with a vertical period around 20 nm, we applied a surface-flattening technique during growth of the respective GaAs spacer layers.¹¹

Transmission electron micrographs (not shown here) depict that the QDs reside on a very thin and continuous wetting layer (WL). Enforced by the long-range strain field of the QDs and the comparatively thin GaAs spacers between the dot planes, the QDs are vertically arranged into columns, whereas they do not exhibit a significant lateral ordering.¹² Highly brilliant x-ray radiation is mandatory to yield sufficient scattered intensity from the QDs, owing to their small volume. We therefore used monochromatic synchrotron radiation from the beamline BW2 at HASYLAB with an energy of 8 keV and an energy resolution of $\Delta E/E = 10^{-4}$. A position-sensitive detector which simultaneously records the intensity along a curved line in reciprocal space was used for recording two-dimensional intensity distributions. Our procedure for the numerical simulations is based on an iterative two-step approach. First, the three-dimensional strain field is calculated applying the finite element method (FEM), which basically employs linear elasticity theory. Thus, the full elastic anisotropy of the zincblende structure is considered. Eventually, the derived deformation fields serve as data

^{a)}Present address: National Institute of Standards and Technology, 100 Bureau Drive, Gaithersburg, MD 20899, USA; electronic address: hanke@physik.uni-halle.de

^{b)}Present address: Department of Engineering, University of Cambridge, Trumpington Street, Cambridge CB2 1PZ, United Kingdom.

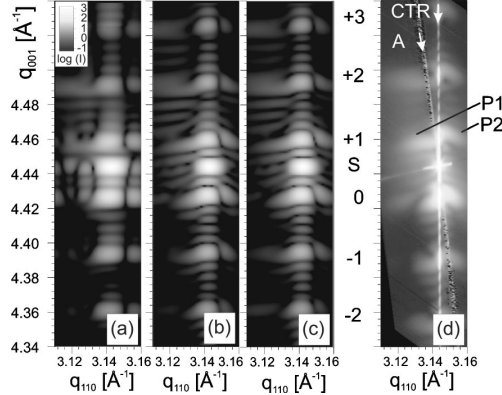


FIG. 1. Measured x-ray intensity distribution in the vicinity of the asymmetric 224 reciprocal lattice point (d) compared to simulations of the scattered intensity calculated using different QD shapes and composition profiles (a–c) as described in Fig. 3. Feature (A) is caused by a detector artefact.

input for numerical scattering simulations on the basis of the distorted-wave Born approximation.⁹

Figure 1 shows a reciprocal space map around the GaAs 224 reflection (d) and simulated intensity distributions (a–c) for different QD shapes and compositions as described later. The diffuse x-ray scattering in Fig. 1(d) exhibits a complicated pattern which results from the simultaneous action of geometry, strain, and chemical composition profile within the QDs. Moreover, the signal contains contributions from the InGaAs WLs and the GaAs matrix. The GaAs substrate reflection (S) appears as a very strong signal at $q_{001} = 4.445 \text{ \AA}^{-1}$. It is vertically intersected at $q_{110} = 3.143 \text{ \AA}^{-1}$ by the crystal truncation rod (CTR), which appears as a bright line. The equally spaced numbered satellites on the CTR originate from the vertical periodicity of the sample structure. Their vertical spacing of 0.0327 \AA^{-1} reveals a QD layer-to-layer period of 19.2 nm, in good agreement with the nominal value of 20 nm. The weaker ancillary maxima between these satellites reflect the overall thickness of the five-fold QD stack.

The laterally extended and homogeneous sample regions of the GaAs matrix and the WLs between the QD columns solely contribute to the intensity on and close to the CTR, because the lateral lattice parameter here is very close to that of the GaAs substrate, and thus only vertical strain exists in that area. This is evidenced by a simulation of the lateral strain tensor component ϵ_{xx} across one QD column as shown in Fig. 2(a) and the vertical strain tensor component ϵ_{zz} as shown in Fig. 2(b). Since the volume of the QDs is small as compared to that of the remaining sample structure, the intensity distribution on and close to the CTR is strongly dominated by scattering from the extended regions between the QD columns. Consequently, the vertical position of the zero-order satellite on the CTR at $q_{001} = 4.427 \text{ \AA}^{-1}$ enables a measure of the mean In content of the WLs: it is assessed to be 2 GaAs lattice constants $a = 5.6532\text{-\AA}$ thick and to contain 37% In. It must be noted that variations of the WL thickness in the simulations essentially alter the intensities of higher-order satellites only, provided that the product of WL thickness and In concentration is kept constant. The assumed thickness corresponds to values previously reported for similar InGaAs/GaAs QD stacks¹² as revealed by transmission elec-

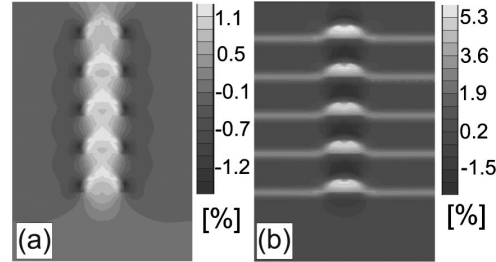


FIG. 2. Maps of the total strain tensor components ϵ_{xx} (a) and ϵ_{zz} (b) for a QD as shown in Fig. 3(b), calculated using the finite element method. Relative strain values as denoted in the scale refer to the GaAs lattice parameters.

tron microscopy. The In concentration of 37% is considerably smaller than the nominal value of 60%. This difference can be explained by In migration from the WL towards the QDs during island formation^{13,14} as substantiated later.

Figure 2(a) shows that only the dot stack comprises regions of nonzero lateral strain. Therefore, only these regions give rise to the diffuse scattering on both sides of the CTR. This makes the diffuse signal an appropriate means to probe the In distribution within the QDs and the transition regions to the adjacent GaAs matrix. The diffuse scattering shows a rather complicated intensity pattern; note, e.g., shape and orientation of the features P1 and P2 in Fig. 1(d), which show the effect of locally compressed and dilatated regions, respectively. The complexity of the intensity distribution prevents straightforward conclusions on the QD morphology. To extract quantitative information, we performed dynamical scattering simulations probing different QD shapes, namely cuboids, pyramids, flat lenses, and inverted cones. In turn, different In concentration profiles were assumed for the respective shapes. Figure 3 shows cross-sectional schemes of three selected model QDs we simulated in this work. A lens-like QD with 60% In content on top of a WL is shown in Fig. 3(a). The second model QD shown in Fig. 3(b) has the same shape, size, and In concentration as the previous one, but

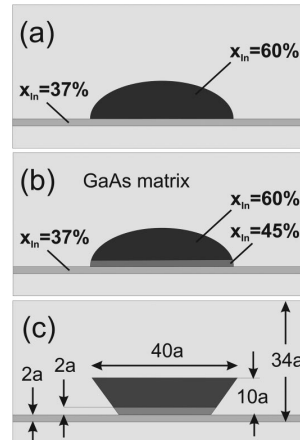


FIG. 3. Model QD shapes and compositions used for scattering simulations. The wetting layer contains 37% In in all three structures. (a) Lens-shaped QD with homogeneous QD apex, containing 60% In. (b) Lens-like QD with a $2 \times a$ GaAs thick transition layer containing 45% In. (c) Inverted-cone-shaped QD with a $2 \times a$ GaAs transition layer containing 45% In. Dot dimensions are given in units of the GaAs lattice parameter a .

comprises a $2 \times a$ thick $\text{In}_{0.45}\text{Ga}_{0.55}\text{As}$ transition layer between WL and the QD apex. The third model QD depicted in Fig. 3(c) exhibits the same vertical chemical composition profile as that of Fig. 3(b), but has an inverted-cone shape. Previous investigations have shown that the in-plane symmetry of the QDs must be at least fourfold,¹² so elongated objects were not considered. Our assumption of the In content increasing from 45% to 60% in the QD apex approximates a steadily increasing In proportion as previously proposed for nonburied InGaAs QDs, based on the evaluation of grazing-incidence x-ray diffraction measurements.¹⁴

The calculated intensity distributions of the three QDs [Figs. 3(a)–3(c)] are shown in Figs. 1(a)–1(c), respectively. All simulations reproduce the periodicity of the fivefold QD stack. However, Fig. 1(a) referring to a lens-like QD without transition layer, does not describe any detail of the diffuse scattering from the dots. This is particularly obvious if the measured features $P1$ and $P2$ are compared to the simulation. In contrast to Fig. 1(a), Figs. 1(b) and 1(c) referring to the lens-like and inverted-cone QD shape with transition layer, respectively, reflect the particular shapes of $P1$ and $P2$ and also other dot-related scattering intensity distributions very well. The rough approximation of a gradually increasing concentration profile by just a single step may be justified by the fact that the exact characteristics of the vertical profile essentially affects the intensities of high-order satellites only. Such high-order satellites are not shown here, because variations of their intensities cannot be resolved experimentally due to their low signal strengths. The remarkable similarity of Figs. 1(b) and 1(c) shows that the diffusely scattered x-ray signal of the measured low-order satellites is largely insensitive to variations of the QD shape. Therefore, the QD shape could not be determined further using the available data. In spite of such experimental limitations, our findings clearly indicate a nonhomogeneous vertical In concentration which increases towards the QD apex. During formation, the upper parts of uncovered QDs can elastically relax well, since no lateral constraints prevent the lattice to expand. Therefore, the QD strain decreases from the bottom to the top of the QD. As long as the QDs are uncovered, lateral In migration from the WL to the QDs, as well as vertical In segregation from the QD bottom to the apex,¹⁵ are both favorable in terms of strain energy.

In summary, high-resolution diffuse x-ray scattering from five closely stacked InGaAs/GaAs quantum dot layers shows a complex intensity pattern which can be well described by dynamical scattering simulations if a vertical In concentration is assumed, which increases from the wetting layer towards the dot apex. A low In concentration in the WL as determined from the data indicates a migration of In from the WL to the QD apex during QD formation.

The authors gratefully appreciate the help of W. Drube (HASYLAB) during experiments. This work was supported by the Deutsche Forschungsgemeinschaft in the framework of Sonderforschungsbereich 296 projects A3 and A7, and by Project No. KO1510/2. R.L.S. acknowledges funding by Bookham Technologies.

- ¹D. Bimberg, M. Grundmann, and N. N. Ledentsov, *Quantum Dot Heterostructures* (Wiley, Chichester, NY, 1999).
- ²V. A. Shchukin, N. N. Ledentsov, and D. Bimberg, *Epitaxy of Nanostructures* (Springer, New York, 2004).
- ³D. Bimberg and N. N. Ledentsov, *J. Phys.: Condens. Matter* **15**, R1 (2003).
- ⁴P. W. Fry, I. E. Itskevich, D. J. Mowbray, M. S. Skolnick, J. J. Finley, J. A. Barker, E. P. O'Reilly, L. R. Wilson, I. A. Larkin, P. A. Maksym, M. Hopkinson, M. Al-Kafaji, J. P. R. David, A. G. Cullis, G. Hill, and J. C. Clark, *Phys. Rev. Lett.* **84**, 733 (2000).
- ⁵P. Jayavel, H. Tanaka, T. Kita, O. Wada, H. Ebe, M. Sugawara, J. Tatebayashi, Y. Arakawa, Y. Nakata, and T. Akiyama, *Appl. Phys. Lett.* **84**, 1820 (2004).
- ⁶N. Liu, H. K. Lyeo, C. K. Shih, M. Oshima, T. Mano, and N. Koguchi, *Appl. Phys. Lett.* **80**, 4345 (2002).
- ⁷N. Liu, J. Tersoff, O. Baklenov, J. A. L. Holmes, and C. K. Shih, *Phys. Rev. Lett.* **84**, 334 (2000).
- ⁸A. Lenz, R. Timm, H. Eisele, C. Hennig, S. K. Becker, R. L. Sellin, U. W. Pohl, D. Bimberg, and M. Dähne, *Appl. Phys. Lett.* **81**, 5150 (2002).
- ⁹D. Grigoriev, M. Hanke, M. Schmidbauer, P. Schäfer, O. Konovalov, and R. Köhler, *J. Phys. D* **36**, A225 (2003).
- ¹⁰M. Hanke, M. Schmidbauer, D. Grigoriev, P. Schäfer, R. Köhler, A.-K. Gerlitzke, and H. Wawra, *Phys. Rev. B* **69**, 075317 (2004).
- ¹¹R. L. Sellin, F. Heinrichsdorff, C. Ribbat, M. Grundmann, U. W. Pohl, and D. Bimberg, *J. Cryst. Growth* **221**, 581 (2000).
- ¹²M. Hanke, D. Grigoriev, M. Schmidbauer, P. Schäfer, R. Köhler, U. W. Pohl, R. L. Sellin, D. Bimberg, N. D. Zakharov, and P. Werner, *Physica E* (Amsterdam) **21**, 684 (2004).
- ¹³A. Krost, F. Heinrichsdorff, D. Bimberg, A. Darhuber, and G. Bauer, *Appl. Phys. Lett.* **68**, 785 (1996).
- ¹⁴I. Kegel, T. H. Metzger, A. Lorke, J. Peisl, J. Stangl, G. Bauer, K. Nordlund, W. V. Schoenfeld, and P. M. Petroff, *Phys. Rev. B* **63**, 035318 (2001).
- ¹⁵L. G. Wang, P. Kratzer, N. Moll, and M. Scheffler, *Phys. Rev. B* **62**, 1897 (2000).

Available online at www.sciencedirect.comSCIENCE @ DIRECT[®]

Physica E 21 (2004) 684–688

PHYSICA Ewww.elsevier.com/locate/physe

Diffuse X-ray scattering of InGaAs/GaAs quantum dots

M. Hanke^{a,*}, D. Grigoriev^a, M. Schmidbauer^a, P. Schäfer^a, R. Köhler^a, U.W. Pohl^b,
R.L. Sellin^b, D. Bimberg^b, N.D. Zakharov^c, P. Werner^c

^aInstitut für Physik, Humboldt-Universität zu Berlin, Newtonstrasse 15, D-12489 Berlin, Germany

^bInstitut für Festkörperphysik, Technische Universität Berlin, Hardenbergstrasse 36, D-10632 Berlin, Germany

^cMax-Planck-Institut für Mikrostrukturphysik, Weinberg 2, D-06120 Halle, Germany

Abstract

We report on structural investigations on multi-fold stacks of $\text{In}_{0.6}\text{Ga}_{0.4}\text{As}$ quantum dots (QDs) embedded within a GaAs matrix. The structures have been grown by means of metalorganic chemical vapor deposition. Cross-sectional transmission electron micrographs prove a pronounced *vertical* QD correlation, while plan-view images do not show any *lateral* ordering. Grazing incidence diffraction within various crystallographic zones clearly reveal a QD shape with a four-fold symmetry. Comparing dynamical scattering simulations, which base on finite element calculations for the strain field show that the shape of the QDs can be described by a prism with a flat top on a thin wetting layer. The mean lateral dot distance evaluated from diffuse X-ray scattering agrees well with the QD density estimated from TEM plan-view images.

© 2003 Elsevier B.V. All rights reserved.

PACS: 68.65.-k; 61.10.-i; 81.15.Kk

Keywords: Diffuse X-ray scattering; InGaAs/GaAs quantum dots; MOCVD

Strained self-organized InGaAs/GaAs quantum dots (QDs) are presently a subject of intense research efforts [1] due to their promising potential for optoelectronic device applications within the optical window of silica fiber at $1.3 \mu\text{m}$ [2] and even at wavelengths beyond. X-ray scattering is a sensitive probe of the spatial strain distribution and can thus yield information on the spatial distribution of indium. This allows to draw conclusions on the shape and chemical composition of buried InGaAs QDs. The QD shape or, more general, the actual chemical composition profile within will decisively affect optical and electronical device properties.

Cross-sectional tunneling microscopy (XSTM) has been widely applied to obtain structural and chemical information on buried InGaAs QDs [3,4]. Thereby, a many-fold variety of different indium profiles has been observed. Among them are QDs with a reversed trapezoidal [5] or a reversed pyramidal [6] indium cone—both of them without any wetting layer underneath, and, a reversed truncated In-enriched core within a comparatively thick wetting layer [7]. We applied transmission electron microscopy (TEM) and non-invasive diffuse X-ray scattering techniques along with dynamical scattering simulations to reveal the structural information of the QDs.

The sample investigated here consists of a five-fold stack of self-organized $\text{In}_{0.6}\text{Ga}_{0.4}\text{As}$ QDs, separated by nominally 20 nm GaAs spacer layers. The structure was grown on an undoped GaAs(001)

* Corresponding author.

substrate using metalorganic chemical vapor deposition (MOCVD). The precursors were trimethylgallium, trimethylindium and pure arsine. Hydrogen was used as carrier gas. The QD layers were each grown at 500°C, all other layers were deposited at higher temperatures. A cross-sectional TEM image of the structure as shown in Fig. 1b indicates a strong vertical correlation of the QDs throughout the entire stack. This correlation results from the long-range strain fields of the compressively strained QDs combined with a relatively small spacer layer thickness, determining the lateral nucleation site of the QDs from the second QD layer on. The QD sheets could be stacked so closely due to a surface flattening technique applied after the growth of each QD sheet [8]. A plan-view image of the structure (Fig. 1a) indicates that the QDs are laterally not correlated.

Complementary to direct imaging techniques we applied high resolution X-ray diffraction (HRXRD) and grazing incidence diffraction (GID) using highly brilliant X-rays with an energy of 8 keV. Since morphological information on the QDs and the surrounding matrix material are of three-dimensional (3D) nature in real space, a 3D record of diffuse intensity in reciprocal space becomes reasonable. Thus, we made particular use of a linear position sensitive detector (PSD) aligned perpendicular to the sample surface in combination with a Si(1 1 1) crystal collimator in front of it

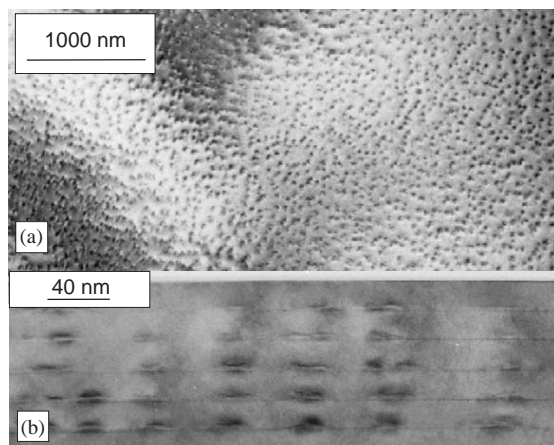


Fig. 1. Transmission electron micrograph in plan-view (a) and cross-section (b). A pronounced vertical ordering of QDs is visible (b), while no indication of a lateral ordering is found (a).

to ensure a sufficiently high resolution. For a detailed description of the experimental setup see Refs. [9,10]. The scattering simulations shown here are based on a dynamical treatment within the framework of distorted wave born approximation (DWBA). The details of the method have been published elsewhere [11].

The actual shape of the QDs critically depends on the applied growth conditions. On the other hand, it distinctly influences optical and electronical properties. Several papers report on a weak QD shape asymmetry [12–14]. However, also elongated QDs with a larger extension along [1 1 0] [15] as well as an inverse lateral orientation have been observed in the InGaAs/GaAs system [16,17].

In order to determine morphological QD parameters as well as strain status and chemical composition, pairs of reciprocal lattice points in GID geometry have been investigated. Fig. 2 shows the out-of-plane intensity distributions in vicinity of 200 and 020 reciprocal lattice points, respectively. Reflections of this type are quasi-forbidden in a zincblende structure because only the difference of atomic formamplitudes f_i enters the scattering process. Hence the signal caused

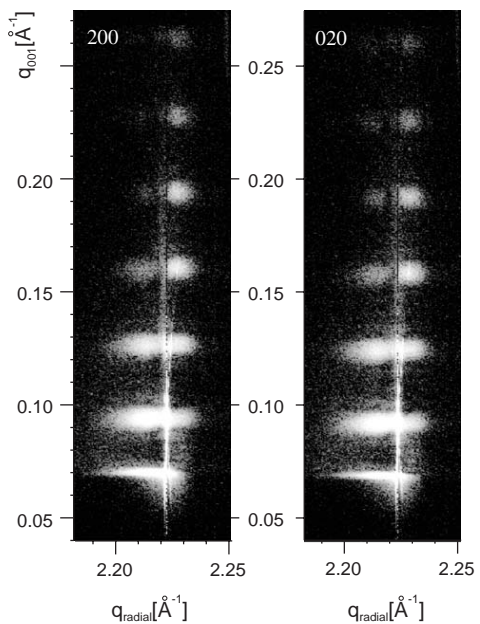


Fig. 2. Diffusely scattered out-of-plane intensity near the 200 and 020 reciprocal lattice points. The similarity of both hints to a QD shape symmetry regarding the different $\langle 1\ 0\ 0 \rangle$ directions.

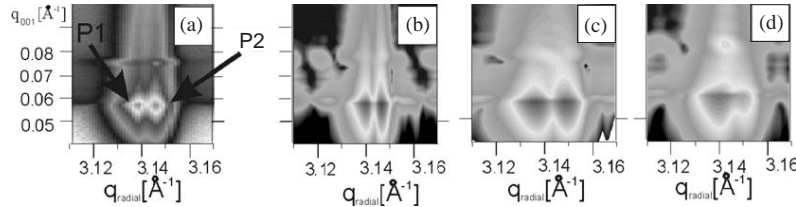


Fig. 3. GID out-of-plane in the vicinity of 220 reciprocal lattice point. (a) depicts the measured distribution, (b–d) show various dynamical scattering simulations based on different QD shapes and lateral QD spacing. For details see text. The gray scale changes from black (low intensity) via white to black (highest intensity) within the two pronounced peaks P1 and P2.

by the GaAs matrix can be suppressed to some extent with respect to the QD signal itself. To ensure that the wavefield is probing the entire QD stack, an incidence angle of 0.5° has been chosen which is clearly above the critical angle of total external reflection α_c . From the vertical superlattice period of $3.239 \times 10^{-2} \text{ \AA}^{-1}$ we can conclude a mean period of 19.4 \AA in real space. The high similarity between the $\langle 1\ 0\ 0 \rangle$ -directions is caused by a strain isotropy with respect to $[1\ 0\ 0]$ and $[0\ 1\ 0]$ -direction. This can be understood in terms of a QD shape symmetry. Also the $[1\ 1\ 0]$ and $[1\ \bar{1}\ 0]$ -direction are equivalent (not shown here), finally indicating an at least four-fold QD symmetry with no preferential lateral alignment.

To reveal the detailed *lateral* and *vertical* chemical profile we made use of highly strain-sensitive diffuse X-ray scattering along with dynamical scattering simulations. According to the iterative ‘brute-force’ method described in Ref. [11] we have systematically explored various QD shapes and composition profiles. Vertical dimensions of the appropriate FEM model have been extracted from cross-sectional TEM images and by the vertical superlattice structures appearing in respective GID measurements. Fig. 3a depicts the measured diffuse intensity distribution around the 220 reciprocal lattice point and respective dynamical simulations (b–d). A 1 nm wetting layer with the same composition as that of the QDs has been introduced in any case. Although the experimental features P1 and P2 appear qualitatively in all simulations, there are conspicuous differences left regarding radial position and intensity ratio, especially in (c) and (d). Model (c) is based on a particular prismatic dot shape—a cuboid $20 \text{ nm} \times 20 \text{ nm} \times 5 \text{ nm}$, which approximates the experimentally found flat, truncated pyramid shape [7], (d) on a pyramidal one of exactly

the same quadratic ground plan, height and composition ($x_h=45\%$). Within the FEM process a laterally periodic arrangement has been considered by applying quasi-periodic boundary conditions at the outermost FEM-nodes. Since the actual shape apparently influences the intensity ratio I_{P1}/I_{P2} , there is no change in radial distance $\Delta q_{P1} - \Delta q_{P2}$. A pyramidal QD will cause a pronounced peak P1 which can be attributed to dilatated sample regions, whereas P2—a fingerprint of laterally compressed areas—appears weaker. This is in clear contradiction to the experimental observation. However, a cuboid QD shape of model (c) causes an intensity ratio of nearly one. Thus, we have got an indication to a prismatic QD with a flat top. In simulation (b) and (c) the QD shape has been fixed (cuboid), however, the lateral distance between the dots changes by a factor of two. l_{lateral} amounts to 40 nm (c) and 80 nm in case (b), which is slightly above the distance visible in Fig. 1b. Since the radial distance $\Delta q_{P1} - \Delta q_{P2}$ shrinks to the same extent as l_{lateral} increases, we could deduce the mean lateral distance between two QDs to about 80 nm. The corresponding QD density of about $2 \times 10^{10} \text{ cm}^{-2}$ is in good agreement with results from plan-view TEM images, although the partial cross-section images a sample region with slightly smaller lateral distances.

Because the indium content does not significantly impact GID-related features, we additionally applied conventional HRXRD. Fig. 4 shows the measured distribution around the asymmetrical GaAs(2 2 4) substrate peak labeled S. The vertical periodicity of the QD stack leads to pronounced superlattice satellites (SL), whereas the diffuse intensity appears within distinct clouds nearby the crystal truncation rod (CTR), indicating a strong vertical QD correlation. Furthermore, the lateral shift refers to locally dilatated (left of

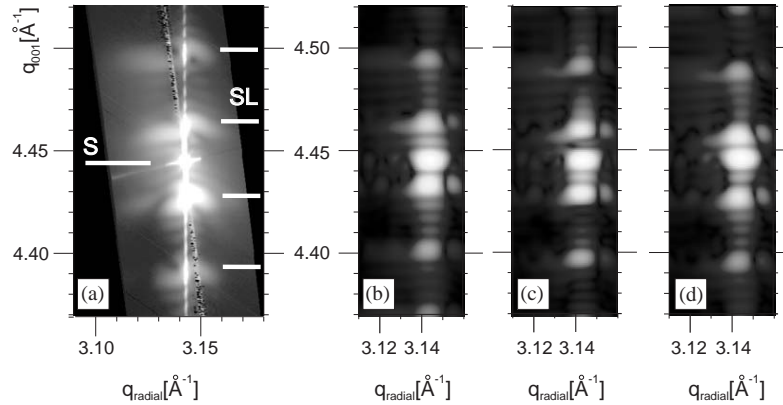


Fig. 4. Measured diffuse intensity in the vicinity of the asymmetrical 224 reciprocal lattice point (a). The pronounced intensity clouds near the CTR indicate a strong vertical dot-dot correlation. (b-d) show respective scattering simulations assuming a cuboid QD shape and indium contents of 30%, 40% and 45%, respectively.

the CTR) and compressed (right of the CTR) regions in the QD stack, which can be attributed to QDs and surrounding matrix material. The vertical distance between the substrate reflection and the 0th order superlattice peak significantly changes with the averaged strain which is related to the indium content. Thus, in case of models considering a cuboid QD shape we gradually modified the indium content between 30% and 45% within a set of simulations. Fig. 4(b-d) shows the respective calculations, whereby the best agreement could be achieved assuming an indium content of 40%. Such a large deviation from the nominal value of 60% is not expected according to TEM studies. Thus, to improve data evaluation further, free parameters in the simulation, e.g. wetting layer thickness and chemical composition have to be considered.

In conclusion we have investigated five-fold stacks of nominally $\text{In}_{0.6}\text{Ga}_{0.4}\text{As}$ QDs within a GaAs matrix grown by MOCVD. TEM of the sample reveal a pronounced vertical QD correlation. Measurements of diffuse X-ray scattering in comparison with dynamical scattering simulations indicate a flat, prismatic dot shape. Furthermore, we could prove a significant influence of the *mean* lateral dot distance to the diffuse scattering, though no lateral ordering of the QDs exists in the sample. The corresponding QD density is well confirmed by TEM images.

We would like to thank B. Struth and O. Konovalov at beamline ID10B (ESRF) and W. Drube at BW2

station (HASYLAB) for their experimental assistance. This project was sponsored by DFG in the framework of the Sonderforschungsbereich 296.

References

- [1] D. Bimberg, M. Grundmann, N.N. Ledentsov, *Quantum Dot Heterostructures*, Wiley, Chichester, 1999.
- [2] N. Ledentsov, D. Bimberg, V. Ustinov, Z.I. Alferov, J.A. Lott, *Jpn. J. Appl. Phys. Part 1* 41 (2002) 949.
- [3] W. Barvosa-Carter, M. Twigg, M. Yang, L. Whitman, *Phys. Rev. B* 63 (2001) 245311.
- [4] B. Grandidier, Y. Niquet, B. Legrand, J. Nys, C. Priester, D. Stivenard, J. Gerard, V. Thierry-Mieg, *Phys. Rev. Lett.* 85 (2000) 1068.
- [5] N. Liu, H. Lyeo, C. Shih, M. Oshima, T. Mano, N. Koguchi, *Appl. Phys. Lett.* 80 (2002) 4345.
- [6] N. Liu, J. Tersoff, O. Baklenov, J.A.L. Holmes, C.K. Shih, *Phys. Rev. Lett.* 84 (2000) 334.
- [7] A. Lenz, R. Timm, H. Eisele, C. Hennig, S. Becker, R. Sellin, U.W. Pohl, D. Bimberg, M. Dähne, *Appl. Phys. Lett.* 81 (2002) 5150.
- [8] R.L. Sellin, F. Heinrichsdorff, C. Ribbat, M. Grundmann, U.W. Pohl, D. Bimberg, *J. Cryst. Growth* 221 (2000) 581.
- [9] M. Hanke, Ph.D. Thesis, Humboldt-Universität zu Berlin, Mensch & Buch Verlag, Berlin, 2002.
- [10] M. Schmidbauer, M. Hanke, R. Köhler, *Cryst. Res. Technol.* 37 (2002) 3.
- [11] D. Groriev, M. Hanke, M. Schmidbauer, P. Schäfer, O. Konovalov, R. Köhler, *J. Phys. D* 36 (2003) A225.
- [12] J. Marquez, L. Geelhaar, K. Jacobi, *Appl. Phys. Lett.* 78 (2001) 2309.
- [13] Y. Nabetani, T. Ishikawa, S. Noda, A. Sasaki, *J. Appl. Phys.* 76 (1994) 347.

- [14] N.N. Ledentsov, P.D. Wang, C.M. SotomayorTorres, A.Y. Egorov, M.V. Maximov, V.M. Ustinov, A.E. Zhukov, P.S. Kop'ev, Phys. Rev. B 50 (1994) 12171.
- [15] W. Yang, H. Lee, T. Johnson, P. Sercel, A. Norman, Phys. Rev. B 61 (2000) 2784.
- [16] T. Hanada, B. Koo, H. Totsuka, T. Yao, Phys. Rev. B 64 (2001) 165307.
- [17] W. Ma, R. Nötzel, H.-P. Schönher, K.H. Ploog, Appl. Phys. Lett. 79 (2001) 4219.

3.2 Deformationsfreie GaAs *quantum dot molecules*

M. Hanke, M. Schmidbauer, D. Grigoriev, P. Schäfer, R. Köhler, T. H. Metzger, Zh. M. Wang, Yu. I. Mazur, G. J. Salamo

Zero-strain GaAs quantum dot molecules as investigated by x-ray diffuse scattering
Appl. Phys. Lett. **89**, 053116 (2006).

Im Stranski-Krastanow Prozess treibt im Wesentlichen der Gitterparameterunterschied die Heteroepitaxie und damit die Entstehung niedrigdimensionaler Strukturen. Absolut verspannungsfreie, technologisch nicht weniger relevante *quantum dots* lassen sich auf diese Weise prinzipiell nicht erzeugen. Einen sehr eleganten Weg geht man dafür mit der sogenannten *droplet epitaxy* (Tröpfchenepitaxie). Im hier untersuchten System GaAs(001)/AlGaAs¹⁵ scheidet man während der MBE zunächst metallisches Gallium ab, das auf der Oberfläche kleine Flüssigkeitstropfen bildet. In einem zweiten Schritt setzt man die so prozessierte Oberfläche einem hohen Arsenfluss aus, durch welchen die Tröpfchen in einkristalline und mit dem Substrat heteroepitaktisch verbundene Nanokristalle umgewandelt werden. Durch geschickte Wahl der Wachstumsbedingungen lassen sich eine ganze Reihe bemerkenswerter Formen herstellen, u.a. *quantum rings* und sogenannte *quantum dot molecules* (QDMs) - eine lokale Anordnung einiger weniger *quantum dots*.¹⁶ Da zu Beginn der Kristallisation die Oberflächenspannung des (noch) metallischen Galliums rasch sinkt, kollabieren die Tröpfchen und verdrängen zunächst Material aus dem Inneren. Unterschiedliche Diffusionsgeschwindigkeiten führen schließlich zu Paaren einzelner *quantum dots*.

Mittels diffuser Röntgenstreuung lässt sich die mechanische Deformation in den GaAs QDMs sehr genau vermessen. Als Mittel der Wahl kam eine symmetrische GID Geometrie zum Einsatz, wobei die diffuse Intensität *in-plane* in der Nähe des 220 Reflexes untersucht wurde. Diese erscheint aufgrund des fehlenden Gittermisfits zentral um die nominelle Si(220) Substratposition, zeigt mithin allein die Fouriertransformierte der Formfunktion der QDMs. Da es sich bei diesen in erster Näherung um zwei rotationssymmetrische Objekte mit einem nahezu konstanten Abstand handelt, lässt sich die fouriertransformierte Formfunktion durch eine Überlagerung zweier Besselfunktionen beschreiben. Eine systematische Veränderung der Simulationsparameter erlaubt zudem die Abschätzung von Größe und mittlerem Abstand der individuellen *quantum dots*.

¹⁵Die Proben wurden am Lehrstuhl Prof. Dr. G. Salamo der University of Arkansas, Fayetteville (USA) hergestellt. Da der relative Gitterparameterunterschied zwischen GaAs und Al_{0.3}Ga_{0.7}As nur 0.046% beträgt, erfolgt das Wachstum der AlGaAs Schicht pseudomorph. Der laterale Gitterparameter setzt sich also in der Schicht fort, so dass die darauf entstehenden GaAs *quantum dot molecules* völlig verspannungsfrei aufwachsen.

¹⁶Hier sei auf Kap. 2.2.3 verwiesen, in dem die Entstehung vergleichbarer Strukturen im heteroepitaktischen System SiGe/Si detailliert untersucht wurde.

APPLIED PHYSICS LETTERS 89, 053116 (2006)

Zero-strain GaAs quantum dot molecules as investigated by x-ray diffuse scattering

M. Hanke^{a)}*Martin-Luther-Universität Halle-Wittenberg, Fachbereich Physik, Hoher Weg 8, D-06120 Halle/Saale, Germany*

M. Schmidbauer

Institut für Kristallzüchtung, Max-Born-Straße 2, D-12489 Berlin, Germany

D. Grigoriev, P. Schäfer, and R. Köhler

Humboldt-Universität zu Berlin, Newtonstraße 15, D-12489 Berlin, Germany

T. H. Metzger

*European Synchrotron Radiation Facility, BP 220, F-38043 Grenoble Cedex, France*Zh. M. Wang,^{b)} Yu. I. Mazur, and G. J. Salamo*Department of Physics, University of Arkansas, Fayetteville, Arkansas 72701*

(Received 16 March 2006; accepted 9 June 2006; published online 2 August 2006)

The authors report on x-ray diffuse scattering at nominally strain-free GaAs(001) quantum dot molecules (QDMs). Al_{0.3}Ga_{0.7}As deposited by molecular beam epitaxy on GaAs(001) acts as barrier layer between the GaAs(001) substrate and subsequently grown QDMs; the adjusted thickness of 50 nm preserves the in-plane lattice parameter. Pairs of lenslike quantum dots are created with preferential orientation along [110] placed on shallow hills. Grazing incidence diffraction along with kinematical scattering simulations indicate completely strain-free QDs which prove a strongly suppressed intermixing between QDMs and the underlying AlGaAs barrier layer. © 2006 American Institute of Physics. [DOI: [10.1063/1.2240114](https://doi.org/10.1063/1.2240114)]

Semiconductor quantum dots (QDs) have pushed an overwhelming interdisciplinary research effort, which comprises a large variety of fabrication techniques^{1,2} and analytical tools. Possible technological applications exploit the improved electrical and optical properties compared with bulk material.^{3,4} Self-formation of QDs via the Stranski-Krastanov process⁵ provides an elegant and simple alternative to expensive and time-consuming template based approaches.⁶ Often the QD formation is accompanied by pronounced lateral,⁷ vertical,⁸ or three-dimensional⁹ assembling on an extended length scale. Quantum dot molecules (QDMs), on the other hand, are individual groups of QDs with a particular *local* arrangement.^{10–12} They are frequently discussed as storage device for quantum bits (qubits).¹³ The simplest QDM (just a pair of QDs) seems a rather promising candidate to locally implement two qubits. However, electronic properties are related to the QD/QDM morphology, which can be investigated by x-ray diffuse scattering.^{5,14} Namely, the isostrain method^{15,16} and scattering simulations based on numerical calculations using linear elasticity theory¹⁷ are well-established approaches towards three-dimensionally resolved strain and composition profiles of QDs and QDMs.

Here we present a structural investigation of nominally zero-strain QDM in the system GaAs/AlGaAs. The samples were grown on epiready GaAs(100) substrates by molecular beam epitaxy applying a droplet epitaxy. After the growth of a 500 nm GaAs buffer layer, 50 nm of Al_{0.3}Ga_{0.7}As were deposited at 600 °C. After a cooling to 550 °C, Ga atoms were supplied to form small liquid droplets on the

Al_{0.3}Ga_{0.7}As surface, corresponding to the amount necessary for the growth of 10.0 ML GaAs. Afterwards, the sample was annealed under arsenic flux to form GaAs QDMs. A detailed description and explanation of the growth scenario is given in Ref. 18. Briefly, the Ga droplets act as Ga nanosource for further growth of GaAs. However, owing to the high temperature involved, the crystallization process is accompanied by strong material redistribution. The crystallization of Ga droplets proceeds at a much faster rate at high temperature so that surface processes on the GaAs surface can play a more important role in the shape evolution of the GaAs nanostructure. At the beginning of the crystallization process the surface tension of the Ga droplet quickly decreases, inducing an abrupt collapse down the center of the droplet, pushing the material away from the center. Eventually, this leads to the formation of square holed round coins. With further annealing and crystallization the material from the edges of the square holed object tends to fill the center hole but at different rates depending on direction. After 45 s annealing GaAs quantum dot pairs are formed (Fig. 1). Since the lattice mismatch between the GaAs substrate and the AlGaAs layer is very small ($\Delta a/a = 4.6 \times 10^{-3}$), the thin Al_{0.3}Ga_{0.7}As layer is grown coherently onto the GaAs substrate, thus ensuring nominally strain-free growth of the QDMs on top of the AlGaAs layer.

The x-ray scattering experiments were performed using highly brilliant synchrotron radiation provided by the ID01 undulator station of the European Synchrotron Radiation Facility (ESRF) in Grenoble, France. An x-ray energy of 8 keV was selected by a Si(111) double crystal monochromator with a relative bandwidth of better than $\Delta E/E = 10^{-4}$. In order to be particularly sensitive to the QDMs located at the surface and to suppress scattering from the underlying mate-

^{a)}Electronic mail: hanke@physik.uni-halle.de
^{b)}Electronic mail: zhmwang@gmail.com

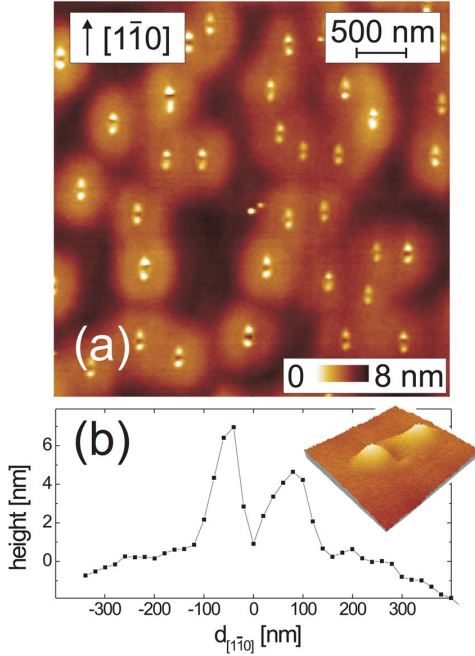


FIG. 1. (Color online) The atomic force micrograph of the sample surface (a) depicts quantum dot molecules oriented along the $[1\bar{1}0]$ direction. (b) gives the height profile through a QDM (inset).

rial, a grazing incidence scattering geometry was employed; thereby, the glancing angle of incidence $\alpha_i=0.25^\circ$ with respect to the surface was chosen below the critical angle of total external reflection ($\alpha_c=0.31^\circ$). In order to improve the in-plane angular resolution and to suppress the overall background a Si(111) crystal analyzer was employed behind the sample. Vertically, a position sensitive detector was used to probe the intensity distribution as a function of the glancing exit angle α_f . With this arrangement, the entire three-dimensional intensity distribution around an in-plane reciprocal lattice point can be recorded with extremely high resolution. Typical values for the in-plane/out-of-plane resolution are $\delta q_\parallel=1\times 10^{-3}$ nm $^{-1}$ and $\delta q_\perp=5\times 10^{-3}$ nm $^{-1}$, respectively.

The scattering geometry has been chosen such that the $[1\bar{1}0]$ axis of the QDM is collinear with the strain-insensitive angular direction $q_{\text{ang}}\equiv q_{1\bar{1}0}$. This enables accurate determination of the QDM size and interdot distance, independent of the strain state of the QDMs. On the other hand, the scattering geometry enables us to probe strain perpendicular to the axis of the QDM, i.e., along the $[110]$ direction. Strain would lead to a small shift of the overall diffuse intensity distribution with respect to the strong substrate reflection which is located at $q_{\text{rad}}=31.436$ nm $^{-1}$. However, no such shift could be observed neither around the 220 nor the $\bar{2}\bar{2}0$ reciprocal lattice point, proving that the QDMs are completely free of strain.

Figure 2(a) shows the experimental x-ray diffuse scattering from the ensemble of QDMs in the vicinity of the 220 reciprocal lattice point. Distinct intensity oscillations are observed in the $q_{1\bar{1}0}$ direction. However, the in-plane envelop function of the experimental data indicates rotational symmetry, suggesting that the shape of the individual QDs within

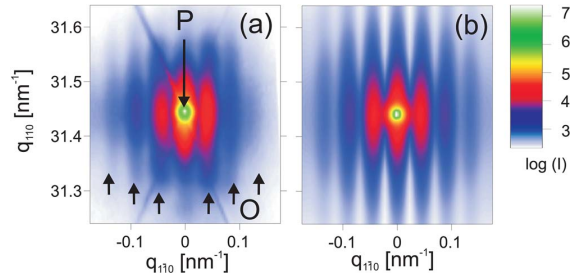


FIG. 2. (Color online) X-ray diffuse intensity distribution in the vicinity of the 220 in-plane reciprocal lattice point. The experimental data (a) shows the substrate reflection (P) which is superimposed by various intensity oscillations (O). (b) depicts a corresponding simulation.

the QDM exhibits rotational symmetry with the symmetry axis oriented along the vertical $[001]$ direction.

The observed intensity distribution can be qualitatively explained within the kinematical scattering approach where the scattered amplitude of a nonstrained homogeneous object is given by the Fourier transform of its shape function, which is defined to be unity inside the object and, accordingly, zero outside. Consequently, the amplitude of the scattered wave from a single rotationally-symmetric QD can be described by a corresponding rotationally shaped distribution in the Fourier space, with a central maximum at $q_\parallel=0$ and a corresponding width of $\Delta q_\parallel=2\pi/R$, with R being the characteristic radius of the QD. The scattered amplitude of the entire QDM is then given by coherent superposition of the two scattered waves from the two individual QDs. Since all QDMs are oriented along the $[1\bar{1}0]$ direction, the corresponding interference phenomena lead to pronounced maxima in the diffuse intensity for $q_{1\bar{1}0}=2\pi\cdot n/d$, where d is the distance between the centers of the two QDs within the QDM and $n=\pm 1, \pm 2, \dots$. Thus, the size of the individual QDs and their spacing within the QDM can be unambiguously distinguished and evaluated independently. Using the given formulas, we can extract $d \approx 140$ nm and $R \approx 35$ nm from the experimental intensity distribution shown in Fig. 2(a).

A more detailed quantitative evaluation can be performed by comparing the experimental intensity distribution with corresponding simulations of diffuse scattering [Fig. 2(b)] using kinematical scattering theory.¹⁹ Respective sections of experiment (open circles) and simulation (solid line) through the central peak in Fig. 2 are displayed in Fig. 3. It is interesting to note that—in accordance with the atomic force micrograph displayed in Fig. 1—a satisfactory simulation can only be achieved by taking into account that the QDMs are grown on an elongated flat hill of about 5 nm height and $W_{110}=400$ nm and $W_{1\bar{1}0}=700$ nm base widths. These hills are due to the high As flux and corresponding limited Ga transport. This is confirmed since by lowering the arsenic flux, two-dimensional growth of GaAs is enhanced and the hills are observed to disappear. In the x-ray scattering they lead to a prominent peak [feature P marked in Figs. 3(a) and 3(b)] in the immediate vicinity of the 220 reciprocal lattice point at $q_{1\bar{1}0}=31.436$ nm $^{-1}$ and $q_{\perp}=0$.

The diffuse intensity apart from feature P is solely related to the QDMs. In particular, the foot slope of the curve [feature F marked in Fig. 3(a)] is sensitive to the base widths and shape of the individual dots. On the other hand, the behavior (position and intensity decay) of the side maxima at

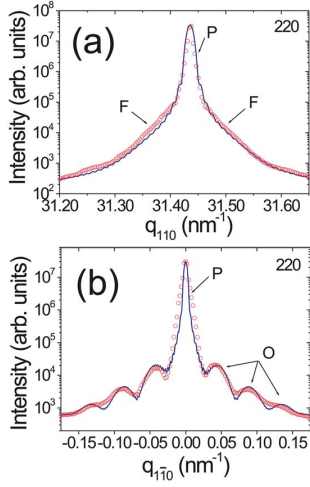


FIG. 3. (Color online) Sections through the intensity distributions shown in Fig. 2, simulations (solid lines), and experimental data (open circles). (a) Perpendicular to the QDM axis (q_{110} direction) extended diffuse scattering shows up (F), which is caused by the shape function of an individual QD. The shape of the prominent central peak (P) is due to scattering from an elongated flat hill ($W_{110}=400$ nm, $W_{1\bar{1}0}=700$ nm, and $H=5$ nm) located below the QDM. (b) Along the QDM axis (q_{110} direction) intensity oscillations (O) are observed, which are caused by interference between the scattered waves from each individual dot.

features O , marked in Fig. 3(b), of the intensity distribution on the curve foot allows for evaluating the spatial dot-dot correlation parameters within the QDM. Excellent agreement between experiment and simulation is achieved when the QDMs are assumed as two flat domes exhibiting a base radius of $R=40$ nm and a height of $h=5$ nm, separated by $d=135$ nm. These parameters are in correspondence with the surface morphology as revealed by atomic force microscopy (AFM) (Fig. 1).

Additionally, we would like to note that in the simulations a small fluctuation ($\sigma=8$ nm) of the QDM extension along [110] is assumed, while the shape and size of the single dots of the QDMs are kept fixed. The resulting good agreement between simulation and experiment is a strong indication that the QDMs are highly monodisperse in size and shape. On the other hand, the experimental data show that the positions of the QDMs are—despite their unique size, shape, and orientation—not correlated but are randomly distributed across the surface.

In conclusion we have applied grazing incidence diffraction and corresponding scattering simulation to reveal morphological parameters of nominally strain-free GaAs QDMs. The revealed QD shape, size, and their particular assembly within the QDMs are in excellent agreement with corresponding AFM images. Moreover, we could prove the absence of any strain within the QDMs which indicates a strongly suppressed intermixing during the QDM growth.

One of the authors (M.H.) acknowledges financial support by the Federal State of Sachsen-Anhalt, Germany within the Cluster of Excellence (CoE) Nanostructured Materials, Project NW3. Fundings by the German Research Foundation Grant No. HA3495/3 for one author (M.H.) and within the SFB 296 Project A3 for another author (D.G.) are highly appreciated. The authors thank the ESRF, Grenoble for providing synchrotron beam time during experiment HS2479.

- ¹V. A. Shchukin, N. N. Ledentsov, and D. Bimberg, *Epitaxy of Nanostructures* (Springer, New York, 2004).
- ²M. A. Herman, W. Richter, and H. Sitter, *Epitaxy, Physical Principles and Technical Implementations* (Springer, Berlin, 2004).
- ³J. Stangl, V. Holý, and G. Bauer, Rev. Mod. Phys. **76**, 725 (2004).
- ⁴M. S. Skolnick and D. J. Mowbray, Annu. Rev. Mater. Res. **34**, 181 (2004).
- ⁵D. J. Eaglesham and M. Cerullo, Phys. Rev. Lett. **64**, 1943 (1990).
- ⁶S. Kiravittaya, A. Rastelli, and O. G. Schmidt, Appl. Phys. Lett. **88**, 043112 (2006).
- ⁷M. Hanke, H. Raidt, R. Köhler, and H. Wawra, Appl. Phys. Lett. **83**, 4927 (2003).
- ⁸J. Tersoff, C. Teichert, and M. G. Lagally, Phys. Rev. Lett. **76**, 1675 (1996).
- ⁹M. Schmidbauer, S. Seydmohamadi, D. Grigoriev, Z. M. Wang, Y. I. Mazur, P. Schäfer, M. Hanke, R. Köhler, and G. J. Salamo, Phys. Rev. Lett. **96**, 066108 (2006).
- ¹⁰J. L. Gray, R. Hull, and J. A. Floro, Appl. Phys. Lett. **81**, 2445 (2002).
- ¹¹R. Songmuang, S. Kiravittaya, and O. G. Schmidt, Appl. Phys. Lett. **82**, 2892 (2003).
- ¹²M. Hanke, T. Boeck, A.-K. Gerlitzke, F. Syrowatka, and F. Heyroth, Appl. Phys. Lett. **88**, 063119 (2006).
- ¹³H. J. Krenner, M. Sabathil, E. C. Clark, A. Kress, D. Schuh, M. Bichler, G. Abstreiter, and J. J. Finley, Phys. Rev. Lett. **94**, 057402 (2005).
- ¹⁴M. Schmidbauer, *X-Ray Diffuse Scattering from Self-Organized Mesoscopic Semiconductor Structures*, Springer Tracts in Modern Physics Vol. 199 (Springer, Berlin, 2004).
- ¹⁵I. Kegel, T. H. Metzger, A. Lorke, J. Peisl, J. Stangl, G. Bauer, J. M. Garcia, and P. M. Petroff, Phys. Rev. Lett. **85**, 1694 (2000).
- ¹⁶B. Krause, T. H. Metzger, A. Rastelli, R. Songmuang, S. Kiravittaya, and O. G. Schmidt, Phys. Rev. B **72**, 085339 (2005).
- ¹⁷T. Wiebach, M. Schmidbauer, M. Hanke, H. Raidt, R. Köhler, and H. Wawra, Phys. Rev. B **61**, 5571 (2000).
- ¹⁸Z. M. Wang, K. Holmes, J. L. Shultz, and G. J. Salamo, Phys. Status Solidi A **202**, R85 (2005).
- ¹⁹M. Hanke, M. Schmidbauer, D. Grigoriev, P. Schäfer, R. Köhler, A.-K. Gerlitzke, and H. Wawra, Phys. Rev. B **69**, 075317 (2004).

3.3 Vertikal gestapelte InGaAs/GaAs *quantum rings*

M. Hanke, Yu.I. Mazur, E. Marega Jr., Z.Y. AbuWaar, G.J. Salamo, P. Schäfer, M. Schmidbauer

Shape transformation during overgrowth of InGaAs/GaAs(001) quantum rings

Appl. Phys. Lett. **91**, 043103 (2007).

In der Literatur finden sich eine ganze Reihe von Arbeiten, die die Herstellung und Untersuchung sogenannter *quantum rings* (QRs) diskutieren. Im System InAs/GaAs lassen sich solche Ringe beispielsweise durch das Überwachsen von InAs Quantenpunkten mittels GaAs herstellen. Die entstehenden Strukturen sind dann oft sehr flache, nur einige Atomlagen dicke, kreisrunde Scheiben mit einer zentralen Öffnung. Vor dem Hintergrund dieser drastischen Formänderung von Dots hin zu Ringen erscheint es naheliegend, dass ein zusätzliches Überwachsen die Ausgangsform der QRs weiter verändert. Ein Blick in die aktuelle Literatur zu diesem Thema zeigt jedoch, dass sich kaum Arbeiten dieser strukturellen Änderung während des erneuten Überwachsens widmen. Das erscheint umso überraschender, als dass sich eine elektrische Kontaktierung (mithin ein Überwachsen) der QRs im Rahmen möglicher opto-elektronischer Applikationen kaum umgehen lässt.

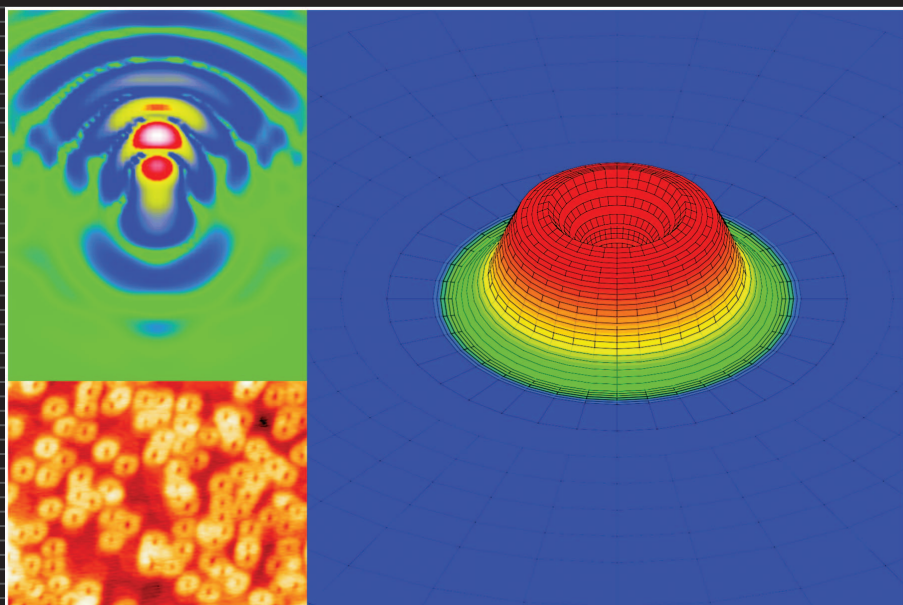
Um mögliche, durch das Überwachsen bedingte strukturelle Änderungen der QRs zu untersuchen, wurden neben einer Referenzprobe (die eine Einfachlage InGaAs QRs enthält) mehrere Zweifachstapel übereinander angeordneter QRs Schichten gezüchtet, wobei die Dicke der GaAs Zwischenschicht zwischen 2 und 10 nm variiert.¹⁷ Dabei zeigen die an der Oberfläche befindlichen QRs sowohl der Referenzprobe als auch des Zweifachstapels mit 10 nm Zwischenschicht nahezu kreisrunde Objekte. Im Falle einer sehr dünnen Zwischenschicht von nur 2 nm bilden sich jedoch an der Oberfläche entlang der [1 $\bar{1}$ 0] Richtung elongierte Ringe mit einem Aspektverhältnis $D_{[1\bar{1}0]} / D_{[110]}$ von etwa 3:2. Tendenziell gewährleistet eine dünne Zwischenschicht eine stärkere Wechselwirkung der übereinander angeordneten QR Lagen, was auf eine ebenfalls elongierte Form der vergrabenen QR hinweist.

Diffuse Röntgenstreuung unter streifendem Einfall (GID) zusammen mit kinematischen Streusimulationen auf Basis von Finite-Elemente-Rechnungen bestätigen unabhängig von der Dicke der Zwischenschicht eine elongierte Form der vergrabenen QRs. Allerdings nimmt mit zunehmender Schichtdicke der deformationsgetriebene Einfluss auf die in der Deckschicht sich ausbildenden QRs ab, so dass diese (ähnlich wie die QRs der Einzellage) keine Richtungsanisotropie aufweisen.

¹⁷Die Proben wurden speziell für diese Aufgabenstellung in der Arbeitsgruppe von Prof. Dr. G. Salamo der University of Arkansas, Fayetteville, (USA) hergestellt.

23 JULY 2007
Volume 91 Number 4

APPLIED PHYSICS LETTERS



0003-6951(20070723)91:4;1-M

AMERICAN
INSTITUTE
OF PHYSICS

APPLIED PHYSICS LETTERS 91, 043103 (2007)

Shape transformation during overgrowth of InGaAs/GaAs(001) quantum rings

M. Hanke^{a)}Institut für Physik, Martin-Luther-Universität Halle-Wittenberg, Hoher Weg 8,
D-06120 Halle/Saale, GermanyYu. I. Mazur, E. Marega, Jr.,^{b)} Z. Y. AbuWaar, and G. J. Salamo
Department of Physics, University of Arkansas, Fayetteville, Arkansas 72701

P. Schäfer

Humboldt-Universität zu Berlin, Newtonstraße 15, D-12489 Berlin, Germany

M. Schmidbauer

Institut für Kristallzüchtung, Max-Born-Straße 2, D-12489 Berlin, Germany

(Received 12 April 2007; accepted 18 May 2007; published online 24 July 2007)

The authors have investigated a shape transformation during the vertical stacking of InGaAs quantum rings (QRs) on GaAs(001). Samples have been grown by means of molecular beam epitaxy. The initial QR layer exhibits nearly round-shaped, flat disks. Especially for a very thin spacer layer of 2 nm, the topmost QRs in a twofold stack tend to be of ellipsoidal shape with preferential elongation along the [1̄10] direction. Grazing incidence diffraction and corresponding x-ray scattering simulations prove an asymmetry in the shape of the buried QRs with respect to different ⟨110⟩ directions. This clearly indicates a significant shape transformation during the overgrowth process from circular toward ellipsoidal QRs. © 2007 American Institute of Physics.
[DOI: 10.1063/1.2760191]

Overgrowth phenomena of low-dimensional semiconductor structures are essential in the course of any optical device application.¹ Interestingly, it was recently found that the case of partial capping of InAs quantum dots (QDs) with GaAs may result in circular or ellipsoidal rings.^{2,3} Of course, the ring geometry is especially attractive for magneto-optical device applications.⁴ Since the shape of the quantum ring (QR) is significant, it is important to understand the effects that can affect the formation of self-organized QRs, such as diffusion, strain, surface and interface energies, and capping. We can try to control all of these effects by developing a good understanding of their role and by a proper choice of growth parameters.

Generally the observed shape transition from QDs to QRs takes place between two limiting scenarios. On the one hand, there is a kinetically limited process considering diffusion.^{5,6} However, from a thermodynamics model^{7,8} one must consider the balance of surface free-energy along the three-phase contact line substrate-QD vacuum. Although it seems more than obvious that an additional overgrowth step may also significantly alter the initial QRs as well, there is less knowledge about related structural changes. In this work we focus directly on how capping of QRs alters the morphology of the buried ring structures and the subsequently grown layers of InAs QRs.

The InGaAs QR samples were grown using a Riber 32P solid-source molecular beam epitaxy system. A 0.5 μm GaAs buffer layer was deposited on semi-insulating GaAs(001) substrates at 580 °C after oxide desorption. This was then followed by 2.2 ML of InAs and the formation of

QDs at 520 °C obtained using the standard Stranski-Krastanov growth mode. Cycles of 0.14 ML of InAs plus 2 s interruption under As₂ flux⁹ were repeated until the total 2.2 ML of InAs were deposited. The QDs were next annealed for 30 s to further improve the size distribution. We applied *in situ* reflection high-energy electron diffraction to monitor the QD evolution. The QDs were then buried with 4 nm of GaAs cap layer at 520 °C, followed by 40 s of growth interruption to produce the QRs. InAs and GaAs growth rates were set to 0.065 and 1 ML/s, respectively. Three samples were grown: a reference sample which consists of only one layer of QRs and two samples that are obtained by stacking two layers of QRs with a GaAs spacer thicknesses of 2 and 10 nm, respectively. The second layer was left uncapped to investigate the morphology of the grown nanostructures.

Figure 1(a) depicts the single QR layer and the twofold stacks of QRs with different spacer layers [(b) and (c)]. The single layer sample contains rather round-shaped, very flat QRs. The inner and outer diameters D_{in} and D_{out} are nearly equivalent with respect to the different ⟨110⟩ directions (see Table I). However, statistic evaluation proves that even for the single layer, the QRs tend to be slightly elongated along [1̄10]. Both twofold QR stacks confirm this tendency in their topmost layer [Figs. 1(b) and 1(c)]. In the case of the very thin 2 nm spacer [Fig. 1(b)], the topmost QRs appear elongated along the [1̄10] direction, while the QRs on the thicker 10 nm spacer are round shaped again (c). This is expected since we know that the thinner the spacer layer, the stronger the impact of buried layers and the better the replica of the underlying QR pattern, which indicates an elongation of the buried QRs as well.¹⁰

The instability of three-dimensional (3D) islands during GaAs overgrowth is due to the preferential nucleation of the

^{a)}Electronic mail: michael.hanke@physik.uni-halle.de^{b)}On leave from Departamento de Física e Ciência dos Materiais, Instituto de Física de São Carlos-USP São Carlos SP 13560-970, Brazil.

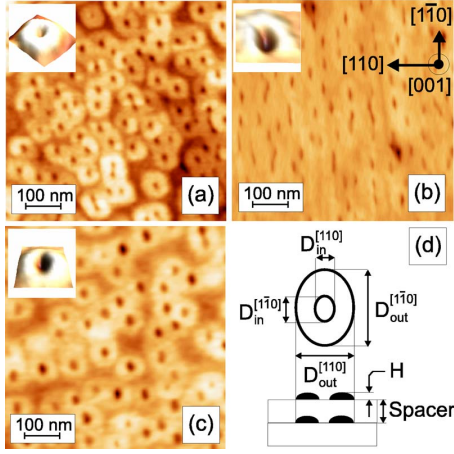


FIG. 1. (Color online) Atomic force microscopy micrographs of the single QR layer (a) and the QR stacks containing two InGaAs QR layers separated by 2 nm (b) and 10 nm (c) GaAs spacers, respectively. (d) gives a QR schema with the abbreviations used in Table I to characterize the QR morphology.

capping layer in the two-dimensional region as well as extensive In–Ga intermixing. The lower strain due to intermixing and consequent InGaAs volume redistribution of the 3D islands is expected to be anisotropic, with the island base enlarging dominantly in the $[1\bar{1}0]$ direction. The specific mechanism by which In leaves the islands is therefore attributed to surface diffusion because cation surface diffusion on the 2×4 surface reconstruction is known to exhibit the same anisotropy. Quantitative high resolution transmission electron microscopy combined with analytical transmission electron microscopy can serve as an appropriate tool to study this effect.

The particular QR shape (e.g., elongated versus circular) will decisively influence the impressed elastic strain, which we utilized as a sensitive measure of the buried QR morphology. In order to probe the three-dimensional elastic strain field, we have applied grazing incidence diffraction (GID). The chosen angle of incidence of 0.3° is close to the critical angle for total external reflection. Respective measurements were performed at beamline ID10B at the European Synchrotron Radiation Facility (ESRF), Grenoble using an x-ray energy of 8 keV. A positional sensitive detector has been placed 500 mm behind the sample enabling an angular resolution along different exit angles α_f . Further on an additional crystal analyzer Ge(220) was used to enhance the angular resolution parallel the sample surface to about 0.03 nm^{-1} .

Figure 2(a) shows the in-plane intensity distribution near the symmetric $(\bar{2}\bar{2}0)$ reflection for the sample with the 10 nm GaAs spacer. The sample's corresponding real space atomic

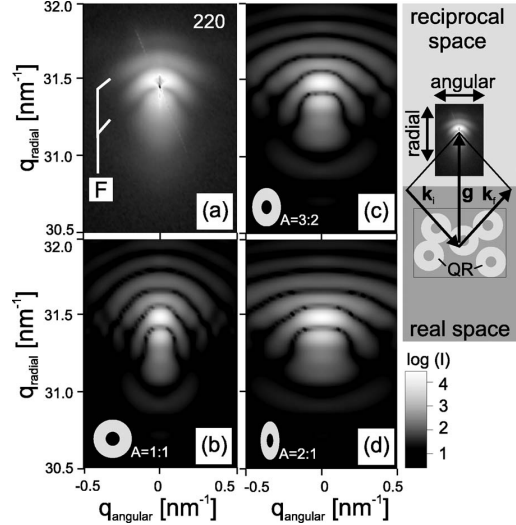


FIG. 2. Schematic drawing on the right side shows a simple view on the relation between real and reciprocal spaces as probed in a grazing incidence diffraction setup. (a) depicts the diffusely scattered intensity around the $(\bar{2}\bar{2}0)$ lattice point as measured. (b)–(d) show respective scattering simulations considering different lateral aspect ratios for the buried quantum dot rings, starting from round-shaped QRs (b) to elongated ellipsoidal QRs (d). The best agreement could be achieved if an aspect ratio A of 3:2 (c) is assumed.

force microscopy (AFM) micrograph in Fig. 1(c) exhibits circular QRs in the topmost surface, which are very similar in size and in shape to those of a single layer [Fig. 1(a)]. Comparatively, the characteristic GID fringe pattern (denoted F) surrounding the intense GaAs($\bar{2}\bar{2}0$) substrate reflection at $q_{\text{radial}} = 31.44 \text{ nm}^{-1}$ and $q_{\text{angular}} = 0$ can potentially serve us as fingerprint of the shape of the buried QRs. However, due to the loss of phase information, it is generally not possible to directly extract quantitative information out of reciprocal space maps. Hence one always relies on x-ray scattering simulations which have been performed via a two-fold numeric approach.¹¹ In order to calculate the actual scattering pattern, we use the three-dimensional strain field \vec{u} which is initially derived from numerical finite element method (FEM). Within the so-called kinematic scattering regime, the diffusely scattered amplitude A_d can be calculated as

$$A_d \propto \sum_{i,k} \varrho(\vec{r}_{ik}) [\exp[i\vec{q}(\vec{r}_{ik} + \vec{u}(\vec{r}_{ik}))] - \exp[i\vec{q}\vec{r}_{ik}]],$$

where $\vec{r}_{ik} = \vec{R}_i + \vec{r}_k$, ϱ the electron density of the crystal lattice, \vec{R}_i gives the position of the i th supercell, \vec{r}_k denotes the po-

TABLE I. Summary of the QR morphology as averaged over an ensemble of about 100 QRs. It gives the inner D_{in} and outer D_{out} diameters with respect to the different $\langle 110 \rangle$ directions. H and D refer to the height and the density of QRs within the topmost layer.

Spacer (nm)	$D_{\text{in}}^{[110]}$	$D_{\text{in}}^{[\bar{1}\bar{1}0]}$	$D_{\text{out}}^{[110]}$	$D_{\text{out}}^{[\bar{1}\bar{1}0]}$	H (nm)	D (cm^{-2})
...	13	17	57	61	0.8	2.4×10^{10}
2.0	11	24	49	75	1.3	2.6×10^{10}
10.0	18	23	71	74	1.8	1.5×10^{10}

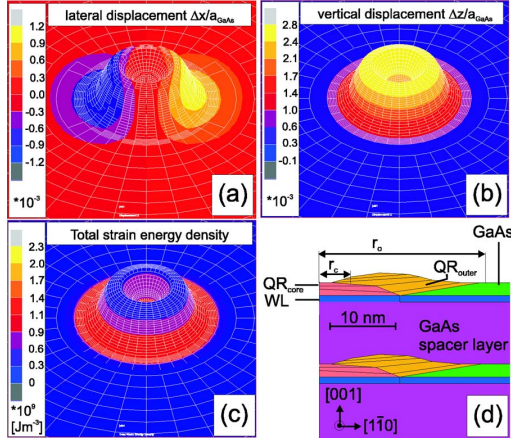


FIG. 3. (Color online) Normalized lateral (a) and vertical (b) displacements and total strain energy density (c) around a surface $\text{In}_{0.4}\text{Ga}_{0.6}\text{As}$ QR placed on a GaAs(001) substrate. The images [(a)–(c)] have been magnified in vertical direction by a factor of 10 for a better view. (d) depicts a cross section (magnification 1:1) through the finite element model. The QRs have been subdivided into regions as, e.g., WL, the quantum ring core (QR_{core}) which originates from the initial InAs quantum dot, the outer QR region (QR_{outer}), and, even further outward, material which was deposited during the QR formation (in the present case, pure GaAs).

sitions of the k th atom within the unit cell, and \vec{u} denotes the displacement vector.

Figures 2(b)–2(d) depict x-ray scattering simulations on the base of three different real space FEM models. All of them consider a stack of two vertically separated QRs with identical morphology of the topmost QRs, which is schematically given in Fig. 3(d): a circular QR with inner and outer diameters of about 10 and 60 nm, respectively. However, different QR shapes (circular versus ellipsoidal) of the buried structure have been considered. Thus, along with the assumed height of only 1.0 nm, the structure well approaches the direct AFM observations of the topmost layer. Structurally different (color-coded) areas in Fig. 3(d) result from the QR formation and hence may indicate various chemical compositions in the FEM model. Those are, namely, the GaAs(001) substrate, a subsequent 0.5 nm thin $\text{In}_{0.4}\text{Ga}_{0.6}\text{As}$ wetting layer (WL), and the inner and outer QR regions also containing 40% of indium. Finally the area further outward, which is not directly influenced by the QR formation, has been modeled by pure GaAs covering the initial wetting layer. Both vector fields of the normalized lateral and vertical displacements $\Delta x/a_{\text{GaAs}}$ and $\Delta z/a_{\text{GaAs}}$ are given in Figs. 3(a) and 3(b). Naturally the QR elastically relaxes outward and in the vertical direction in order to accommodate the lattice mismatch. However, the total strain energy density in Fig. 3(c) approaches zero toward the top, which indicates a perfectly relaxed QR apex. This result is somewhat surprising since the considered QR height is rather small.

We emphasize that the indium distribution within the buried QRs does not significantly influence the scattering pattern (not shown). This effect can be related to the strong matrix impact onto the QRs due to embedding. Thus, prima-

rily the QR shape (instead of its particular three-dimensional composition profile) drives the overall shape of the incorporated elastic strain. Consequently we have modified the buried QR morphology within respective FEM models, while the surface QR has not been changed. Assuming a buried circular QR (duplicated 10 nm underneath the surface QR) yields the scattering pattern in Fig. 2(b). Although this simulation already delivers the typical fringe pattern (F), distinct differences to the experiment, as presented in Fig. 2(a), remain, e.g., the curvature of the fringes. In the course of further simulations [Figs. 2(c) and 2(d)], the outline of the buried QR was compressed with respect to the $\langle 110 \rangle$ direction corresponding to aspect ratios $A = D_{[1\bar{1}0]} / D_{[110]}$ different from one, $A = 3:2$ (c) and $A = 2:1$ (d). This dependence enables an estimate of the aspect ratio A for the buried QRs. The best agreement could be achieved in case of 3:2, which well confirms the directly observed aspect ratio in Fig. 1(b) for the thinnest 2 nm spacer layer (see also Table I). On the other hand, it proves that for even thicker spacers the QR shape has been transformed during overgrowth from initially round-shaped QRs of a single layer [Fig. 1(a)] toward ellipsoidal QRs with an aspect ratio $A = D_{[1\bar{1}0]} / D_{[110]}$ of about 3:2. However, due to the comparatively thick spacer layer of, e.g., 10 nm, the influence of the buried QRs onto the subsequent layer vanishes. Thus, the resulting topmost layer contains QRs which are rather round shaped and hence very similar to those of a single layer. This is further confirmed by the rotational symmetry of strain energy [Fig. 3(c)] which does not show any asymmetry due to the elongated buried QR.

One of the authors (M.H.) acknowledges financial support from the Federal State of Sachsen-Anhalt, Germany, within the Cluster of Excellence (CoE) *Nanostructured Materials* (Project No. NW3). The authors thank the ESRF for providing beamline during experiment HS-3162.

¹M. Sztucki, T. H. Metzger, V. Chamard, A. Hesse, and V. Holý, *J. Appl. Phys.* **99**, 033519 (2006).

²J. M. Garcia, G. Medeiros-Ribeiro, K. Schmidt, T. Ngo, J. L. Feng, A. Lorke, J. P. Kotthaus, and P. M. Petroff, *Appl. Phys. Lett.* **71**, 2014 (1997).

³I. Kegel, T. H. Metzger, A. Lorke, J. Peisl, J. Stangl, G. Bauer, J. M. Garcia, and P. M. Petroff, *Phys. Rev. Lett.* **85**, 1694 (2000).

⁴A. Lorke, R. J. Luyken, A. O. Govorov, J. P. Kotthaus, J. M. Garcia, and P. M. Petroff, *Phys. Rev. Lett.* **84**, 2223 (2000).

⁵A. Lorke, R. Blossey, J. M. Garcia, M. Bichler, and G. Abstreiter, *Mater. Sci. Eng., B* **88**, 225 (2002).

⁶A. Lorke, R. J. Luyken, J. M. Garcia, and P. M. Petroff, *Jpn. J. Appl. Phys., Part 1* **40**, 1857 (2001).

⁷R. Blossey and A. Lorke, *Phys. Rev. E* **65**, 021603 (2002).

⁸A. Lorke, J. M. Garcia, R. Blossey, R. J. Luyken, and P. M. Petroff, *Adv. Solid State Phys.* **43**, 125 (2003).

⁹Diffusion can be influenced not only by changing the growth temperature but also by using cracked As_2 , which is more reactive than As_4 and thus reduces the mobility of the group III elements. Changing the As background from As_4 to As_2 , structures ranging from elongated islands to rings could be obtained (Ref. 6).

¹⁰J. Tersoff, C. Teichert, and M. G. Lagally, *Phys. Rev. Lett.* **76**, 1675 (1996).

¹¹M. Hanke, M. Schmidbauer, D. Grigoriev, H. Raidt, P. Schäfer, R. Köhler, A.-K. Gerlitzke, and H. Wawra, *Phys. Rev. B* **69**, 075317 (2004).

3.4 Positionskorrelierte InGaAs/GaAs *step bunches*

M. Hanke, M. Schmidbauer, R. Köhler, H. Kirmse, M. Pristovsek

Lateral short range ordering of step bunches in MOCVD grown InGaAs/GaAs superlattices

Jour. Appl. Phys. **95**, 1736 (2004).

In vielen Materialsystemen neigen atomare Stufen an Oberflächen fehlgeschnittener Kristalle¹⁸ infolge langreichweiter Wechselwirkung zu lokaler Bündelung. Die Kristalloberfläche besteht in solchen Fällen dann nicht aus äquidistanten atomaren Stufen, sondern vielmehr aus sogenannten Stufenbündeln (*step bunches*), die durch ausgedehnte Terrassen voneinander getrennt sind.

Die vorliegende Arbeit beschäftigt sich mit Mechanismen der Selbstorganisation an Stufenbündeln im System InGaAs/GaAs sowie deren Charakterisierung mittels direktabbildender Rastersondenverfahren und diffuser Röntgenstreuung. Die Strukturen bestehen aus Fünffachstapeln $\text{In}_{0.19}\text{Ga}_{0.81}\text{As}/\text{GaAs}(001)$ mit nominellen Dicken von 2.5 nm bzw. 4.2 nm, wobei die Subtratorientung um 2° in Richtung [1̄10] verkippt ist.¹⁹ Atomkraftmikroskopie an der Oberfläche zeigt (001) orientierte Terrassen, die von Stufenbündeln (mittlere Höhe 2.7 nm) getrennt sind. Dabei weisen die Stufenbündel ein laterales Aspektverhältnis Länge zu Breite von etwa 10 auf.

Der Querschnitt in Transmissionselektronenmikroskopie (TEM) zeigt am ersten Interface (Substrat/InGaAs) noch keine Stufenbündel, diese bilden sich offenbar erst in späteren Schichten heraus. Es fällt zudem auf, dass die Stufenbündel nicht exakt übereinander angeordnet sind. Vielmehr beobachtet man eine zur Probensenkrechten geneigte Vererbungsrichtung. Die diffuse Röntgenstreuung in der Nähe des symmetrischen (004) Reflexes zeigt aufgrund der vertikalen Überstruktur ein sehr komplexes Bild, wobei sich jedoch die verschiedenen Beiträge aus lateraler und vertikaler Korrelation der Stufenbündel qualitativ gut separieren lassen. Darüber hinaus deutet die Form²⁰ der Überstruktursatelliten auf ein *short range order* Modell der Stufenbündel hin. In diesem Grenzfall besteht nur auf kleinen Längenskalen Positions korrelation.

¹⁸Weicht die Oberflächenorientierung eines Kristalls von einer ausgezeichneten kristallographischen Richtung ab, so führt dies auf atomarer Skala im Allgemeinen zu Stufen.

¹⁹Die Proben entstanden am Lehrstuhl Prof. Dr. W. Richter der Technischen Universität Berlin.

²⁰genauer gesagt der funktionale Zusammenhang von Halbwertsbreite und lateralem Impulsübertrag in der diffusen Streuung

Lateral short range ordering of step bunches in InGaAs/GaAs superlattices

M. Hanke^{a)}, M. Schmidbauer, R. Köhler, and H. Kirmse

Institut für Physik, Humboldt-Universität zu Berlin, Newtonstrasse 15, D-12489 Berlin

M. Pristovsek

Institut für Festkörperphysik, Technische Universität Berlin, Hardenbergstrasse 36, D-10632 Berlin

(Received 3 October 2003; accepted 18 November 2003)

In the present paper we report on structural investigations of fivefold In_{0.2}Ga_{0.8}As/GaAs superlattices which have been grown by means of metal organic chemical vapor deposition on vicinal GaAs(001) substrates. Cross-sectional transmission electron micrographs exhibit an initially flat and nonfaceted grooved surface, while step bunching occurs during subsequent growth stages with an inclined vertical inheritance approximately 45° off the (001) direction. A reconstructed sample cross section on the base of high resolution x-ray diffraction data qualitatively confirms the local morphology proved by transmission electron microscopy. Moreover, a line shape analysis of diffusely scattered intensity using Gauss profiles indicates a lateral short range ordering of step bunches. © 2004 American Institute of Physics. [DOI: 10.1063/1.1640786]

I. INTRODUCTION

Steps on a surface can serve as a nonartificial template for the formation of anisotropic nanostructures, such as, e.g., quantum wires¹ and two-dimensional ordered quantum dots.² Bunches of steps—separated by extended flat terraces—tend to be much straighter than individual ones because of higher stiffness. In order to utilize those templates in real device structures one needs to control the self-assembly process. Further on, it is highly desirable to tune morphological parameters such as bunch height and separation width, which in fact can be adjusted independently by a proper choice of growth conditions.³ The strong interest in the presently investigated material combination InGaAs/GaAs is driven by the expectation of building optoelectronic devices for the 1.3 μm optical window in silica fiber, e.g., on a base of InAs quantum dots embedded within a strain-reduced InGaAs matrix.⁴ In addition to this technological viewpoint, step bunching has attracted fundamental interest as well. Different pathways toward step bunching have been discussed in terms of either energetics^{5–7} or kinetics, e.g., Refs. 8 and 9.

Recent work on molecular beam epitaxial growth of strained InGaAs on vicinal GaAs(001) wafers shows considerable uniformity and lateral order of step bunches, but only for a comparatively low highly regular step bunching indium content of 9%.¹⁰ We have applied metal organic chemical vapor deposition (MOCVD), which can provide even at higher strain or larger indium content.

Since scattering techniques probe extended ensembles of nanoscopic objects, they have become the method of choice for nondestructive investigations of both (i) lateral ordering within a single layer and (ii) vertically correlated interface roughness in superlattices, e.g., Refs. 11–14. Moreover, it is a sensitive technique, which can probe strain in lateral peri-

odic structures, like those caused by a dislocation network.¹⁵

Usually ordering phenomena are discussed in the framework of two limiting ideal cases: short range ordering (SRO) and long range ordering (LRO), respectively. Whereas for LRO the correlation within domains is assumed to be perfect, ordering disappears at larger distances in SRO.^{16,17} Theoretical studies of the systems InAs/GaAs and Si/Ge indicate¹⁸ the absence of a pronounced lateral LRO of quantum dots due to the comparatively weak elastic anisotropy. We could also prove SRO for one-dimensional objects like step bunches in a vertical InGaAs/GaAs superlattice grown on a miscut surface.

II. SAMPLE

All the investigated samples were grown by means of MOCVD, which was performed in a double wall horizontal quartz reactor with a purged strain-reduced window for optical *in situ* characterization. The carrier gas was hydrogen (3 l/min) at a total pressure of 10 kPa; the AsH₃ (arsine) partial pressure was 100 Pa. The metal organic sources were trimethyl gallium (TMGa) and trimethyl indium (TMIn). A TMGa partial pressure of 0.5 Pa resulted in a growth rate at 873 K of 900 nm/h, a typical parameter for buffer growth to achieve step bunching on vicinal substrates. In the reactor there is no sample rotation implemented; thus, the thermocouple temperature was always found to be very close to the actual surface temperature. The samples were grown on vicinal 2° [110] (A) and [110] (B) oriented Te-doped GaAs(001) wafers. Prior to epitaxy the substrates were wet etched. Before the actual growth could start, an approximately 500 nm thick GaAs buffer layer was grown. At this thickness the step bunching is saturated, as also observed in the literature.^{19–21} On this buffer layer the vertical InGaAs/GaAs superlattices (SLs) were grown. They consist of five periods InGaAs (2 nm) and GaAs (4 nm) with a nominal indium content of 20%.

^{a)}Present address: Fachbereich Physik, Martin-Luther-Universität Halle-Wittenberg, Hoher Weg 8, D-06120 Halle/Saale, Germany; electronic mail: hanke@physik.uni-halle.de

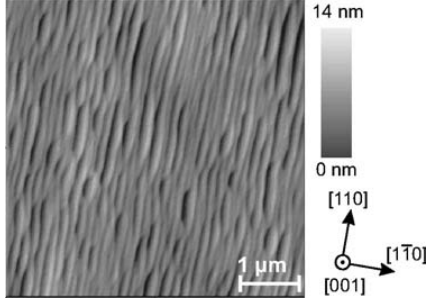


FIG. 1. The atomic force micrograph (a) shows well pronounced step bunches with an aspect ratio of approximately 10.

We could directly observe remarkable differences in the lateral bunch aspect ratio at the topmost surface by applying atomic force microscopy. The lateral bunch aspect ratio R can be defined by

$$R = \frac{\langle x_{\parallel} \rangle}{\langle x_{\perp} \rangle} \quad (1)$$

where $\langle \cdot \rangle$ denotes the *averaged* length parallel and perpendicular to the structures, respectively. Whereas the topmost bunches on a [110] (A) wafer exhibit an aspect ratio R of nearly 3 (not shown here), we found a significantly higher ratio of 10 in the case of the [1-10] (B) wafer (see Fig. 1). Hence, we will focus on the structure grown on the [1-10] (B) substrate.

III. EXPERIMENT

The x-ray scattering experiments have been prepared at beamline BW2 at HASYLAB using monochromatic x rays with an energy of 8 keV and an energy width $\Delta\lambda/\lambda$ of approximately 10^{-4} . We made particular use of a position sensitive detector (PSD), which was placed 750 mm behind the sample. By using lateral slits of 1 mm directly behind the sample and additionally in front of the PSD we could establish a sufficiently high resolution of $4.3 \times 10^{-3} \text{ \AA}^{-1}$ perpendicular to the scattering plane, whereas the much better resolution *in plane* amounts to $2.9 \times 10^{-4} \text{ \AA}^{-1}$ parallel to the surface and $4.3 \times 10^{-4} \text{ \AA}^{-1}$ perpendicular to it.

IV. RESULTS AND DISCUSSION

Figure 2 shows the diffusely scattered intensity around the 004 lattice point for two different scattering planes. The intense streaks crossing both patterns are artifacts caused by the monochromator (marked M) and the position sensitive detector (P), respectively. Figure 2(a) depicts the diffuse scattering in a plane collinear with the bunches; thus it contains the [110] direction. In the limit of perfect one-dimensional steps and/or SBs there is no contribution to the corresponding scattering plane. However, the intensity distribution contains information about the vertical sample structure, which particular periodic arrangement causes intensity oscillations along the crystal truncation rod (CTR).

In contrast, Fig. 2(b) shows the distribution within a plane perpendicular to the previous one, which is defined by

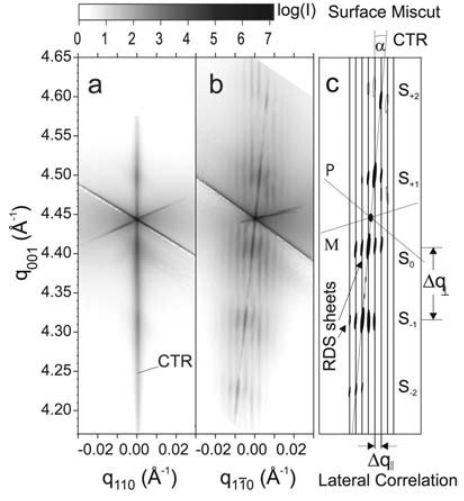


FIG. 2. Diffusely scattered intensity around the 004 reflection, where the incoming beam runs *along* the bunches (along the [110] direction) in (a) and perpendicular to it in (b). (c) depicts a schema of the measured distribution (b).

the [1-10] and [001] directions. Here, different vertical and lateral features are superimposed and merge into a very complicated pattern, which parts are better discussed by means of the schematic drawing in Fig. 2(c). The monodispersely distributed step bunches and in particular their lateral periodic separation by extended (001) terraces give rise to characteristic grating truncation rods (GTRs) in the diffuse scattering up to the fifth order. Those rods are perfectly oriented along [001], indicating a lateral ordering which exactly follows the [1-10] direction. From the lateral distance Δq_{\parallel} of $3.76 \times 10^{-3} \text{ \AA}^{-1}$, we can estimate an averaged lateral bunch spacing $\langle d_{\parallel} \rangle$ of 1671 Å. This is in good agreement with the atomic force micrograph of the topmost surface in Fig. 1. Moreover, the cross-sectional transmission electron micrograph, Fig. 3, depicts nearly the same bunch separation for

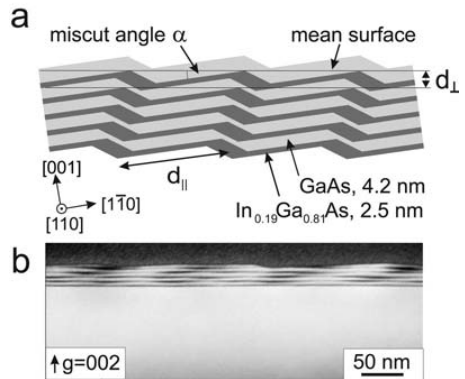


FIG. 3. A schematic cross section of the sample as derived from the lateral and vertical periodicity and location in high resolution x-ray diffraction data, which is in excellent agreement with the cross-sectional transmission electron micrograph (b). It is worth noting that step bunching subsequently develops during growth since there is no substrate prepattern visible.

the underlying interfaces. A very intense crystal truncation rod crosses the whole diffuse intensity pattern, at an angle of 2.3° which confirms the initial substrate miscut.

Moreover, the vertical superstructure (five periods of InGaAs/GaAs) causes equidistantly spaced vertical superlattice peaks ($S_{-2,\dots,+2}$), whose separation Δq_\perp is closely related to the SL period $d_{\text{InGaAs}} + d_{\text{GaAs}}$, where the distance between the zeroth order SL peak reflects the strain averaged along the entire stack. Dynamical scattering simulations (not shown here) reveal layer thicknesses of $d_{\text{GaAs}} = 4.2 \text{ nm}$ and $d_{\text{InGaAs}} = 2.5 \text{ nm}$ and an averaged indium concentration of $x_{\text{In}} = 19\%$. Since the lateral maxima at various SL peaks are inclined with respect to the [001] direction, the vertical inheritance is supposed to be inclined.

A detailed inspection of Fig. 2(b) indicates that the SB height has to be identical to the vertical SL period $d_{\text{InGaAs}} + d_{\text{GaAs}}$ itself, since the CTR obviously crosses the lateral GTRs exactly at the maxima of subsequent SL peaks, which yields the relation

$$\sin \alpha = \Delta q_\parallel / \Delta q_\perp = \langle d_\perp \rangle / \langle d_\parallel \rangle, \quad (2)$$

where α denotes the miscut angle.

Taking this morphological particularity into account, a cross section through the discussed structure has been reconstructed. Figure 3(a) depicts a possible configuration considering the results by high resolution x-ray diffraction (HRXRD). The cross-sectional transmission electron micrograph in Fig. 3(b) qualitatively confirms the proposed model.

All the micrographs give clear evidence that step bunches do not immediately emerge at the initial interface, which is free of any undulation. Therefore step bunching and its vertical inheritance are rather phenomena driven by strain relief during subsequent growth than a simple replication of a prepattern.

The existence of correlation peaks up to high orders enables one to distinguish between SRO and LRO models. Therefore we have extracted a horizontal one-dimensional intensity cut along $q_{[1\bar{1}0]}$ at $q_z = 4.316 \text{ \AA}^{-1}$ [Fig. 4(a)]. The correlation peaks are equidistantly spaced, yielding the mean lateral distance $\langle d_\parallel \rangle$. On the other hand, the experimental peak widths δq [shown as dots in Fig. 4(b)] increase with peak order. Since the connecting parabolic fit (line) does not exactly match the experimental data, the “random walk” SRO model cannot perfectly describe the morphology. However, applying this model we estimate a rms standard deviation $\sigma = 166 \text{ \AA}$ of the mean lateral distance $\langle d_\parallel \rangle$.

V. CONCLUSION

In conclusion, we have investigated MOCVD grown InGaAs/GaAs fivefold stacks on 2° [110] (A) and [110] (B) GaAs (001) wafers by HRXRD and direct imaging techniques like transmission electron and atomic force microscopy. The observed step bunches at the topmost surface with a mean lateral distance between 150 and 200 nm have to be formed during subsequent growth, since the initial GaAs miscut surface does not show a faceted grooved morphology. The particular shape of diffuse x-ray scattering in the vicinity of the 004 reciprocal lattice point indicates a step bunch

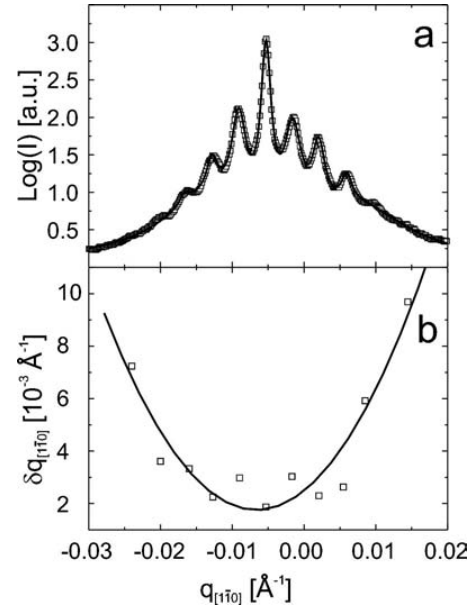


FIG. 4. (a) Experimental intensity cut (dots) along $q_{[1\bar{1}0]}$ at $q_z = 4.316 \text{ \AA}^{-1}$ through the diffuse intensity pattern in Fig. 2(b) connected by a Gaussian fit. (b) plots the experimental peak widths (full widths at half maximum) (dots) as a function of $q_{[1\bar{1}0]}$ and a corresponding parabolic fit.

height that is nearly equal to the vertical superlattice period. Taking the experimentally estimated layer thicknesses and the actual miscut angle into account, a typical sample cross section has been reconstructed. Line shape analysis of one-dimensional cuts through the first order vertical superlattice peak of the 004 reciprocal space map proves lateral short range ordering.

ACKNOWLEDGMENTS

We would like to thank W. Drube for the experimental setup at beamline BW2 at Hasylab. This project was sponsored by the German Research Society in the framework of the Sonderforschungsbereich 296.

- ¹K. Ploog, R. Nötzel, and M. Ilg, *J. Vac. Sci. Technol. B* **11**, 1675 (1993).
- ²Zhu, K. Brunner, and G. Abstreiter, *Appl. Phys. Lett.* **73**, 620 (1998).
- ³F. Liu, J. Tersoff, and M. G. Lagally, *Phys. Rev. Lett.* **80**, 1268 (1998).
- ⁴Y. Qiu, P. Gogna, S. Forouhar, A. Stintz, and L. Lester, *Appl. Phys. Lett.* **79**, 3570 (2001).
- ⁵J. Tersoff, Y. H. Phang, Z. Zhang, and M. G. Lagally, *Phys. Rev. Lett.* **75**, 2730 (1995).
- ⁶D.-J. Liu and J. Weeks, *Phys. Rev. Lett.* **79**, 1694 (1997).
- ⁷Z. M. Wang, L. Däweritz, and K. H. Ploog, *Surf. Sci.* **459**, L482 (2000).
- ⁸M. Krishnamurthy, M. Wassermeier, D. R. M. Williams, and P. M. Petroff, *Appl. Phys. Lett.* **62**, 1922 (1993).
- ⁹C. Duport, P. Nozières, and J. Villain, *Phys. Rev. Lett.* **74**, 134 (1995).
- ¹⁰Z. Wang, J. Shultz, and G. Salamo, *Appl. Phys. Lett.* **83**, 1749 (2003).
- ¹¹Y. H. Phang, R. Kariotis, D. E. Savage, and M. G. Lagally, *J. Appl. Phys.* **72**, 4627 (1992).
- ¹²Z. H. Ming, A. Krol, Y. L. Soo, Y. H. Kao, J. S. Park, and K. L. Wang, *Phys. Rev. B* **47**, 16373 (1993).
- ¹³V. M. Kaganer, S. A. Stepanov, and R. Köhler, *Phys. Rev. B* **52**, 16369 (1995).
- ¹⁴M. Schmidbauer, R. Opitz, T. Wiebach, and R. Khler, *Phys. Rev. B* **64**,

- 195316 (2001).
- ¹⁵J. Eymery, D. Buttard, F. Fournel, H. Moriceau, G. Baumbach, and D. Lübbert, Phys. Rev. B **65**, 165337 (2002).
- ¹⁶J. Stangl *et al.*, J. Vac. Sci. Technol. B **18**, 2187 (2000).
- ¹⁷L. Kegel, T. H. Metzger, J. Peisl, P. Schittenhelm, and G. Abstreiter, Appl. Phys. Lett. **74**, 2978 (1999).
- ¹⁸V. Holý, G. Springholz, M. Pinczelits, and G. Bauer, Phys. Rev. Lett. **83**, 356 (1999).
- ¹⁹T. Fukui and H. Saito, Jpn. J. Appl. Phys., Part 2 **29**, L483 (1990).
- ²⁰M. Kasu and T. Fukui, Jpn. J. Appl. Phys., Part 2 **31**, 864 (1992).
- ²¹J. Ishizaki, K. Ohkuri, and T. Fukui, Jpn. J. Appl. Phys., Part 1 **35**, 1280 (1996).

4 SiGe/Si Nanowhisker

M. Hanke, C. Eisenschmidt, P. Werner, N. D. Zakharov, F. Syrowatka, F. Heyroth, P. Schäfer, O. Konovalov

Elastic strain relaxation in axial Si/Ge whisker heterostructures
Phys. Rev. B **75**, 161303(R) (2007).

In der vorliegenden Veröffentlichung wird das Relaxationsverhalten eindimensionaler MBE Whisker im System SiGe/Si(111)²¹ diskutiert. Dafür standen neben homoepitaktischen (deformationsfreien) auch heteroepitaktische Whisker mit eingebetteten etwa 10 nm dicken (ein bzw. drei) Germaniumschichten zur Verfügung. Zum Einsatz kamen hochaufgelöste Weitwinkelbeugung in der Nähe des asymmetrischen (115) Reflexes und die Methode der Finiten Elemente zur numerischen Bestimmung der Deformationstensors.

Während sich erwartungsgemäß bei den reinen Siliziumwhiskern keine mechanische Deformation nachweisen ließ, zeigen die heteroepitaktischen Vergleichsproben eine deutliche Deformation des Kristallgitters mit einem mittleren Relaxationskoeffizienten von etwa 51%.²² Interessanterweise führt sowohl eine vergrabene Einfachlage als auch der Dreifachstapel zu einem vergleichbaren Maß an Relaxation, was nahelegt, dass die Schichten weitestgehend unabhängig voneinander elastisch relaxieren.

Mittels Finite-Elemente-Berechnungen wurden anschließend auf Grundlage der aus der Weitwinkelbeugung bestimmten Germaniumkonzentration die Komponenten ϵ_{xx} und ϵ_{zz} des Tensors der totalen Deformation numerisch bestimmt. Dabei zeigt sich aufgrund des größeren Gitterparameters von Germanium eine vertikale und nach außen gerichtete laterale Expansion des Kristallgitters innerhalb der Germaniumschichten. Zugleich führt jedoch letzterer Anteil infolge der Steifigkeit zu einer lateralen *Kompression* in der Whiskerspitze. Dieser doch auf den ersten Blick überraschende Effekt verursacht also ein vorgespanntes (lateral komprimiertes) Kristallgitter oberhalb vergrabener Germaniumschichten und könnte damit maßgeblich für den seit längerem bekannten Umstand einer endlichen (auf etwa 25% begrenzten) Germaniumkonzentration in SiGe/Si Whiskern verantwortlich sein.

²¹Die Proben entstanden am Max-Planck-Institut für Mikrostrukturphysik in Halle. (Dr. Peter Werner, Dr. Nikolai Zakharov)

²²Null entspricht einem idealen pseudomorph verspannten System, 100% dagegen vollständiger Relaxation.

Elastic strain relaxation in axial Si/Ge whisker heterostructures

M. Hanke and C. Eisenschmidt

Martin-Luther-Universität Halle-Wittenberg, Institut für Physik, Hoher Weg 8, D-06120 Halle/Saale, Germany

P. Werner and N. D. Zakharov

Max-Planck-Institut für Mikrostrukturphysik, Weinberg 2, D-06120 Halle/Saale, Germany

F. Syrowatka and F. Heyroth

Interdisziplinäres Zentrum für Materialwissenschaften, Heinrich-Damerow-Straße 4, D-06120 Halle/Saale

P. Schäfer

Humboldt-Universität zu Berlin, Institut für Physik, Newtonstraße 15, D-12489 Berlin, Germany

O. Konovalov

European Synchrotron Radiation Facility, BP 220, F-38043 Grenoble Cedex, France

(Received 14 March 2007; revised manuscript received 11 April 2007; published 23 April 2007)

The elastic behavior of molecular beam epitaxy-grown SiGe/Si(111) nanowiskers (NWs) has been studied by means of electron microscopy, x-ray scattering, and numerical linear elasticity theory. Highly brilliant synchrotron radiation was applied to map the diffusely scattered intensity near the asymmetric (115) reciprocal lattice point. The larger lattice parameter with respect to the Si matrix causes a lateral lattice expansion within embedded Ge layers. This enables a clear separation of scattering due to NWs and laterally confined areas aside. Finite element calculations prove a lateral lattice compression in the Si matrix close to the NW apex above buried threefold and single Ge layer stacks. This suggests an incorporation probability, which additionally depends on the radial position within heteroepitaxial NWs.

DOI: [10.1103/PhysRevB.75.161303](https://doi.org/10.1103/PhysRevB.75.161303)

PACS number(s): 68.70.+w, 61.10.Nz, 68.37.Lp

One-dimensional semiconductor structures, also referred to as nanowires and nanowiskers (NWs), have attracted much interest during recent years due to their manyfold potential applications in electronics, photonics, and sensing devices, for example.^{1,2} So, at first glance it may be surprising that the homoepitaxial growth of Si whiskers via the vapor-liquid solid (VLS) mechanism was already explored nearly 40 years ago,³ however, only on a μm scale. Silicon NWs can be successfully grown by applying the VLS process. In the case of the mainly used chemical vapor deposition technique, a Si containing gas/precursor is cracked at Au droplets acting as seeds. Si adatoms are subsequently solved in the liquid metal. Due to a supersaturation within this droplet, Si precipitates predominantly at the liquid-solid interface and a nanowisker appears. A somewhat completely different situation occurs if NWs are grown by molecular beam epitaxy (MBE) via the VLS mechanism as applied in the present experiments. This concerns, e.g., the role of the metal seed, the morphology of the NWs, and the aspect ratio of their lengths and widths. Surface diffusion especially, including the metal used as well as Si, strongly influences the growth process. More recently, various groups have demonstrated Si NWs on Si,^{4,5} Ge NWs on Si,⁶ axial heterostructures by embedding Ge layers into Si NWs,^{7,8} as well as radial core-shell Si/Ge NWs.⁹ The mutual impact of the chemical composition, the established elastic strain and its eventual relaxation influences the further growth sequence regardless of the particular structure or growth method. Regarding characterization, most groups, however, still rely on direct imaging techniques such as electron microscopy, whereas x-ray scattering techniques very recently emerge in the NW field.¹ In this

paper, we applied electron microscopy, diffuse x-ray scattering, and numerical finite element method (FEM) to probe composition, strain, and elastic relaxation within heteroepitaxial Si/Ge NWs.

The samples have been grown on (111)-oriented five inch Si wafers, which were cleaned by conventional RCA procedure. Our MBE system includes three electron-beam guns for the evaporation of Au and Si as well as of Ge.⁷ A thin Au film with a nominal thickness of 2 nm was deposited on the substrate at a substrate temperature T_S of 525 °C forming small gold droplets. During the following NW growth, the constant Si and Ge fluxes amounted to 0.05 and 0.01 nm/s, respectively. Since in the vapor-liquid-solid mechanism the gold droplets act as the intermediate and hence liquid medium, they will not induce additional strain into the NWs.

Both the chemical profile and the closely related strain distribution within the NWs determine mechanical and optical properties of the NWs. Thus, to probe the three-dimensional strain profile we have employed high resolution x-ray diffraction (HRXRD). Respective experiments were performed at the beamline ID10B at the European Synchrotron Radiation Facility (ESRF) using an x-ray energy of 7951 eV. In the actual setup we applied a positional sensitive detector (PSD) with a nominal pixel size of 60 μm corresponding to a resolution of 0.004 Å⁻¹. An additional 1 mm slit in front of the PSD restricts the resolution perpendicular to the scattering plane to about 0.006 Å⁻¹.

Figure 1 shows reciprocal space maps of the diffuse intensity near the asymmetric (115) reflection for the three samples depicted in Fig. 2: pure Si NWs (a), NWs containing a single Ge disk (b), and a threefold vertical stack (c). In the

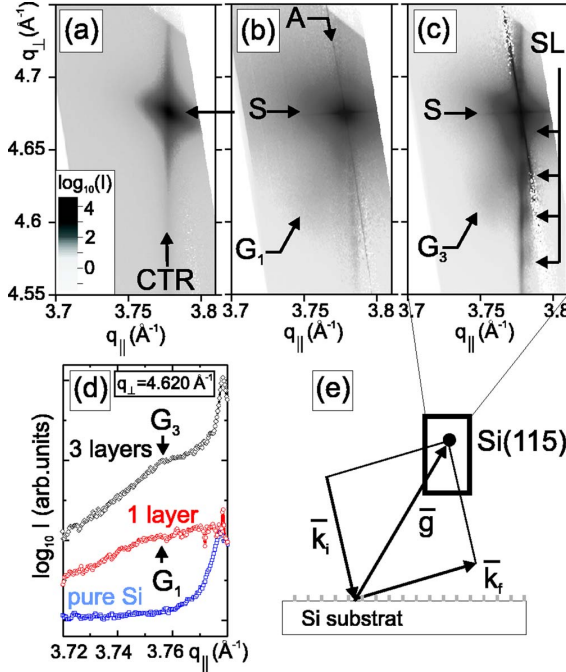


FIG. 1. (Color online) Diffusely scattered intensity near the asymmetric Si(115) reflection (S) for samples with pure Si NWs (a), those containing a single Ge layer (b), and three layers (c), respectively. Since pattern (a) only reveals diffuse intensity near the substrate reflection (S), the further distributions (b) and (c) probe laterally relaxed lattice sites (G_1 and G_3). Due to the vertical superstructure in the threefold system, additional intensity oscillations (SL) become prominent along the crystal truncation rod (CTR) in (c). (d) shows line scans through the reciprocal space maps (a)-(c) at $q_{\perp}=4.620 \text{ \AA}^{-1}$ for a quantitative estimate of the positions G_1 and G_3 . Scheme (e) illustrates how the diffraction vector \bar{g} may probe diffuse intensity in reciprocal space by varying the directions of the incident and exit wave vectors, \bar{k}_i and \bar{k}_f .

limit of pure Si, no elastic strain is anticipated in the structure. In such an ideal limit there are, hence, no deformed lattice sites, which may cause additional diffuse scattering. However, as soon as a heteroepitaxial layer is embedded within the NWs, the various lattice constants will induce strain energy. During the further NW growth it may be lowered because a one-dimensional structure provides excellent conditions to elastically relax perpendicular to its axial direction. The transmission electron micrographs (TEM) in Figs. 2(b)–2(d) indicate that this favorably happens elastically, thus without the formation of misfit dislocations.

The scattering vector q_{115}^{Si} displays nearly equivalent, non-zero lateral, $q_{\parallel}^{\text{Si}}=3.778 \text{ \AA}^{-1}$, and vertical, $q_{\perp}^{\text{Si}}=4.674 \text{ \AA}^{-1}$, components. Thus, it probes the normalized lattice constant parallel ($\Delta a/a_{\parallel}$) and perpendicular ($\Delta a/a_{\perp}$) to the mean surface with similar sensitivity. Consequently, sample areas, which may laterally relax, imply diffuse intensity well separated from contributions due to laterally confined regions. This enables in particular a clear distinction between scattering due to NWs and the adjacent planar structure. Scattering

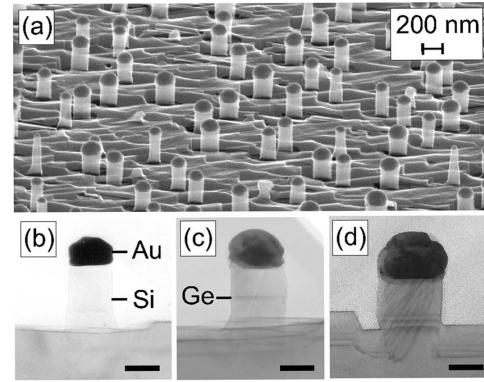


FIG. 2. Scanning electron micrograph of a sample containing pure Si NWs (a). (b) to (d): TEM micrographs of individual NWs of pure Si, NWs with an embedded single Ge layer and with three layers, respectively. The bar corresponds to 100 nm.

on nonstrained, pure Si NWs accordingly cause only an intense Si(115) reflection (S), Fig. 1(a). Additional intensive spots G_1 and G_3 in Fig. 1(b) and 1(c) serve as fingerprints of the embedded heteroepitaxial layers. The scattered intensity cloud around G_1 in Fig. 1(b) is caused by a single layer and appears comparatively weak at about $q_{\parallel}=3.759 \text{ \AA}^{-1}$, $q_{\perp}=4.620 \text{ \AA}^{-1}$. The larger extension of peak G_1 (compared with G_3) refers to a broader size distribution of the NW radii, which is about $\pm 10\%$ for the single and $\pm 5\%$ for the three layers sample. However, for the three-fold embedded Ge structure, the feature becomes more intense, whereas its position does not change significantly. Moreover, the presence of a (115) reflection clearly indicates zinc-blende stacking along the [111] axis. The lateral and vertical lattice deformations ($\Delta a/a_{\parallel,\perp}$) directly correspond to respective peak positions in reciprocal space ($\Delta q/q_{\parallel,\perp}$), which eventually yields a relaxed lattice mismatch:

$$(\Delta a/a)_{\text{rel}} = P_{111}[(\Delta a/a)_{\perp} - (\Delta a/a)_{\parallel}] + (\Delta a/a)_{\parallel}. \quad (1)$$

Here we consider the orientation dependent factor P_{111} :^{10,11}

$$P_{111} = \frac{C_{11} + \frac{2}{3}(2C_{44} - C_{11} + C_{12})}{C_{11} + 2C_{12}}. \quad (2)$$

Close positions of peak G_1 and G_3 , Fig. 1(d), and hence a similar value for $(\Delta a/a)_{\text{rel}}=0.010$, indicate about 24% Ge within the heterostructure—Independent of the particular number of layers. Further on, the relaxation parameter $R=(\Delta a/a)_{\parallel}/(\Delta a/a)_{\text{rel}}$ gives the degree to which the lattice has been relaxed. It yields 0.0 for an ideal pseudomorphically strained layer, 1.0 for fully relaxed layers, and about 0.51 for the structures investigated here. A similar value for both structures indicates that the threefold layers (compared with the single layer) do not increase the degree of relaxation, whereas the amount of material in a certain strain status naturally increases for the threefold system. In other words: there is no cumulative strain effect. Each Ge layer acts independent from each other in terms of relaxation.

RAPID COMMUNICATIONS

ELASTIC STRAIN RELAXATION IN AXIAL Si/Ge...

PHYSICAL REVIEW B 75, 161303(R) (2007)

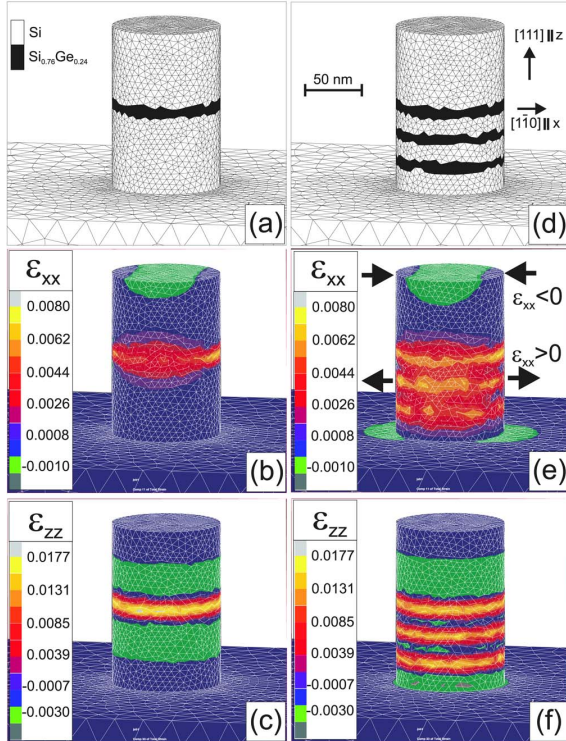


FIG. 3. (Color online) Model structures used for the FEM simulations and their results. Lateral (b),(e) and vertical (c),(f) total strain tensor components, ϵ_{xx} and ϵ_{zz} , as numerically revealed by finite element calculations. The models consider a single Ge layer (a) and a threefold vertical structure (d), respectively according to the micrographs, as shown in Fig. 2.

Considering the Ge content revealed by HRXRD, we have simulated the relaxation behavior within the NWs. In this regard, finite element calculations serve as a well-established analytical tool to calculate strain and relaxation in low-dimensional structures on the base of linear elasticity theory. (See, for example, Refs. 12 and 13). Both models displayed in Fig. 3(a) and 3(c) outline a single cylindrical NW according to the mean dimensions as revealed by electron microscopy (radius 50 nm, height 150 nm). The NWs are placed on a Si(111) substrate with lateral dimensions of $200 \times 200 \times 200$ nm³, which sufficiently ensure a realistic

elastic interaction. Since the first model (a) considers a single 10 nm Si_{0.76}Ge_{0.24} disk embedded in the center, the further one (d) regards three subsequent layers (10 nm) vertically separated by 15 nm silicon spacers. The resulting lateral and vertical components of the total strain tensor, ϵ_{xx} and ϵ_{zz} , are plotted in Fig. 3(b), 3(c), 3(e), and 3(f). Obviously the larger Ge lattice causes either for single or multifold layers a vertical lattice expansion ($\epsilon_{zz} > 0$) within the disks, whereas adjacent regions within the Si matrix undergo a compression ($\epsilon_{zz} < 0$), which becomes in particular prominent for the single layer. An embedded multilayer structure yields, on the other hand, vertically well separated areas of lateral expansion ($\epsilon_{xx} > 0$) marked by arrows in Fig. 3(e). However, it turns into negative values of about -0.1% at the NW apex Fig. 3(b) and 3(e), which indicates laterally compressed lattice sites, in particular close to the NW axis. This result proves a radial dependence of the lateral lattice parameter at the growth front above buried heteroepitaxial Ge layers, and hence suggests different incorporation probabilities at various radii. Moreover, it strongly supports the observation that Ge can be incorporated in axial Si/Ge NWs only in a Si-rich alloy up to about 25% Ge.¹⁴

The elastic strain and its relaxation in a set of MBE-grown Si/Ge NWs on Si(111) have been studied by means of electron microscopy, high resolution x-ray diffraction, and numerical finite element method. The samples contain either pure Si NWs, NWs with an embedded single SiGe layer, or a threefold stack of SiGe layers. The quasi-one-dimensional morphology of NWs sufficiently provides elastic relief perpendicular to the axial direction, which is proved by finite element calculations. Different degrees of lateral relaxation within NWs and adjacent laterally confined areas enable a clear distinction between respective contributions to the intensity pattern around the asymmetrical (115) reflection. Finite element calculations indicate moreover a laterally compressed Si matrix above buried Ge layers, which can be attributed to the stiffness of the NW lattice. Since this effect depends on the radial position at the NW apex, it suggests a radial dependent incorporation probability in vertically structured NWs.

We acknowledge financial support by the Federal State of Sachsen-Anhalt, Germany, within the Cluster of Excellence (CoE) *Nanostructured Materials*, Project Nos. NW2 (P.W.) and NW3 (M.H.), and Project No. NODE 015783. The authors thank the ESRF for providing beamtime during experiment HS-2652.

¹C. P. T. Svenson, W. Seifert, M. W. Larsson, L. R. Wallenberg, J. Stangl, G. Bauer, and L. Samuelson, *Nanotechnology* **16**, 936 (2005).

²H. J. Fan, P. Werner, and M. Zacharias, *Small* **2**, 700 (2006).

³R. S. Wagner, *Whisker Technology* (Wiley, New York, 1970).

⁴T. I. Kamins, R. S. Williams, D. P. Basile, T. Hesjedal, and J. S. Harris, *J. Appl. Phys.* **89**, 1008 (2001).

⁵N. Ozaki, Y. Ohno, and S. Takeda, *Appl. Phys. Lett.* **73**, 3700

(1998).

⁶T. I. Kamins, X. Li, and R. S. Williams, *Nano Lett.* **4**, 503 (2004).

⁷L. Schubert, P. Werner, N. D. Zakharov, G. Gerth, F. Kolb, L. Long, U. Gösele, and T. Y. Tan, *Appl. Phys. Lett.* **84**, 4968 (2004).

⁸Y. Wu, R. Fan, and P. Yang, *Nano Lett.* **2**, 83 (2002).

⁹L. J. Lauhon, M. S. Gudikson, D. Wang, and C. M. Lieber, *Nature (London)* **420**, 57 (2002).

RAPID COMMUNICATIONS

HANKE *et al.*

PHYSICAL REVIEW B 75, 161303(R) (2007)

- ¹⁰J. Hornstra and W. J. Bartels, *J. Cryst. Growth* **44**, 513 (1978).
¹¹Vergard's law has been applied for the elastic constants of $\text{Si}_{0.76}\text{Ge}_{0.24}$.
¹²S. Christiansen, M. Albrecht, H. P. Strunk, and H. J. Maier, *Appl. Phys. Lett.* **64**, 3617 (1994).

- ¹³M. Hanke, T. Boeck, A.-K. Gerlitzke, F. Syrowatka, and F. Heyroth, *Phys. Rev. B* **74**, 153304 (2006).
¹⁴N. Zakharov, P. Werner, G. Gerth, L. Schubert, L. Sokolov, and U. Gösele, *J. Cryst. Growth* **290**, 6 (2006).

5 Zusammenfassung

Gegenstand der vorliegenden Arbeit bildet die Charakterisierung meso- und nanoskopischer kristalliner Halbleiterstrukturen mit modernen Methoden der Röntgenbeugung, direktabbildender Rastersondenverfahren sowie numerischer Simulationen. Dabei geht es zum einen um die Methodik zur Bestimmung struktureller Eigenschaften wie Form, Größe, chemischer Zusammensetzung und mechanischer Deformation. In Ensembles nahezu identischer Objekte spielt zusätzlich die Positions korrelation eine Rolle für das Streuszenario. Andererseits nehmen die zugrundeliegenden Mechanismen der Selbstorganisation eine herausragende Stellung ein. Dies beinhaltet sowohl die Entstehung einzelner Objekte (*self-formation*) als auch deren laterale und/oder vertikale Anordnung (*self-assembling*).

In hochauflösten Beugungsexperimenten lässt sich sehr genau die Variation des lokalen Gitterparameters bestimmen. Eine zentrale Ursache für mechanische Deformationen bildet die chemische Zusammensetzung. Fern von Absorptionskanten verschwindet deren direkter Einfluss auf die diffuse Streuung nahezu vollständig, während die mechanische Deformation als Kontrastmechanismus dominiert. Man kann jedoch von der diffusen Streuung ausgehend (allerdings über den Umweg der Deformation) auf die Komposition schließen - ein essentieller Punkt, um Wachstums- und Selbstorganisationsphänomene zu verstehen. Dabei geht es nicht allein um die Bestimmung gemittelten Parameter sondern vielmehr um möglichst dreidimensional und im Nanometerbereich aufgelöste chemische Profile.

Etwa die Hälfte der Veröffentlichungen beschäftigt sich mit LPE-SiGe/Si Inseln, wobei die entwickelten Verfahren allgemein anwendbar sind. Verallgemeinert betrachtet, zeigt sich hier (wie auch an den untersuchten selbstorganisierten Nanostrukturen im System InGaAs/GaAs) eine starke wechselseitige Beeinflussung von lokaler Strainverteilung während des Wachstums und sich ausbildender Morphologie.

Am Beispiel von SiGe/Si(001) Inseln wird exemplarisch ein zweistufiges, iteratives Verfahren vorgestellt, das ausgehend von numerisch (mittels der Methode der Finiten Elemente) bestimmten Deformationsfeldern die Verteilung der diffusen Streuung im reziproken Raum liefert. Auf diesem Wege lässt sich, unterstützt durch direkte Verfahren, die Entstehung solcher Inseln rekonstruieren. Es konnte gezeigt werden, dass das be-

reits von einer einzelnen Insel im Substrat verursachte Deformationsfeld die Entstehung lateraler Korrelation dominiert. Lineare Inselanordnungen entstehen durch Nukleation weiterer Inseln am Ende einer bereits bestehenden Formation und belegen damit einen kollektiven Charakter deformationsinduzierter Selbstorganisation.

Ein Teilespekt widmet sich der gezielten Beeinflussung von Selbstorganisation. Während sogenanntes *directed self-assembling* auf Template im engeren Sinn (beispielsweise lithographisch prozessierte Strukturen) verzichtet, lässt sich durch lokale anodische Oxidation nahezu jede beliebige Inselanordnung realisieren. Insbesondere können auf diese Art Stranski-Krastanow Inseln mit Strukturgrößen unterhalb des Gleichgewichtswertes gezüchtet werden.

Neben *quantum dots* werden in der Literatur zunehmend auch komplexere, niedrigdimensionale Halbleiterstrukturen mit wohldefinierter innerer Symmetrie diskutiert. Im Rahmen der Arbeit wurden u.a. *quantum rings*, sogenannte *quantum dot molecules*, aber auch lineare Strukturen wie *step bunches* und axiale Whisker in Hinblick auf die dem Wachstum zugrundeliegenden Mechanismen der Selbstorganisation untersucht. In vertikalen InGaAs/GaAs *quantum ring* Übergittern führt das Überwachsen zu einer Formänderung von ursprünglich zirkulären Ringen hin zu Ellipsoiden. Sowohl in dieser Probenklasse als auch für lineare Stufenbündel koppelt unterhalb einer kritischen Dicke der Zwischenschicht das durch die eingebetteten Nanostrukturen verursachte Deformationsfeld mit der darauf folgenden Lage und bildet damit die Ursache für eine vertikale Positions korrelation.

Der heteroepitaktische Einbau einzelner Germaniumschichten in axiale SiGe/Si Whisker führt aufgrund des lokal größeren Gitterparameters zu einer lateralen Expansion des Kristallgitters innerhalb der Schichten, jedoch infolge der Steifigkeit zu einer *Kompression* in der darüberliegenden Siliziummatrix.

Anhang

Während direktabbildende Verfahren im engeren Wortsinn *anschauliche* Resultate (im Ortsraum) liefern, bedarf die Interpretation von Intensitätsverhältnissen im Fourieraum einiger ergänzender Informationen. Im Folgenden sollen deshalb in gestraffter Form die verwendeten experimentellen Streu- bzw. Beugungstechniken und die damit zugänglichen Bereiche im reziproken Raum näher erläutert werden.

Für die anschließenden Überlegungen wird von einer einfallenden monochromatischen Planwelle mit Wellenvektor \vec{K}_0 ausgegangen. Unter der Voraussetzung elastischer Streuung bleibt die Länge des gestreuten Wellenvektors \vec{K}_s unverändert, und es gilt $K = |\vec{K}_0| = |\vec{K}_s| = 2\pi/\lambda$, wobei λ die Wellenlänge der Strahlung ist. Bei elastischer Streuung ist die Geometrie des Streuprozesses durch den Differenzvektor $\vec{Q} = \vec{K}_s - \vec{K}_0$ bestimmt.

Im Ortsraum geben die Wellenvektoren die Ausbreitungsrichtung von Wellen an, ihre Einheit ist jedoch $(\text{Länge})^{-1}$. Trägt man sie im reziproken Raum auf, so ergibt

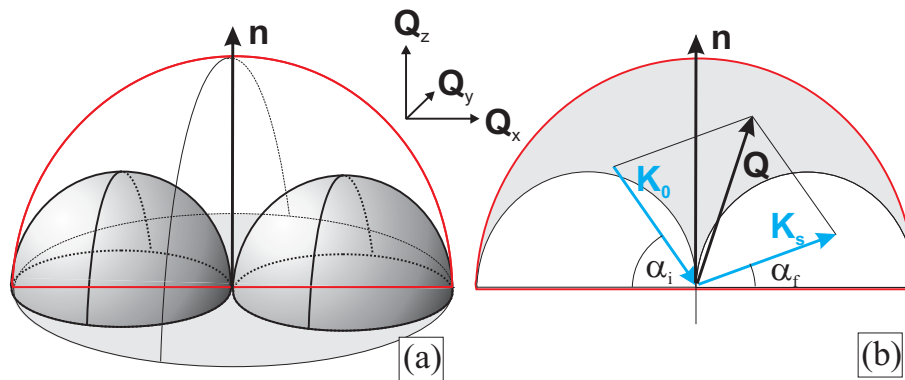


Abbildung 1: Modifizierte 3-dimensionale *EWALD*-Konstruktion. Der Radius der großen Halbkugel (a) beträgt $4\pi/\lambda$. Sie begrenzt für eine feste Wellenlänge λ den prinzipiell zugänglichen Bereich im reziproken Raum. Die Gebiete des reziproken Raumes innerhalb der beiden kleinen Halbkugeln, der sogenannten Laue-Zonen, sind für den Aufpunkt des Beugungsvektors \vec{Q} nur dann erreichbar, wenn entweder \vec{K}_s in den Kristall hineinzeigt ($\alpha_f < 0$) oder \vec{K}_0 von der Unterseite den Kristall beleuchtet ($\alpha_i < 0$) (Lauefall). Zeigt dagegen der Aufpunkt in den übrigen Bereich, so liegt der sogenannte Braggfall vor. (b) Halbkreisförmig berandet ist die Fläche komplanarer Streuung, die die Oberflächennormale \vec{n} enthält. Für alle anderen Gebiete enthält die durch \vec{K}_0 und \vec{K}_s aufgespannte Streuebene den Vektor der Oberflächennormale \vec{n} nicht (nicht-komplanare Streuung).

sich eine sehr praktische graphische Interpretation des Streuprozesses mit Hilfe der modifizierten *EWALD*schen Konstruktion, wie sie in Abb. 1 dargestellt ist. Im Rahmen dieser Konstruktion wird der reziproke Raum in zwei qualitativ verschiedene Bereiche aufgeteilt. In Bragg-Geometrie zeigt \vec{K}_0 in den Kristall hinein, \vec{K}_s hinaus, Abb. 1(b). Für jede mögliche Kombination der beiden Vektoren unter dieser Bedingung liegt der Aufpunkt des Beugungsvektors \vec{Q} innerhalb der großen Halbkugel, deren Radius $4\pi/\lambda$ beträgt, exklusive der Bereiche, die durch die beiden Halbkugeln halben Radius' begrenzt sind. Befindet sich der Aufpunkt dagegen in einer der kleinen Halbkugeln, so liegt Transmissionsgeometrie vor.

Maßgeblich für die Streugeometrie sind also die Winkel, die die Wellenvektoren \vec{K}_0 und \vec{K}_s in Bezug auf ein gewähltes Koordinatensystem einnehmen, siehe Abb. 1(b). Der Wellenvektor der einfallenden Welle \vec{K}_0 ist gegeben durch einen polaren Winkel α_i und den azimutalen Winkel β , analog ist \vec{K}_s über α_f und γ bestimmt:

$$\vec{K}_0 = \frac{2\pi}{\lambda} (\cos \alpha_i \cos \beta, \cos \alpha_i \sin \beta, -\sin \alpha_i) \quad (1)$$

$$\vec{K}_s = \frac{2\pi}{\lambda} (\cos \alpha_f \cos \gamma, \cos \alpha_f \sin \gamma, \sin \alpha_f) \quad (2)$$

Somit lässt sich der Beugungsvektor \vec{Q} schreiben:

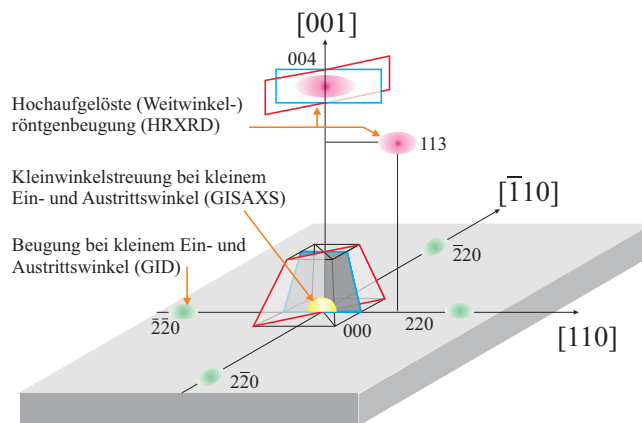


Abbildung 2: Beispielsweise definieren die in Kap. 2 eingehend behandelten SiGe Inseln im reziproken Raum aufgrund ihrer kristallographischen Orientierung zwei ausgezeichnete Beugungsebenen, die stellvertretend für alle anderen Reflexe in der Nähe des 004 Gitterpunktes eingezeichnet sind: (i) aufgespannt durch [001] und [110] (blau berandet) bzw. (ii) durch [001] und [100] (rot berandet).

$$\vec{Q} = \frac{2\pi}{\lambda} \begin{pmatrix} \cos \alpha_f \cos \gamma - \cos \alpha_i \cos \beta \\ \cos \alpha_f \sin \gamma - \cos \alpha_i \sin \beta \\ \sin \alpha_f + \sin \alpha_i \end{pmatrix} \quad (3)$$

Eine Streugeometrie heißt komplanar, wenn die Oberflächennormale \vec{n} in der von \vec{K}_0 und \vec{K}_s aufgespannten Streuebene enthalten ist, Abb. 1(b). Andernfalls ist die Geometrie nicht-komplanar. Wählt man das Koordinatensystem so, dass die z-Komponente in Richtung des nach außen gerichteten Normalenvektors zeigt, und \vec{K}_0 keine Komponente in y-Richtung besitzt, so ist komplanare Streuung auf die Q_x - Q_z -Ebene beschränkt.

Abgesehen von der Unterteilung in komplanar und nicht-komplanar differenziert man weitergehend je nach Lage des Aufpunktes von \vec{Q} noch zwischen verschiedenen experimentellen Streumethoden. In Abb. 2 sind die dabei zugänglichen Gebiete des reziproken Raumes anhand einiger ausgewählter Reflexe für einen [001]-orientierten kubischen Kristall eingezeichnet. Das Gebiet der hochaufgelösten Weitwinkelbeugung umfaßt Bereiche im reziproken Raum (hkl) mit l größer Null, wobei zu berücksichtigen ist, dass nur Reflexe mit $|\vec{Q}| \leq 4\pi/\lambda$ zugänglich sind. Man unterscheidet abhängig vom Vorhandensein einer Komponente Q_x symmetrische, bei denen diese verschwindet, und asymmetrische Reflexe. Mit der Kleinwinkelstreuung unter kleinem Ein- und Austrittswinkel tastet man die unmittelbare Umgebung des reziproken Ursprungs (000) ab. Die Beugung unter streifendem Ein- und Austritt stellt die extremste Form nicht-komplanarer Beugung dar. Der Beugungsvektor besitzt eine große laterale Komponente bei fast verschwindendem vertikalen Impulsübertrag. Dies umfaßt die Menge der Gitterpunkte (hkl) mit $l=0$ und $h>0$ oder $k>0$, von denen jene des Typs 220 grün in Abb. 2 eingezeichnet sind.

Die zunächst gemachte Voraussetzung eines divergenzfreien Primär- und gebeugten Strahles führt zu der Idealvorstellung, dass der Aufpunkt von \vec{Q} nur auf einen einzigen durch \vec{K}_0 und \vec{K}_s wohldefinierten Punkt im reziproken Raum zeigt. Das ist insofern vereinfacht, als dass aufgrund der experimentellen Primärstrahldivergenz, der endlichen Detektorakzeptanz und der Wellenlängenverteilung über ein bestimmtes Gebiet (das Auflösungselement) im reziproken Raum integriert wird. Dabei hängen Größe und Form dieses Gebietes stark von den experimentellen Gegebenheiten ab.

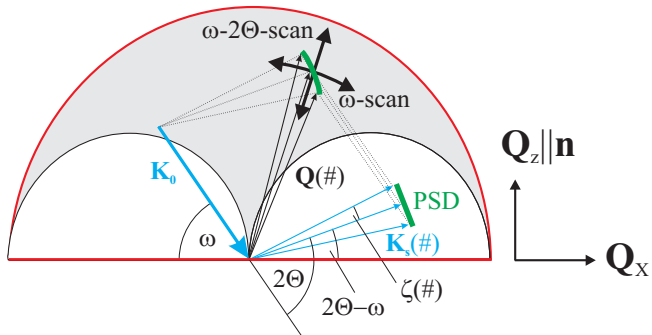


Abbildung 3: komplanare Geometrie mit positionsempfindlichem Detektor. Entlang des grünen Streifens (PSD) wird die Intensität ortsaufgelöst gemessen. Die Position auf dem PSD lässt sich im reziproken Raum am Aufpunkt von \vec{Q} abtragen. Damit ergibt sich eine anschauliche Interpretation des erfassten Bereiches im reziproken Raum. Durch systematische Veränderung der Winkel ω und 2Θ lässt sich eine 2-dimensionale Intensitätsverteilung messen. Ändert man beispielsweise ω und 2Θ im Verhältnis 1:2 ($\omega/2\Theta$ -Scan) bleibt die Richtung des Beugungsvektors erhalten, nur sein Betrag ändert sich. Das führt zur einer Verschiebung des Aufpunktes von \vec{Q} entlang seiner Richtung. Eine reine ω -Bewegung bedeutet Längeninvarianz für \vec{Q} . Der Aufpunkt beschreibt in diesem Fall einen Kreisbogen um den Ursprung.

Hochaufgelöste Röntgenbeugung²³

Zuerst wird der Fall hochaufgelöster komplanarer Weitwinkelbeugung diskutiert, bei dem die Beugung zunächst auf die Q_x - Q_z -Ebene beschränkt ist. Man spricht von einem symmetrischen Reflex, wenn die Netzebenennormale $[hkl]$ kolinear zur Oberflächennormale \vec{n} verläuft, von einem asymmetrischen Reflex, wenn beide einen Winkel ungleich Null einschließen. Der prinzipielle Unterschied zwischen symmetrisch und asymmetrisch besteht in dem Umstand, dass \vec{Q}_{symm} nur eine sehr kleine Komponente parallel zur Kristalloberfläche besitzt. Beim asymmetrischen Reflex setzt sich der Beugungsvektor dagegen aus einer parallelen und vertikalen Komponente vergleichbarer Größenordnung zusammen. Bei den meisten in dieser Arbeit untersuchten Proben, weisen die Substrate eine (001) Orientierung auf. Somit sind (00l) Reflexe symmetrischer Natur, während z.B. (113), (224) oder (404) asymmetrisch sind. Im komplanaren Fall folgt für β und γ direkt die Forderung $\beta=\gamma=0$. Damit vereinfacht sich (3) zu:

²³engl.: **H**igh **R**esolution **X**-**R**ay **D**iffraction (HRXRD)

$$\vec{Q} = \frac{2\pi}{\lambda} \begin{pmatrix} \cos \alpha_f - \cos \alpha_i \\ 0 \\ \sin \alpha_f + \sin \alpha_i \end{pmatrix} \quad (4)$$

Praktisch realisiert man das Abtasten des reziproken Raumes durch Winkelbewegungen eines die Probe tragenden Goniometers. Durch kombinierte Bewegungen von Probe und Detektor lässt sich der Aufpunkt des Beugungsvektors \vec{Q} prinzipiell zu beliebigen Positionen innerhalb des grau unterlegten Bereiches in Abb. 1(b) bewegen. Als Zwischenresultat erhält man eine winkelabhängige Intensitätsverteilung, die, um sie im reziproken Raum darstellen zu können, noch transformiert werden muss in eine Verteilung als Funktion reziproker Koordinaten.

Bei der Mehrzahl der Messungen kamen ein- und zweidimensional auflösende Detektoren (PSD bzw. CCD) zum Einsatz. Trägt man die Lage des Detektorfensters in Abb. 1(b) ein, ergibt sich Abb. 3, die in gewisser Vereinfachung eine Überlagerung von Orts- und reziprokem Raum darstellt. Einerseits ist das Detektorfenster als grüner Streifen am Aufpunkt von \vec{K}_s eingezeichnet. Dies entspricht der Position im Ortsraum. Auf den reziproken Raum übertragen, bedeutet dies ein simultanes Abtasten der Intensitätsverteilung am Aufpunkt von \vec{Q} entlang einer Linie. Da die Länge von \vec{K}_s stets $2\pi/\lambda$ beträgt, unterliegt diese Linie beim Übergang zum reziproken Bild einer leichten Verkrümmung. Dennoch erlaubt diese Darstellung eine sehr anschauliche Interpretation, welche Bereiche des reziproken Raumes bei einer bestimmten Konfiguration durch den Detektor überstrichen werden.

Röntgen-Kleinwinkelstreuung unter streifendem Ein- und Austritt²⁴

GISAXS ist eine Technik, mit der die Streuung unter kleinen Ein- und Austrittswinkeln in Vorwärtsrichtung untersucht wird. Dabei werden Bereiche des reziproken Raumes in der Nähe des Ursprunges abgetastet. Eng damit verwandt ist die Reflektometrie, die sich definitionsgemäß auf den komplanaren Teil beschränkt. Da unter diesen Bedingungen die Länge des Streuvektors sehr klein bleibt, ist GISAXS eine nahezu deformationsunempfindliche Methode. In gewisser Hinsicht erweist sich gerade dieses Nichtwahrnehmen als großer Vorteil von GISAXS, wodurch sich unabhängig vom Deformationszustand das

²⁴engl.: Grazing Incidence Small Angle X-ray Scattering (GISAXS)

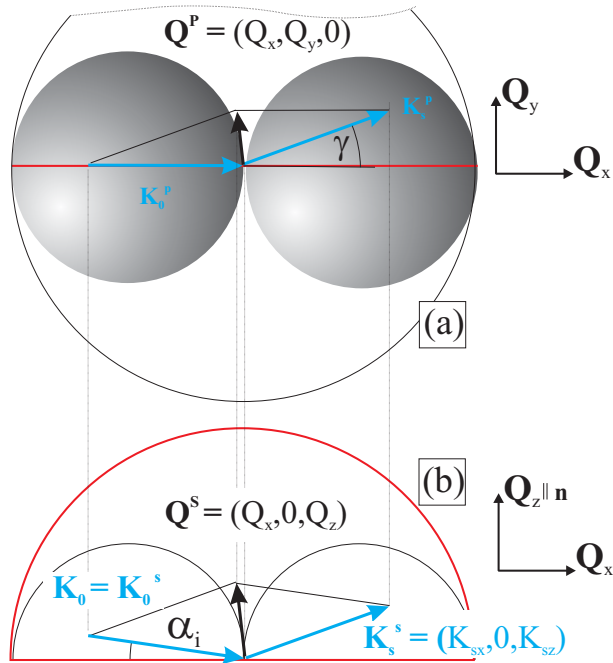


Abbildung 4: GISAXS Geometrie (a) projiziert auf die Q_x - Q_y -Ebene und (b) im Schnitt der Q_x - Q_y -Ebene. Während die laterale Komponente des Impulsübertrages als Funktion von Q_z in (b) durch die Lauekugeln begrenzt ist, gibt es in (a) eine solche Begrenzung für Q_y nicht. Da die diffuse Intensität im Allgemeinen schnell mit Q_z abfällt, liegt in diesem Vorgehen oft die einzige Möglichkeit, große laterale Impulsüberträge, respektive kleine Längen im Ortsraum, bei gleichzeitig kleinem Q_z abzutasten.

Dichteprofil untersuchen lässt.

Trotz vieler Gemeinsamkeiten zwischen GISAXS und *x-ray reflection* (XRR) gibt es insbesondere in Hinblick auf die *in-plane* erreichbaren lateralen Impulsüberträge bemerkenswerte Unterschiede. In Abb. 4 sind zwei aufeinander senkrecht stehende Schnitte durch den reziproken Raum in GISAXS Geometrie gezeigt. Der Wellenvektor der einfallenden Welle \vec{K}_0 trifft unter einem sehr kleinen Winkel α_i , der kleiner oder in der Größenordnung des kritischen Winkels der Totalreflexion $\alpha_{krit.}$ ist, die Oberfläche. Da die gestreute Intensität stark mit steigendem Q_z abfällt, ist man in der komplanaren Ebene in Teilbild (b) auf einen kleinen lateralen Impulsübertrag Q_x beschränkt. Diese Beschränkung lässt sich jedoch umgehen, indem man diese Ebene verlässt und Bereiche außerhalb untersucht, wo es selbst für den Extremfall $Q_z=0$ keine vergleichbare Begrenzung für Q_y gibt.

Für die Vermessung einer Intensitätsverteilung *in-plane*, also parallel zur Kristal-

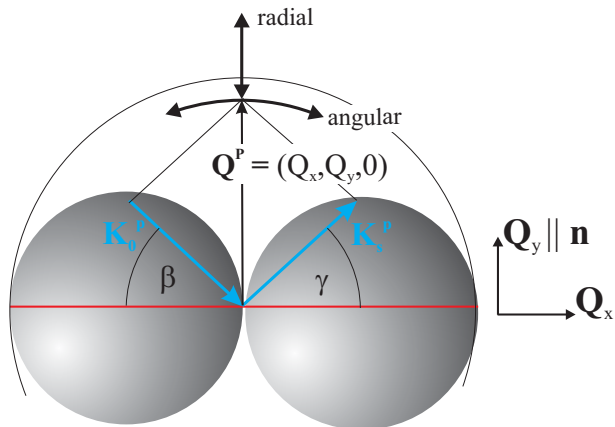


Abbildung 5: GID Geometrie in einem *in-plane* Schnitt. Der einfallende Strahl trifft die Kristalloberfläche unter einem kleinen Winkel α_i und wird an den senkrecht stehenden Netzebenen gebeugt. Der resultierende Beugungsvektor \vec{Q} unterscheidet sich dabei nur wenig von seiner *in-plane* Komponente Q^P . Durch gleichsinniges Verändern der Winkel β und γ lässt sich eine Intensitätsverteilung in radialer Richtung erfassen, ändert man β allein, beschreibt der Aufpunkt des Beugungsvektors einen Kreisbogen um den Ursprung (angularer Scan). Durch das Kombinieren beider Meßmodi lässt sich die Intensitätsverteilung 2-dimenional vermessen. Bei der Verwendung eines eindimensional auflösenden Detektors lassen sich so auch 3-dimensionale Intensitätsverteilungen erfassen.

oberfläche, empfiehlt es sich, den PSD horizontal (parallel zur Kristalloberfläche) zu stellen. Durch Rotation der Probe um ihre Oberflächennormale, lässt sich dann eine 2-dimensionale Intensitätsverteilung aufnehmen. Um dabei den sehr intensiven spekulär reflektierten Strahl (und damit Detektorübersprechen) zu minimieren, bieten sich prinzipiell zwei miteinander kombinierbare Möglichkeiten an. Zum einen kann mittels eines Absorberdrahtes vor dem PSD die sehr intensive spekulare Reflexion unterdrückt werden. Darüber hinaus lässt sich die Intensität nochmals deutlich verringern, indem die spekuläre Bedingung leicht verletzt wird, also $\alpha_i \neq \alpha_f$ gilt. Die damit verbundene außermittige Rotation des PSD um die Oberflächennormale ist bei den praktizierten Abweichungen einiger 0.1° jedoch vernachlässigbar. Mit horizontal positioniertem PSD kann man darüber hinaus auch *out-of-plane* Intensitätsverteilungen vermessen, wobei verschiedene Q_z -Werte bei konstantem lateralem Impulsübertrag durch gleichzeitiges Verändern von α_i und α_f im Verhältnis 1:1 realisiert werden.

Beugung unter streifendem Ein- und Ausfall²⁵

GID ist die extremste Ausprägung nicht-komplanarer Beugung. Als Folge sehr kleiner Ein- und Austrittswinkel nimmt die Oberflächennormale \vec{n} einen Winkel von etwa 90° gegen die Beugungsebene ein. Wegen sehr kleiner Vertikalkomponenten von \vec{K}_0 und \vec{K}_s besitzt der Beugungsvektor ebenfalls nur eine minimale vertikale Komponente, so dass GID nahezu unempfindlich auf vertikale Gitterdeformationen reagiert. Ein großer Vorteil (wie auch für GISAXS) besteht in der hohen Oberflächensensitivität. Diese resultiert aus dem raschen Abklingen des einfallenden Wellenfeldes mit zunehmender Tiefe im Regime der Totalreflexion.

In Abb. 5 sind die geometrischen Verhältnisse bei GID auf die Kristalloberfläche projiziert dargestellt. Zum einen lässt sich der reziproke Raum in radialer Richtung durch gleichsinniges Verändern von β und γ im Verhältnis 1:2 abtasten. In gewisser Weise komplementär dazu ordnet sich der angulare Scan ein, wobei nur die Richtung des Beugungsvektors, nicht jedoch dessen Länge geändert wird. Der Aufpunkt von \vec{Q} beschreibt bei Veränderung von β dann einen Kreisbogen um den reziproken Ursprung.

²⁵engl.: Grazing Incidence Diffraction (GID)

Tabellarischer Lebenslauf

Persönliche Daten

Name, Vorname:	Hanke, Michael
Akad. Grad:	Dr. rer. nat.
Geburtsdatum:	04.09.1972
Geburtsort:	Dessau
Nationalität:	Deutsch
Wohnort:	06773 Gräfenhainichen, Poetenweg 62
Familienstand:	verheiratet, ein Kind (geb. 31.07.1997)

Ausbildung

1979-1991	Polytechnische und Erweiterte Oberschule Gräfenhainichen
1991	Abitur
1991-1997	Physikstudium, Humboldt-Universität zu Berlin
05/1997	Diplom in Physik (mit Auszeichnung)
06/1997-07/2002	wissenschaftlicher Mitarbeiter am Institut für Physik, Humboldt-Universität zu Berlin
07/2002	Promotion (summa cum laude)
09/2003-11/2003	Wissenschaftlicher Assistent (C1) an der MLU
12/2003-10/2004	DFG Forschungsstipendiat NIST Gaithersburg, MD (USA)
seit 11/2004	Wissenschaftlicher Assistent (C1) an der MLU

Eingeworbene Drittmittel

12/2003-10/2004	DFG Forschungsstipendium HA3495/1-1 zum Thema <i>Röntgenographische Untersuchungen an hochperfekten Siliziumeinkristallen zur Bestimmung der Avogadrokonstante</i>
05/2005-12/2008	DFG Sachbeihilfe HA3495/3-1 zum Thema <i>Laterales Wachstum von Si- und SiGe-LPE Schichten auf struk- turierten Substraten</i>
2005	DFG Zuwendung zu einer Kongressreise HA3495/4-1
07/2007-06/2009	DFG Sachbeihilfe HA3495/5-1 zum Thema <i>Untersuchungen zum Wachstum von SiGe/Si Dots aus der Flüssigphase</i>

- 06/2007-05/2010** DFG Sachbeihilfe HA3495/6-1 zum Thema *Kohärente Röntgenstreuung an individuellen SiGe/Si Nanostrukturen*
- 06/2005-06/2008** Forschungsnetzwerk *Nanostrukturierte Materialien* des Landes Sachsen-Anhalt, Projekt NW3

Dienstanschrift

Martin-Luther-Universität Halle Wittenberg
Fakultät für Naturwissenschaften II
Institut für Physik - Festkörperanalytik
Hoher Weg 8
D-06120 Halle (Saale)
Tel.: +49/(0)345/5525452 Fax: +49/(0)345/5527212
email: hanke@physik.uni-halle.de

Halle, den 22.11.2007

(Dr. Michael Hanke)

Eidesstattliche Erklärung

Hiermit erkläre ich an Eides statt, dass die Habilitationsschrift selbständig und ohne fremde Hilfe verfaßt, andere als die angegebenen Quellen und Hilfsmittel nicht benutzt und die den benutzten Werken wörtlich oder inhaltlich entnommenen Stellen als solche kenntlich gemacht wurden.

Halle, den 22.11.2007

(Dr. Michael Hanke)